INTERACTIONS BETWEEN PROTEINS AND BIOMATERIALS - AN EXPERIMENTAL AND COMPUTATIONAL MULTISCALE STUDY

by

EVANGELOS LIAMAS

A thesis submitted to the University of Birmingham for the degree of DOCTOR OF PHILOSOPHY

School of Chemical Engineering
University of Birmingham
November 2017

Abstract

Understanding the interactions between proteins and biomaterials underpins the development of novel biomaterials that, depending on the application, could produce a specific response towards the surrounding tissue. In this thesis, a combination of molecular dynamics (MD) simulations and experimental techniques was deployed to systematically study the effect of the biomaterial surface chemistry on the adsorption of proteins, and the impact of protein adsorption on the wear of a metallic biomaterial. It was found that the surface chemistry could have a significant impact on the protein adsorption process because it affects the driving forces of adsorption, as well as the kinetics, the conformation, and the functionality of the adsorbed protein. Furthermore, the adsorbed proteins could greatly affect the lifetime of a metallic biomaterial via tribocorrosion process where the biomaterial surface is subjected to friction.

Single molecule force spectroscopy (SMFS) and quartz crystal microbalance (QCM) were used to study the adsorption mechanisms of fibronectin on -CH_3, -OH, COOH, and -NH_2 terminated alkanethiol self-assembled monolayers (SAMs). The same model surfaces were constructed in MD simulations to investigate the adsorption of a fibronectin fragment. It was found that the adsorption of fibronectin on charged surfaces is driven by electrostatic interactions, while on uncharged surfaces by van der Waals forces and hydrophobic interactions. Adsorption on positively charged and non-polar surfaces could denaturate the protein, whilst they adopt a "side-on" conformation. In contrast, proteins adopt a "head-on" conformation on negatively charged and polar uncharged surfaces, whilst the impact on the structural integrity of the proteins is insignificant. Adsorption on charged surfaces is specific, with the cell-binding site active on positively charged surfaces and inactive on negatively charged. In contrast, adsorption on uncharged surfaces

is non-specific, and the cell-binding site could be active or inactive depending on the trajectory of the protein during the adsorption. Furthermore, an electrochemical quartz crystal microbalance (EQCM) was utilized to investigate how the rate of the cathodic and anodic reactions on the surface of a metallic biomaterial could affect the adsorption of protein. It was found that an excessive amount of electrons on the titanium surface could decrease protein adsorption, whilst electron depletion could facilitate protein adsorption.

An EQCM and a tribometer were employed to investigate the impact of proteins on the wear of a metallic biomaterial. It was found that the presence of albumin inhibits the repassivation rate of oxide film by hindering the rate of cathodic reaction, while it also accelerates the rate of anodic reactions. Albumin could increase the degradation of titanium when it is subjected to friction by affecting the repassivation and the mechanism of mechanical wear, which is shifting from plastic deformation to delamination upon increasing thickness of the passive film. Electrochemical force spectroscopy was utilized to investigate the effect of albumin on the formed debris and its impact on the mechanical wear of titanium. It was found that albumin could significantly increase the mechanical wear of titanium by increasing the adhesion of debris onto the sliding interface and by acting as lubricant that enhances its rolling efficiency.

Overall, this thesis is a comprehensive multiscale study that combines experimental and computational techniques to highlight the importance of biomaterial surface chemistry on protein adsorption. The findings advance our understanding on the interactions between proteins and biomaterials and can provide a guide not only in designing surfaces that produce a specific response towards the surrounding tissue, but also in increasing their lifetime by reducing the mechanical wear at the sliding interface of metallic biomaterials.

Acknowledgements

This thesis represents the work of the past 4 years of my life. A long journey that shaped me to who I am today, through beautiful and difficult moments. I would like to take the opportunity and thank the people that made this journey possible, and me a better researcher and person.

First and foremost, I would like to express my sincere gratitude to my supervisor Dr Zhenyu J. Zhang for his continuous support and guidance, both professionally and personally. The joy and enthusiasm he has for research has been inspiring for me, and it has been an honour to be his first Ph.D student.

I would also like to thank Professor Owen Thomas, Dr Paul Mulheran, Dr Richard Black, Dr Karina Kubiak-Ossowska, and Dr Leo Lue for their guidance and precious help through this project.

A special thanks to Dr Anna Neus Igual Muñoz for making my academic mission to the Polytechnic University of Valencia a great experience.

My sincere thanks also go to the thesis committee, Dr Sophie Cox and Dr David Cheung, for their insightful comments that helped me to widen my perspectives.

I gratefully acknowledge the funding sources that made this Ph.D thesis possible. The department of Chemical and Process Engineering of University of Strathclyde, the school of Chemical Engineering of the University of Birmingham, and the COST-action fund.

Of course, a sincere thanks to all my colleagues and friends, the people I met and made this journey an unforgettable one.

Last but not least, I would like to thank my family (Evdoksia, Eleftheria, Theologos, Dimitris) for their unconditional love, support, and faith in me. I would have not made it without them and I hope that this thesis makes them proud.

Contents

List of Figures

List of Tables

List of Abbreviations

AM-AFM	Amplitude-modulation atomic force microscope
AFM	Atomic force microscope
bbc	Body-centred cubic
BSA	Bovine serum albumin
ECAFM	Electrochemical atomic force microscope
ECM	Extracellular matrix
EQCM	Electrochemical quartz quartz microbalance
FM-AFM	Frequency-modulation atomic force microscope
FN	Fibronectin
hcp	Hexagonal closed-packed
HSA	Human serum albumin
MC	Monte Carlo
MD	Molecular dynamics
MM	Molecular mechanics
OCP	Open circuit potential
PBS	Phosphate buffer saline
PHSRN	Proline-histidine-serine-arginine-asparagine
PME	Particle mesh Ewald
QCM	Quartz quartz microbalance
RGD	Arginine-glycine-aspartic acid
RMSD	Root-mean-square deviation
SAMs	Self-assembled monolayers

SMD	Steered molecular dynamics
SMFS	Single molecule force spectroscopy
SNOM	Scanning near field microscope
STM	Scanning tunnelling microscope
UHV	Ultra-high vacuum
VDW	Van der Waals

Chapter 1

Introduction

1.1 Motivation

Humankind has been using synthetic materials to replace tissue lost from an injury or disease from the antiquity [1]. Initially, such material was selected from the items available in the environment, such as wood or leather. Over the past century, naturally derived materials were replaced by more advanced materials such as polymers, ceramics, and metal alloys that have improved properties over their predecessors. Gradually, the advances over the years led to the field of biomaterials. Nowadays, biomaterials save and improve the lives of millions of people every year. They are used in a range of applications, spanning from artificial hips and vascular stents to contact lenses and cosmetic implants. The global market for biomaterials in 2016 was USD 70.90 billion and is projected to reach USD 149.17 billion by 2021, corresponding to an annual growth rate of 16 % [2].

An important aspect of biomaterials, regarding their biocompatibility, is their interaction with the surrounding biological systems. Unlike donor tissue or organs, synthetic biomaterials are not attacked by the immune system because they lack immunologically recognisable biological motifs [3]. However, when a biomaterial, such as a prosthesis or a medical device, is inserted into the human body, an injury is caused to the surrounding tissue that initiates the process of wound healing and a response towards the implanted biomaterial. The first of the multiple steps in such process is the interaction of the released proteins towards the biomaterial. Subsequently, the body begins the formation of a provisional matrix on the biomaterial that will provide a scaffold to direct the cells

towards the injury and will initiate procedures such as proliferation and differentiation. Eventually, an extracellular matrix (ECM) will be formed to replace the damaged tissue [4]. Therefore, the interaction between any biomaterial with the surrounding tissue is highly dependent on the ability of the provisional matrix, and more specifically of the adhesive molecules such as fibronectin, to adsorb onto its surface.

The adhesive proteins contain various sites that bind with other proteins or with cells during the formation of the provisional matrix. The conformation of the proteins upon adsorption will determine whether these active sites remain functional and able to bind with other proteins and cells, or will be hidden and, thus, inactive [5]. Therefore, an in-depth understanding of the biomaterial-protein interactions, and how it affects the properties of protein at the surface, is ultimately important to predict the response of the human body and design improved biomaterials and coatings. There are several factors that affect the interaction between protein and biomaterial surface, such as the surface properties of biomaterials, the properties of proteins, or other external factors, which will be discussed in detail in the following sections of this chapter. Since the physiological conditions in the body fluids and the properties of proteins cannot be modified, understanding how the surface properties of a biomaterial affect the adsorption process of proteins is the main theme in the present thesis.

Apart from the effect of surface properties of biomaterials on protein adsorption, the effect of proteins on biomaterials is equally important. Human body creates a very aggressive environment that affects the properties and lifetime of biomaterials when in contact. For instance, it can accelerate the corrosion of metallic biomaterials [6, 7], whose degradation is further enhanced in applications where friction takes place, such as in artificial joints or dental implants [8, 9]. A better understanding of how the presence of proteins affect the degradation and properties of an implanted biomaterial, would contribute to the development of biomaterials with expanded lifetime and improved functionality.

1.2 Aim and objectives

The aim of this thesis is to investigate the interactions between proteins and biomaterials surfaces, the adsorption of protein, and their implications on the corrosion and wear of metallic biomaterials that are used as implants. The result is a comprehensive multiscale study, which combines experimental and computational technique to study the interactions at the atomic scale, but also investigates the impact of protein adsorption on the lifetime of a metallic biomaterial.

On the first part of this thesis, which includes chapters 3 and 4, a combination of explicit solvent molecular dynamic (MD) simulations (Chapter 3) and advanced experimental techniques (Chapter 4) was used to investigate the effect of biomaterials surface chemistry on protein adsorption at the atomic and molecular level. The adsorption of proteins on biomaterial surfaces is driven by electrostatic, van der Waals, and hydrophobic interactions. To further understand how these forces affect the adsorption, four model surfaces were prepared using self-assembled monolayers to replicate a negatively charged, a positively charged, a hydrophobic, and a hydrophilic surface. Fibronectin was selected as a model protein because it is one of the main adhesive and cell-binding proteins. The protein adsorption trajectories in MD simulations were analysed to identify the driving forces of adsorption against each surface. The MD also provided an insight on the conformation of the protein upon adsorption, the impact of adsorption on the structural integrity of the protein, the mobility of the protein upon adsorption, and the availability of the cell-binding domain following adsorption. In order to study experimentally the interaction between single proteins and the aforementioned surfaces, an atomic force microscope (AFM) was used. Fibronectin was attached on the end of an AFM tip using a combination of gold-sulphur and His-Tag interactions, and single molecule force spectroscopy (SMFS) was performed against the SAMs surfaces. Furthermore, a quartz crystal microbalance (QCM) was used to quantify the amount of adsorbed fibronectin on each surface and correlate it to the individual interactions.

Chapters 3 and 4:

- Aim
  - Investigate the effect of biomaterials surface chemistry on fibronectin adsorption at the atomic and molecular scale
- Objectives
  - Construct, both computationally and experimentally, self-assembled monolayers that replicate a negatively charged, a positively charged, a hydrophobic, and a hydrophilic surface
  - Analyse protein adsorption trajectories, acquired from MD simulations, to identify the adsorption driving forces, as well as the kinetics, conformation, and functionality of adsorbed protein on the aforementioned surfaces
  - Quantify adhesion strength and adsorption amount of fibronectin on the aforementioned surfaces, using SMFS and QCM, and correlate it to the individual interactions

The second part of this thesis, which includes chapters 5 and 6, focuses on the impact of protein adsorption on the lifetime of a metallic biomaterial. Chapter 5 focuses on the effect of surface potential on the adsorption of protein, but also on the effect of protein on the corrosion of pure titanium. An electrochemical quartz crystal microbalance (EQCM) was used to quantify the adsorption of bovine serum albumin (BSA) onto a titanium surface, in order to understand how the surface potential affects protein-biomaterial interaction. Furthermore, the EQCM was used to quantify the effect of BSA on the corrosion behaviour of pure titanium under cathodic, anodic, and open circuit potential (OCP) conditions. Chapter 6 investigates the effect of proteins on the tribocorrosion behaviour of pure titanium. A tribometer was used to measure the effect of BSA in the mechanical wear and the accelerated corrosion of titanium surfaces under cathodic, anodic, and OCP conditions.

The wear was quantified with a confocal microscope. Furthermore, an electrochemical atomic force microscope was used to measure the impact of the debris in tribocorrosion applications, and to identify the effect of BSA on it.

Chapters 5 and 6:

- Aim
  - Investigate the effect of surface potential on the adsorption of BSA, as well as the impact of BSA adsorption on the corrosion and tribocorrosion of pure titanium
- Objectives
  - Quantify the adsorption of BSA on pure titanium under cathodic, anodic, and open circuit potential (OCP) conditions using an EQCM
  - Measure the corrosion of pure titanium on the presence and absence of BSA under cathodic, anodic, and OCP conditions using and EQCM
  - Measure the wear of pure titanium under cathodic, anodic, and OCP conditions in the presence and absence of BSA using a tribometer
  - Identify the role of debris on mechanical wear by measuring the interaction between debris particles and the titanium surface using an AFM

Chapters 3-6 will be published under the name stated on each chapter.

1.3 Proteins

Proteins are biomolecules that perform a large number of crucial functions in the human body. They provide mechanical support in the tissue, transport molecules, function as catalysts, control cell differentiation and proliferation, and transmit nerve impulses [10]. Their exceptional multi-functionality is a result of composition and structure.

The building blocks of proteins are amino acids consisting of a central carbon atom (α-carbon) that is attached to a carboxylic acid group (-COOH), an amino group (-NH_2), a hydrogen atom, and a specific functional side chain (-R), as shown in Figure 1.1. Because the amino acids are zwitterions, the carboxyl and amino groups can be charged depending on the surrounding environment. In neutral pH, the carboxyl group is deprotonated (-COO^-) and the amino group is protonated (-NH_3^+) [11]. However, in acidic solutions, only the amino group is charged, while in basic solutions only the carboxyl group is charged. There are 20 different amino acids found in proteins, which have a wide range of structural and chemical properties. Depending on the charge of their side chain, amino acids can be divided in four categories; polar uncharged (hydrophilic), non-polar (hydrophobic), positively charged, and negatively charged.

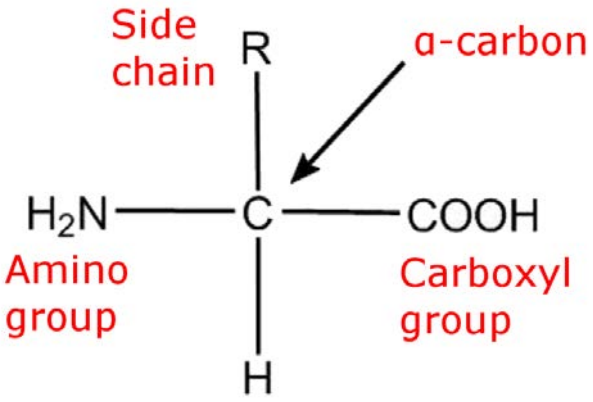

Figure 1.1: General representation of an amino acid. The important functional groups are labelled with red colour.

Proteins are formed when the carboxyl group of one amino acid and the amino group of another amino acid are linked together to form a peptide bond. The resulting molecule is called a dipeptide. A series of amino acid residues linked together form a polypeptide chain, which is consisted of a backbone of repeating units and distinctive side chains (Figure 1.2). By convention, the beginning of the polypeptide chain is the amino group (N-terminus) and the end is the carboxyl group (C-terminus). In neutral pH, the N-terminus is positively charged and the C-terminus negatively charged and, therefore, the polypeptide chain has a polarity. The linear sequence of the polypeptide chain is the primary structure of a protein

(Figure 1.3a). Proteins usually contain more than 50 residues in their polypeptide chain - considering that there are 20 available amino acids a tremendous number of different combinations is possible.

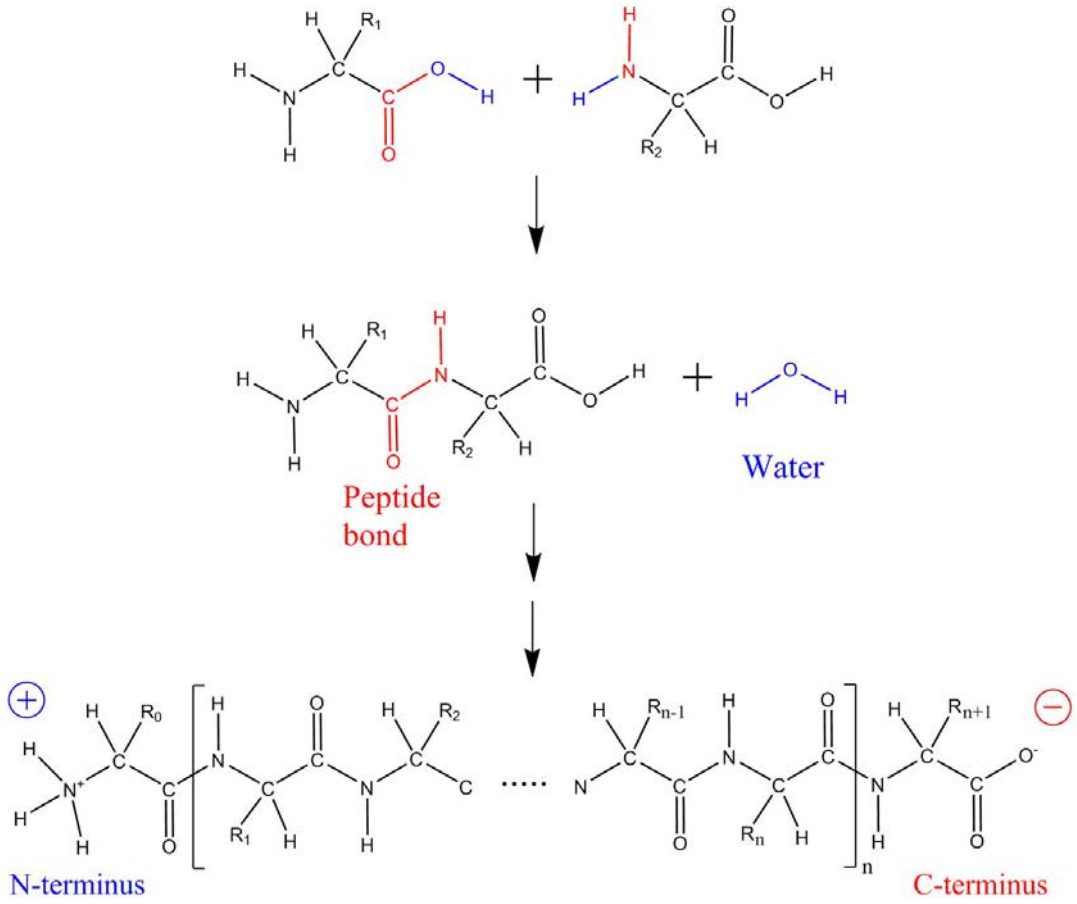

Figure 1.2: Representation showing the formation of a polypeptide chain where amino acids form peptide bonds during condensation reactions.

The polypeptide chain of the proteins do not remain in a linear structure but twists and bends due to the flexibility of the backbone bonds, which results in its three-dimensional structure. Although many structures can potentially be formed by the polypeptide chain, the most thermodynamically stable are the α-helix and the β-pleated sheet (Figure 1.3b). In the α-helix, the polypeptide chain forms a helix that has a rod-like shape. Every turn in the helix requires 3.6 residues and is stabilised by hydrogen bonds between the CO and NH groups of the backbone chain. More specifically, the CO group of each residue on the polypeptide chain forms a hydrogen bond with the NH group of the residue that is

four places ahead of it [10]. Consequently, all the hydrogen bonds are in parallel with the helix, while all CO groups facing towards one end of the helix and all NH groups towards the opposite. Furthermore, all the side chains of the residues are facing outside, which allows them to easily interact with their environment. The β-pleated sheet is consisted of adjacent extended domains of the polypeptide chain called β-strands (Figure 1.3b). The adjacent β-strands are stabilised by the formation of hydrogen bonds between the CO and NH groups of their backbones. Depending on the direction of the β-strands, the β-sheets can be parallel or antiparallel. Apart from α-helices and β-pleated sheets, polypeptide chains can also form loops and turns, which are not periodic. The division of the polypeptide chain to turns, α-helices, and β-sheets is referred as the secondary structure of the protein.

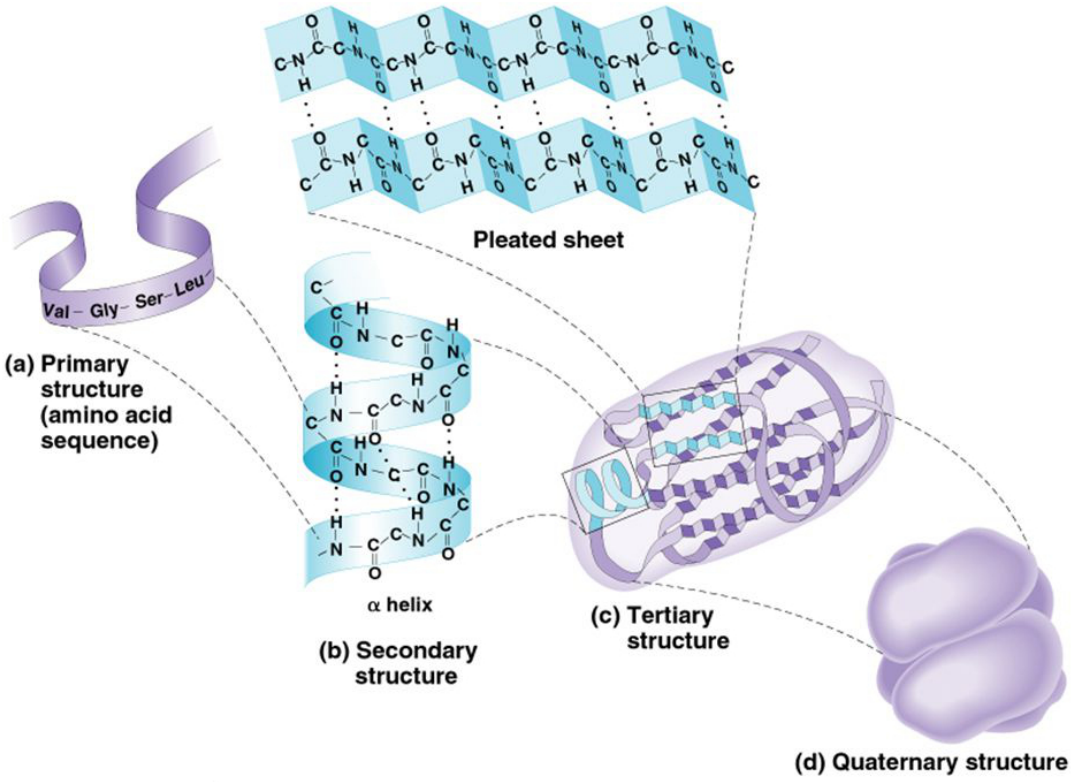

Figure 1.3: (a) Primary, (b) secondary, (c) tertiary, and (d) quaternary structure of a protein. Copyright Pearson Education Inc.

The three-dimensional structure of a whole protein is referred to as tertiary structure (Figure 1.3c) in which the interacting residues are present in distant sections of the protein.

As a contrast, the secondary structure is determined by the interactions between localized residues. Furthermore, while secondary structure is held together by hydrogen bonds between the backbone CO and NH groups of the polypeptide chain, the interactions between side groups are more important in the tertiary structure. There are four different types of interactions between side groups that resulting in the tertiary structure; hydrophobic interactions, covalent bonds, electrostatic interactions, and hydrogen bonds. These interactions are described in section 1.8. Possibly the most important driving forces in protein folding are the hydrophobic interactions. Because protein folding takes place in an aqueous environment, the polar and charged residues tend to remain exposed on the protein surface, while the hydrophobic residues are mainly buried in the core of the protein. While hydrophobic interactions drive the folding of the protein, van der Waals forces, covalent bonds between cysteines, electrostatic interactions between opposing charged residues, and hydrogen bonds between polar residues are stabilizing the molecular structure of proteins.

Some proteins, such as haemoglobin, consist of more than one polypeptide chain. Each polypeptide chain is called a subunit, and depending on the number of subunits a protein contains is called monomer, dimer etc. The subunits may or may not be identical with each other [11]. The interactions and the arrangements of subunits in proteins that consist of more than one polypeptide chain are referred to as the quaternary structure (Figure 1.3d).

It is apparent that the three-dimensional structure of the protein is determined by the residue sequence of its polypeptide chain. Protein folding is a highly cooperative process in which a specific amino acid sequence of a polypeptide chain will always result in the same protein conformation without accumulating intermediate structural forms [10]. It is the final conformation that makes a protein functional. For example, the active sites in enzymes that catalyse specific chemical reactions are composed of residues from different regions of the protein that came together after the folding. If the structure of the protein was altered, then the enzyme would become inactive and non-functional. There

are several reasons that can lead to denaturation of the protein such as pH, temperature, ionic strength, and adsorption that are explained in section 1.7.

1.3.1 Fibronectin

Fibronectin is a large glycoprotein that is found primarily in the plasma as a dimer. Glycoproteins are a group of protein that contain groups of covalently attached carbohydrates on their surface, which could protect the underlying polypeptide chain [12]. It is an essential protein that is involved in processes such as inflammation, wound repair, malignant metastasis, and thrombosis [13]. It is also used by bacteria as a "bridge" to invade the human cells [14].

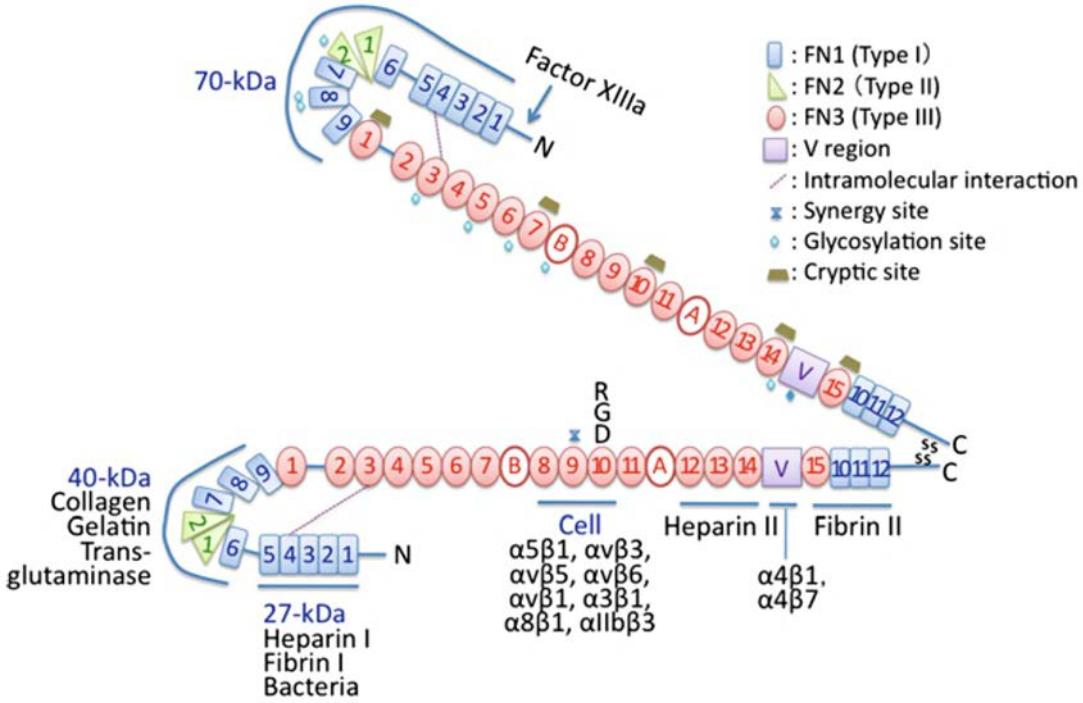

Figure 1.4: Diagram of the modular structure of fibronectin. Fibronectin is a dimer, consisting of two similar polypeptide chains linked at the C-terminus with two disulphide bonds. It contains 12 type I modules (blue squares), 2 type II modules (green triangles), and 15 type III modules (red circles). Fibronectin binds a range of receptors in different domains that are underlined in the figure. Adapted from [15].

Fibronectin is synthesized in the liver by hepatocytes and is found in the plasma with a concentration of approximately 300 µg/mL [15]. It consists of two subunits, each of them

having a molecular weight of 220 kDa and containing approximately 2500 residues [16]. The two subunits are similar but not identical, and are held together by a pair of disulphide bonds at the C-terminus (Figure 1.4). Each subunit is composed of three types of different modules; 12 type I (FNI), 2 type II (FNII), and 15 type III (FNIII) [17]. Each type I module contains approximately 45 residues, with 4 cysteines forming 2 disulphide bonds. They contain a covalent and a non-covalent binding site for fibrin, and have a key role for the assembly of the extracellular matrix. A typical type II module contains nearly 60 residues, with 4 cysteines forming 2 disulphide bonds perpendicular to each other. Among others, they bind with collagen and gelatin. Type III modules contain approximately 90 residues each, while none of them is cysteine. The lack of disulphide bonds makes the modules flexible. Each type III module contains 7 β-strands that form a "sandwich" of anti-parallel β-sheets, while the core between the two β-sheets is hydrophobic.

The main role of the FNIII modules is to mediate protein-protein interactions. The 10^{th} type III module (FNIII^{10}) contains the sequence arginine-glycine-aspartic acid (RGD), which is used to bind with cells through integrins present on their membrane. The RGD site is situated on the loop between the F and G β-strands and is approximately 10 Å exposed from the protein surface, which facilitates the interaction with the integrins. In addition, module FNIII^{9} contains the sequence proline-histidine-serine-arginine-asparagine (PHSRN) which is a synergy region that affects the specificity and affinity of the integrin binding. While both subunits in the fibronectin dimer contain the cell-binding region, only one is exposed in the solution and available for binding while the other is in a cryptic site. The binding of fibronectin with integrins is of crucial importance for the formation of the extracellular matrix and for cell processes such as adhesion, differentiation, proliferation, and migration [18].

1.3.2 Albumin

Albumin is a multifunctional protein that has the ability to bind with various ligands. It has a high affinity to metals such as Cu^{2+}, Mg^{2+} and Ca^{2+}, it is a reservoir of the signalling

agent nitric oxide, and transports a wide range of drugs, metabolites, nutrients and other molecules from the bloodstream to the target organs [19]. Due to the above properties it is used in a range of biochemical and pharmaceutical applications. Furthermore, because the sequence and structure of albumins from different organisms are very similar to each other, some albumins can be allergenic.

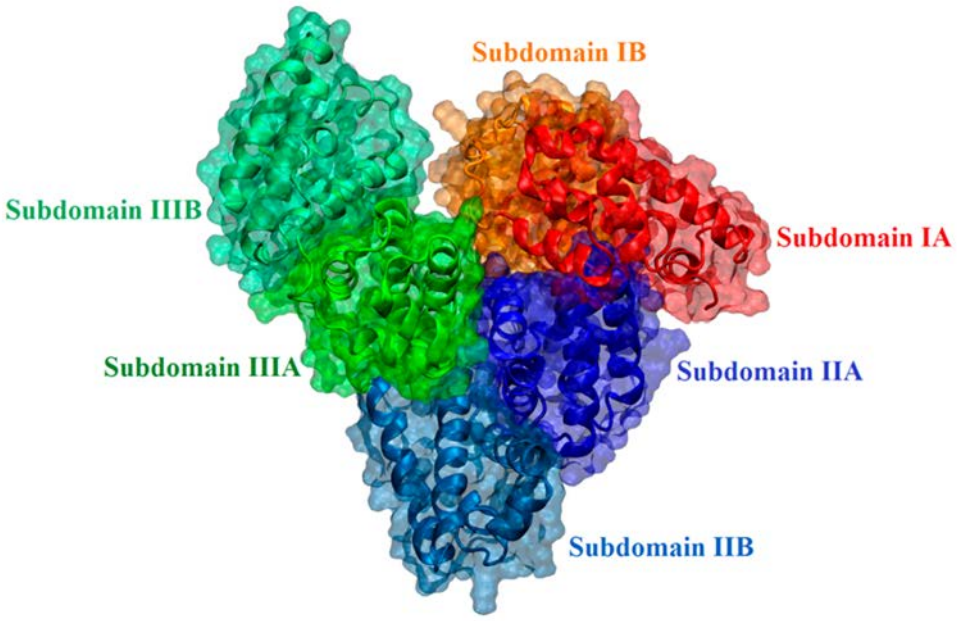

Figure 1.5: Schematic representation of the tertiary structure of albumin. The sub-domains are shown with different colours. Adapted from [20].

Albumin is the most abundant soluble protein in the human body and, hence, is widely studied. It is produced by the liver and is usually found in the plasma with a concentration of 50 mg/mL [21]. Human serum albumin (HSA) has a molecular weight of approximately 65 kDa and contains 585 residues that create 29 α-helices [22]. It is heart-shaped and is divided in three homologous domains, which are further divided in two sub-domains (Figure 1.5). Although the domains are similar in size and shape, only 20 % of their residue sequence is similar [23]. HSA contains 35 cysteine residues that create 17 disulphide bridges. The free cysteine is present on protein surface and can protect against oxidative damage, while it can also be used to label the protein or attach nanoparticles and other molecules on it [24–28]. The extended disulphide bond network enhances the structural integrity of albumins and as a result they do not denaturate easily [20]. Albumin has the

largest diffusion coefficient among serum proteins and is generally the first that adsorbs onto biomaterial surfaces before they are gradually replaced by proteins with a greater affinity towards the surface, such as fibronectin and fibrinogen [11]. Furthermore, albumin adsorption could reduce the friction and wear of polymeric biomaterials used as joints because it mediates the interaction of the sliding surfaces [29].

1.4 Biomaterials

A biomaterial can be defined as "any material of synthetic as well as of natural origin in contact with tissue, blood, and biological fluids, and intended for use for prosthetic, diagnostic, therapeutic, and storage applications without adversely affecting the living organism and its components" [30]. What differentiates biomaterials from other materials is that they must meet certain criteria of biocompatibility, which is the ability of a material to perform with an appropriate host response in a specific application [31]. Biomaterials are used to construct medical devices that find practice in a plethora of applications that save and improve the lives of millions of people every year. They replace damaged parts (kidney dialysis machine, artificial hip joints), improve functions (cardiac pacemakers, intraocular lenses), assist in healing (bone plates and screws, sutures), or even correct a cosmetic problem (mammoplasty and chin augmentation) [32].

An important aspect regarding the biocompatibility of materials is their interaction towards complex biological systems. There are several types of implant-tissue responses that are dependent on the properties of the biomaterial [3]. First of all, in the most undesirable case, surrounding tissue cells will die when the material used is toxic. If the material is nontoxic, there are three possible scenarios; (a) if it is biologically inactive, then a fibrous tissue of variable thickness will form around it, (b) if it is biologically active, it will interact with the surrounding tissue and will form strong bonds, and (c) if it is biodegradable, the adjacent tissue will gradually replace it. It should be noted that it is the surface of a biomaterial that interacts with the surrounding tissue and biological fluids. Furthermore, while the material itself dictates its mechanical properties, phenomena such

as corrosion, adsorption, friction, and lubrication all occur on the surface. Due to the lack of neighbour atoms, the properties of the surface tend to be different than that of bulk material, which results in a different response from the surrounding tissue.

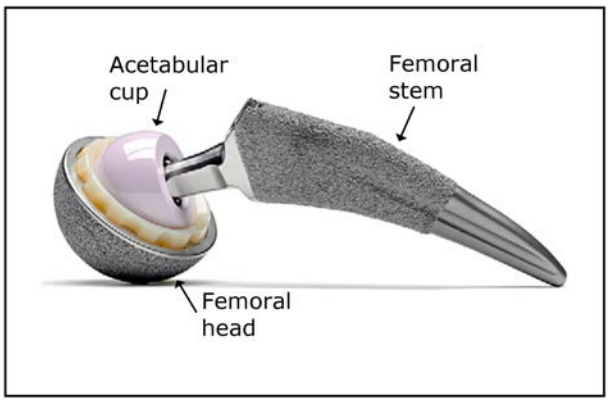

Figure 1.6: An artificial hip. The femoral stem is made from titanium alloy, the femoral head is alumina-zirconia ceramic, and the acetabular cup is made from ultra-high molecular weight polyethylene infused with vitamin E antioxidant. Adapted from [3].

There are three main classes of biomaterials, metallic, ceramic, and polymeric, with each of them associating with different advantages and disadvantages that are mentioned in the following paragraphs. In most medical implants, a combination of biomaterials is used to exploit their properties. A great example is an artificial hip joint, as shown in Figure 1.6. It combines the mechanical strength of metal alloys, with the low friction and durability of the ceramics, and the shock absorption of the polymers.

1.4.1 Polymeric biomaterials

Synthetic polymeric biomaterials are the most widely used materials in biomedical applications. Due to their flexibility, they are primarily used in cardiovascular devices and soft tissue augmentation, but also in orthopaedics, dental implants, and drug delivery systems [11]. Their main advantage over other biomaterials, such as metals and ceramics, is that they are resilient, easy to fabricate, relatively cheap, and can be available in a wide range of mechanical and physical properties. Some drawbacks of the polymeric biomaterials arise from the fact that they contain various chemical compounds, catalysts, and additives

required for their synthesis. These chemicals can be released overtime into the surrounding environment and initiate host reactions that can cause clinical complications.

Polymers are organic macromolecules, which are consisting of many repeating units linked together with covalent bonds. They can be linear or branched, while different regions of the carbon chain can interact between them with bonded (cross-linking) or non-bonded interactions. Changes in the molecular weight, the degree of cross-linking, or composition of the polymers have dramatic effects on mechanical properties and can be tuned to provide the desired result [33]. Due to the wide range of polymeric compositions, the surface can be polar, non-polar, positively or negatively charged. Therefore, the interaction of polymeric materials towards the surrounding tissue can greatly vary and could be tuned to initiate a desired response from the surrounding tissue.

1.4.2 Ceramic biomaterials

Ceramics are primarily used as components for biomedical implants, such as dental implants and hip joints. They are usually composed of inorganic compounds that are held together with ionic and covalent bonds. Due to the strength of these bonds, planes of atoms and ions cannot slip past one another, which make them very hard but brittle at the same time. Their advantages include strong resistance towards compression, low friction, and low wear rate. For this reason, they are used as coatings at sliding interfaces, such as the bearing surface of hip joints. Although they are among the most inert biomaterials, their major drawbacks are the poor tensile properties and brittleness. Ceramics such as hydroxyapatite have been used as coatings on metallic implants to enhance the fixation of bone to implants. However, delamination of the ceramic on the interface with the metal could lead to implant failure [11].

Ceramics can be classified in three categories; bio-inert, bio-active, and bio-degradable. Bio-inert ceramics, such as alumina, do not interact with the surrounding tissue and are resistant to corrosion. Upon contact with biological fluids, a fibrous tissue forms around them that can make the implant loose if not fixed tight. For this reason, they

are mainly used to support structurally other implants in the form of bone screws and plates. Bio-active ceramics, such as hydroxyapatite, interact with the surrounding tissue and form strong bonds with it. Accordingly, they are used as coatings on metal prosthesis to promote the integration with the surrounding tissue. Lastly, bio-degradable ceramics are slowly degraded upon implantation and are replaced by endogenous tissue [32]. They are primarily used in the form of artificial bone and they are mostly different calcium phosphate phases.

1.4.3 Metallic biomaterials

Metallic biomaterials are strong, ductile, and tough but may corrode. Biomaterials made from metal and alloys are primarily used in load-bearing orthopaedic applications, such as knee and hip prostheses, due to their high tensile and fatigue strength [11, 34]. At the atomic level, metals consist of positively charged ions that are held together by loosely bound electrons in a closely packed atomic arrangement. As a result, the position of the metal ions can be shifted without destroying the crystal structure and, thus, allowing plastic deformation. Some of the most widely used metals are titanium and its alloys, cobalt-chromium-molybdenum alloys, and stainless steel.

The biocompatibility of metallic implants is highly dependent on the surface oxide film, which acts as a barrier between the bulk metal and the surrounding biological environment. It not only protects the metal from corrosion but also provides an excellent interface to interact with the surrounding tissue [35]. Furthermore, it inhibits the release of metal ions that can combine with other biomolecules and cause allergies and cytotoxicity, such as alteration of osteoblastic cell behaviour or stimulation of cell functions [36,37]. However, in applications where the metallic biomaterial is subjected to mechanical friction, the passive film can be broken down. Consequently, it could cause several problems, such as the release of metal ions into the surrounding tissue, which would affect the biocompatibility of the implant.

Titanium

Titanium is one of the most commonly used metallic materials for biomedical applications, not only due to its outstanding mechanical properties but also its high biocompatibility. It is an allotropic material which, in its elemental form, has a hexagonal closed-packed crystal structure (hcp) for temperatures up to 882.5 °C (phase a). Above this temperature it transforms to body-centred cubic (bcc) (phase b) until its melting point at 1668 °C [38]. There are four grades of pure titanium, depending on the content of several impurities and especially oxygen which has a large effect on its strength and ductility [32]. In general, higher percentage of impurities leads to increased strength but reduced ductility. The addition of alloying elements to titanium allows to significantly change its mechanical properties by stabilizing phase a or b and favouring the properties of the desired phase. For instance, addition of elements that stabilize phase a, such as aluminium, result in alloys with higher strength. In contrast, addition of elements that stabilize phase b, such as vanadium, leads to alloys with higher hardness.

Due to its superior strength-to-weight ratio and its elastic modulus, which is similar to bone, it makes an ideal choice for orthopaedic implants [39]. In contrast, its poor shear strength makes it less ideal for applications such as bone screws and plates, whilst because it tends to gall it is not suitable in applications where there is metal on metal sliding. Titanium's excellent resistance to corrosion is a result of a titanium oxide (TiO_2) film formed on its surface in vivo conditions. The film has a thickness of approximately 10 nm and protects the metal from further oxidation [32].

Titanium and its alloys are generally characterized as inert biomaterials. Following implantation, a thin fibrous layer could form around the titanium that separates it from the surrounding tissue. To improve its bioactivity and osseointegration several chemical and physical surface modifications have been developed [40].

1.5 Corrosion

The biological fluids in the human tissue mainly contain water, dissolved gases, electrolytes, and proteins. As a result, they create a very aggressive environment for the materials that come in contact with it and can lead to corrosion [11]. Corrosion can be defined as "an irreversible interfacial reaction of a material with its environment, resulting in the loss of material or in the dissolving of one of the constituents of the environment into the material" [41].

As for metals, the corrosion is a result of an irreversible oxidation reaction (redox) between the metal and an oxidizing agent, which produces an oxidized metal and a reducing agent; the metal is oxidized by the oxidizing agent that consumes the transferred electrons. Therefore, all redox reactions consist of 2 partial reactions; an oxidation reaction (anodic partial reaction) and a reduction reaction (cathodic partial reaction) [42]. For instance, in the oxidation of iron, the corrosion is caused by the proton H^+ which is the oxidizing agent, as shown in reaction 1.1.

$$\begin{aligned} \mathrm{Fe} &\longrightarrow \mathrm{Fe^{2+}} + 2\,\mathrm{e^-} && \textit{anodic partial reaction} \\ 2\,\mathrm{H^+} + 2\,\mathrm{e^-} &\longrightarrow \mathrm{H_2} && \textit{cathodic partial reaction} \\ \hline \mathrm{Fe} + 2\,\mathrm{H^+} &\longrightarrow \mathrm{Fe^{2+}} + \mathrm{H_2} && \textit{overall reaction} \end{aligned} \tag{1.1}$$

The above reactions also show the transfer of electrons between the cathodic and the anodic reactions; the iron is oxidized while the hydrogen proton is reduced. Any chemical transformation that involves a transfer of charge at the interface between an electrode and an electrolyte can be defined as an electrochemical reaction [42]. Therefore, the corrosion reactions that involve oxidation of a metal are electrochemical reactions.

As described with the oxidation of iron, during corrosion the metal is oxidized to produce a dissolved ion M^{n+} and a transfer of n electrons per oxidized atom [43]. This can

be generalized in reaction 1.2 that describes an active dissolution where an active metal is in direct contact with the surrounding solution.

$$M \longrightarrow M^{n+} + ne^- \tag{1.2}$$

However, the metals and alloys that are used in biomedical applications are in the passive state where they have a thin oxide film formed on their surface. In this case a passive dissolution is taking place as shown in reaction 1.3.

$$M + nH_2O \longrightarrow MO_n + 2\,nH^+ + 2\,ne^- \tag{1.3}$$

The released electrons (ne^-) are consumed by the cathodic reactions, of which the most important in aqueous conditions are the reduction of hydrogen, the reduction of dissolved oxygen, and the reduction of water (reactions 1.4, 1.5, and 1.6 respectively).

$$2\,H^+ + 2\,e^- \longrightarrow H_2 \tag{1.4}$$

$$O_2 + 2\,H_2O + 4\,e^- \longrightarrow 4\,OH^- \tag{1.5}$$

$$H_2O + e^- \longrightarrow \frac{1}{2}\,H_2 + OH^- \tag{1.6}$$

A convenient way to study electrochemical reactions is with an electrochemical cell. It is a device that consists of two electrodes (working and counter electrodes) that are connected with an electric conductor (usually potentiostat) and are immersed into an electrolyte. The potentiostat can adjust the current between the working and a counter electrode in order to maintain the potential between working and reference electrode at the desired value. The potential of the electrodes is measured by a third reference electrode, which in the absence of an external current is called open circuit potential (OCP) or corrosion potential.

At OCP, the rate of cathodic and anodic reactions is the same and, therefore, the flow of current is zero. By applying well-defined potentials between the electrodes, the behaviour

of the metal under different corrosion conditions can be studied. For example, application of a cathodic potential will favour the reduction of hydrogen and oxygen (reactions 1.4 and 1.5). Because these reactions take place on the interface between electrode and electrolyte, the hydrogen ions and oxygen species must diffuse from the bulk solution [44]. While the external applied potential reaches more negative values, the rate of the reduction reactions is increased until eventually it exceeds the rate by which the species are transported on the interface. Consequently, the rate of diffusion of the aforementioned species becomes the limiting factor that controls the rate of the reduction. In contrast, application of an anodic potential favours the oxidation of the metal (reaction 1.3). The released metal ions react with water and form metal oxide (Figure 1.7). As the metal oxide (passive film) continues to grow, the rate by which the metal ions are leaving the metal surface is reduced, which in turn reduces the corrosion rate of the metal. Eventually, the thickness of the film reaches a maximum value and the current that passes through it becomes independent of the applied potential. However, a further increase of the potential will lead to transpassive dissolution, where the passive films breakdown.

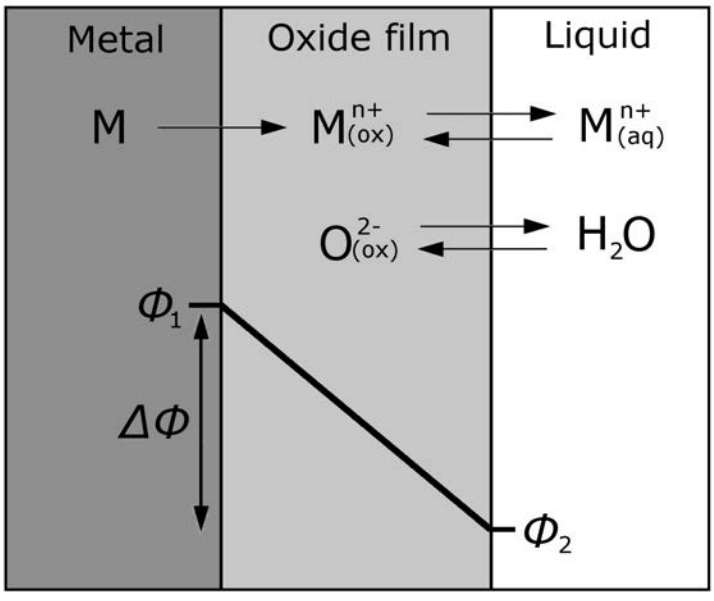

Figure 1.7: Schematic illustration of the current drop (Φ) through the passive film.

According to Faraday's law the current density that flows between the working and the counter electrodes, and consequently through electrode and electrolyte interface, is propor-

tional to the rate of the corrosion reaction. Therefore, by performing a potential sweep on the system, and measuring the current density at the same time, a potentiodynamic polarization curve can be produced that will provide information about the kinetics of the reaction [42]. There are three distinct regions during a potentiodynamic polarization curve: the active region, the passive region, and the transpassive region (Figure 1.8). In the active region, and up to the passivation potential, the surface of a metal is oxide free and the current is increased linearly with the potential. At the passivation potential, a transition of metal surface from the active to the passive state (passivation) occurs and an oxide film starts to form on the surface of the metal. As the film thickens, the current is reduced until eventually it reaches a plateau where the passive film reaches its maximum thickness. The passive state continues until a transpassivation potential is reached, where the passive film breakdown and the current is increased.

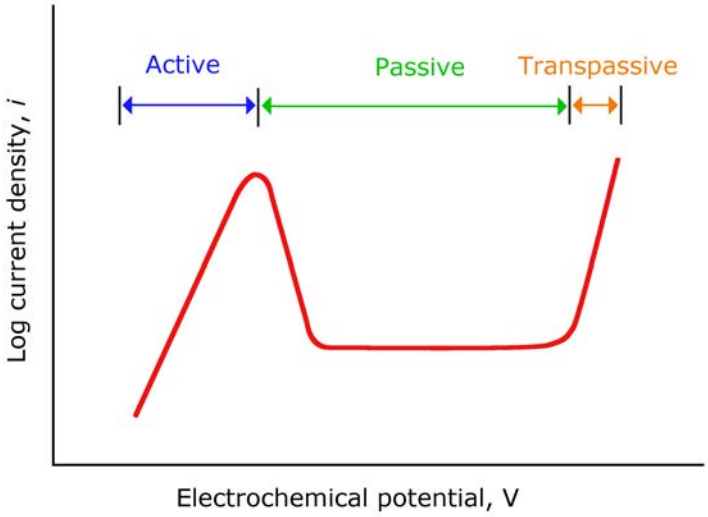

Figure 1.8: Schematic illustration of a polarization curve. The three distinct regions are shown with blue (active), green (passive), and orange (transpassive).

1.5.1 Tribocorrosion

The surface of metallic biomaterials are covered with a thin passive film that protects it from corrosion and increase the biocompatibility of the implant. The corrosion rate is limited by the following factors: a) the rate that metal ions are transported from the metal-film interface to the film-electrolyte interface, and b) the rate of dissolution of the

passive film [45]. Under normal conditions (non-corrosive, not subjected to mechanical damage), both processes are slow and the rate of corrosion is negligible. However, when the biomaterial is involved in applications where it is subjected to friction, the thickness of the passive film is gradually reduced and the active metal is exposed to the electrolyte. This results in active dissolution of the metal until, eventually, the passive film is reformed. The synergistic effect between corrosion and mechanical wear results in accelerated corrosion. A schematic illustration of the material flow during tribocorrosion between a passive metal (1st body) and an inert indenter (2nd body) is shown in Figure 1.9. During sliding the indenter detaches particles (3rd body) from the surface of the passive metal, which further accelerate the corrosion.

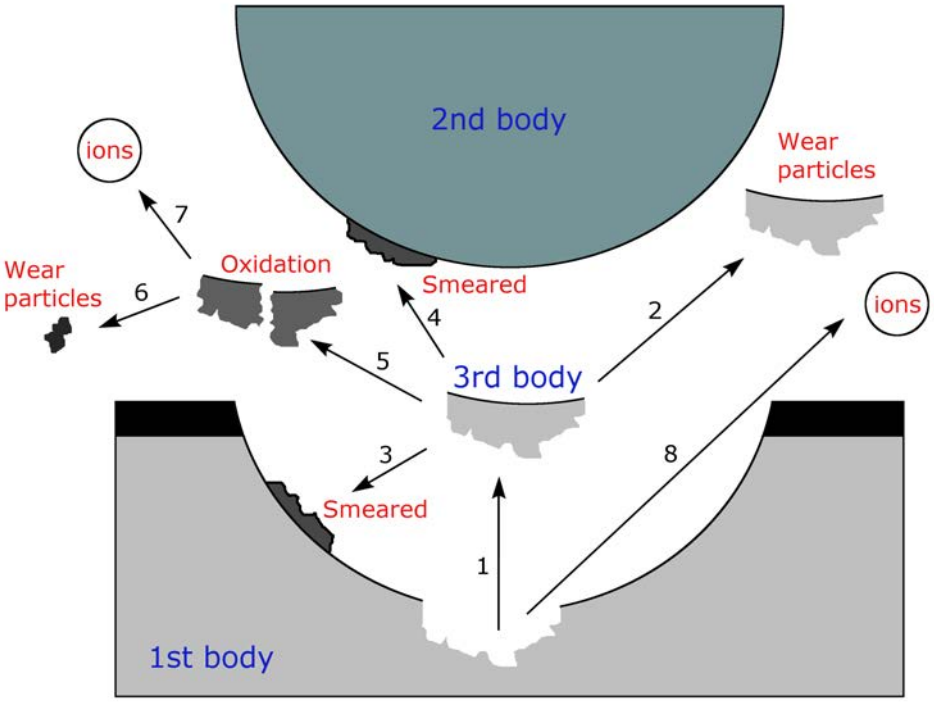

Figure 1.9: Schematic illustration of the material flow during tribocorrosion between a passive metal (1st body) and an inert indenter (2nd body). The sliding (1) detaches particles (3rd body) that can be (2) ejected from the contact, (3, 4) smeared onto the 1st and 2nd bodies, or (5) fragmented to smaller particles. The smaller particles can be then (6) rejected from the contact or (7) further corrode and release metal ions. Metal corrosion also occurs (8) from the 1st body after detachment of the particle. Modified from [43]

A tribocorrosion system combines both corrosion and mechanical wear as mechanisms of degradation. The two mechanisms create a complex system that cannot be considered

separately but rather a synergistic effect - corrosion is accelerated by wear and wear can be influenced by corrosion [46]. When the passive film is removed due to sliding, the active metal underneath is exposed to the aggressive environment (depassivation). Consequently, the corrosion rate is increased (wear accelerated corrosion) and the surface is quickly degraded. At the same time, the passive film has a significant influence on the mechanical wear of the surface. For instance, the oxide film can have a different coefficient of friction that can enhance or reduce the wear. Furthermore, the debris of the passive film could accumulate on the region of mechanical impact that can further increase the wear [47]. There are several techniques to study the tribocorrosion behaviour of a metal, such as potentiodynamic, corrosion potential, galvanic cell, electrochemical noise and electrochemical impedance spectroscopy, but one of the most convenient is the potentiostatic technique.

In the potentiostatic technique a fixed potential is applied in a three electrode set-up, and the potential is measured as a function of time while the sliding takes place. Consequently, this method can provide information about the state of the metal surface and the kinetics of the electrochemical reactions that occurring in the system. Prior to sliding, the flow of current is low due to the presence of passive film on the metal surface. However, upon sliding, the flow of current is increased by several orders of magnitude, which indicates that the current flows predominantly through the active metal area. The measured current is the sum of the current created by the anodic and the cathodic reactions. As explained earlier, at the corrosion potential the rates of the cathodic and the anodic reactions are in equilibrium and the measured current is zero. For anodic applied potentials, the rate of the reduction reactions is negligible and the current is due to the metal oxidation. In contrast, at cathodic potential the metal oxidation becomes negligible and the measured current is due to the rate of the reduction reactions. Some applications exploit this phenomenon to reduce the corrosion, by supplying extra electrons to the metallic surface in a technique known as cathodic protection [48, 49]. The total loss

due to the metal oxidation can be calculated using Faraday's Law (Equation 1.7) [43];

$$m = \frac{I \times M \times t}{n \times F} \tag{1.7}$$

where m is the oxidized metal mass during time t, I is the anodic current, M is the atomic mass of the metal, n is the oxidation valence, and F is Faraday's constant (96,500 C/mol).

Proteins can have a great impact on a tribocorrosion process because they influence the rate of anodic and cathodic reactions and, thus, the rate of corrosion [50–52]. Furthermore, the presence of proteins could lead to accelerated wear because they enhance the rolling efficiency of debris particles [53].

1.6 Self-Assembled Monolayers

In biomaterials applications, tailoring surface chemistry is an important aspect in order to produce the desired response from the surrounding tissue [54]. Self-assembled monolayers (SAMs) provide an excellent system to understand the interfacial phenomena due to their versatility and simplicity [55]. SAMs are molecular structures that are assembled from organic molecules after their adsorption on solid surfaces [56]. The adsorption can be spontaneous or epitaxial, while the adsorbates form crystalline and semi-crystalline structures. The SAMs molecules contain a functional "head" group that has an affinity towards the surface, and a "tail" group that contains the desired chemical group. There is a plethora of SAMs molecules that are tailored for a variety of surfaces and applications. However, the most extensively used and studied group are the alkanethiols [55].

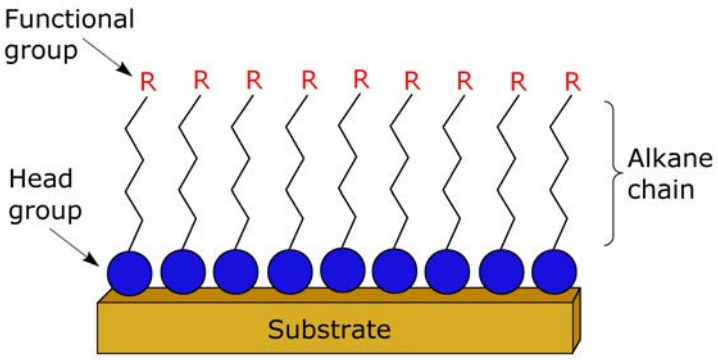

Figure 1.10: Schematic representation of self-assembled monolayers from alkanethiols. The head group (blue circle) binds onto the gold surface (yellow substrate) mainly with a sulphur-gold bond, while a range of functional end groups (red R) can be selected.

Alkanethiols are consisted of the ligand or "head" group which is sulphur, a terminal functional group, and a spacer (alkane-chain) that connects the two ends and has a varying length (Figure 1.10). Alkanethiols can adsorb on a range of noble metals, which is the group of metallic chemical elements that have an excellent resistant to oxidation, such as gold, silver, platinum, palladium, etc. However, most SAMs are prepared on gold because they have an inert character and are easy to prepare and handle in ambient environment. SAMs spontaneously form a two-dimensional assembly on the surface of the gold, driven by intermolecular interactions and bond formation of the SAMs molecules with the surface [55]. The intermolecular interactions in alkanethiols are hydrophobic interaction between the alkane-chains of the SAMs molecules. Furthermore, alkanethiols utilize the sulphur-gold bond to chemisorb onto the surface, which is considered to be an oxidative addition of the S-H bond, followed by a reductive elimination of the hydrogen that results in the formation of thiolate species [54, 57]. The metal-sulphur interaction stabilizes the SAMs molecules on the gold while the terminal functional groups determine the surface properties of the organic interface. The spacer, which acts as a physical barrier between the gold surface and the organic interface, can vary in length, depending on the number of carbon atoms on the backbone chain.

The resulted surface can be polar uncharged, non-polar, positively charged, negatively charged, or a combination of them. The surface chemistry of the organic interface can be

easily controlled by selecting the desired functional groups, whilst two or more alkanethiols solutions can also be combined to form mixed SAMs surfaces for further control of the surface chemistry and to replicate surfaces such as those found at multicomponent polymeric biomaterials [54, 58].

1.7 Protein adsorption

Protein adsorption is the first step that will determine the reaction of the tissue towards the implant. The second step, but equally critical, is the conformation of proteins after adsorption. If the cell-binding site on the adsorbed protein becomes inactive due to improper conformation, then a foreign body reaction could be initiated that could lead to implant failure [5, 59]. As described in section 1.4, the biomaterial surface can be active or inactive. If it is inactive (or non-fouling) the amount of adsorbed proteins on the surface of the biomaterial is low. Without having the proteins to mediate cell-binding on the surface, a fibrous film is formed around the surface that separates the biomaterial from the tissue. In some applications, such as in artificial blood vessels or heart valves where coagulation must be prevented, this is desired. In other cases, such as in artificial bones and hip joints, it is important for the biomaterial to develop a strong interaction and integrate with the surrounding tissue. In this case an active biomaterial surface is used that enhances protein adsorption.

Protein adsorption is driven by i) an increase in entropy caused by desorption of water molecules and ions from the biomaterial surface, as well as from protein structural alterations, ii) interactions between the protein and the surface (electrostatic and hydrophobic interactions, van der Waals forces, hydrogen bonds) [60]. It is a process that involves various steps and is affected by many factors that will be explained in the following sections. Although biological fluids are multicomponent solutions and several additional factors affect protein adsorption, such as protein-protein interactions and the Vroman effect that are discussed in the following chapters, single protein buffer solutions can be used to investigate the fundamental aspects of protein adsorption, such as adsorption kinetics and

interactions with surfaces. In order to adsorb onto a biomaterial surface the protein has to diffuse from the bulk solution onto the surface of the biomaterial. The size and the concentration of the protein will affect the rate of diffusion (section 1.7.1). Once the protein is in close proximity to the surface they will start interacting with electrostatic interactions, hydrophobic effect, van der Waals forces, and hydrogen bonds (section 1.8). Depending on the biomaterial surface properties, the protein will adopt a different conformation and orientation on the surface. For example, a positively charged surface will attract the negatively charged regions of the protein, while a negatively charged surface the positively charged regions (Figure 1.11b). Furthermore, proteins tend to adsorb more strongly on highly charged and on hydrophobic surfaces, which could result in denaturation and affect functionality. The adsorption could also lead in an orientation that can make the active site present on some proteins inaccessible and, thus, not available to perform its function (Figure 1.11b). Over time, the adsorbed proteins could spread on the surface and create more bonds with it, which could denaturate the proteins and affect their functionality. However, as the density of the adsorbed proteins is increased and the surface becomes saturated, the spreading is reduced by steric repulsion between adjacent proteins and the denaturation of the adsorbed proteins is reduced.

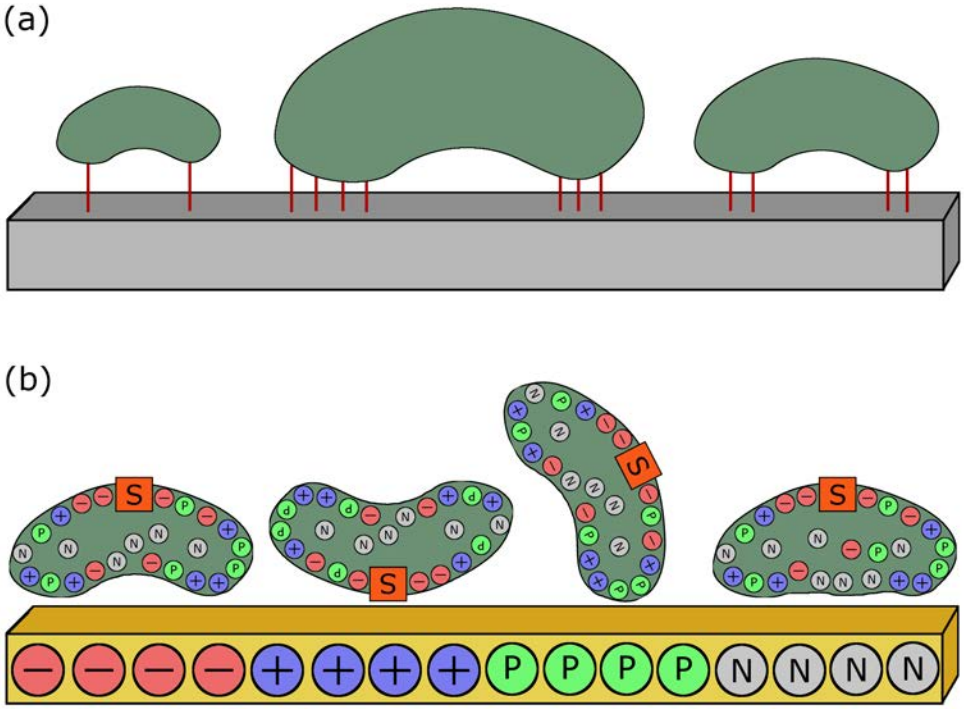

Figure 1.11: Schematic representation that shows (a) the higher affinity of larger proteins towards a surface, and (b) the effect of surface charge and hydrophobicity during protein adsorption, as well as the impact on the functionality of the adsorbed protein (the active site is indicated by S). The P and N indicate a positively and a negatively charged surface respectively.

Biological fluids are multicomponent solutions containing a plethora of proteins and molecules that could adsorb on the surface. The smallest particles in biological fluids are water molecules and ions, which are the first to adsorb onto the biomaterial surface due to their high diffusivity and concentration. Subsequently, proteins in the solution with high diffusion rates and concentration will arrive more quickly on the surface, followed by larger proteins. Over time, proteins with higher affinity towards the surface will replace proteins with lower affinity. This exchange of adsorbed proteins from those that have higher affinity is called "the Vroman effect" [61]. As seen in Figure 1.12, although proteins A and B arrived first on the surface and adsorbed, they were gradually replaced by protein C that has the highest affinity among them towards the surface.

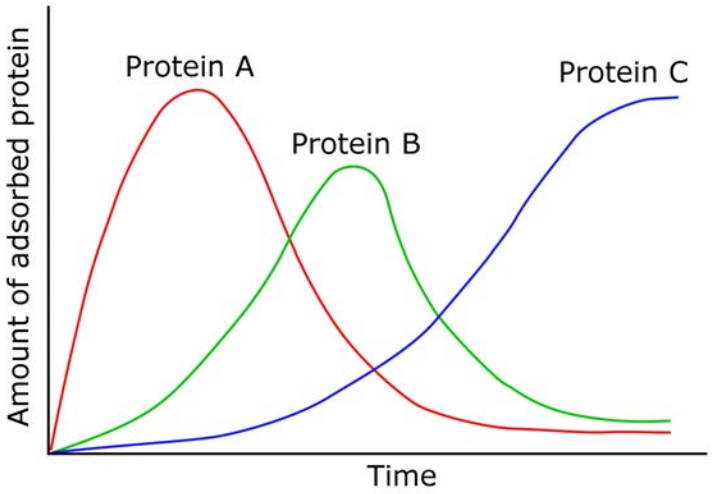

Figure 1.12: Example of the Vroman effect in a solution that contains three proteins. Protein A is adsorbed faster on the surface, followed by protein B and then protein C. However, the affinity of protein C towards the surface is larger and it will gradually replace the other 2 proteins.

There are three main aspects that influence protein adsorption; protein diffusion, adsorption kinetics, and protein affinity towards the surface. They will be discussed in details in the following sections.

1.7.1 Protein diffusion

In order for protein adsorption to take place, the proteins have to diffuse from the bulk solution onto the biomaterial surface. Diffusion is the random movement of particles along a concentration gradient in a system [62]. The concentration gradient can be caused by factors such as temperature, pressure, or by external forces such as gravity. Simple diffusion is described by Fick's second law (Equation 1.8):

$$\frac{\delta C}{\delta t} = D\frac{\delta^2 C}{\delta x} \qquad \textit{Fick's second law} \tag{1.8}$$

where C is concentration, t is time, D is the diffusion coefficient, and x is the distance. When the rate of diffusion equals the rate of adsorption and for short times Fick's second

law results in Equation 1.9 [11]:

$$\frac{\delta n}{\delta t} = C_0 \left(\frac{D}{\pi t}\right)^{1/2} \tag{1.9}$$

where n is the surface concentration of protein, C_0 is the bulk concentration of protein, and t is time. As can be seen in equation 1.9, a higher concentration of protein in bulk solution, as well as a larger diffusion coefficient, will result in a larger number of protein molecules arriving on the surface over time. The translational diffusion coefficient, D_t, is given by the Stokes-Einstein law (Equation 1.10) [63]:

$$D_t = \frac{\kappa T}{6\pi\eta r} \qquad Stokes - Einstein\ law \tag{1.10}$$

where κ is the Boltzmann constant, T is the temperature, η is the viscosity of the solution, and r is the radius of the protein. It is therefore seen in equation 1.10 that a higher temperature, as well as a smaller protein radius and lower solution viscosity, will result in a larger diffusion coefficient and, thus, a larger number of proteins arriving on the biomaterial surface over time.

1.7.2 Adsorption kinetics

The rate by which proteins adsorb on a biomaterial surface, the so-called adsorption kinetics, evolves as the adsorption progresses. Initially, proteins could adsorb onto the biomaterial surface rapidly. Consequently, the adsorption rate when plotted against time is linear, which is characteristic of a diffusion controlled process. At this stage the biomaterial surface has large empty spaces and the arriving proteins can adsorb anywhere. Gradually, as the surface of the biomaterial is covered with adsorbed proteins, the adsorption is inhibited by steric repulsion between approaching and adsorbed proteins. Consequently, the adsorption rate is decelerated until it eventually reaches a steady-state where the whole biomaterial surface is covered with proteins (Figure 1.13).

The adsorption of proteins onto the biomaterial surface up to a point where they fill

a closed-packed monolayer can be explained by the Langmuir adsorption isotherm. It shows that as the bulk concentration of protein is increased, the total amount that is being adsorbed onto a surface is increased until it eventually reaches a plateau (saturation value) at higher protein concentrations [64]. The Langmuir isotherm equation is given by Equation 1.11 [3]:

$$\theta = \frac{[P]}{K_D + [P]} \tag{1.11}$$

where θ is the fractional occupancy of the surface (ranging from 0 to 1), [P] is the bulk concentration of protein, and K_D is the dissociation constant for the protein surface interaction.

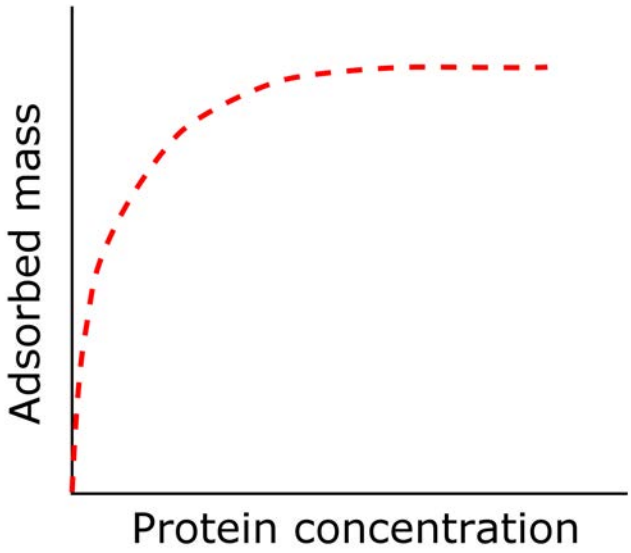

Figure 1.13: Example of protein adsorption following the Langmuir adsorption isotherm. Initially, the adsorption rate is increased linearly with the protein concentration. Gradually, the adsorption rate is reduced until it eventually reaches a plateau.

The Langmuir adsorption isotherm model requires four conditions to be satisfied by a system in order to describe sufficiently the adsorption [65]: i) the adsorption sites must be of equal adsorption energy, ii) each site can bind only one molecule, iii) the adsorbed molecules do not interact with each other, and iv) the adsorption must be a dynamically reversible process. However, a typical protein adsorption process can violate these conditions because: i) a protein undergoes structural conformation upon adsorption

that can change the energy and size of the adsorption site, ii) due to protein aggregation a site can bind more than a molecule, iii) protein-protein interaction have a significant impact on the adsorption process, and iv) the adsorption can be effectively irreversible with different degrees of spreading and packing. Therefore, although protein adsorption isotherms take often the shape of a Langmuir isotherm, the conditions are rarely satisfied, such as in cases of surfaces that have a very low affinity for protein adsorption. Still, although there are other models that can describe protein adsorption, such as the Freudlich or the BET model, the Langmuir model remains the best model to describe an protein adsorption process.

1.7.3 Protein-biomaterial affinity

The affinity between proteins and biomaterials is affected by: (a) the protein properties, (b) the properties of biomaterial surfaces, and (c) external factors.

Protein properties

The protein properties that influence protein adsorption are the composition, the size, and the structural integrity. As described earlier, proteins are composed of residues that self-assemble in an aqueous environment. Generally, the hydrophobic residues are buried in the core of the protein while the hydrophilic (neutral and charged) residues are exposed and available to interact with surfaces. Consequently, the overall charge of the protein, as well as the distribution of charge on its surface, can significantly influence protein adsorption.

Apart from composition, larger proteins are more likely to have a larger area of interaction with surfaces upon adsorption. Consequently, a greater amount of interactions with the surface could result in stronger adhesion in comparison to smaller proteins (Figure 1.11a).

Lastly, proteins with a small amount of cross-linking in their structure are more likely to unfold to a greater extent during their adsorption onto the surface. Consequently, a

greater area of interaction with the surface could result in a greater adhesion [11].

Surface properties

The surface properties that influence protein adsorption can be grouped in three categories; geometrical, chemical, and electrical [11]. Surfaces with topographical features not only provide an overall larger surface to interact with proteins but also provide more sites where the protein can adsorb. For instance, if the protein is adsorbed next to a step or in a groove, then the area of interaction with the surface will be greater, which could enhance the adhesion.

Depending on the chemical composition of the surface, the type of interaction towards the surface will be different. Due to the polyelectrolyte nature of the protein, a charged surface will develop electrostatic interactions with the protein; a positive surface will attract the negative patches of the protein, while a negative surface the positive patches. Similarly, on polar but neutral surfaces, the protein-surface interactions will be dominated by van der Waals interactions and hydrogen bonds, whilst a hydrophobic surface could cause the protein to expose its hydrophobic core on the surface (Figure 1.11b). The surface could also have patches with different chemical composition that would lead to a different conformation of protein upon adsorption.

Lastly, the potential of a surface could also affect protein adsorption. For example, during metal oxidation a number of ions and electrons are present on the metal-electrolyte interface. This charged species could attract positively or negatively charged regions of the protein and, thus, affect protein adsorption.

External parameters

The external parameters that influence protein adsorption are: temperature, ionic strength, pH, and buffer composition. An elevated temperature could result in higher diffusivity of the protein through the solvent and generally increase the amount of adsorbed protein [66].

When the pH of a solution is equal to the isoelectric point of a protein (pI) the protein

contains the same amount of positive and negative charged species and the net balance of the protein is zero. However, when the pH is lower than the isoelectric point then the carboxylic groups of the residues are protonated, which result in the protein acquiring an overall positive charge. In contrast, at pH higher than the isoelectric point the amino groups of the residues are deprotonated and the proteins have an overall negative charge. Consequently, pH has a significant influence in protein adsorption since if the protein and the surface have opposite charge they will be attracted and the adsorption will be accelerated [67]. Also, because at the isoelectric point the electrostatic repulsion between proteins is equal to zero, a higher packing density can be achieved during adsorption.

The ionic strength of a solution determines the Debye length, which is associated with the damping distance of the electric potential created around charged proteins and surfaces. A higher ionic strength reduces the Debye length and the electrostatic interactions become shorter, which can lead in protein aggregation. Consequently, the interactions between like charges are enhanced while interactions between opposite charges are hampered [67].

Lastly, some substances promote protein precipitation (kosmotropes) while others decelerate it (chaotropes) [68].

1.8 Types of interactions

When a protein arrives on the surface of a biomaterial it interacts with it through noncovalent bonds. Noncovalent bonds release only 1-5 kcal/mol energy when they are formed, which is approximately 10-100 times lower than that of covalent bonds [69]. These bonds are weak and transient in physiological conditions. However, when a large number is formed simultaneously they produce a large enough force to adhere a protein onto a surface. There are four types of noncovalent interactions, of varying strength and of different nature, that occur during protein adsorption: electrostatic interactions, van der Waals forces, hydrogen bonds, and hydrophobic interactions.

1.8.1 Electrostatic interactions

Electrostatics interactions are long-range interactions between charged species or particles. They can be either attractive or repulsive, depending on the charges; alike charges repel each other, while opposite charges are attracted. The energy of electrostatic interaction, E, is given by the Coulomb's interaction (Equation 1.12):

$$E = \frac{kq_1q_2}{Dr} \tag{1.12}$$

where k is the Coulomb's constant (k=9.0×10^9 J·m·C^{-2}), q_1 and q_2 are the signed charges of the particles, D is the dielectric constant, and r is the distance between the charges [70]. The electrostatic interactions in a solution are greatly affected by the ions present in the solution. Generally, an increased number of ions present in a solution lowers the energy required to break an electrostatic bond. The interactions between charged residues of a protein, as well as the interaction between them and charged surfaces, are determined by electrostatic interactions.

1.8.2 Hydrogen bonds

The hydrogen bond is essentially an electrostatic interaction, which has a major influence on the structure of the proteins during folding and helps to stabilize them. It is formed when a hydrogen atom that is bound to an electronegative atom, such as oxygen and nitrogen, is shared with another electronegative atom [71]. The electronegative atom that is covalently bound to hydrogen is pulling electron density from the hydrogen leaving it partially positively charged. Consequently, it can bind with a partially negatively charged atom through electrostatic interaction. The group that contains the electronegative atom tightly linked to the hydrogen is called hydrogen-bond donor, while the electronegative atom that is less tightly linked to the hydrogen is called hydrogen-bond acceptor. The distance between atoms forming the hydrogen bond is shorter than van der Waals interactions and close to a covalent bond. Furthermore, the energies associated with hydrogen bonds are

between those for van der Waals forces and covalent interactions.

The hydrogen bond is directional, and therefore its strength is greatly affected by the angle between donor, acceptor, and hydrogen; it has the highest strength when the three atoms participating in the hydrogen bond (the two electronegative atoms and the hydrogen) are aligned on a straight line. The hydrogen bond between water molecules is one of the strongest among many other hydrogen bonds in biological systems, as a result of the electronegativity of the molecule and the optimum angle of the hydrogen bond [69].

1.8.3 Van der Waals forces

Van der Waals forces are weak, non-specific attractive forces between two atoms or molecules when they come very close to each other, which arise from electrostatic interactions of permanent and/or induced dipoles [70]. There are three types of van der Waals forces; permanent dipole-permanent dipole interactions, permanent dipole-induced dipole interactions (also known as Debye force), and induced dipole-induced dipole interactions (also known as London dispersion forces). They are of varying strength and are responsible for a plethora of interactions between non-bonded neighbouring atoms.

Permanent dipole-permanent dipole interactions are the strongest of the three although weaker than electrostatic interactions between charged species. They are formed between dipole molecules/groups and they usually contain highly electronegative atoms covalently bonded with less electronegative atoms. During their interaction they usually tend to align the dipoles in order to increase the attraction force. Their energy is depended on their distance with a factor of r^{-3} and is reduced rapidly with the distance.

When a neutral group is approached by a permanent dipole then its electrons are polarized according to the approaching dipole. A dipole moment is induced on the neutral group and forms an attractive interaction with the permanent dipole (Debye force). The Debye forces are much weaker than the permanent dipole-permanent dipole interaction.

The London dispersion forces are the weakest interactions of the three. They are formed between neutral molecules/groups due to rapid random fluctuations of their electrons,

which can create an uneven distribution of electrons and, thus, a short term dipole [69]. London forces are important only for atoms that are in contact because their energy is proportional to r^{-6}.

1.8.4 Hydrophobic interactions

Non-polar substances are poorly dissolved in water and they tend to aggregate. This is called the hydrophobic effect. Although it appears that there is an attractive force that is bringing the non-polar molecules together, in reality it is a pseudo force [71]. The acting force that is resulting in aggregation of non-polar molecules is their exclusion from the aqueous phase. The exclusion is entropically driven because the surface of an aggregate that contains hydrophobic molecules is smaller than the sum of the surface area that the molecules would individually occupy [70]. The hydrophobic interactions are the dominant driving forces in protein folding and become very important when proteins are adsorbed onto hydrophobic surfaces.

Chapter 2

Methodology

2.1 Atomic Force Microscopy

2.1.1 Introduction

Atomic force microscope (AFM) belongs to the family of scanning probe microscopes, which includes the scanning tunnelling microscope (STM) and the scanning near field optical microscope (SNOM) among others. It is a relatively modern technique since it was first discovered by Binnig, Quate, and Gerber in 1986 [72]. Since then, its popularity among the scientific community has been increased and has opened new perspectives in the investigation of surfaces.

AFM has similar working principles with a phonograph, where a stylus moves on the surface of a vinyl disk and tracks any surface features to produce sound. A sharp probe is mounted on the end of a flexible microcantilever whose movement is detected with a laser beam. By bringing the tip in contact with a sample and raster-scanning an area on it, a three-dimensional representation of the surface could be produced. Thus, AFM obtains the images by "sensing" a surface with a sharp probe rather that "seeing" it as it happens in radiation based microscopes (such as optical or electron microscopes) [73].

Consequently, new possibilities of interacting with a sample are being opened, which offers AFM a range of advantages over other imaging techniques. For example, the maximum resolution of optical microscopy is approximately 200 nm due to the limitation by the wavelength of light. However, the maximum resolution by AFM is only limited by the probe-sample interactions, as well as the tip radius. Therefore, a lateral resolution of $<$

1 nm and a vertical resolution of ~ 0.1 nm can be achieved [74]. Furthermore, since AFM probe is in direct contact with the sample, it can provide a range of other information regarding the probe-sample interaction, and even allows the direct manipulation of the sample at the molecular level. However, what really puts AFM in a class of its own is that it can perform under a broad range of environments (air, vacuum, or liquid) and does not require any complicated or invasive sample preparation, while the sample can be reused after imaging. This makes it highly versatile and opens many opportunities in the field of biological investigations because proteins, cells, and other biomolecules can be studied in their natural environment with the minimum disturbance.

Due to its ability to provide high resolution morphological images under physiological conditions, AFM has been used in the studies of biomolecules such as DNA [75–77], proteins [78–82], cells [83–85], bacteria [86, 87], and cell membranes [88]. Besides imaging, AFM can be used for more sophisticated analyses due to its ability to investigate the surface interactions of a sample, or to study intermolecular and intramolecular interactions. Among others, AFM was used to investigate the adhesion forces of the biotin-avidin complex [89], the interaction between membrane receptors and peptide [90], the interaction between antibody and antigen [91], the interaction between nucleotides [92], or the unfolding of proteins [93]. The versatility and adaptability of the AFM in a plethora of applications have made it a powerful tool in the investigation of biomolecules.

2.1.2 Working Principle

In the heart of AFM is a nanoscopic probe, which usually has a cylindrical cone or a pyramidal shape, mounted on the end of a flexible microcantilever (Figure 2.1). The cantilevers are attached to a glass chip for easier handling and are most commonly V-shaped or beam-shaped, which have different torsional properties. Both the probe and the cantilever are made from silicon or silicon nitride, while the upper surface of the cantilever is usually coated with a thin layer of a reflective metal such as gold.

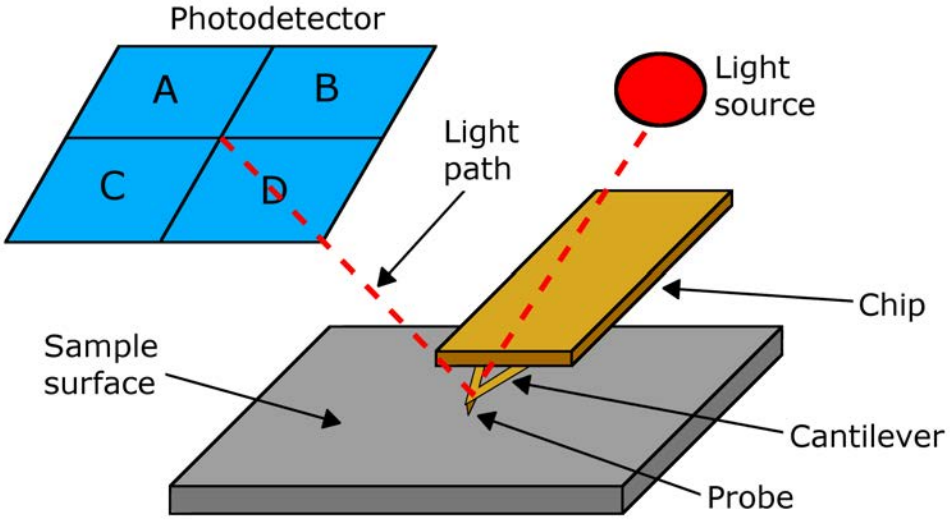

Figure 2.1: Schematic diagram to describe the working principle of an AFM. A sharp probe is mounted on the end of a flexible cantilever. Either the AFM chip or the sample is mounted on a piezoelectric actuator that allows the movement on the z, y, and z directions, which brings the probe in contact with the sample and raster-scan its surface. A laser beam is deflected from the cantilever onto a photodetector that can, subsequently, detect the movement of the cantilever and produce a 3D representation of the surface morphology.

The sample and the probe are brought in contact with the aid of a piezoelectric actuator, which moves either the sample (scanned-sample) or the chip (scanned-tip) depending on the particular AFM system [73]. Both systems have their advantages and disadvantages. For example, the size and thickness of the sample in the scanned-sample system is limited due to insufficient space. This could also cause difficulties in liquid imaging or in the fitting and use of other accessories. However, it can generally achieve a higher resolution imaging than the scanned-tip system due to a lower level of mechanical noise. In contrast, on the scanned-tip system, the image resolution could be limited due to the higher noise level. However, scanned-tip AFM can be equipped with a wide range of accessories, such as temperature-controlled stages or electrochemical cells, which makes it more versatile than the scanned-sample system.

The piezoelectric actuator enables the relative movement between the tip and the sample in three dimensions. The piezo, connected and controlled by a feedback circuit, moves in the Z direction to bring the sample and the probe in contact. Once the sample

and the tip are in contact, the piezo moves in the X and Y direction to raster-scan the selected area. During the scanning, the cantilever bends upwards and downwards as it follows the surface. Its movement is monitored by an optical lever system that is composed of a light source and a photodetector (Figure 2.1) [94]. A laser beam emitted by the light source is reflected by the cantilever towards a photodetector that is usually divided into four segments. The photodetector detects the vertical movement and the lateral or torsional bending of the cantilever. The vertical movement is determined by the difference in the signal between A+B and C+D, while the torsional bending by the difference between A+C and B+D (Figure 2.1). Because the distance that the cantilever travels during its movement is three orders of magnitude lower than the distance between the cantilever and the photodetector, the AFM has an extremely high sensitivity.

The force ($F(z)$) that is developed between a microscopic particle (such as the tip of the probe) and a surface, separated by a distance z, depends on the Lennard-Jones potential ($U(z)$) and is given by the following equation (2.1):

$$F(z) = \nabla U(z) = -\frac{dU(z)}{dz} \tag{2.1}$$

As it can be seen in Figure 2.2, when the surface and the probe are separated by a distance z_0 the interaction force between them is zero. For distances larger than z_0 the probe is attracted towards the surface due to van der Waals forces, while for distances smaller than z_0 the particle feels a repulsive force due to the overlapping of their atomic orbitals.

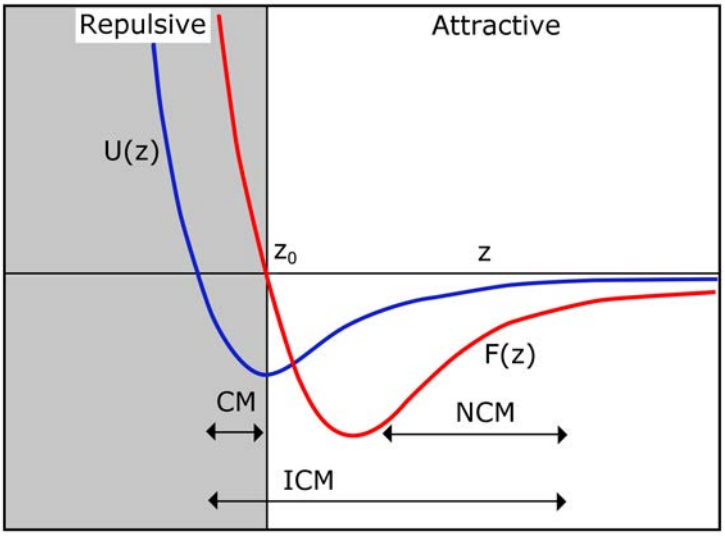

Figure 2.2: Distance dependence of Lennard-Jones potential $U(z)$ (blue) and force $F(z)$ (red) versus tip-surface separation. Depending on the distance between tip and surface the AFM can operate in contact mode (CM), non-contact mode (NCM), or intermittent-contact mode (ICM). Modified from [94].

The imaging modes of the AFM can be classified as static or dynamic, depending on the oscillation of the cantilever [95]. In static mode, the cantilever does not oscillate, while in dynamic mode the cantilever is oscillating near its resonance frequency. The main mode for static imaging is contact mode (CM), while for dynamic imaging are intermittent-contact mode (ICM) and non-contact mode (NCM).

Contact mode

Contact mode is the simplest and most direct AFM imaging mode. The probe remains permanently in contact with the surface and it exploits the repulsive short-range forces between the probe and the sample (Figure 2.2). The Z piezo brings the probe in contact with the surface (Figure 2.3) and by raster-scanning it produces a topographical image of nanoscale resolution. Contact mode can operate in two modes; the constant force mode and the constant height mode.

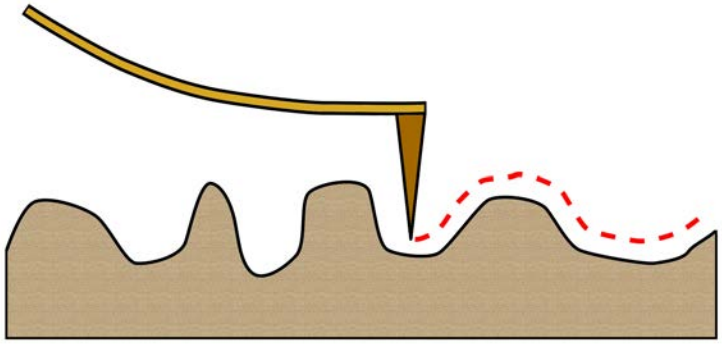

Figure 2.3: Graphical representation of AFM imaging with contact mode. The probe is engaged permanently on the surface and follows the topography in order to produce a three dimensional graphical representation.

In the constant force mode, the feedback mechanism keeps the deflection of the cantilever, and hence the force developed between probe and sample, constant. Once the probe is in contact with the sample surface, the cantilever bends and the difference in the deflection of the laser beam is detected by the photodetector. Prior to imaging, a desired setpoint is selected to keep the deflection constant during scanning. The feedback system checks constantly the deflection and compares it with the selected setpoint. If the two values do not coincide then the Z piezo is extended or retracted in order to match the deflection with the setpoint and, thus, maintain a constant force. The resulted topographical image is derived from the movement of the Z piezo while it moves to adjust the deflection with the setpoint.

During the constant height mode, the feedback mechanism is off and the Z piezo remains at a fixed position during the scanning. The acquired topographical image is generated from the photodetector signal collected during scanning. A drawback of the constant height mode is that it can only be performed on atomically flat surfaces, in contrast to the constant force mode that can be performed on surfaces with larger topographical features. However, meeting this condition, constant height mode can produce images faster and with sharper resolution than the constant force mode.

The contact mode is generally used to image hard samples, or particles that are well adhered onto a surface. It is generally not affected by capillary forces in ambient environment (although capillary forces can still slightly increase the force that the tip

exerts on the sample) and is faster than dynamic modes. Furthermore, because the lateral deflection of the cantilever can also be measured during scanning in contact mode, it can provide valuable information concerning different frictional properties of a surface caused among others by adsorbates [96]. However, contact mode is not recommended to image soft or fragile samples. Because the setpoint is set in relation to the free cantilever deflection (when it is not in contact with the surface), possible drifts of the cantilever cannot be realised since the probe is constantly in contact with the surface. Consequently, although the imaging is in constant deflection, it may not be in constant force and could potentially damage the sample. Another reason is that lateral forces during the scanning can deform the surface or move molecules/particles that are not well adhered [97]. As a result, this can damage the sample and affect the quality of the image. Therefore, when imaging soft or easily deformable surfaces, such as biological samples, the dynamic modes are preferred.

Dynamic mode

Dynamic modes were developed to overcome the problems arising from contact mode imaging. In dynamic mode, the cantilever oscillates near its resonance frequency, either through a bimorph placed in the base of the cantilever holder (acoustic mode) or by directly driving a cantilever, coated with a magnetic layer, with external coils (magnetic mode). The magnetic mode was developed more recently and is superior to the acoustic mode because it produces less noise and better control of the oscillation dynamics [98]. There are two main dynamic imaging modes, depending on the interaction between probe and sample, as shown in Figure 2.2.

The first dynamic mode is the intermittent-contact mode. In contrast to contact mode where the probe is permanently engaged on the surface, in intermittent (or tapping) mode the probe is periodically engaged and disengaged from the surface. A desired setpoint is selected prior to the scanning that corresponds to the amplitude of oscillation of the cantilever, which is why intermittent-contact mode is also referred to as amplitude-

modulation atomic force microscopy (AM-AFM). The amplitude of oscillation changes when the probe approaches the surface or when it encounters topographical features during the raster scanning (Figure 2.4). In response, the feedback mechanism adjusts the Z piezo in order to maintain constant oscillatory amplitude. Similar to the constant force contact mode, the topographical image is derived from the movement of the Z piezo to maintain the oscillatory amplitude of the cantilever. The intermittent-contact mode can be used both in ambient and liquid environment, although imaging in ambient requires stiffer cantilevers to overcome the capillary forces that arising from condensation of atmospheric moisture on the surfaces. This mode is the most frequently operating mode when imaging biological systems since it does not create any friction during scanning and it is not destructive to the sample.

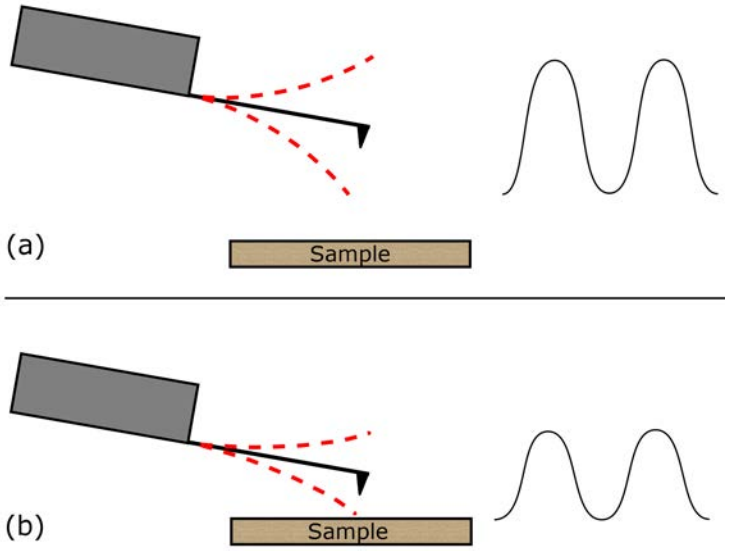

Figure 2.4: Graphical representation of the intermittent-contact mode. (a) The free oscillation of the cantilever away from the sample is near its resonance frequency. (b) When the cantilever approaches the surface its frequency is dampened. In response, the feedback mechanism moves the Z piezo in order to maintain the oscillatory amplitude equal to the selected setpoint.

The second dynamic mode is the non-contact mode. Similar to the intermittent-contact mode, the cantilever is oscillated near its resonance frequency in non-contact mode but at much reduced amplitude. However, in contrast to the contact and the intermittent-contact mode, the cantilever never touches the surface. As the probe approaches the surface, long range interactions between the surface and the probe cause a phase shift between the

driving and oscillatory frequencies (Figure 2.5). In response, the feedback mechanism adjusts the Z piezo in order to readjust the phase at the initial value, and a topographical image is derived from the movement of the Z piezo. Since the feedback mechanism controls the frequency, the mode is also referred to as frequency-modulation atomic force microscopy (FM-AFM). Because the surface-probe interaction is minimised in non-contact mode, it can produce the highest resolution among all other modes. However, this is only valid in optimal conditions such as in ultra-high vacuum (UHV). In ambient and liquid environment, capillary forces and electrostatic interactions could interfere and degrade the imaging resolution, although recent developments in the technique have resulted in liquid imaging with the highest resolution [99].

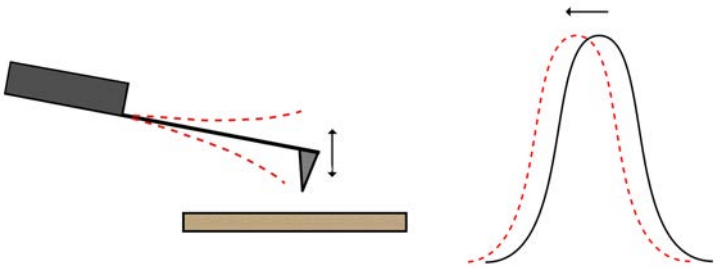

Figure 2.5: Graphical representation of non-contact mode. The cantilever is oscillating above the sample near its resonance frequency. When it is brought in close proximity with the sample the interactions with it cause a shift in the resonance frequency. The feedback mechanism readjusts the Z piezo in order to re-establish the selected frequency.

Dynamic modes can also provide information regarding the surface properties of a sample by recording the phase shift during scanning. Areas with similar morphology could affect the oscillating frequency in different ways due to attraction or repulsion of the cantilever over these areas. Despite the advantages over contact mode imaging, dynamic mode imaging in liquid is challenging and there is still a lot of room for improvement. Oscillation of the cantilever by acoustic driving excites many different mechanical resonances of the liquid cell that results in a wide range of resonances, which makes it difficult to identify the appropriate peak [95]. Also, imaging in liquid causes a high damping to the resonance frequency of the cantilever, which reduces the quality factor (Q factor) and

results in lower image resolution. There are several solutions to these problems such as the use of cantilevers with higher Q factor or oscillation of the cantilever by different methods (magnetic or more recently secondary laser beam) [100, 101].

Force spectroscopy

Besides the acquisition of high resolution surface imaging, AFM can be used to measure the forces between the AFM probe and the sample with piconewton sensitivity, and provide an insight on the properties of the sample, the probe, or the medium in-between. In force spectroscopy measurement, the probe (or the sample, depending on where the piezoelectric motor is mounted) approaches the sample on the normal direction, makes contact, and then retracts away from the surface. This process produces a force curve with the raw data of the cantilever deflection versus the extension of the piezoelectric motor. A representative force curve is shown in Figure 2.6 a. At point A, the probe is far from the sample and it does not detect any force towards it. As the probe approaches the sample (red line), it starts to experience attractive interactions that eventually become stronger than the stiffness of the cantilever, which results in a "jump to contact" event with the surface (Figure 2.6 a, point B). In the absence of attractive forces, the cantilever would not jump to contact with the surface, while in the presence of repulsive forces the cantilever would bend towards the opposite direction. Once in contact with the surface, the cantilever experiences a repulsive force due to interaction of the atomic shells and it bend upwards. The Z piezo continues to extend and the deflection of the cantilever is increased until it reaches the setpoint at C. At this point the Z piezo reverses its movement and starts the withdrawing (blue line). Initially, the deflection of the cantilever follows the path of the approaching curve but strong attractive forces keep it in contact with the surface past the point where it jumped in contact during the approach (point D). Eventually, the force that tends to separate the probe from the surface becomes larger than their attraction and the cantilever jumps off the surface at point E.

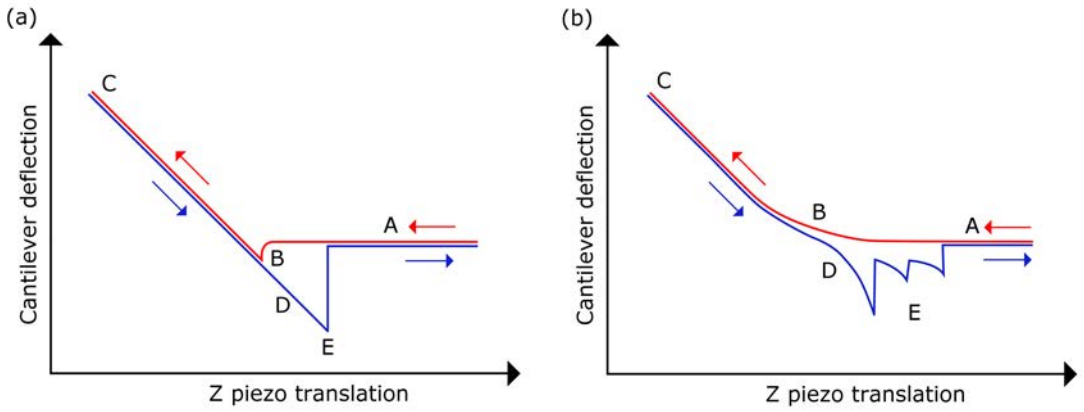

Figure 2.6: Schematic representation of force curves showing the deflection of the cantilever as measured by the photodetector versus the Z piezo displacement. The red line shows the approach of the cantilever towards the surface and the blue line the retraction. (a) Idealized force curve. From A to B the cantilever is approaching the surface and makes a contact with it at B, where the tip suddenly jumps to meet the surface. The cantilever keeps bending until it reaches the setpoint deflection at C and then it withdraws. At D the cantilever is attracted on the surface and it bends downwards until it eventually detaches from the surface at point E. (b) Example of force curve against a soft sample. The cantilever is approaching the surface from A to B where the probe deforms the surface. Eventually the deformation stops and the cantilever continue to bend until the setpoint (C) where it begins to withdraw towards D. At E the force curve reveals multiple peaks that indicate multiple detachment events.

Due to the characteristics of surface, different samples will produce various force curves. For example, Figure 2.6 b shows an example of the interaction between a probe and a soft sample. The main differences from the previous example are on points B and E. At point B the force curve indicates that the probe is indenting or deforming the sample and the deflection is not proportional to the extension of the Z piezo. Furthermore, at point E, the force curve shows multiple peaks, which indicates multiple detachment events and is characteristic of desorption and unfolding of molecules such as polymers or proteins.

The AFM cantilever, within the operational limits, can be treated as a spring [102]. Therefore, the deflection of the cantilever can be translated into force using Hookes law:

$$F = -kx \tag{2.2}$$

where F is the force experienced by the cantilever, k is the spring constant, and x is the deflection of the cantilever. Consequently, the Z piezo displacement and the cantilever

deflection can be converted into sample-tip distance and force by knowing the sensitivity of the system and the spring constant of the cantilever [103]. The nominal spring constant is provided by the manufacturer of the cantilever, but it can also be calculated by the geometry of the cantilever or with the thermal tuning method [95, 104]. In the thermal tuning, a series of frequency sweeps is performed on the AFM cantilever, which behaves like a harmonic oscillator driven by thermal noise, to determine its natural frequency. The sensitivity of the cantilever translates the change in deflection to distance travelled by the Z piezo and can be calculated by performing a force curve onto a hard sample where the change in deflection coincide with the distance travelled in the Z direction.

Apart from the forces between uncharged bodies that can be described by the Lennard-Jones interactions as explained earlier, there are several other forces that can act on the probe during force spectroscopy such as electrostatic, capillary, viscosity of the medium etc. In ambient environment, the electrostatic forces can be minimised by grounding the system [94]. The main forces that act on the system are the capillary forces, caused by condensed water vapour at the contact, which generates additional attractive forces between the surfaces. In a liquid environment, the capillary force disappears and the probe-surface interaction is governed by electrostatic and van der Waals (VDW) forces. Furthermore, in electrolytes the surfaces tend to develop a charge that is caused by the presence of ions; a layer of ions with opposing charge is bound on the surface, followed by a layer of counter ions on top of them, which results in the formation of a double layer. The DLVO theory well describes the interaction of bodies in liquid by combining the effect of VDW attraction and electrostatic repulsion. Generally, the larger the ionic concentration in a solution, the shorter the double layer and, consequently, the shorter the range of electrostatic forces [74].

The force spectroscopy is not limited to measure the interactions between an AFM probe and a sample. A range of particles, such as microspheres, can be attached at the end of a tipless cantilever to reveal the interaction between the attached particles and the surface. Furthermore, force spectroscopy is used to investigate single molecule events, in a

technique called single molecule force spectroscopy (SMFS). For example, protein molecules can be attached on the end of an AFM probe and perform force spectroscopy in order to investigate the intramolecular (protein folding) or intermolecular (protein-biomolecule) interactions. The approach is the same as in force spectroscopy. The attached molecule is brought in contact with the sample and interacts with it. Subsequently, the Z piezo is retracted and creates tension on the adsorbed molecule until eventually it starts to unfold and detaches from the surface. The produced force curve usually results in a saw-tooth shape, showing the unfolding and detachment of the adsorbed protein (chapter 4). By using a soft cantilever, it is possible to quantify these events in the piconewton scale.

2.1.3 Experimental approach

In this thesis, both force spectroscopy and single molecule force spectroscopy were utilized. In chapter 6, an alumina particle was attached at the end of a tipless cantilever (Figure 2.7 a) and was brought in contact with a titanium sample (Figure 2.7 b) in protein solutions. The force spectroscopy was performed in an electrochemical cell in a technique named electrochemical atomic force microscopy (ECAFM), where the AFM is coupled with a three-electrode electrochemical cell. As explained in chapter 1, the application of a negative or positive potential on the sample result in a surplus of charge that affects its surface properties and, thus, the interaction with the probe (alumina).

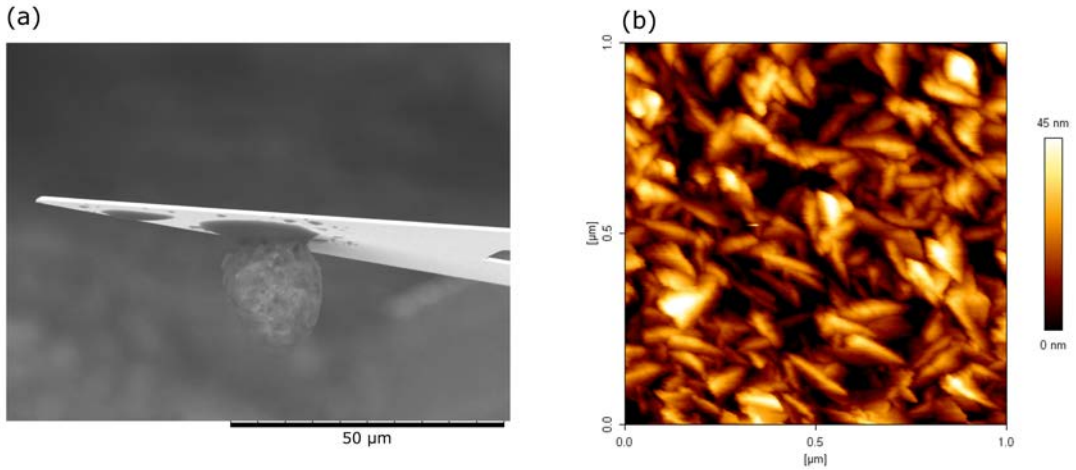

Figure 2.7: (a) Scanning electron microscopy image of alumina particle attached on the end of a tipless AFM cantilever. (b) Atomic force microscopy image of titanium surface.

Single molecule force spectroscopy was used in chapter 4 to investigate the interaction between a protein fragment and a variety of surfaces. The desired fragment was attached onto the cantilever in two steps. On the first step, a trisNTA-EG_3-C_{16}-SH linker (Figure 2.8 a) synthesised by collaborator was attached onto a gold-coated AFM probe through the gold-sulphur bond (Figure 2.8 b) [57]. During the second step, the desired protein molecule was attached with the linker through the His-Tag interaction (Figure 2.8c) [105].

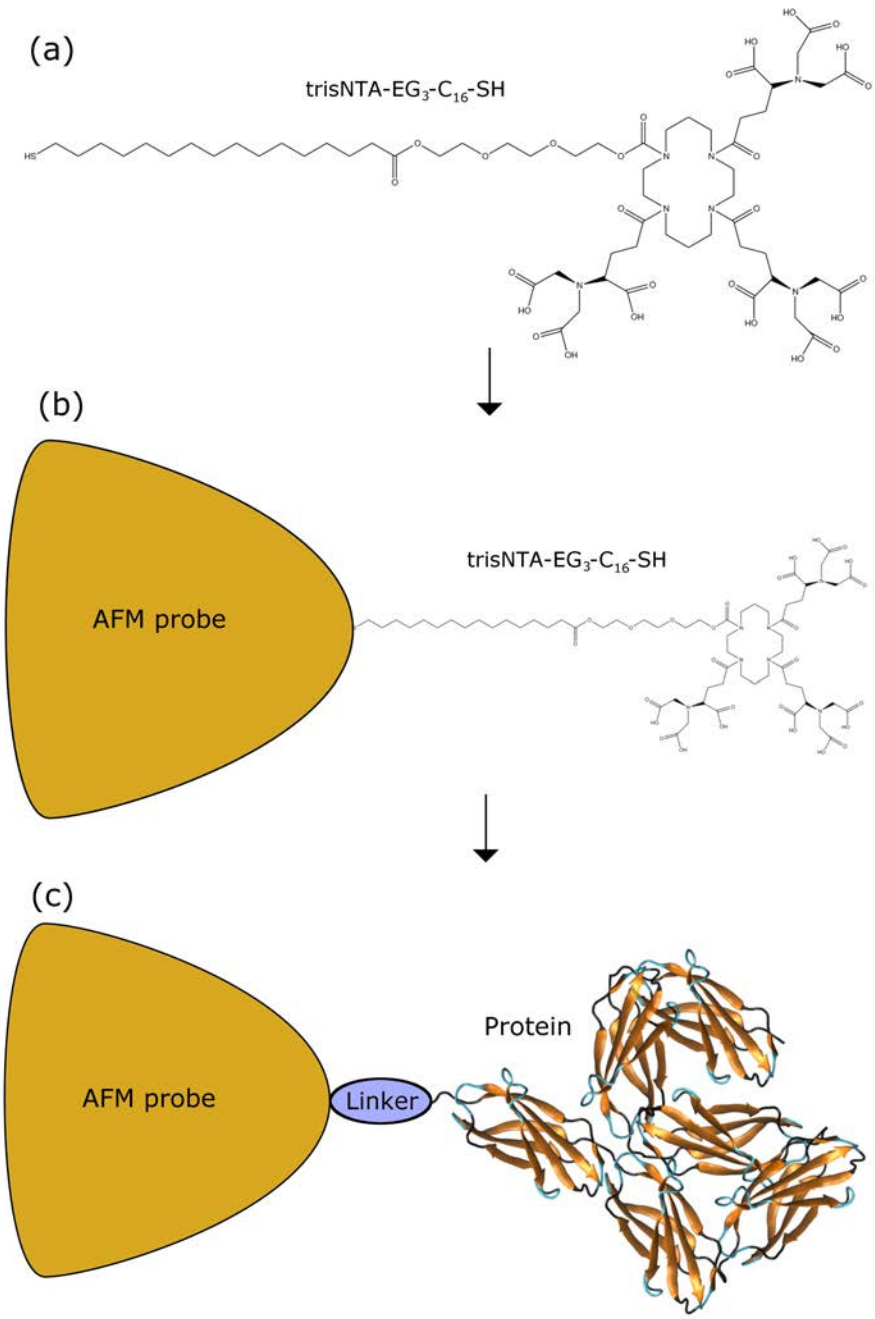

Figure 2.8: Functionalization of AFM probe. (a) Linker, (b) chemisorption of linker onto gold-coated AFM probe through sulphur-gold bond, (c) attachment of protein fragment onto linker through His-Tag.

2.2 Quartz Crystal Microbalance

2.2.1 Introduction

The quartz crystal microbalance (QCM) is a high resolution mass sensing technique that can accurately measure the amount of mass adsorbed onto a surface as a function of time, or characterise the viscoelastic properties of the adsorbed mass. It is based upon the piezoelectric effect of a quartz crystal, and it was firstly used when Sauerbrey discovered that a change in the resonance frequency of a quartz crystal is in linear relation to the change of the bound mass on the crystal [106]. It is an easy to use and inexpensive technique, which eliminates the need for specific labelling of the investigated molecules, and can perform well in complex and often optically opaque solutions [107].

The QCM has been widely used to study a wide range of biomolecules, such as adsorption of bacteria [108, 109], immobilisation of oligonucleotides [110, 111], cell-attachment [112, 113], virus adhesion [114, 115], and protein adsorption [112, 116–119]. Furthermore, it can be combined with an electrochemical cell (EQCM) and measure changes in the mass of adsorbed molecules, or corrosion phenomena, while performing electrochemistry in the desired solution [120–123].

2.2.2 Theory

At the heart of the QCM is a quartz crystal, with both sides coated by a thin electrode layer. A graphical representation of a QCM can be seen in Figure 2.9. Most QCM crystals are AT-cut to provide a stable oscillation at room temperature without being affected from changes in the temperature [124]. Upon application of an alternating current on the electrodes, a mechanical shear deformation is observed on the crystal with a characteristic frequency, f, and lateral amplitude of approximately 1-2 nm [107]. Any mass already bound on the quartz crystal, such as the electrode or molecules adsorbed on it, will oscillate with the same frequency and lateral movement. If there is no energy loss during the

oscillation, then the process is considered elastic. In contrast, if energy is being lost during the oscillation, then the process in inelastic. Any additional mass bound on the crystal will cause a change in the oscillation frequency, and the change in mass (Δm) can be quantified (with ng sensitivity) using Sauerbrey's equation:

$$\Delta f_m = -\frac{2f_0^2}{A\sqrt{\rho_q \mu_q}} \cdot \Delta m = -C_f \cdot \Delta m \qquad \textit{Sauerbrey's equation} \qquad (2.3)$$

where Δf_m is the measured resonance frequency (Hz), f_0 is the intrinsic resonance frequency of the unloaded crystal, Δm is the mass change (g), A is the mass sensitive area of the electrode, ρ_q is the quartz density (2.65 g/cm^3), μ_q is the shear modulus of the crystal (2.95×10^{11} dyn/cm^2), and C_f is the quartz sensitivity factor [107].

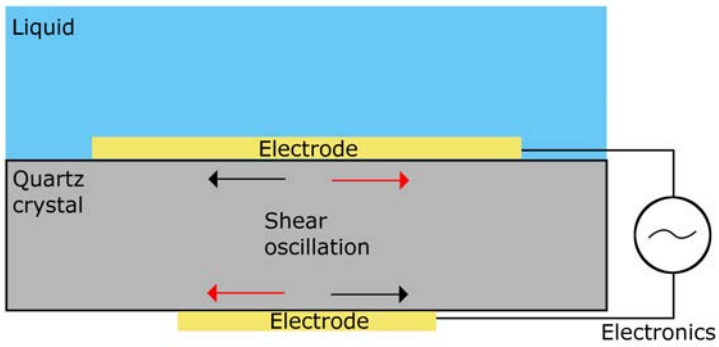

Figure 2.9: Graphical illustration of a quartz crystal microbalance. The quartz crystal is oscillating at its resonance frequency due to the piezoelectric effect. Any adsorbed mass on the electrode results is a frequency change and can be measured using the Sauerbrey's equation.

The Sauerbrey equation can be used accurately only for elastic masses bound to the crystal, with a total mass less than 2 % of the crystal mass. This also applies to thin films or to tightly adsorbed molecules that appear rigid to the QCM [125]. It can also be seen from the Sauerbrey equation that the sensitivity of the QCM depends linearly on the resonance frequency of the crystal; the larger the resonance frequency the greater the sensitivity [126]. The shear wave caused by the oscillating crystal is decaying fast due to the viscosity of the medium. The penetrating depth in the medium at the lateral direction for a 5 MHz QCM is approximately 250 nm at 20 °C [127]. As a result, QCM only senses

objects in close proximity with the surface and is "surface specific"". Furthermore, a number of different metals can be used as electrodes such as gold, platinum, and titanium.

QCM is usually used in the continued resonance mode, where the shift in the frequency due to the change in mass is measured. It can be operated in both air and liquid, and provides information about the conditions at the interface between electrode-air or between electrode-liquid. QCM can be connected with a pump to automatically control the flow of liquid in the system. The flow is usually under laminar direction in order to minimise the impact on the crystal [107]. QCM can also be coupled with an electrochemical cell in order to perform experiments that measure the corrosion of the metal and provide information about the reactions taking place at the interface [126].

2.2.3 Experimental approach

In this thesis, the quartz crystal microbalance was used to study the adsorption of protein onto a range of surfaces. In chapter 4, the QCM was used in liquid mode to measure the adsorption of fibronectin onto gold surfaces modified with self-assembled monolayers. The flow of the protein solution in the QCM was controlled with a peristaltic pump (Figure 2.10 a). In chapter 5, EQCM (coupled with a three electrode electrochemical cell) was used to investigate the corrosion of pure titanium in various BSA solutions, and to study the BSA adsorption onto titanium under cathodic and anodic conditions. The QCM chamber was immersed into a container to allow EQCM operation and was not connected to a pump (Figure 2.10 b).

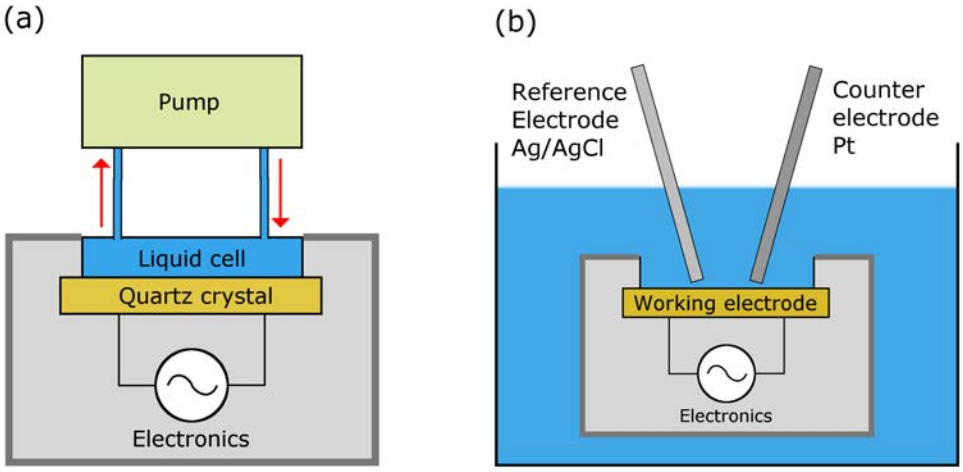

Figure 2.10: Graphical illustration of (a) a QCM connected with a peristaltic pump, (b) a QCM connected with a three electrode electrochemical cell (EQCM). The working principle is based on the piezoelectric effect as described earlier. The use of a pump allows the flow of liquid in the QCM chamber and the loading with protein solution, while on the EQCM the quartz crystal acts as the working electrode and allows the monitoring of electrochemical reactions.

2.3 Tribocorrosion

Tribocorrosion refers to the combined process of corrosion and wear on the surface of a material. Phenomena related to tribocorrosion play a major role in the field of biomaterials because they can limit the lifetime and the performance of various implants. Some of the most common areas where tribocorrosion phenomena occur in biomaterials are in joints and dental implants [6, 8, 9, 46, 128–131]. The theory of tribocorrosion was explained in detail in chapter 1, and only a description of the experimental set-up will be given.

In chapter 6 of this thesis, the tribocorrosion behaviour of pure titanium in albumin solution was investigated, using an arrangement such as the one shown in Figure 2.11. The device is a rotary pin-on-disk tribometer coupled with an electrochemical cell. In this method, the disk, holding a flat specimen, is rotated without translation against a pin that is not rotating neither translating [132]. The pin was bearing an alumina sphere and was under a constant force equal to 5 N. As a result of the rotating motion, a circular pattern (wear track) is produced on the planar specimen. This method produces unidirectional, constant-velocity shearing forces at the pin and the specimen that can be measured with

a shear force sensor on the arm. The force of friction is then given by equation 2.4:

$$F = \mu \times N \tag{2.4}$$

where F is the frictional force between pin and specimen, μ is the friction coefficient, and N is the normal force that the pin applies onto the specimen.

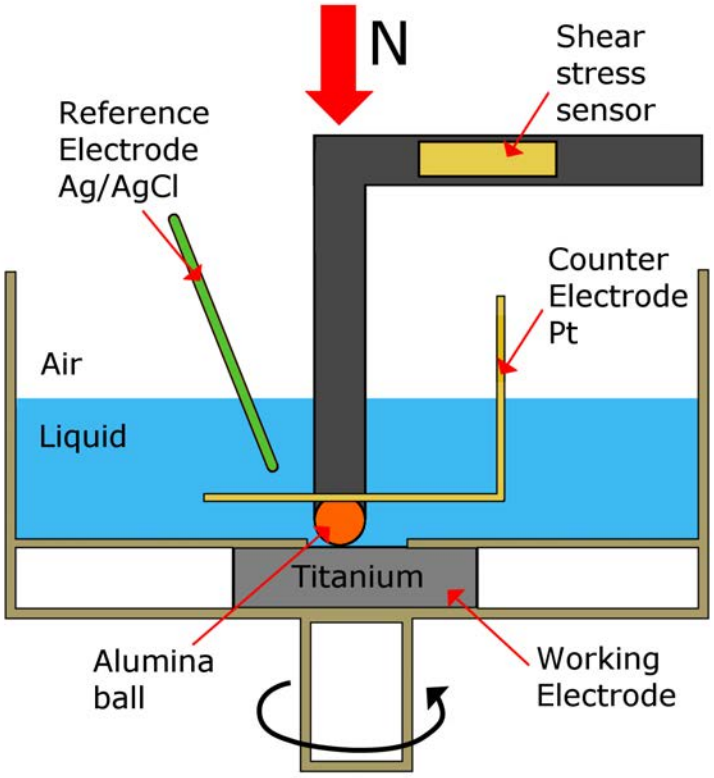

Figure 2.11: Schematic illustration of a tribocorrosion device. The configuration is consisted of a pin-on-disk tribometer coupled with a three electrode electrochemical cell. A force (N) was applied on the specimen (titanium) that wasf rotating against an alumina sphere while a sensor on the arm holding the pin was measuring the shear force.

2.4 Molecular Dynamics Simulations

2.4.1 Introduction

Protein adsorption is governed by a set of interactions between the protein, the surface, and the surrounding medium. One of the most direct approaches to investigate these interactions at the atomic level is molecular simulations, which are an excellent complement

to experimental work. Molecular simulations are essential in order to advance our understanding of biomolecules and have been used in applications such as drug design [133, 134], protein-protein [135, 136] and protein-cell membrane interactions [137, 138], or protein-folding [139–141]. In the field of biomaterials, they can be used to provide information about the structure and function of proteins, to provide a close-up on the mechanism of protein adsorption and the interactions occurring between individual atoms, or to proactively design biomaterials at the atomic scale [67, 142–153]. Molecular simulations can be classified in two major categories; quantum mechanics (QM) and classical mechanics (CM) simulations.

Quantum mechanics considers the electrons as the fundamental particles of the system and applies the Schrödinger equations to calculate the properties and behaviour of the system. They are very accurate and do not require any fitted parameters due to ab initio calculations. Although they can predict the behaviour of a system with precision, they are extremely expensive in computational power. Therefore, they can only be used in the study of systems containing a few tens of atoms, and for computational times of approximately a few picoseconds. Quantum mechanics are very useful in the calculation of the interactions between atoms, and therefore are used for the development of the parameters that are used in classical mechanics simulations. For instance, Bordner et al used quantum mechanical interaction energies to calculate the van der Waals force field parameters of several alkanes and nonalkane compounds [154].

In classical mechanics simulations, the atom or a group of atoms is taken as the fundamental unit of the system and an empirical force field is used to calculate the interactions between the atoms (or group of atoms). CM computational methods are less demanding in computational power than QM and can be used to study systems containing tens of thousands of atoms in the time frame of tens of nanoseconds. If a group of atoms are used as the fundamental unit in the system (coarse-grain simulations), then the size and the time frame of the system can be greatly extended. However, this comes with the cost of reduced accuracy. Classical mechanics simulations can be further divided to

molecular mechanics (MM), Monte Carlo (MC), and molecular dynamics (MD).

In MM simulations, a force field equation is used to calculate the potential of a molecular structure, based on the position of the atoms in space relative to each other, and the bonds that are created between them. The thermal energy is not taken into consideration for the calculations and, therefore, they are taking place in zero Kelvin [155]. Molecular mechanics are often used prior to molecular dynamics in order to minimise the energy in a system by relaxing any bends, twists, stretched covalent bonds, and to prevent overlaps between atoms. In MC simulations, the atoms of a molecular structure are randomly moved within a specific move set (defined by values such as dihedral rotation of a covalent bond, etc.) in order for the molecule to scan all the conformations that it can possibly take. The interactions between the fundamental units are calculated through a force field equation. MC is very useful in applications were it is needed to calculate the thermodynamic properties of a system. However, because the algorithms that are used for the movement of the atoms are not time dependent, MC cannot be used for applications where kinetic information is needed. In molecular dynamics simulations the interactions between the fundamental units are also calculated with a force field equation but, in addition, Newton's laws of motion are used to predict the movement of the atoms and, thus, the movement of the molecule.

Both MC and MD have their advantages and disadvantages, and the selection of one over the other is based on the system that is under investigation. For example, in a protein adsorption application, if the goal is to study which conformation of protein is the most favourable on a specific surface, then the most efficient method would be MC because it can consider all possible conformations with high efficiency. This of course would require an implicit solvent model as random overlapping between atoms from the protein and atoms from water molecule would result in unacceptable values of potential when water molecules are represented explicitly. On the other side, if the goal is to investigate the trajectory of a protein during adsorption then the appropriate method would be molecular dynamics. Since MD can provide the information given by MC (although slower), it can

be used in explicit solvent systems, and in addition it provides kinetic information, it is the most commonly used method in biomolecular systems.

2.4.2 Theory

In molecular dynamics simulations, every atom in the system experiences a force that is specified by a force field equation. The equation calculates all the interactions between a specific atom and the surrounding atoms in the system, and determines how the atom will move in space. The general form of the equation, referred to as "Class I force field", has 5 contributors and is given by equation 2.5 [156]:

$$U_{total} = U_{bond} + U_{angle} + U_{dihedral} + U_{vdW} + U_{Coulomb} \tag{2.5}$$

The bonded terms describe the stretching (U_{bond}), the bending (U_{angle}), and the torsional rotation ($U_{dihedral}$) of covalently bonded pairs of atoms, while the non-bonded interactions are used to calculate the van der Waals forces (U_{vdW}) and the electrostatic interactions ($U_{Coulomb}$). The first three terms of the equation represent the interactions between pairs of atoms that are covalently bonded, while the last two represent the non-bonded interactions between atoms (Figure 2.12).

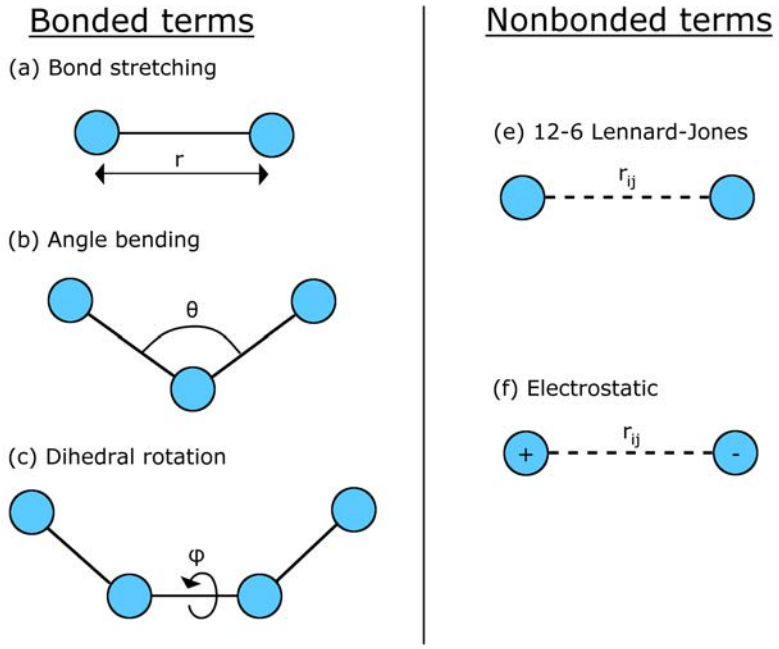

Figure 2.12: Bonded and non-bonded contributions to the potential energy as given by the force field equation.

Each term of the equation is given by the formulas shown in equations 2.6-2.8.

$$U_{bond} = \sum_{bonds\ i} k_i^{bond}(r_i - r_{0i})^2 \tag{2.6}$$

$$U_{angle} = \sum_{angles\ i} k_i^{angle}(\theta_i - \theta_{0i})^2 \tag{2.7}$$

$$U_{dihedral} = \sum_{dihedral\ i} k_i^{dihe}[1 + cos(n_i\phi_i - \gamma_i)] \tag{2.8}$$

where r, θ, and ϕ are the bond length, bond angle, and dihedral angle of covalent bonds, in relation to a reference position. The parameters, k, reflect the stiffness of the system and are calculated by a combination of empirical techniques and quantum mechanical calculations.

The van der Waals interactions are calculated by the Lennard-Jones (L-J) 12-6 interactions and account the forces between all pairs of non-bonded atoms, while the electrostatic

interactions are calculated by Coulomb's law (equations 2.9 and 2.10):

$$U_{vqW} = \sum_{i} \sum_{j>i} 4\epsilon_{ij} \left[\left(\frac{\sigma_{ij}}{r_{ij}} \right)^{12} - \left(\frac{\sigma_{ij}}{r_{ij}} \right)^{6} \right] \tag{2.9}$$

$$U_{Coulomb} = \sum_{i} \sum_{j>i} \frac{q_i q_j}{4\pi\epsilon_0 r_{ij}} \tag{2.10}$$

where the ϵ_{ij}, and σ_{ij} show the well-depth and the collision diameter for pair of atoms i and j separated by a distance r_{ij}, while q_i and q_j are the partial charges of atoms and ϵ_0 is the permittivity of free space [155]. Since MD uses empirical parameters to calculate the interactions between atoms, it is important that the correct parameters will be used in order to achieve accurate results [157].

Following the calculation of the total force acting on each atom through the force field equation, the Newtonian equation of motion (equation 2.11) is applied to the atoms in order to predict their movement:

$$m_\alpha \vec{r}_\alpha = -\frac{\partial}{\partial \vec{r}_\alpha} U_{total}(\vec{r}_1, \vec{r}_2, ..., \vec{r}_N), \ \alpha = 1, 2, ..., N \tag{2.11}$$

where m_α is the mass of atom α, $\vec{r}_\alpha$ is its position, and U_{total} is the total potential energy that depends on all atoms in the system and is given by the force field equation (Equation 2.5) [156].

The combination of force field equation and the Newtonian equation produces a molecular dynamics simulation in a process that is presented in Figure 2.13 [155]. The process starts at step 1 where every atom in the simulation system has an initial position (x_0) and velocity (v_0). The cycle counter (n) is set to 0 (step 2) whilst the position and velocity are updated with these values (x_n, v_n) at step 3. At the next step (step 4), the force field equation is applied to all the atoms in the system and, subsequently, the force acting on each atom is calculated by the differentiation of the equation (step 5). Subsequently, the acceleration of each atom is calculated through the Newtonian equation (step 6). The acceleration is taken as constant for the time interval of each step (Δt) and

it is differentiated to calculate the velocity of each atom (step 7), which is then added to the previous velocity (step 8). In explicit molecular dynamics simulation the timestep, Δt, is approximately 1-2 fs. The updated velocity is taken as constant over the time interval of the step in order to calculate the distance travelled by the atom (step 9), which is used to update the position of the atom (step 10). The cycle counter is set to n=1 (step 11) and the procedure is repeated to calculate the new velocity and position of each atom (step 12).

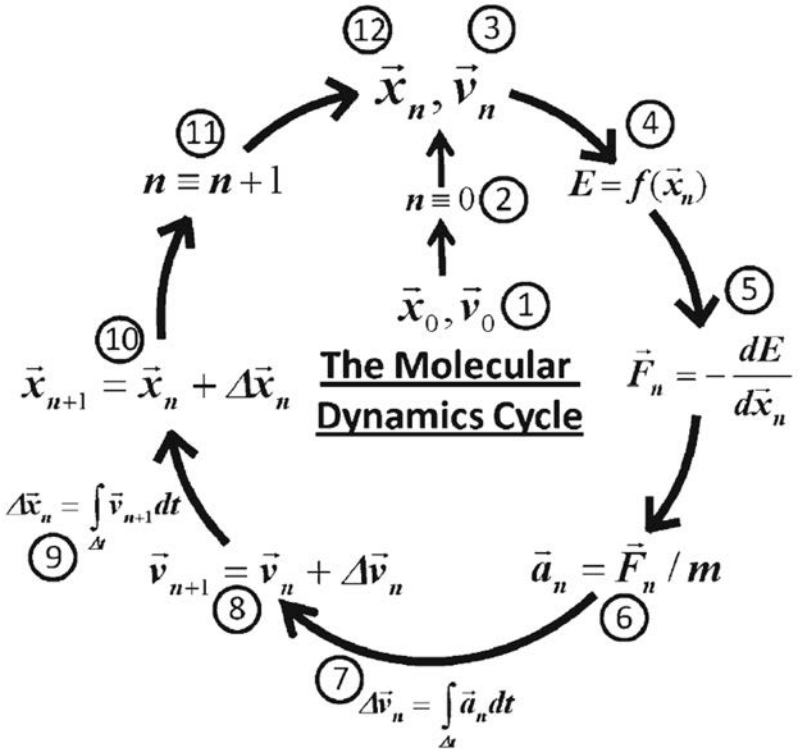

Figure 2.13: Graphical illustration of a process followed in a molecular dynamics simulation. The process starts at step 1 where every atom in the simulation system has an initial position (x_0) and velocity (v_0). The cycle counter (n) is set to 0 (step 2) and the position and velocity are updated with these values (x_n, v_n) at step 3. At the next step (step 4) the force field equation is being applied on all the atoms in the system and, subsequently, the force acting on each atoms is calculated by the differentiation of the equation (step 5). Subsequently, the acceleration of each atom is calculated through the Newtonian equation (step 6). The acceleration is taken as constant for the time interval of each step (Δt) and it is differentiated to calculate the velocity of each atom (step 7), which is then added to the previous velocity (step 8). The updated velocity is taken as constant over the time interval of the step in order to calculate the distance travelled by the atom (step 9), which is used to update the position of the atom (step 10). The cycle counter is set to n=1 (step 11) and the procedure is repeated to calculate the new velocity and position of each atom (step 12). Adapted from [155].

In order to avoid surface effects at the boundaries of a simulation system, periodic conditions are applied. Therefore, if the simulation system represents the "real space", the content of the unit cell is replicated to infinity with identical "images" around it. This can be better visualised in Figure 2.14 in a two dimensional system. The unit cell in the middle, marked by the red square, represents the "real space" of the system. This unit cell is surrounded from all sides by an infinite number of repeating images. When an atom is exiting the system from one side, it is replaced by another atom entering the system from the other side, resulting in the same number of atoms in the system at all times. Furthermore, the atoms present in the "real space" are subjected to forces from all other atoms in the system, included those of the atoms in the surrounding cells. Although the periodicity eliminates any surface effects, two limitations are arising. The first is that the net charge of the "real space" should be equal to zero. The second is that the calculation of non-bonded interactions, including those with the surrounding images, is not feasible and requires a simplification.

As explained earlier, the non-bonded interactions in a molecular dynamics system are given by the Lennard-Jones and the electrostatic interactions. A common practise for the simplification of the Lennard-Jones interactions is to truncate them by setting a user-defined cut-off distance on the calculations. In addition, in order to avoid any artefacts caused by an abrupt drop in the calculated potential, a switching function is added that smooths gradually the L-J interactions to zero. For instance, a 10-12 switching function means that the L-J interactions are calculated normally in the first 10 Å, then they are gradually decreased between 10 Å and 12 Å, and any L-J interactions beyond 12 Å are ignored. Since the L-J interactions are short-ranged, the error due to the truncation is inconsequential. However, if a similar method of truncation is being applied for the calculation of the long-range electrostatic interactions, then a significant amount of error would be introduced in the system.

A convenient solution to this problem is the use of the Ewalds summation methods, such as particle mesh Ewald (PME) [158]. Ewald summation calculates the sum of the

electrostatic interactions on each box first, and then the sum of the electrostatic interactions on spheres of increasingly larger radii [159]. Ewalds summation methods approximate the electrostatic forces acting on an atom in the "real space" considering the interactions coming from the surrounding images. Particle mesh Ewald performs a similar calculation by placing a charged particle into a grid and calculating the electrostatic interactions by weighting functions according to the distance of the grid points from the charged particle [156]. Consequently, PME reduces the calculation time needed to compute the Ewald summation. Although the Ewalds summation method still introduces some flaws, such as that a molecule in the "real space" can feel forces coming from its own image in surrounding cells, the error in the system is minimal and much lower than if truncation methods similar to L-J cut-off distance were used.

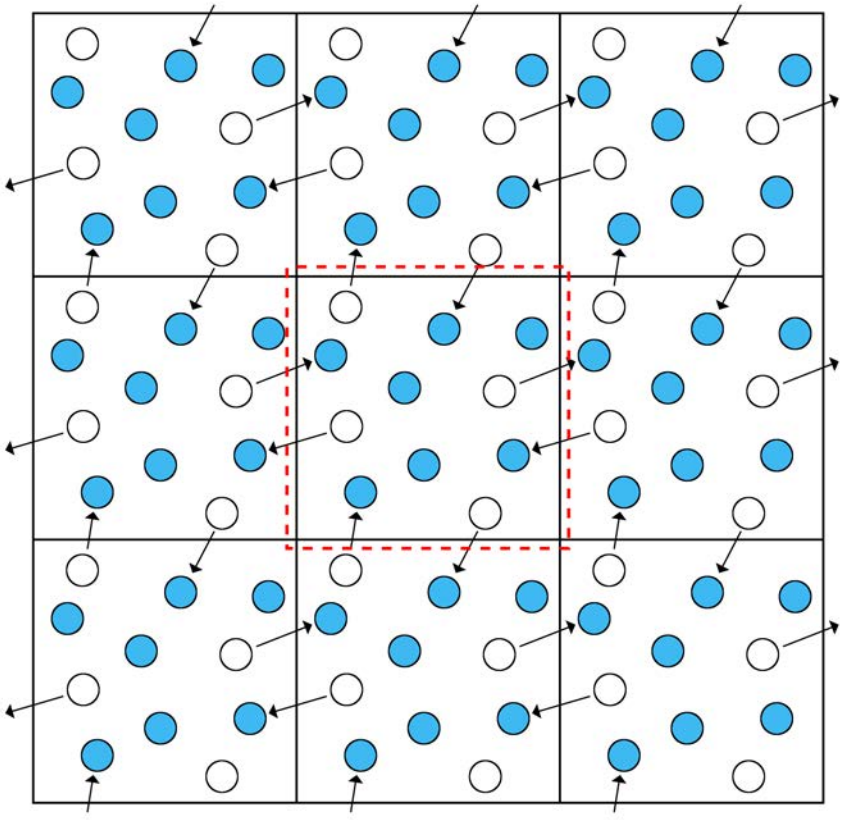

Figure 2.14: Graphical representation of the periodic boundary conditions for a two dimensional system. Marked by red square is the real-space system, while it is surrounded by images of this cell. The arrows show the movement of the atoms. When an atom exits the system from one side, it is replaced by another atom entering the system from the other side. The blue circles represent the atoms present at the system, while the open circles the position of the atoms before they leave the system.

Molecular dynamics simulations can be performed with explicit or implicit solvent. In molecular dynamics simulations of protein adsorption, such as in the present study, it is important to take consideration the solvation of the system and the impact of the solvent on the adsorption. In explicit solvent simulation, all the water molecules and ions are included, which provides the most accurate results because water molecules are very active components and play a major role in the adsorption process due to their interaction with the protein and the surface. However, because the water molecules could represent approximately 90 % of the atoms in the system [157], 90 % of the computation time is spent calculating the interactions and behaviour of water molecules rather than the protein-surface interaction that is the main focus. In order to decrease the computation power and amount of time that is needed to perform a simulation, implicit solvent methods can be also used. There are several methods that use a mean-field approximation to represent the effect of the aqueous solution in the system. For example, one of the simplest methods to represent an implicit solvent is to replace the dielectric constant used for the calculation of the electrostatic interactions (the dielectric constant in water is approximately 79 as opposed to 1 in air). However, because protein adsorption is dominated by nonbonded interactions between protein, surface, and solvent, this method is not recommended in such systems. A more accurate implicit solvent method to describe adsorption phenomena uses the Poisson-Boltzmann (P-B) equation to calculate the free energy of molecular solvation [160]. P-B methods calculate more accurately the electrostatics interactions but they neglect the hydrophobic effect. Even though this problem can be addressed by adding an additional term to the force field, it creates other problems, such as discriminating between hydrophobic and hydrophilic surfaces. In conclusion, although implicit solvent methods reduce the computational power needed for a simulation and can address several factors, they are still inadequate to replicate the real behaviour in protein adsorption systems.

2.4.3 Experimental approach

In this thesis, molecular dynamics simulations using the NAMD code were performed to investigate the adsorption of a fibronectin fragment onto a series of SAMs surfaces. NAMD is designed for high performance simulation of large biomolecular systems and excels performing in parallel platforms, such as those used in the present study [156]. The simulations were performed in explicit solvent, resulting in systems of 100,000+ atoms, for simulation times of around 100 ns. In order to simulate such large systems in a reasonable timescale, the simulations were performed in two supercomputers, the Archie-West and the Archer. The CHARMM potential functions were used by NAMD that are designed for biological systems, while the PME method was used to calculate the electrostatic interactions [161]. The simulations were performed in the NVT ensemble, which represent a constant number of atoms (N), volume (V), and temperature (T) in the system.

Chapter 3

Adsorption of fibronectin fragment onto surfaces using fully atomistic Molecular Dynamics simulations

3.1 Introduction

Biomaterials are generally defined as materials that interact with living matter and can be used to construct synthetic tissue and organs in order to replace or augment the function of their predecessors [162]. Upon exposure to biological fluids, the surface of a biomaterial is covered with a dynamic layer of host proteins, which mediates the cell-biomaterial interactions through receptors present on the cell-membrane [155]. Consequently, the protein-surface interaction plays a significant role in determining whether the biomaterial will be accepted or it will cause an inflammatory reaction that could lead to rejection of the implant [5,59]. Therefore, a molecular-scale insight on the protein adsorption processes on a range of surfaces with different characteristics underpins the design of biomaterials with enhanced biocompatibility.

Fibronectin, a large glycoprotein that is found predominantly in the extracellular matrix and the plasma [17], is one of the most important proteins that mediate the biomaterial-cell interaction [15, 18]. It is a main cell-receptor and influences processes such as cell adhesion and differentiation, whilst it is also involved in applications such as inflammation and wound repair [18]. It has a molecular weight of approximately 440 kDa

and is consisted of two similar chains that are held together with a couple of disulphide bonds in the C-terminal. Fibronectin contains a cell-attachment region that allows it to bind specifically with integrins on the surface of the cells. It is composed of the cell-binding and the synergy domains that contain the amino acid sequences Arg-Gly-Asp (RGD) and Pro-His-Ser-Arg-Asn (PHSRN) respectively. The domains are situated in the $FNIII^{10}$ and $FNIII^{9}$ modules that can undergo reversible unfolding as a mechanism of elasticity to promote cell-binding [163]. In order for the cell to bind with fibronectin, it is crucial that the cell-binding domain remains exposed to solvent after the adsorption because mismatched conformation or denaturation of the protein will inhibit the cell-binding [164].

One of the most important factors that affect protein-surface interactions is the surface chemistry of a biomaterial. The surface of a material can be hydrophobic or hydrophilic, positively or negatively charged. Since fibronectin is a polyampholyte (contains both cationic and anionic groups), each of the aforementioned surfaces would have a different level of impact on its conformation upon adsorption. A very convenient method to engineer surfaces with the desired chemical properties is with the use of self-assembled monolayers (SAMs), which are thin films of ordered molecular assemblies that are formed by spontaneous adsorption of organic molecules on surfaces [54–56]. SAMs have been widely used in the past as a model surface to study the protein-surface interactions both experimentally and computationally, and have been proved effective model surfaces to study protein adsorption [165–170]. It has been found that while proteins adsorb strongly on hydrophobic surfaces, this causes structural deformation on the protein which affects their ability for cell-binding [165, 169, 170]. In contrast, the adsorption on hydrophilic surfaces is weaker but the adsorbed proteins maintain their structural integrity and ability for cell-binding.

Computational modelling has been playing a major role in advancing our understanding on protein adsorption because it provides an insight on the adsorption pathways and the individual interactions between protein and surface. There are several computational studies on the effect of surface charge, hydrophobicity, and ions on protein adsorption

[20, 67, 146, 147, 152, 153, 171–174]. It has been reported that electrostatic interactions play a key role in driving the proteins onto charged surfaces, where the adsorption takes place between charged surfaces and oppositely charged residues [146, 147, 152, 172]. In adsorption on hydrophobic surfaces, it was found that the interplay between the hydrophobic surface and hydrophobic patches onto the protein determine the affinity of the protein towards the surface [146, 153]. The ions also play a key role during adsorption on charged surfaces because they screen the electric field, which can promote or inhibit protein adsorption [20, 147, 174].

Fibronectin adsorption has been studied in the past using molecular simulations [149, 150, 175, 176]. It was found that adsorption on hydroxyapatite surfaces is driven by electrostatic interactions, while $FNIII^{10}$ undergoes two stages of adsorption - a pre-adsorption driven by Coulombic interactions, followed by a post-adsorption when the driving force shifts from Coulombic to van der Waals interactions, while the binding site remains exposed [149, 176]. Other studies report that adsorption of $FNIII^{7\text{-}10}$ on positive surfaces results in more cell-binding domains accessible than that upon adsorption on negatively charged surfaces, while adsorption on hydrophobic surfaces denature the protein and results in loss of the cell-binding ability of the protein [150, 175]. However, the aforementioned studies were either inadequate to replicate the real behaviour of fibronectin adsorption due to the use of monte carlo and implicit solvent methods, or they focused on fibronectin adsorption on a single surface (hydroxyapatite). As explained in chapter 2, implicit solvent model and monte carlo simulations do not represent water molecules explicitly, in order to reduce the processing power needed in expense of accuracy. In contrast, explicit solvent simulations can provide superior results but they are computationally expensive. The present work was performed on two of the largest supercomputers available in United Kingdom- the Archer and the Archie-west. This resulted in a comprehensive, fully atomistic molecular dynamics study, which systematically studied the adsorption of fibronectin on a range of surfaces. Consequently, the results will advance our understanding on the protein adsorption mechanisms, focusing on the surface chemistry of

different substrates and how they interact with the protein residues, but also taking under consideration the importance of water molecules and ions in this process.

Although there has been some progress towards the understanding of the adsorption pathways and interactions during adsorption, it is still far from being fully understood. The perpetual development in the computing processing power allows more detailed simulations of larger systems over longer periods of simulation time. In the present work, fully atomistic Molecular Dynamics simulations were employed to investigate the effect of surface chemistry on the adsorption of the FNIII$^{8\text{-}10}$ domain of fibronectin. The protein trajectories were analysed to identify the driving forces during adsorption, the impact of the adsorption on the structural integrity of the protein, as well as the availability of the cell-binding domain after adsorption.

3.2 Methods

All simulations were performed with NAMD 2.6 package, using the Charmm27 force field, while the images were analysed with the VMD software [156, 177]. The CHARMM force field was primarily developed to study biomolecules in aqueous solutions and it has been found that CHARMM produces reasonable good results in protein adsorption systems, although in some cases it could underestimate the adsorption strength on some surfaces [178]. The fibronectin fragment FNIII$^{8\text{-}10}$ used in the present work was extracted from the domain FNIII$^{7\text{-}10}$ solved by Leahy et al. [179] and was downloaded from the protein database (PDB code: 1FNF). The protein fragment FNIII$^{8\text{-}10}$ contains the residues 1236 to 1509 of the overall fibronectin sequence.

Initially, FNIII$^{8\text{-}10}$ was placed in a rectangular box filled with water molecules (TIP3P model) that extended at least 17 Å from every protein atom, resulting in a system of approximately 100,000 atoms. To neutralize the protein fragment that has an overall charge of -5 e, additional NaCl ions were added to maintain an ionic strength of 0.05 M (mol/L). This ionic concentration, which is reduced in comparison to physiological conditions, was used to accelerate the adsorption kinetics so they can be studied in the

time frame used in this work (∼100 ns). Subsequently, the system was set to perform a trajectory of 100 ns (the computational details are the same as for the adsorption trajectories and are given below). The structure of the fragment after 60 ns of dynamics was used as the starting structure for all of the following adsorption simulations.

To test the specificity of protein adsorption and its dependence from the starting position, four different arrangements were used as initial orientations - the surfaces were placed in either (x,z) or (y,z) planes, which were placed against either side of the protein. The protein-surface distance varied between 7 Å and 20 Å - it was kept at approximately 20 Å against charged surfaces but below 10 Å on neutral surfaces to facilitate protein adsorption. Every system had approximately 100,000 to 120,000 atoms. To carry out the protein adsorption simulation, the system was initially subjected to 1000 steps of water energy minimisation, followed by 100 ps of water equilibration at a temperature of 300 K. Subsequently, the system (water and protein) was minimised for 10,000 steps, before being heated up to 300 K for 45 ps, and equilibrated at the constant temperature of 300 K for 555 ps. Finally, the production of the trajectories was performed for 100 to 150 ns at the NVT ensemble. The SHAKE algorithm and periodic boundary conditions were used for the simulations. The cut off distance for the van der Waals interactions was 12 Å, while the smooth particle mesh Ewald (PME) summation was used for the electrostatic interactions [158].

3.2.1 Model surfaces

Two different types of models were used in this work; a silica surface and a surface mimicking self-assembled monolayer (SAMs). The silica surface had been used in the previous work [180] from which further information can be found, and was used as a well established system to study fibronectin adsorption and optimize the parameters. In brief, the atoms of the SiO_2 surface were fixed in space in order to represent a slab that has been cut from the bulk crystal in such a way that left siloxide ($\equiv SiO^-$) groups on the top of the slab and under-coordinated silica species on the bottom. As a result, the surface has an

intrinsic dipole moment across it. Because periodic conditions were used in all simulations, the two opposing surfaces across the water/peptide space represent the electric field above a single negatively charged surface with siloxide species on top [181]. The dimension of the surface was 70 x 145 Å, and it was placed along the long axis of the protein fragment.

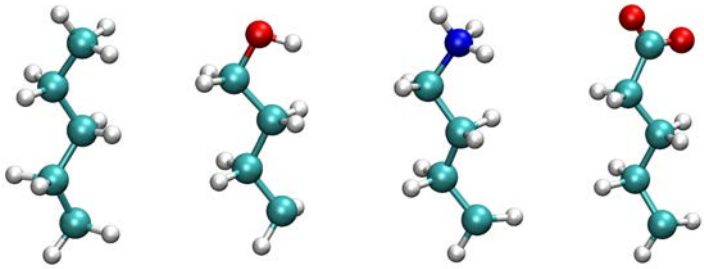

Figure 3.1: Building molecules for the SAM replicated model surfaces. From left to right; methyl-terminated (-CH_3), hydroxyl-terminated (-OH), amine-terminated (-NH_3^+), and carboxyl-terminated (-COO^-). Each molecule is consisted of a four carbon chain in addition to the functional end group. The carbon, hydrogen, oxygen, and nitrogen atoms are represented with teal, white, red, and blue respectively.

The SAMs surfaces were constructed with four different terminal functionalities; methyl (-CH_3), hydroxyl (-OH), amine (-NH_2), and carboxyl (-COOH), as shown in Figure 3.1. It has been found that in physiological conditions (pH=7.4) approximately 10% of the amine surface and 50% of the carboxyl surface is protonated (-NH_3^+) and deprotonated (-COO^-) respectively [182]. However, in the current study, all the amine molecules were in the protonated (-NH_3^+) and all the carboxyl molecules were in the deprotonated (-COO^-) state in order to achieve a homogeneous surface. Therefore, the aforementioned end groups represent a non-polar surface (hydrophobic), a polar uncharged surface (hydrophilic), a positively charged surface, and a negatively charged surface respectively. The selected molecules were truncated from the following amino acids with the desired end group; an isoleucine (methyl group), a serine (hydroxyl group), a lysine (amine group), and an aspartic acid (carboxylic acid group). Each molecule has a backbone consisted of 4 carbon molecules in addition to the designated functional group, while the broken C-C bond was patched with hydrogen atoms to satisfy the valence requirements.

The individual molecules were placed parallel to each other with a distance of 4.97

Å between them [183] to generate the SAMs surfaces shown in Figure 3.2. Those basic surfaces were used in pairs (one on top of the other with the functional groups facing outside) in order to build four different systems of SAMs surfaces; (i) an amine-carboxyl, (ii) a methyl-hydroxyl, (iii) a methyl-methyl, and (iv) a hydroxyl-hydroxyl. Each of the SAMs surfaces contained 16,000 atoms and had dimensions of 140x75x14 Å. The thickness of each surface was larger than the cut-off distance of the van der Waals forces (12 Å) in order to zero the interaction between the outer surface and the the protein in the system. Although the electrostatic interactions are long-ranged and the charge of the outer surface could still affect the adsorption, the interactions with the inner surface were dominating due to being closer to the surface. On the first system (amine-carboxyl), basic surfaces (Figure 3.2) containing terminal functionalities with opposite charges were placed on the two sides of the surface, resulting in a surface that had an intrinsic dipole moment perpendicular to it. Similar to the arrangement for silica surfaces described above, the 3D periodicity of the simulation box creates a force field across the water/protein medium that mimics the electric field created from charged surfaces, such as titanium or polymethylmethacrylate coatings [184]. The first three carbon atoms (from the bottom) of every SAM molecule were fixed in space, leaving the last carbon on the backbone and the terminal functional group free to move. NaCl ions with concentration of either 0.8 M or 1.0 M were introduced to the simulation box for the adsorption on the positively or the negatively charged side, respectively. In the second system (methyl-hydroxyl), basic surfaces with methyl and hydroxyl functional groups were placed on the opposing sides of a surface to build a hydrophilic-hydrophobic system. Only the first carbon of each SAM molecule was fixed in space, while the other three carbons and the end group were able to move. This was the first uncharged system that was built, which allowed the protein to adsorb either on the hydrophilic or the hydrophobic surface. However, in order to achieve specific adsorption onto hydrophobic or hydrophilic surface, the last two systems were built that have either methyl (methyl-methyl) or hydroxyl (hydroxyl-hydroxyl) on both sides (systems iii and iv respectively) of the surface whilst the first three carbons are fixed

in space. NaCl ions of 0.05 M were added in all of the uncharged systems.

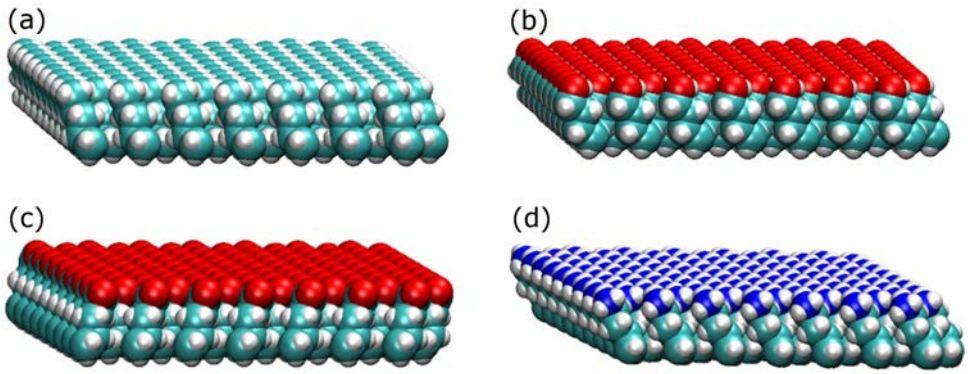

Figure 3.2: SAMs replicated model surfaces; (a) methyl-terminated (-CH_3), (b) hydroxyl-terminated (-OH), (c) carboxyl-terminated (-COO^-), and (d) amine-terminated (-NH_3^+). The distance between subsequent molecules is equal to 4.97 Å. The colour scheme is the same a previously.

3.3 Results

3.3.1 Protein structural features

The protein fragment $FNIII^{8\text{-}10}$ is consisted of 274 amino acids (4,184 atoms) and has overall dimensions of 115x23x23 Å. The polypeptide chain is organised into three similar type III modules, and each module has 7 anti-parallel β-strands that form a sandwich of β-sheets (Figure 3.3). It also contains a hydrophobic core and, due to the lack of disulphide bonds, it has a soft and flexible structure. The modules $FNIII^{10}$ and $FNIII^{9}$ contain the cell-binding and the synergy regions respectively, which are on the same side of the protein fragment. The cell-binding site contains the amino acid sequence Arg-Gly-Asp (RGD) that is used to bind with integrins onto the surface of the cells. The synergy region contains the sequence Pro-His-Ser-Arg-Asn (PHSRN), which determines the specificity and the affinity of the integrin binding [17]. The distance between them is approximately 37 Å, while the RGD site is kept approximately 10 Å from the surface of the protein which promotes the interaction with integrins. The RGD site contains a positively (Arg) and a negatively (Asp) charged residue that give an overall charge of 0 e, whereas the PHSRN site contains a positively charged residue (Arg) that results in an overall positive charge of

+1 e. Both sites are hydrophilic, with a hydropathy index of -8.4 for the RGD and -13.6 for the PHSRN (Table 3.1) [185]. The overall charge of the fragment is -5 e, which is not distributed equally among the three modules - module FNIII^{8} has an overall charge of -4 e, FNIII^{9} of -1 e, while FNIII^{10} is neutral. The uneven distribution of charge results in an overall dipole moment of approximately 750 D, which is oriented almost perpendicular to the long axis of the protein. It points towards the side that contains the cell-binding and synergy regions and, therefore, indicates a positive patch, which is consistent with previous studies [175].

Table 3.1: Charged and hydrophobic residues of individual domains and full length FNIII$^{8\text{-}10}$ fragment. The last two columns show the total charge and hydropathy index of the domains, while the rest of the columns show the number of residues per labelled characteristic [185].

domain	residues	hydrophobic	hydrophilic	charged	positive	negative	total charge	hydropathy
FNIII^{8}	91	28	63	18	11	7	-4	-31
FNIII^{9}	89	26	63	17	9	8	-1	-40.4
FNIII^{10}	94	29	65	16	8	8	0	-10.8
FNIII$^{8\text{-}10}$	274	83	191	51	28	23	-5	-82.2
RGD	3	0	3	2	1	1	0	-8.4
PHSRN	5	0	5	1	1	0	1	-13.6

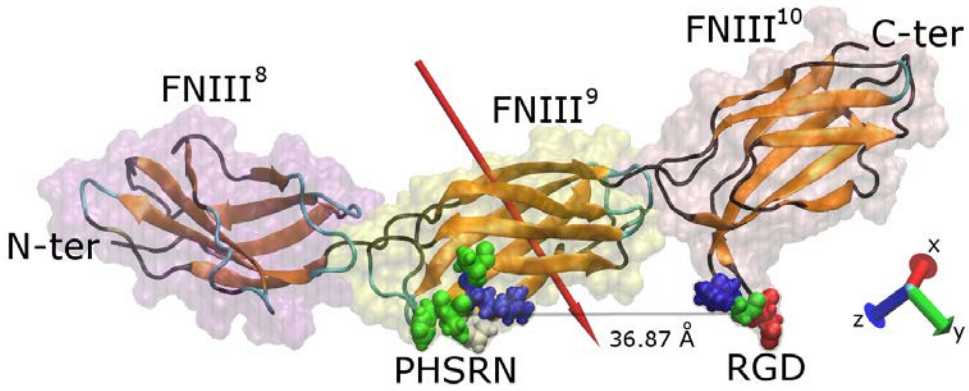

Figure 3.3: Graphical representation of a FNIII$^{8\text{-}10}$ fragment of fibronectin. The secondary structure (color-coded; with orange, teal, and black represent β-sheets, loops, and coil respectively), along with the protein "ghost" surface of the modules that comprise the fragment are visible. The red arrow indicates the dipole moment of the fragment, while the cell binding (RGD) and synergy (PHSRN) sites, as well as the distance between them, are shown. The water molecules are not shown for clarity, while the amino acids shown are color-coded; with blue, red, white, and green represent positively charged, negatively charged, hydrophobic, and polar uncharged respectively.

3.3.2 Simulation in water

Besides the effect of surface charge and hydrophobicity on the adsorption characteristics of FNIII$^{8\text{-}10}$, another important consideration is the structural integrity of the fragment. The specific fragment was chosen because it contains the cell-binding and synergy regions. In order to bind successfully with the cell receptors, the cell-binding region must be exposed and the distance between RGD and PHSRN must remain unaffected. To establish whether the fragment maintains its integrity during the simulations, it was placed in a simulation box filled with water molecules and NaCl ions, and was allowed to perform its trajectory for 100 ns. Figure 3.4 a shows the root-mean-square deviation (RMSD) that measures the deviation in the averaged distance between the atoms of the superimposed proteins (comparing to the protein structure at t=0 ns) for each individual module and the overall fragment. The RMSD curves for each module remain constant throughout the simulation, confirming that the fibronectin modules maintained their structural integrity. There is some notable fluctuation with the RMSD of the overall fragment, which could be attributed to the bends between subsequent modules that were observed visually from the protein trajectories. Figure 3.4 b shows the measured distance between the RGD and PHSRN sites. The distance is approximately 37 Å initially, but decreases to a final value between 30 and 35 Å. After 70 ns of simulation time the fragment was heavily bended between the ninth and tenth modules. In order to have a structure for the fragment that represents better its conformation at the present conditions of water and ions, the structure of the fragment at t=60 ns was chosen as the initial structure for all the adsorption simulations. The difference between the structures at t=0 ns and t=60 ns is shown on Figure 3.4 c. It is apparent that the core structure of the modules maintain their integrity, whilst the loops between subsequent β-strands reveal twists and bends.

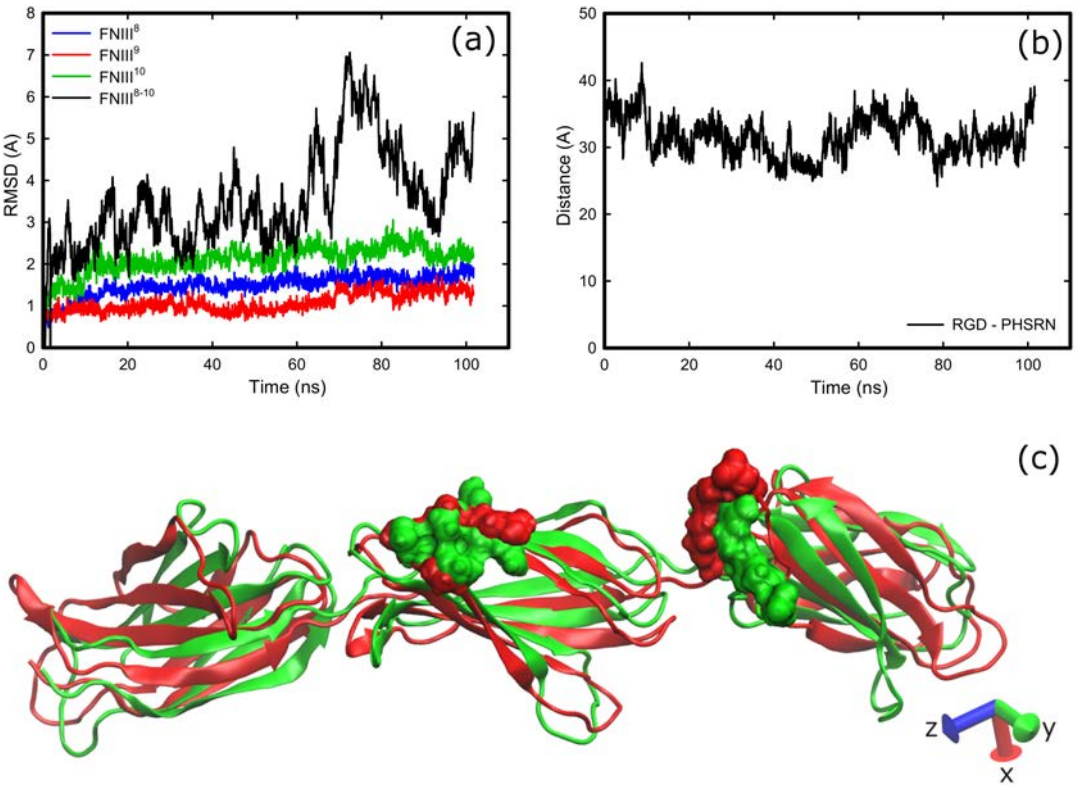

Figure 3.4: (a) RMSD calculated for the trajectory of FNIII$^{8\text{-}10}$, (b) Evolution of distance between RGD and PHSRN sites during the trajectory of FNIII$^{8\text{-}10}$, (c) Structural difference of FNIII$^{8\text{-}10}$ at t=0 ns (green) and t=60 ns (red).

Figure 3.5 shows the surface charge and hydrophobicity maps of FNIII$^{8\text{-}10}$ from the four sides along its long axis. For the sake of clarity, the four sides of the fragment presented in Figure 3.5 a, b, c, and d, are named as FNs1, FNs2, FNs3, and FNs4 respectively. It can be seen that the distribution of charged amino acids in each side is not regular, which results in various regions having different partial charges. Consequently, it is likely that different regions of the protein will interact with the target surfaces, resulting in various conformations following adsorption. It is also shown that the hydrophobic residues are gathered around the core of the protein while the hydrophilic residues are exposed to the surrounding environment. The areas in the green circles indicate the RGD and PHSRN sites, which are both hydrophilic.

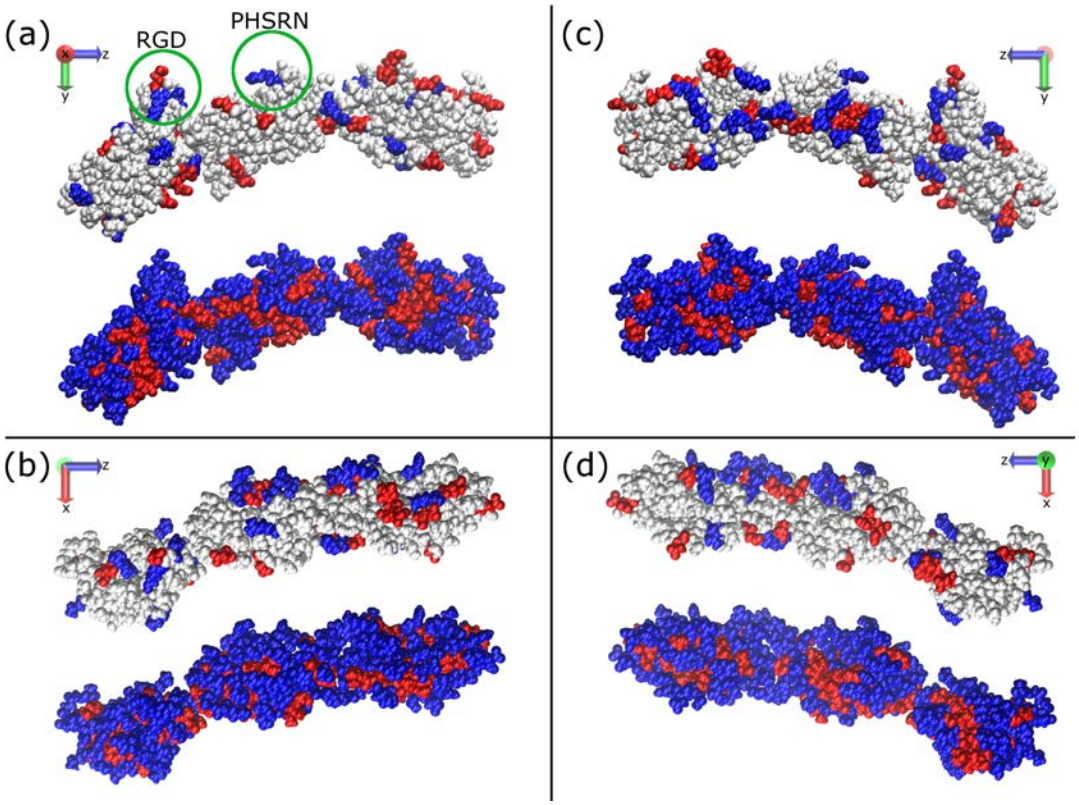

Figure 3.5: Graphical representations of the FNIII$^{8\text{-}10}$ domain showing the charge (top of each quadrant, color-coded; with white are uncharged amino acids, with blue are positively charged, and with red are negatively charged) and hydrophobicity (bottom of each quadrant, color-coded; with red are hydrophobic and with blue are hydrophilic); (FNs1, FNs3) the two sides of the protein on the y-z plane, (FNs2, FNs4) the two sides of the protein on the x-z plane.

3.3.3 Adsorption on positively charged surfaces

Figure 3.6 shows the adsorption process of the FNIII$^{8\text{-}10}$ fragment on positively charged surfaces that include a silica surface (uncoordinated side) and an amine (-NH_3^+) surface in the present work. Due to an increased number of charged species, the surface charge density of the amine surface is much greater than that of silica, which results in a greater electric field. In order to produce a similar electric field in the amine system as in the silica system, a greater amount of NaCl ions had to be added to screen the field. Due to the polarising effect created by the charged surfaces in both systems, the Na^+ and Cl^- ions were driven on the opposite charge surfaces, which partially screens the force field beyond the Debye length. Measurements on the dipole moment of the protein in both systems showed that 0.80 M of NaCl ions was needed in the SAMs system to replicate the

conditions of 0.05 M NaCl in the silica system. In both systems, FNs3 (Figure 3.5) side of the protein was made to face the positively charged surface as the initial configuration. During the first few nanoseconds, the protein fragment was found to quickly rotate along its long axis and align its dipole moment in parallel with the electric field imposed by the charged surfaces. Subsequently, the protein was attracted towards the positively charged surfaces, starting with the FNIII^{8} module and followed by the FNIII^{10}.

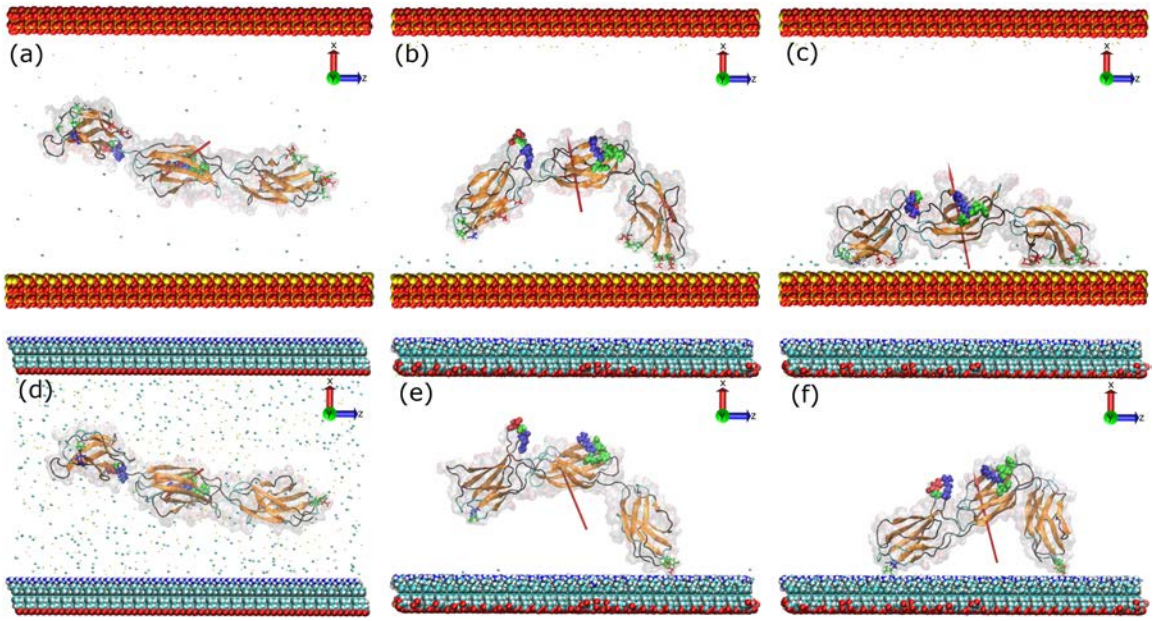

Figure 3.6: Adsorption process of FNIII$^{8\text{-}10}$ on silica (top) and on amine surface (bottom) for; beginning of simulation (t=0 ns), anchoring event (t=3.1 and 5.3 ns), end of simulation (t=100 ns). The secondary structure (color-coded; with orange, teal, and black represent β-sheets, loops, and coil respectively), along with the protein "ghost" surface of the modules that comprise the fragment are visible. The red arrow indicates the dipole moment of the fragment, while the cell binding (RGD) and synergy (PHSRN) sites are shown. The water molecules are not shown for clarity, while the amino acids shown are color-coded; blue, red, white, and green represent positively charged, negatively charged, hydrophobic, and polar uncharged respectively

On the silica surface, the initial anchoring occurs in just 3.1 ns with residue Ser1261 which is polar, neutral, and slightly hydrophilic. Following the anchoring event, more residues in the same module adsorbed on the surface with residues Asp1263 and Glu1312 (both negatively charged) having stronger preference for adsorption than the rest. Eventually, the other end of the fragment approached and anchored on the surface with residue Thr1509 at 23.3 ns. Normally, Thr1509 is polar, neutral and slightly hydrophilic but

because it was the last residue on the polypeptide chain (C-terminus) it has a negative charge. At the end of the simulation, a total of 19 residues were found to adsorb on the silica surface (the adsorption took place in the given order): Ser1261, Asp1263, Tyr1311, Glu1312, Thr1509, Thr1429, Ala1428, Thr1265, Ser1288, Ser1286, Arg1508, Pro1480, Asp1279, Asp1289, Glu1278, Glu1424, Asp1438, Val1426, Asp1377. Of these adsorbed residues, 6 are polar neutral, 4 are hydrophobic, 8 are negatively charged, and 1 is positively charged. A similar adsorption process was observed with the amine surface. After a quick rotation and alignment of the dipole moment in parallel to the electric field, the FNIII^{8} side of the fragment was anchored onto the amine surface with Glu1312 (negatively charged) at 5.3 ns. Subsequently, the other end of the protein was anchored at 50.5 ns with Thr1509 due to the electrostatic attraction. In contrast with the silica surface, only the anchoring residues adsorb onto the surface but no others, which could be attributed to a strongly bound layer of water molecules and ions onto the amine surface. The initial rotation resulted in the cell-binding region to remain exposed to the solution in both systems (Figure 3.6 c and 3.6 f).

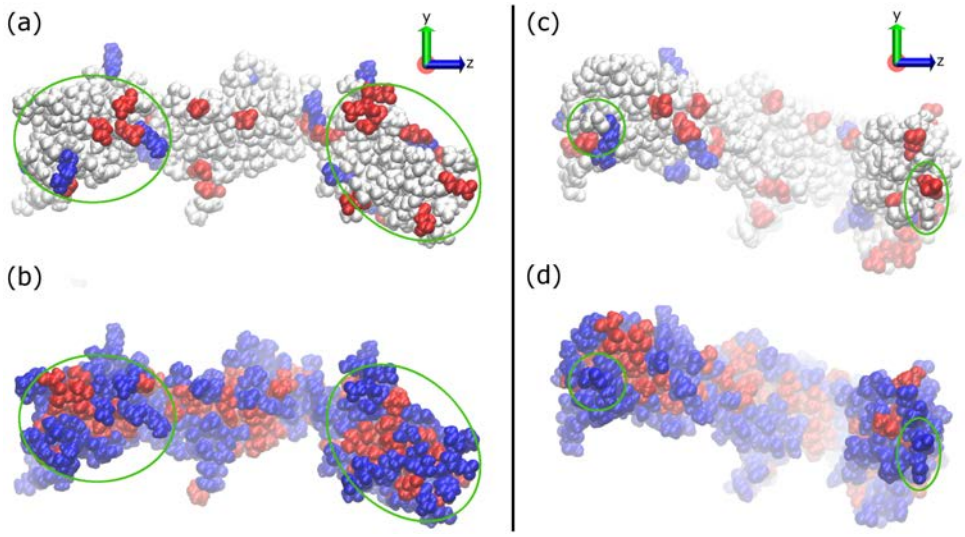

Figure 3.7: Surface charge (top) and hydrophobicity (bottom) maps of the FNIII$^{8\text{-}10}$ fragment, as viewed from the surface side, on the final stage of adsorption onto silica (a,b) and amine (c,d) surfaces. The surface atoms are not shown for clarity. The depth cueing option of VMD is being used to indicate the distance of each atom from the surface. The areas inside the green circles indicate the areas that are in contact with the surface. The colour scheme is the same as in Figure 3.5.

The surface charge maps (Figure 3.7) reveal that the side of the protein in contact with the positively charged surfaces has an increased presence of negatively charged residues than positive ones, which is expected because of the electrostatic interactions. This strong interaction between oppositely charged species also explains the adhesion of a positively charged residue (Arg), which is forced on the silica surface due to its position among other negatively charged residues on the protein. Furthermore, of the negatively charged residues in contact with the silica surface, eleven were belong to $FNIII^{8}$ module as opposed to eight on the $FNIII^{10}$ module. Because significantly more residues were found to adsorb on the silica surface than on amine surface, the contact area between protein and silica surface increases accordingly. It is worth noting the residues that were in contact with the positively charged surfaces are mainly hydrophilic (either neutral or charged), which could be due to the increased amount of hydrophilic residues present on the protein as opposed to charged ones.

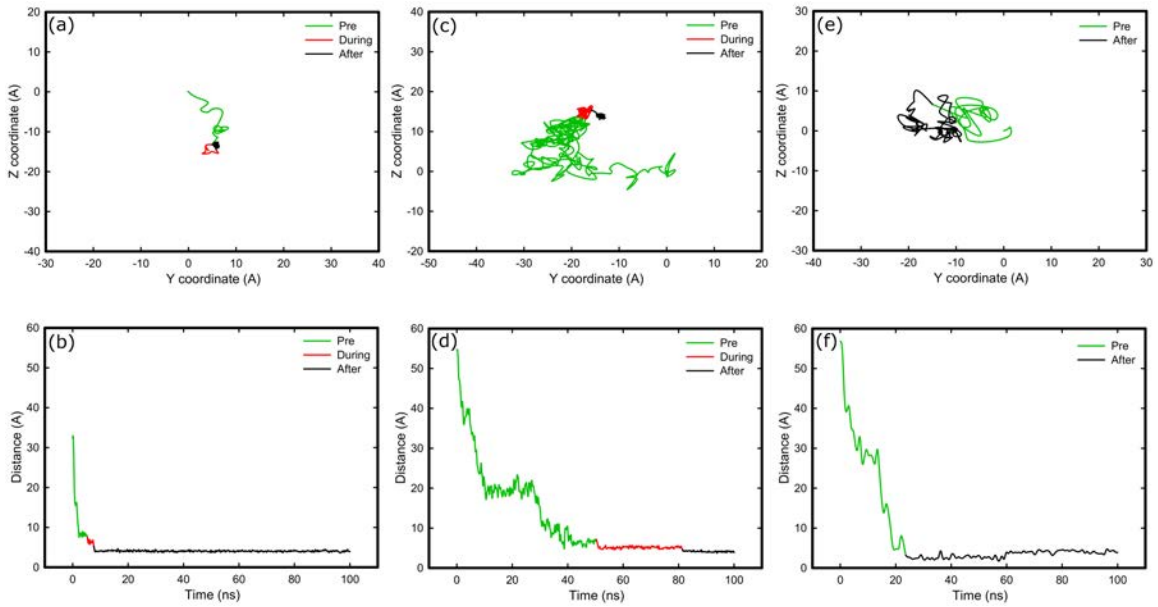

Figure 3.8: Diffusion of binding residues over the surface (top), and distance of residues perpendicular to the surface over time (bottom) for; anchoring residue of $FNIII^{8}$ in amine system (a, b), anchoring residue of $FNIII^{10}$ in amine system (c, d), anchoring residue of $FNIII^{10}$ in silica system (e, f). Green is the trajectory before anchoring, red during the anchoring, and black after anchoring. It is observed that the mobility of the anchoring residue is greatly reduced after anchoring on amine surface, while it also has to overcome a barrier. In contrast, the impact on the mobility of the anchoring residue on the silica surface is smaller.

Figure 3.8 shows the trajectories of residues responsible for anchoring and their distance to the surface in both simulation systems. It is apparent for the amine system that the residue has an increased mobility prior to anchoring, as shown in Figures 3.8 a and 3.8 c (green trace). The mobility of the anchoring residue is decreased when it is in a close proximity with the surface, as indicated by the red trace in Figures 3.8 a and 3.8 c. Subsequently, the residue overcomes a "barrier" and binds more strongly with the surface as indicated by the reduced mobility of the black trace in Figures 3.8 a and 3.8 c. A further evidence of this barrier is shown in Figures 3.8 b and 3.8 d, which indicates a jump in the distance between the residue and the surface upon overcoming the barrier. This barrier is likely a strongly bound layer of water molecules and ions on the amine surface. In contrast, this barrier was not observed in the silica system (Figure 3.8 f), which suggests that either the barrier was absent or that the anchoring residue was not able to penetrate it. Furthermore, even after anchoring the protein remained mobile along the surface (Figure 3.8 e), which suggests a weaker binding than the amine surface.

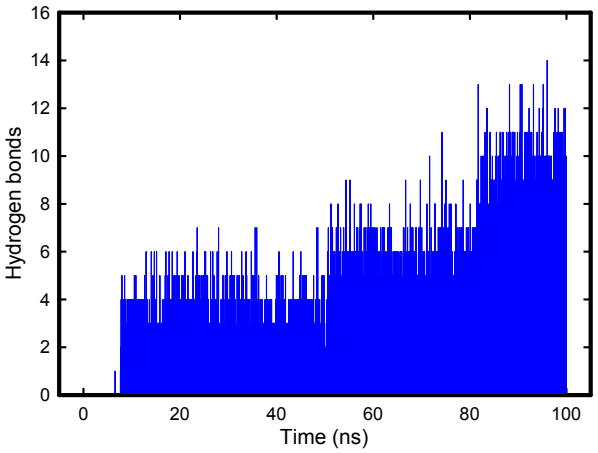

Figure 3.9: Evolution of the number of hydrogen bonds between FNIII$^{8\text{-}10}$ and the amine surface over time, which is increased as the adsorption progresses.

The number of hydrogen bonds between the protein and the amine surface is shown in Figure 3.9 as a function of simulation time. Right after the initial anchoring, there are between 4 and 6 hydrogen bonds developed between the surface and FNIII^{8} module. At approximately 50 ns, when the other end (module FNIII^{10}) of the protein was anchored

onto the surface, the bonds were increased to between 6 and 8. Eventually, by the end of the simulation, there are approximately 12 hydrogen bonds between protein and surface.

3.3.4 Adsorption on negatively charged surfaces

Because the protein fragment has a negative overall charge, the electric field implemented would force it towards the positive surface. However, despite its negative charge, fibronectin can also adsorb on negatively charged surfaces due to attraction with positively charged regions on the protein [186]. In order to promote the adsorption onto a negative surface, the electric field was further screened with the addition of 1 M NaCl ions (as opposed to 0.8 M for adsorption on the positive surface). FNs1 side of the protein was made to face the carboxyl surface as the initial configuration. In contrast to adsorption on the positively charged surfaces where the electric field forces the fragment to rotate and to adsorb, the protein fragment undergoes Brownian motion. The fragment approached the surface several times without any anchoring event until eventually, after 53 ns, it was anchored onto the surface with Lys1469, which is a positively charged residue (Figure 3.10 a). It appears that, after a weak initial binding, the residue penetrated a barrier (Figure 3.10 c) and bound firmly on the surface as indicated from its immobilisation (Figure 3.10 b). The charge and hydrophobicity maps (Figure 3.10 d and 3.10 e) show that the side that is in close proximity to the surface contains mainly neutral residues. Lys1469 was the only residue that was adsorbed onto the carboxyl surface, which could be attributed to the absence of negatively charged residues from the contact area that would be able to penetrate the barrier.

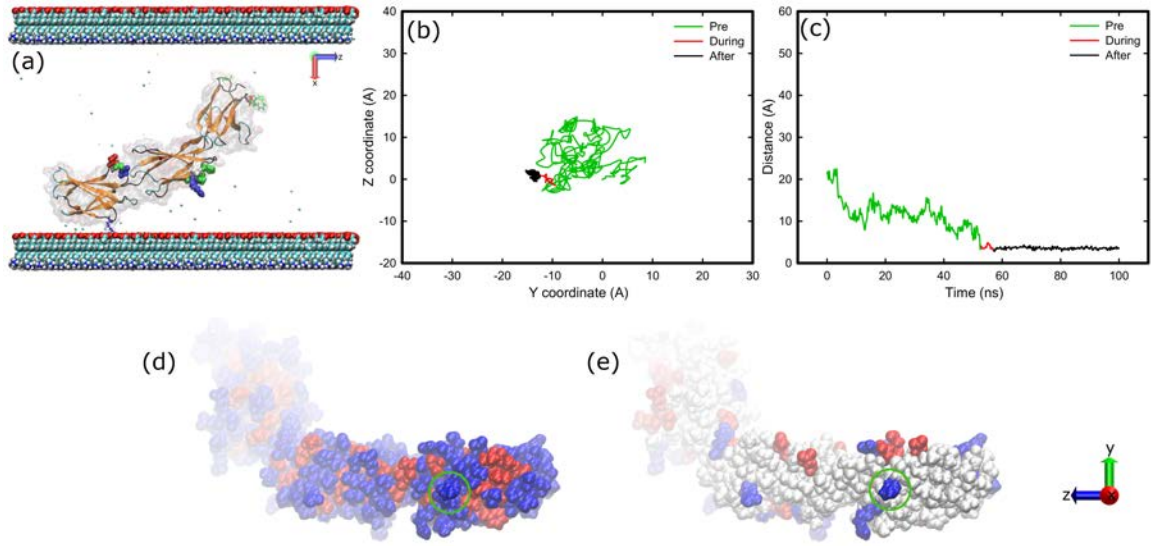

Figure 3.10: Adsorption of FNIII$^{8\text{-}10}$ onto carboxyl surface, which results in immobilisation of the anchoring residue; (a) snapshot at the end of simulation, (b) diffusion of the anchoring residue over the surface, (c) distance of the anchoring residue perpendicular to the surface over time. (Bottom) Hydrophocity (d) and surface charge (e) maps of the FNIII$^{8\text{-}10}$ fragment, as viewed from the surface side, on the final stage of adsorption onto carboxyl surface. The surface atoms are not shown for clarity. The depth cueing option of VMD is being used to indicate the distance of each atom from the surface. The areas inside the green circles indicate the areas that are in contact with the surface. The colour scheme is the same as previously.

3.3.5 Adsorption on hydrophobic surfaces

Figure 3.11 shows the adsorption process of the fibronectin fragment onto a methyl surface, when it was inserted between a methyl and a hydroxyl surface (methyl-hydroxyl system). The initial orientation of the protein was side FNs1 facing the methyl surface (Figure 3.5). In the absence of electric field, the protein fragment performed a non-specific Brownian motion in the aqueous solution until the FNIII^{10} module was anchored on the methyl surface with Thr1431 (polar uncharged) after 35 ns. Subsequently the following residues were found to adsorb onto the surface; Gly1480, Pro1479, Pro1459, Ser1458, Lys1478, and Pro1430. Of the total 7 residues in contact with the methyl surface, 3 are hydrophobic, 3 are polar uncharged and 1 is positively charged (Figure 3.11 f). At the final stage of adsorption (Figure 3.11 a), the fragment had a "head-on" conformation, while the cell-binding region remained exposed to the solution. As indicated on Figure 3.11 b, the fragment maintains its mobility on the surface after the anchoring event, whilst there are

approximately 10 hydrogen bonds formed at the final stage of the adsorption trajectory (Figure 3.11 c). Although the difference in the electronegativity of the C-H bond is only 0.35 in the Pauling scale and it is considered nonpolar, it can still participate in hydrogen bonding as has been shown in the past [187]. The surface charge and hydrophobicity maps (Figure 3.11 e and 3.11 f) show that the side of the protein facing the methyl surface contains mainly uncharged hydrophilic residues.

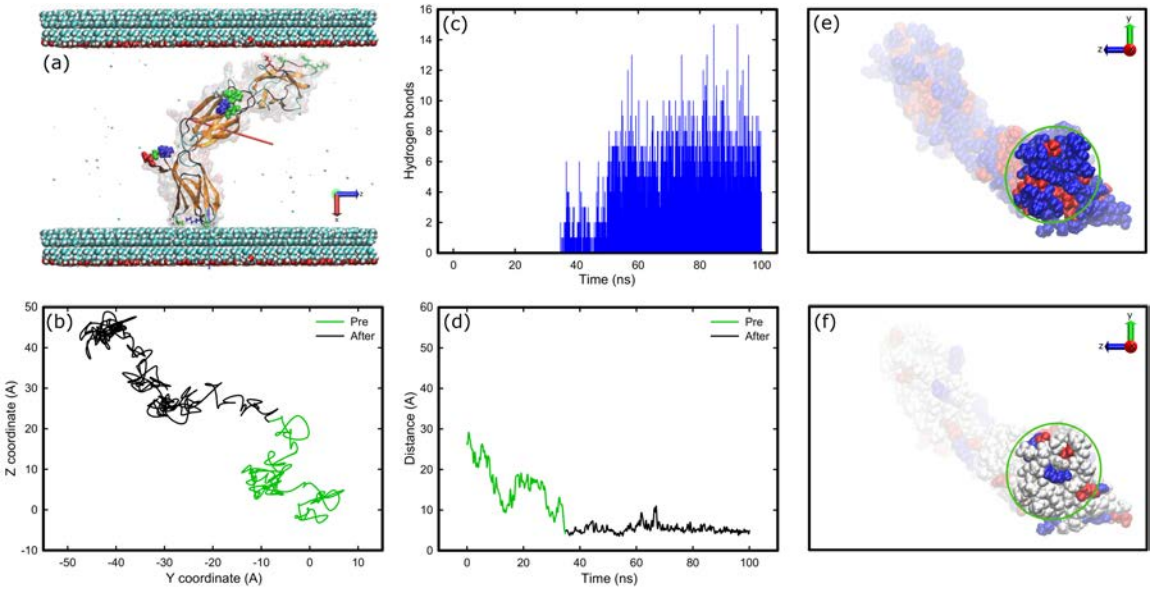

Figure 3.11: Adsorption of FNIII$^{8\text{-}10}$ on a methyl surface (methyl-hydroxyl system); the snapshot at the end of simulation (a) reveals a "head-on" adsorption, while the diffusion of the anchoring residue over the surface (b) shows that the mobility of the anchoring residue is not affected. The evolution of the number of hydrogen bonds between FNIII$^{8\text{-}10}$ and methyl surface (c) increases over time as the distance of the anchoring residue perpendicular to the surface (d) is decreased. The hydrophobicity (e) and surface charge (f) maps of the FNIII$^{8\text{-}10}$ fragment, as viewed from the surface side, on the final stage of adsorption onto methyl surface on the methyl-hydroxyl system show a large concentration of hydrophilic residue wile most of them are uncharged. The surface atoms are not shown for clarity. The depth cueing option of VMD is being used to indicate the distance of each atom from the surface. The areas inside the green circles indicate the areas that are in contact with the surface. The colour scheme is the same as previously.

Figure 3.12 shows the adsorption of FNIII$^{8\text{-}10}$ when it was inserted between two surfaces that are methyl-terminated (methyl-methyl system). It was found that various initial orientations could cause different interfacial conformations after adsorption - FNs4, FNs1, and FNs3 result in "head-on", "beta-on", and "side-on" conformation respectively. As "head-on", "side-on", and "beta-on" conformation is defined the adsorption where the top,

the side, or the β-sheet of the protein is in contact with the surface respectively. However, with the initial configuration of FNs2 facing the hydrophobic surface, the anchoring, and thus adsorption, failed repeatedly. The results also suggest that when the adsorption resulted in "head-on" conformation (Figure 3.12 a) the cell binding and synergy sites remained exposed to the solvent and available for cell-binding, while for the other two conformations the access to the binding sites was inhibited (Figures 3.12 e and 3.12 i). Furthermore, when the final conformation was "head-on" or "side-on" the protein fragment maintained its mobility after the anchoring (Figures 3.12 d and 3.12 l), while for the "beta-on" conformation the movement was highly inhibited after the anchoring (Figure 3.12 h), suggesting stronger adsorption for the latter.

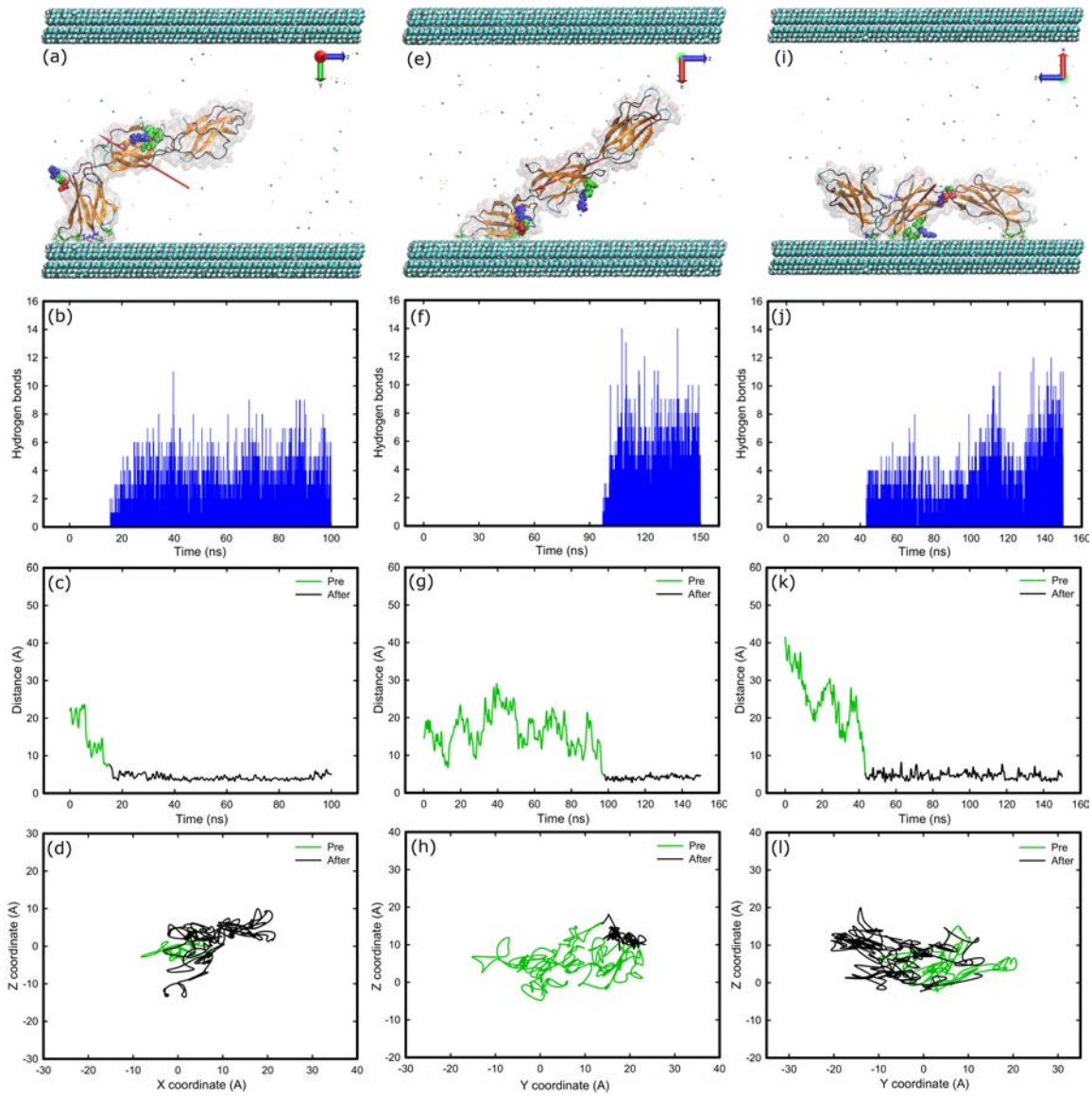

Figure 3.12: Adsorption of FNIII$^{8\text{-}10}$ on methyl surfaces with three different orientations; (a-d) "head-on", (e-h) "beta-on", (i-l) "side-on". Snapshots at the end of simulation (a, e, i) reveal different conformations while the evolution of the number of hydrogen bonds between FNIII$^{8\text{-}10}$ and methyl surfaces over time (b, f, j) is being increased as more residues anchor on the surface. The distance of the anchoring residues perpendicular to the surfaces over time (c, g, k) shows that once the anchoring takes place the residue remains on the surface while its movement can be affected as shown from the diffusion of the anchoring residues over the surface (d, h, l). The colour-coding is the same as previously.

The initial anchoring took place with the FNIII^{10} module in all cases; with Asn1457 (15.5 ns), Thr1431 (97.3 ns), Asn1457 (43.5 ns) followed by Ser1378 (102 ns) on the other end of the protein fragment responsible for "head-on", "beta-on", and "side-on" adsorption processes respectively. All of the anchoring residues are polar uncharged. At the final

stage of adsorption, the following amino acids were found in contact with the surface; on "head-on" the Asn1457, Gly1456, Gly1455, Thr1454, Thr1509, Gly1480, Lys1478, Pro1479, Vs1481, on "beta-on" the Thr1431, Asn1457, Pro1459, Ser1458, Gln1461, Phe1463, Ser1475, Gly1476, Thr1464, Tyr1446, Pro1466, and on "side-on" the Asn1457, Gly1456, Gly1455, Thr1454, Ser1378, Pro1376, Thr1355, Lys1275, Asn1276. In total, 20 residues were polar uncharged, 6 were hydrophobic, 2 were positively charged and 1 negatively charged.

The evolution of hydrogen bond formation shows an adsorption kinetics perspective of the adsorption progress. Furthermore, they provide an indication of the adhesion strength, especially during adsorption on non-charged surfaces where electrostatic interactions are not involved. The number of hydrogen bonds formed between protein and surface is higher when protein adsorbed with a "beta-on" conformation (Figure 3.12 f) than with "head-on" conformation (Figure 3.12 b), approximately 10 versus 6 hydrogen bonds respectively. The evolution of hydrogen bonds in the "side-on" conformation (Figure 3.12 j) visualises the progress of adsorption as the first, second, and third modules eventually bound with the surface resulting in a total of 11 hydrogen bonds. In addition to the number of hydrogen bonds, the comparison between Figures 3.13 a and 3.13 c shows that a larger area of protein was in contact with the surface at the "beta-on" conformation, which could explain the greater number of hydrogen bonds between surface and protein. In fact, 11 amino acids are adsorbed onto the surface in "beta-on" conformation versus 9 in "head-on" or "side-on" conformation. Lastly, the surface charge and hydrophobicity maps showed that the area of protein in contact with the surface was mainly hydrophilic, highlighting the importance of hydrophilic residues at the early stages of adsorption.

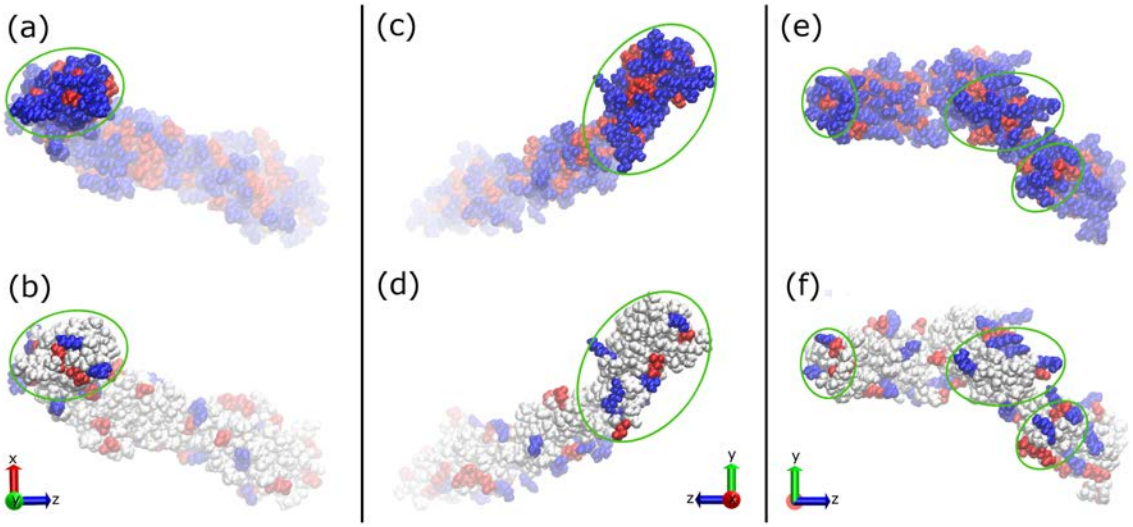

Figure 3.13: Hydrophobicity (top) and surface charge (bottom) maps of the FNIII$^{8\text{-}10}$ fragment, as viewed from the surface side, on the final stage of adsorption on methyl surfaces on three different orientations; (a,b) "head-on", (c,d) "beta-on", (e,f) "side-on". The surface atoms are not shown for clarity. The depth cueing option of VMD is being used to indicate the distance of each atom from the surface. The areas inside the green circles indicate the areas that are in contact with the surface, showing adsorption with side FNIII^{10} during "head-on" and "beta-on" conformation while all three modules are in contact with the surface during "side-on" conformation. The colour scheme is the same as in Figure 3.5.

3.3.6 Adsorption on hydrophilic surfaces

Figure 3.14 shows the adsorption of FNIII$^{8\text{-}10}$ on hydroxyl surface. Two different combinations were used - one being methyl-hydroxyl (Figure 3.14 a) and another being hydroxyl-hydroxyl (Figure 3.14 d). Also, on the methyl-hydroxyl system, only the first carbons of the SAMs molecules were fixed in space, giving a larger freedom of motion to the molecules that composed the surface, as opposed to the first three carbons for the other systems. The initial orientation for both systems was with side Fns1 of the protein facing the hydroxyl surface but the initial distance between protein and surface on the methyl-hydroxyl system was double than that in the hydroxyl-hydroxyl system.

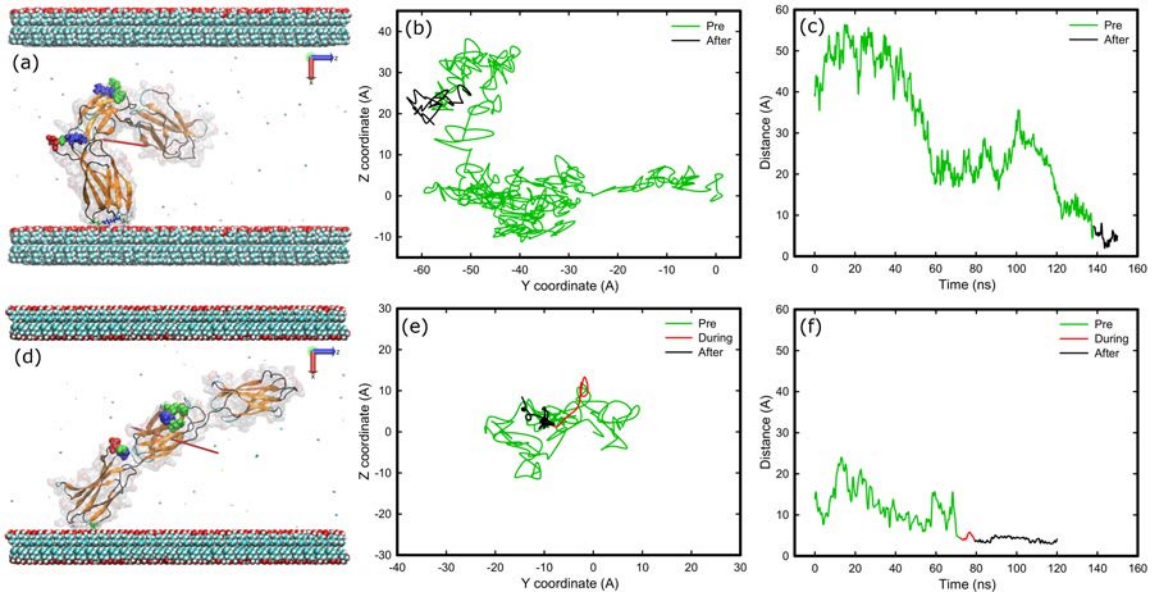

Figure 3.14: Adsorption of FNIII$^{8\text{-}10}$ on hydroxyl surfaces on two different systems; (a-c) methyl-hydroxyl, (d-f) hydroxyl-hydroxyl. The snapshots at the end of simulation (a, d) reveal "head-on" conformation, while the diffusion of the anchoring residues over the surface (b, e) and the distance of the anchoring residues perpendicular to the surfaces over time (c, f) indicate a barrier during anchoring on hydroxyl-hydroxyl surface that is absent on the other surface. The colour-coding is the same as previously.

In both systems, the FNIII^{10} module anchored first, with Asn1457 (138.5 ns) in the methyl-hydroxyl system and with Thr1429 (71.7 ns) on the other. Both anchoring residues are polar uncharged. Subsequently to the initial anchoring the following residues were adsorbed onto the surface; on the methyl-hydroxyl system the Asn1457, Pro1479, Lys1478, Gly1480, and on the hydroxyl-hydroxyl with Thr1429, Pro1430, Thr1431, Pro1479. In total 4 residues were polar uncharged, 3 were hydrophobic, and 1 was positively charged.

The adsorption resulted in a "head-on" conformation in both cases, while the cell-binding and synergy regions remained exposed as can be seen in Figure 3.14 a and 3.14 d. In the hydroxyl-hydroxyl system, the anchoring residue has to penetrate a barrier (Figure 3.14 f), which was not found in the other system (Figure 3.14 c). Furthermore, in the methyl-hydroxyl system, the protein maintained a relative mobility after adsorption (Figure 3.14 b), whilst the protein was immobilised after adsorption on the hydroxyl-hydroxyl system (Figure 3.14 e). The surface charge and hydrophobicity maps in Figure 3.15 reveal that both hydrophilic and hydrophobic residues are in contact with the surface, while the

number of hydrogen bonds evolved between protein and hydroxyl surface at the final stage of adsorption is approximately 8 for the hydroxyl-hydroxyl system.

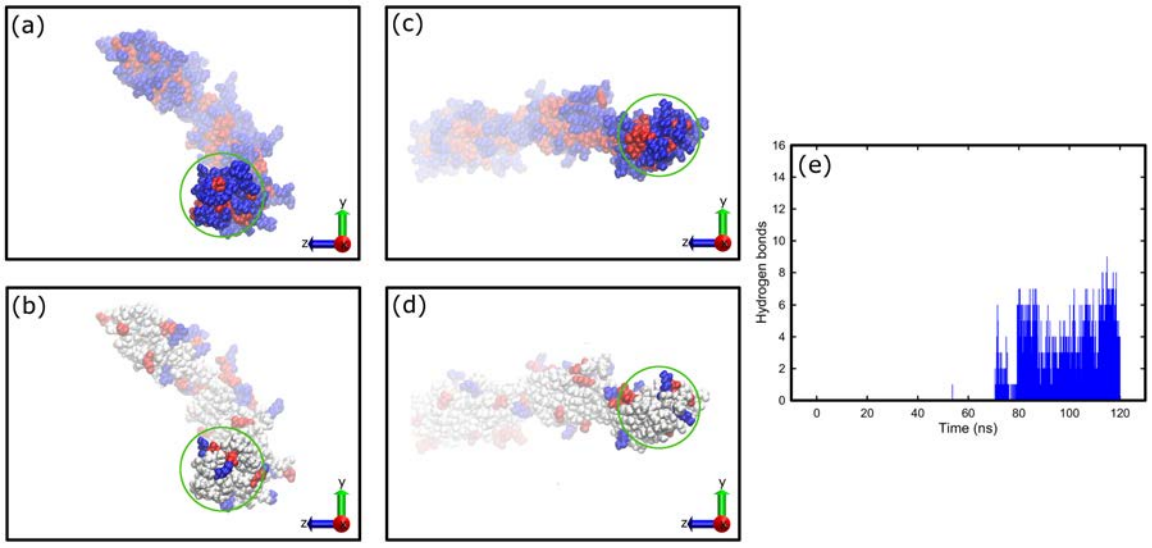

Figure 3.15: (a-d) Hydrophobicity and surface charge maps of the FNIII$^{8\text{-}10}$ fragment, as viewed from the surface side, on the final stage of adsorption onto hydroxyl surfaces on two different systems; (a,b) methyl-hydroxyl, (c,d) hydroxyl-hydroxyl. The surface atoms are not shown for clarity. The depth cueing option of VMD is being used to indicate the distance of each atom from the surface. The areas inside the green circles indicate the areas that are in contact with the surface, which is module FNIII^{10} on both cases. The colour scheme is the same as previously. (e) Evolution of the number of hydrogen bonds between FNIII$^{8\text{-}10}$ and the hydroxyl surface over time.

3.4 Discussion

3.4.1 Adsorption simulations on charged surfaces

Simulation results confirm that the electrostatic interactions are the main driving force for the adsorption of fibronectin fragment on the positively charged systems. In contrast, due to the lack of an electric field, the driving forces involved in the adsorption on carboxyl surfaces are different. More specifically, whilst adsorption on positively charged surfaces is fast and driven by the electric field, adsorption on carboxyl surface is slow and the fragment is moving in a non-specific trajectory due to Brownian motion. On both silica and amine surfaces, the initial anchoring was rapid and resulted in "side-on" conformation, while 2 out of 2 of the produced simulations resulted in successful adsorption (Table

3.2). In contrast, on carboxyl surface, the anchoring was slow and only 1 of the produced simulations resulted in adsorption.

Table 3.2: Number of successful adsorptions, initial anchoring residues, resulted conformation, availability for cell binding domain after adsorption, specific orientation, mobility after anchoring, and anchoring time on each type of surface.

Surface	Successful adsorptions	Anchoring residues	Resulted conformation	Cell-binding domain	Specific orientation	Mobile	Anchoring time (ns)
Hydrophobic	4/14	Thr1431	head-on	exposed	No	Yes	35.0
		Thr1431	beta-on	buried	No	No	97.3
		Asn1457	head-on	exposed	No	Yes	15.5
		Asn1457 & Ser1378	side-on	buried	No	Yes	43.5
Hydrophilic	2/3	Asn1457	head-on	exposed	No	Yes	138.5
		Thr1429	head-on	exposed	No	No	71.7
+ve charged	2/2	Ser1261 & Thr1509	side-on	exposed	Yes	Yes	3.1
		Glu1312 & Thr1509	side-on	exposed	Yes	No	5.3
-ve charged	1/2	Lys1469	-	buried	No	No	53.0

Due to the presence of the electric field, positively charged residues are attracted towards the negatively charged surfaces, whilst the negatively charged residues are pulled towards the positively charged surfaces. Consequently, the fragment could unfold when present in strong field by opposing forces because proteins contain both negatively and positively charged residues. A convenient way to reduce the field in a simulation system is to increase the number of ions; the ions form a layer of opposing charge on the surface that screens the electrostatic field over the Debye length and reduces the forces acting on the protein. This implies that the amount of ions could have a significant influence on the adsorption kinetics, whilst a small field is desired to promote and accelerate protein adsorption. In order to maintain a similar electric field for the silica and the amine surface, the ion concentration in the amine system was kept 16 times greater than that in silica and equal to 0.8 M. In comparison to the NaCl concentration in physiological conditions (0.15 M), the used salt concentration was significantly larger. However, this concentration was necessary in order keep the field above the surface at realistic values and to maintain the integrity of the protein fragment. Because the protein fragment has an overall negative charge of -5 e, ionic conditions aforementioned were used to study the adsorption onto the positively charged surfaces (both silica and amine). In contrast, the concentration of NaCl was kept high enough to screen the electric field completely, so that adsorption

onto the carboxyl surface could be facilitated. Otherwise, the protein fragment was driven away from the surface due to the electrostatic repulsion. As a consequence, the speed of adsorption on the carboxyl surface was greatly decreased and became non-specific, which is in agreement with previous study on adsorption of lysozyme on silica surface [174]. It was found that the presence of ions in MD simulations slow down the rate of adsorption and provides the protein with more time to explore the favourable positions, which is crucial in order to study protein adsorption on surfaces with like charge.

The accelerated adsorption on positively charged surfaces, unlike that on carboxyl surface, is because the force field imposed could prompt the protein fragment moving towards the positively charged surfaces. After the anchoring event on the silica surface, the fragment maintains a relative mobility across the surface as indicated by the trajectories (Figures 3.8 e). In contrast, the anchoring residues were immobilised upon adsorption on amine surface (Figures 3.8 a and 3.8 c). It is very likely that the contrast adsorption characteristics observed is due to the rigidity of the substrate. Unlike the atoms that are fixed in space on the silica surface, the molecules that compose the amine surface possess certain degree of flexibility because only the first few carbons atoms next to the underlying substrate are fixed in space. As a result, the amine surface can be considered as a "soft" surface that allows the anchoring residues to penetrate the SAMs molecules, create more bonds and, consequently, inhibit their surface movement. The explanation is supported by detailed snapshots of the negatively charged anchoring residues on the two surfaces discussed (Figure 3.16). Because the atoms are densely packed on the silica surface, both the anchoring residues and the ions are present at well-defined distances from the surface that are determined from the van der Waals volume of the atoms (the space between the silica surface and the water molecules in Figure 3.16 a is due to the van der Waals volume of the atoms). In contrast, due to the increased mobility of the SAMs molecules, large free volume available on the surface allows not only the ions and the water molecules but also the anchoring residue to penetrate between adjacent SAMs molecules. The immobility of the anchoring residues is further enhanced by the higher charge of

the SAMs surfaces as compared to the silica. As a consequence, when the residues are in contact with the charged SAMs surfaces, they develop an enhanced interaction that constrains their mobility.

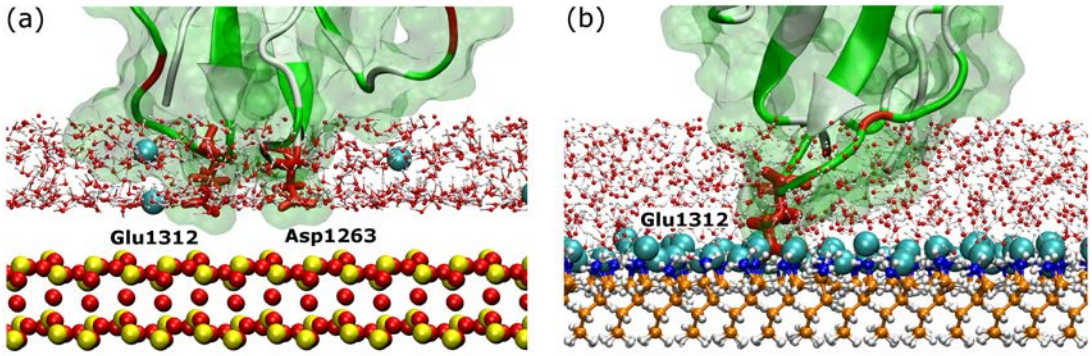

Figure 3.16: Anchoring site between FNIII^{8} module and (a) silica or (b) amine surface. Anchoring residues are shown by thick red sticks and are annotated. The surface is shown by CPK representation (Silica surface: with red and yellow are the oxygen and silicon atoms respectively. Amine surface: with orange, blue, and white are the carbon, nitrogen, and hydrogen atoms respectively). The teal spheres are Cl^{-} ions.

It is also worth noting that the anchoring residues have to overcome an energy barrier to adsorb firmly on the SAMs surfaces, which was not observed on the silica surface. The barrier is induced by a combined layer of ions and water molecules strongly bound to the charged underlying substrate. To anchor successfully, the residue has to compete with the water molecules and the ions for the available free volume. Due to a greater charge in the SAMs surfaces than the silica, the bound layer was adsorbed more strongly. Consequently, it was more difficult for the anchoring residue to replace some of the bound species and occupy a space on the surface. However, once this was done, a smaller distance between the anchoring residue and charged functional groups on the SAMs surface was resulting in a stronger adhesion, which reduced further the mobility of the anchoring residue (Figures 3.8 a, 3.8 c, and 3.10 b). This phenomenon was enhanced during adsorption onto the carboxyl system. The extra ions introduced to screen the electric field could further strengthen the combined layer consisting of water molecules and ions bound on the surface, which significantly reduce the possibility of further residues to adsorb. The barrier became almost impenetrable in the time scale studied in this work, and the non-specific, slow

movement of the protein fragment further prevented any possible subsequent adsorption.

The initial anchoring on both positively charged surfaces took place with the $FNIII^{8}$ module, which could be due to a number of possibilities. Firstly, the $FNIII^{8}$ module is closer to the positively charged surface than the $FNIII^{10}$ module at the initial configuration, and less distance is required to reach the surface. Secondly, the overall charge of $FNIII^{8}$ is -4 e as opposed to 0 e of the $FNIII^{10}$ module, which could result in a stronger attractive interaction with the positive functional groups on the surface. Residue Thr1509 was found responsible for subsequent surface anchoring with the $FNIII^{10}$ module. Because it is the last residue on the polypeptide chain (C-terminus), it possesses a negative charge on its backbone, which causes attraction and anchoring towards the positively charged surface. The anchoring could be further facilitated by the flexibility of the C-terminus.

Due to the presence of an electric force field in both positively charged systems, the adsorption always causes the protein to have its dipole moment aligned with the field. Since the cell-binding region has a positive patch present around it, it remained exposed to the solvent and available for subsequent cell-binding. In contrast, due to the non-specific adsorption onto the carboxyl surface, the availability of the cell-binding domain is not clear. However, due to the positive patch around the cell-binding region it is likely that it would be unavailable.

3.4.2 Adsorption on uncharged surfaces

The adsorption on uncharged surfaces is mainly driven by van der Waals interactions. The protein fragment follows Brownian motion in the water box until one of the residues comes in close proximity with the surface and anchors on it. As a consequence, the protein could adopt various conformations upon the adsorption on uncharged surfaces, which is dependent on both the initial orientation of the protein against the uncharged surface and the non-specific trajectory of the protein prior to surface adsorption.

For adsorption on methyl surface, the initial anchoring takes place with the $FNIII^{10}$ module, which might be because this module is more hydrophobic than module $FNIII^{8}$,

having a hydropathy index of -11 as opposed to -31 of the latter. It is worth noting that hydrophilic residues rather than the hydrophobic ones are responsible for anchoring on hydrophobic surfaces. It is widely known that the polypeptide chain of a protein contains both hydrophobic and hydrophilic residues [70]. Therefore, because the self-assembly of proteins takes place in an aqueous environment, the hydrophobic residues are mainly on the core of the protein driven by the hydrophobic effect. Consequently, the hydrophilic residues remain exposed to the solution and, thus, they are readily available to approach the surface and form the initial anchoring. Once the protein is adsorbed, it occupies the free volume over the surface and excludes the water molecules and ions from the protein-surface interface. As a result, the hydrophobic residues that were buried in the core of the protein tend to come closer to the methyl surface driven by the hydrophobic effect, which leads to stronger interaction between the protein and the methyl surface. However, it is not clear why only polar uncharged residues but not charged residues are involved during the initial anchoring on methyl surfaces. It could have been a random event because approximately a fourth of the total hydrophilic residues that compose $FNIII^{8\text{-}10}$ are charged, which reduces the chances of anchoring with one of them.

The adopted conformations at the final stage of adsorption onto methyl surfaces are non-specific and not affected by the initial anchoring or starting orientation. This is supported by that anchoring with the residue Thr1431 results in both "head-on" and "beta-on" conformation, while anchoring with the residue Asn1457 results in both "head-on" and "side-on" conformation. Furthermore, the final conformation of the fragment is not dependent on the starting orientation of the protein since with the side FNs1 facing the surface the adsorption resulted both in "head-on" and "beta-on" conformation. Consequently, the possibility of the cell-binding region to remain exposed after adsorption on methyl surface was irrelevant to the starting orientation or the anchoring.

In contrast with the adsorption on charged SAMs surfaces, $FNIII^{8\text{-}10}$ on methyl surface maintains a relative mobility across the surface after the adsorption and is not immobilised, at least for three out of four cases. The only exception is when the adsorbed protein

adapts a "beta-on" conformation where the mobility is significantly reduced, although its mobility was still larger than that on the charged surfaces. It might be because the "beta-on" conformation not only facilitates an increased number of residues adsorbed on the surface, but also excludes water molecules from the protein-surface interface, resulting in an enhanced adhesion due to the hydrophobic effect between hydrophobic residues from the core of the protein and the methyl surface. In fact, the hydrophobic effect could be the main reason for the decreased mobility during "beta-on" adsorption, because although "side-on" conformation could facilitate a greater number of hydrogen bonds between protein and surface than the "beta-on" conformation, the protein is not immobilised after the "side-on" adsorption. No signs of a strongly bound layer of water molecules and ions were observed during the adsorption on methyl surfaces, as opposed to the adsorption onto charged SAMs surfaces, which was expected since the surfaces were uncharged. This was further supported by that the ions are dispersed randomly in the water box and not adjacent to the surface due to the lack of electric field.

On both hydrophilic systems, the initial orientation of FNIII$^{8\text{-}10}$ was with the side FNs1 facing the surface. The anchoring took place with two polar uncharged residues, with Thr1429 on the hydroxyl-hydroxyl system and Asn1457 for the methyl-hydroxyl, and both resulted in "head-on" conformation. Both the anchoring residues are present on the FNIII^{10} module of the protein, which was responsible for the anchoring onto the methyl surface as well. Therefore, it is likely that the anchoring is irrelevant to the hydrophobicity of the module and it is a non-specific event that depends on the Brownian motion of the protein. Because the initial distance between FNIII$^{8\text{-}10}$ and the hydroxyl surface on the methyl-hydroxyl system was larger than the other system, the protein fragment had more space to rotate and it was adsorbed almost perpendicular to the surface. This further supports that protein adsorption on uncharged surfaces is non-specific and is highly depended on the Brownian motion of the protein prior to adsorption. Due to the greater distance from the surface, it took the fragment approximately 140 ns to anchor as opposed to the 80 ns required on the other system.

A layer of water molecules was expected to be bound onto the hydroxyl surfaces due to van der Waals and hydrogen bonds interactions between them and the hydroxyl surface, although not as firmly as on the charged surfaces that was bound by electrostatic forces. However, the results suggest that the anchoring residue had to penetrate a barrier only during the adsorption on the hydroxyl-hydroxyl system. The only change on the characteristics of the hydroxyl surface was the number of carbons that were kept fixed in space; on the methyl-hydroxyl system only the first carbon atoms were fixed in space while on the hydroxyl-hydroxyl the first 3 carbon atoms. Therefore, it is likely that because on the hydroxyl-hydroxyl system the building SAMs molecules had a lower degree of freedom than the other system, the water molecules formed a more compact layer bound on the hydroxyl surface, which caused the observed barrier on this system. Furthermore, it would be expected that the greater degree of flexibility of the building SAMs molecules on the methyl-hydroxyl system would have a greater impact on the mobility of the adsorbed protein, as was seen during adsorption on charged surfaces. However, the mobility of the protein was reduced to a greater extent after the adsorption onto the hydroxyl-hydroxyl system than onto the methyl-hydroxyl system. Due to a greater number of anchoring hydrophobic residues present on the hydroxyl-hydroxyl system, it is possible that the reason for the reduced mobility on the hydroxyl-hydroxyl system was arising from an increased interfacial tension between the hydrophobic anchoring residues and the hydroxyl surface [188]. Lastly, the adsorption on both hydrophilic systems resulted with the cell-binding region exposed on the solution and available for subsequent cell-binding.

3.4.3 Structural changes upon adsorption

The RMSD values (Figure 3.17) show that module $FNIII^{9}$ maintains the highest structural integrity during the simulations, possibly because it is the module in the middle and is protected by the other two modules. As a contrast, module $FNIII^{10}$ was found to have the lowest structural integrity, which could be attributed to the mobility of the loop containing the RGD site that provides flexibility to the region in order to facilitate cell-binding. The

modules are deformed during surface adsorption, as expected, whilst the deformation experienced on charged surfaces is nearly twice of that on non-charged surfaces. However, the RMSD values for each individual module are around 2 even after adsorption, suggesting that the modules remain intact and do not change their structure. The increased values of RMSD for the entire protein suggest that the fragment bends or twists on the loops connecting subsequent modules. The bend between subsequent modules of the protein fragment in the present MD experiments might be greater than that in the native protein due to a lack of stabilisation coming from the remaining parts of the protein. The distance between the RGD and PHSRN sites is approximately 30 Å in cases of no adsorption, but is within the range between 20 and 40 Å when there is surface adsorption. This could have an effect on the ability of the protein to bind with the cells and further investigation is needed. Lastly, no differences in the structural integrity of the protein fragment were observed between adsorption on hydrophilic and on hydrophobic surfaces. It is known that adsorption on hydrophobic surfaces can result in denaturation of the adsorbed proteins, however, this cannot be seen in the present study due to the time scales used in MD simulations.

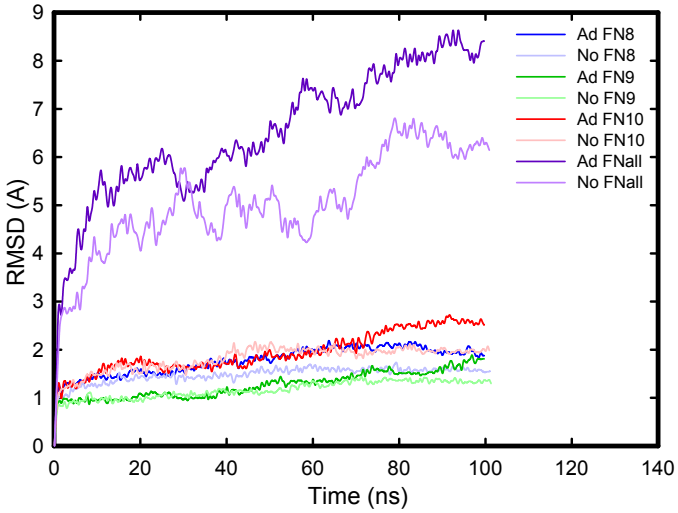

Figure 3.17: Average RMSD values for the individual modules ($FNIII^{8}$-$FNIII^{10}$) and for the whole fragment (FNall), in cases of adsorption (Ad) and no adsorption (No) onto surfaces. It is observed that adsorption has an insignificant impact on the structural integrity of the individual modules, while the differences for the whole fragment are arising from bends between individual modules.

3.5 Conclusions

In the present study, the effect of surface chemistry on the adsorption mechanism of the fibronectin fragment $FNIII^{8\text{-}10}$ was investigated and the following conclusions can be drawn. When the adsorption was driven by a long range electric field, as it happens on silica and amine surfaces, the adsorption is rapid and site-specific. The dipole moment of the protein quickly aligns with the electric field and the protein is rotated, whilst the strong attraction results in a "side-on" conformation on the amine surface. Furthermore, due to a positive patch around the cell-binding site, the protein remains functional upon adsorption on amine and able for subsequent cell-binding. In contrast, upon further screening of the electric field, as it happens on the carboxyl surface, the adsorption becomes slow and non-specific. The anchoring residues are of opposing charge of the surfaces or hydrophilic, while a strongly bound layer of water molecules and ions inhibits the anchoring and adsorption of protein on charged surfaces. Furthermore, "softer" surfaces have a higher impact on the mobility of the proteins after adsorption as they highly restrict their movement.

The adsorption on uncharged surfaces is slow and non-specific. The protein undertakes Brownian motion until the right residue is in the right place at the right time to facilitate the anchoring event. The anchoring residues, both for hydroxyl and methyl surfaces, are polar uncharged, highlighting their importance at the initial stages of adsorption. The conformations of the fragment upon adsorption can be "head-on", "beta-on", and "side-on", and they were independent of the initial orientation of the fragment or the initial anchoring residue. The "beta-on" conformation was found to be the strongest, as it facilitates the exposure of core hydrophobic residues due to hydrophobic effect. Lastly, the rigidity of the surface had a small effect on the water layer bound on the surface and suggested that proteins adsorbed weaker on the "softer" surface.

Chapter 4

Effect of surface chemistry on the adsorption of fibronectin

4.1 Introduction

Upon contact with biological fluids, the surface of a biomaterial is approached by a plethora of proteins. The interactions between these proteins and the biomaterial surface are largely responsible for the biocompatibility of an implant, because they will determine the response of the surrounding tissue towards it. On biologically active biomaterials that promote the integration of the implant with its surrounding tissue [3], the proteins adsorb onto the biomaterial surface and mediate cell-attachment. However, the cell's ability to successfully bind with the adsorbed proteins is governed primarily by the protein's conformation state upon adsorption on the surface. Improper conformation could inhibit cell-binding and cause an immune response that will ultimately lead to rejection of the implant [5, 59]. Among others, an important factor that is responsible for the conformation of proteins upon adsorption is the surface chemistry of a given biomaterial [189–191]. This is the reason that medical devices often use a coating in order to enhance their biocompatibility and, consequently, their functionality. For instance, calcium phosphate based alloys, such as hydroxyapatite, are often used to enhance the osseointegration of dental implants [192]. Therefore, a better understanding on the effect of surface chemistry on protein adsorption will lead towards the development of novel and improved biomaterials.

Among the proteins that mediate surface-cell interaction is fibronectin. It is a large

glycoprotein with a molecular weight of approximately 440 kDa, and is composed of two nearly identical polypeptide chains linked via two disulphide bonds near their carboxyl termini [193]. Fibronectin mediates cellular adhesion to surfaces through the cell binding region that is situated in the 9^{th} and 10^{th} type III domains and binds specifically with integrins located on the surface of the cells [194]. Successful binding will initiate different cell functions such as proliferation and differentiation [18]. Similarly to most proteins, fibronectin is a polyampholyte molecule that contains cationic, anionic, hydrophobic, and hydrophilic groups. As a result, the charge and hydrophobicity of a surface will significantly affect the protein-surface interaction, as different parts of the protein will approach and adsorb on the surface [195, 196]. Consequently, the protein will adopt different conformations on the surface that could hinder the cell-binding ability of the protein. Similarly, highly charged or hydrophobic surfaces could deform the adsorbed proteins and inhibit cell-binding [150, 197].

The interactions between proteins and biomaterials at molecular level were poorly understood until recently because there were no quantitative destruction-free methods to study them. The development of the AFM force spectroscopy in the past decade was proven an important tool for the study of those interactions. Atomic force microscopy can be used to obtain high resolution images of the morphology of a biological sample under physiological condition, but it is also capable of measuring the molecular forces down to a few piconewtons [75, 198]. The produced force curves can provide information on local material properties such as elasticity, adhesion, hardness, and surface charge densities [103]. Furthermore, functionalisation of the AFM tip with desired molecules allows measurements between specific molecules or between molecule and surface, in a technique known as single-molecule force spectroscopy (SMFS). The SMFS technique was firstly used to study the biotin-avidin complex, by functionalising an AFM cantilever with biotin molecules and measuring the rapture forces against avidin-coated surfaces [89]. Since then it has been widely used to study inter- and intramolecular interactions, such as ligand-receptor adhesion forces, protein-protein interactions, and protein unfolding [90, 93, 199].

Previous studies on fibronectin, using single molecule force spectroscopy, were mainly focused on the interaction of fibronectin towards other molecules or on its mechanical stability [163, 200–203]. For example, a study on the interaction between fibronectin and integrins revealed two barriers that correspond to the attachment of the main and synergy cell-binding sites of fibronectin with integrins [200]. The study highlighted the importance of both sites on the activation of the integrin, which result in conformational changes and reorientation of domains. Other studies on the unfolding of the type III modules of fibronectin showed that the modules contain the cell-binding site are mechanically the weakest, which highlight the ability of the domain to promote cell-binding [163, 201, 203]. However, the interactions between fibronectin and biomaterial surfaces, using single molecule force spectroscopy, have not been studied extensively. One of the most relevant studies investigated the adsorption of fibronectin against surfaces with well-defined chemistries [170]. It was reported that fibronectin adopts a more rigid conformation on hydrophobic or unfavourable surfaces, which hinders its unfolding. However, the aforementioned study used full-length fibronectin that was pre-adsorbed on the target surfaces and not functionalised on the AFM cantilever. Consequently, the interactions were non-specific and only 15-20 % of acquired data displayed stretching events. Another study investigated the desorption forces of fibronectin against a negatively charged surface [193]. The followed method was similar to the previous study, using force spectroscopy against full-length fibronectin pre-adsorbed on mica. It was found that on large protein concentrations the molecular packing on the surface prevented denaturation upon adsorption, which resulted in force curves with successive rupture events indicating protein unfolding. In contrast, at small protein concentrations, fibronectin was partially denaturated upon adsorption and the produced force curves were lacking dominant pulling events that indicate protein unfolding.

Because it is likely that a stronger attraction is associated with fast adsorption kinetics and increased adsorption amount, a Quartz Crystal Microbalance (QCM) was used to examine the adsorption of protein on well-defined surfaces. The QCM is a high resolution

mass sensing technique based on the piezoelectric effect of a quartz crystal, which is used among others to quantify the adsorption kinetics of protein on a surface. QCM has been employed in the past to study the adsorption of protein on a variety of surfaces. It has been reported that adsorption of the protein fragment rTp0483 on SAMs surfaces showed the greatest binding on negatively charged surfaces, as opposed to positively charged, hydrophilic, and hydrophobic [204]. This is attributed to the partially positive charge of the fragment in physiological conditions. Furthermore, rTp0483 showed the greatest affinity towards the negatively charged surface, which explains the greater adsorption, followed by the hydrophilic. Another study used COOH and NH_2 terminated SAMs, in different ratios, to control the surface chemistry of gold-coated QCM crystals. They found that although fibronectin is partially negatively charged in PBS (-5.7 mV) it could adsorb both on negatively and positively charged surfaces [186]. More interestingly, the adsorption on negatively charged surface was greater than that on positively charged surface. The adsorption to negatively charged surface was attributed to microscopic polarization of the protein and short-range forces.

Although there has been some progress in the study of quantitative forces at the molecular lever between proteins and surfaces, as well as the effect of surface chemistry on protein adsorption, it is still far from understood. The aim of the present study is to quantify the interaction of fibronectin with a range of well-defined surfaces, and to correlate those interactions with the adsorption kinetics and the adsorption amount. For this reason, single molecule force spectroscopy was used to quantify the forces that are developed between a fibronectin fragment and a range of well-defined surfaces, which provide an insight on the conformation of the fragment upon adsorption. Furthermore, a quartz crystal microbalance was used to measure the adsorption of fibronectin on the same surfaces.

4.2 Materials and methods

4.2.1 Preparation of Self-Assembled Monolayers

Alkanethiols 6-Mercapto-1-Hexanol (HS−$(CH_2)_6$−OH), 1-Hexanethiol (HS−$(CH_2)_5$−CH_3), 6-Amino-1-Hexanethiol (HS−$(CH_2)_6$−NH_2) and 6-Mercaptohexanoic acid (HS−$(CH_2)_5$−COOH) were purchased by Sigma-Aldrich Company Ltd (UK). The assembled SAMs of their respective alkanethiols will be referred to hereafter as OH, CH_3, NH_2 and COOH SAMs, respectively. Gold-coated QCM crystals were used as substrates and were purchased by OpenQCM (Novaetech, Italy). Before the preparation of SAMs the gold surfaces were cleaned with piranha solution. For the preparation of the SAMs surfaces the protocol as described by the technical bulletin AL-266 by Sigma-Aldrich was followed [205, 206]. In brief, the gold-coated QCM sensors were immersed in ethanolic alkanethiol solutions (2 mM in absolute ethanol) and SAMs were allowed to assemble for 24 h. To terminate self-assembly, the samples were rinsed and sonicated for 2 mins in absolute ethanol before they were dried with N_2 gas. The final SAMs surfaces were characterised with static contact angle measurements using a theta optical tensiometer (Attension, Biolin Scientific). The contact angle values for the CH_3, COOH, NH_2 and OH terminated SAMs were found as 101±1°, 11±1°, 50±1° and 35±1° respectively, which is in agreement with previous studies [169, 207–209].

4.2.2 Functionalisation of AFM tips

A combination of the sulfur-gold bond and the His-Tag system was utilised for the functionalisation of the AFM tip, in a variation of a protocol developed by Gruber et.al [57, 105, 210]. Gold-coated AFM chips were purchased from Bruker (NPG-10, USA), cleaned with UV/ozone, and immersed in a solution of absolute ethanol containing 2 mM of 11-Mercapto-1-Undecanol (Sigma-Aldrich, UK), 0.02 mM of trisNTA-EG_3-C_{16}-SH, 2 mM EDTA (Sigma-Aldrich, UK) and 2 mM TCEP (Fisher Scientific, UK) for 24

h [210]. To terminate the self-assembly, the AFM chips were rinsed in subsequent baths of absolute ethanol and an aqueous solution (pH=7.5) containing 40 mM HEPES (Fisher Scientific, UK), 40 mM EDTA, and 85 mM NaCl (Fisher Scientific, UK) and dried with N_2 gas. Subsequently, the tips were immersed in a protein solution containing 0.5 μM of a Histidine-tagged fibronectin fragment (FN-050, R&D systems, UK) and 200 μM Nickel(II) chloride (Sigma-Aldrich, UK), and they were placed in an incubator at 37 °C for 1.5 h. The fibronectin fragment stretches from $FNIII^8$ to $FNIII^{14}$ modules, which contains the cell-binding region, and since every module is around 4 nm (see Chapter 3) it is expected to be approximately 30 nm in the extended linear form. The zeta potential of the fibronectin fragment in 1 M HEPES solution was identified with a Zetasizer (Malvern, UK) at -14±1 mV. Finally, the AFM chips were rinsed with 1 M HEPES solution and were loaded onto the AFM to perform force spectroscopy experiments.

4.2.3 Force spectroscopy

The force measurements were performed using an atomic force microscope by JPK (Nanowizard II, Germany). The measurements were done in a fluid cell at room temperature, in 1 M HEPES (pH=7.5) solution. The AFM was loaded with the functionalised cantilevers as well as control cantilevers from every step of the functionalisation process; (i) bare gold AFM chips (Gold), (ii) bare gold tips that were immersed into the protein solution and resulted in physisorbed proteins (Gold-FN), (iii) gold AFM tips functionalised with the trisNTA-EG_3-C_{16}-SH linker but without protein (Gold-linker), (iv) gold AFM tips with linker and protein chemisorbed on it (Gold-linker-FN). The AFM cantilevers were calibrated with the thermal method prior to the experiments [104]. A force equal to 1 nN was applied on the tip which was approaching the SAMs surface with a velocity of 1 μm/s. Once the tip was on the surface it maintained contact for 3 s before it was retracted and repeat. The force curves were taken from 16 different positions (4x4 grid) on the surface used, while the distance between each position was 10 μm. The tests were repeated 4 times with different AFM chips to ensure the reproducibility of the measurements.

4.2.4 Mass adsorption

The adsorption of fibronectin onto the SAMs surfaces was quantified using a quartz crystal microbalance by openQCM (Novaetech, Italy). For this part of the project, and for practical reasons, a full-length fibronectin was used that was purchased from Merck (fc010, UK). Studies in the past have shown that the adsorption behaviour of the fibronectin fragment $FNIII^{7\text{-}10}$, which is similar to the one used in this study, exhibits very similar adsorption behaviour with the full-length fibronectin [196]. The SAMs coated QCM crystals were loaded onto the QCM and a solution of 25 μg/mL fibronectin in 1xPBS was loaded into the system. The QCM was connected to a peristaltic pump (Ismatec, Germany) that maintained a flow of 60 μL/min. The adsorbed mass was calculated using the Sauerbrey equation (Equ. 4.1) [106]:

$$\Delta f_m = -\frac{2f_0^2}{A\sqrt{\rho_q \mu_q}} \cdot \Delta m = -C_f \cdot \Delta m \qquad \textit{Sauerbrey's equation} \qquad (4.1)$$

where Δf_m is the measured resonance frequency (Hz), f_0 is the intrinsic resonance frequency of the unloaded crystal, Δm is the mass change (g), A is the mass sensitive area of the electrode, ρ_q is the quartz density (2.65 g/cm^3), μ_q is the shear modulus of the crystal (2.95×10^{11} dyn/cm^2), and C_f is the quartz sensitivity factor. The negative sign in the formula shows that a reduction in the frequency is due to a mass increase on the surface of the crystal. A total of 7 measurement was repeated against each surface to ensure the reproducibility of the results.

4.2.5 Statistical analysis

All data were presented as mean values ± the standard error of the mean. An analysis of variance (ANOVA) was used to evaluate the significance of the measured parameters.

4.3 Results and Discussion

4.3.1 Interaction between gold and SAMs surfaces

The functionalisation of the AFM tip with the fibronectin fragment was a 2 step process. Initially, a linker (trisNTA-EG_3-C_{16}-SH) was attached onto a gold-coated AFM tip via the sulfur-gold interaction. Subsequently, the fibronectin fragment was attached to the linker using the His-Tag interaction. To ensure the quality of the results, force measurements were performed between the AFM tip and the SAMs surfaces at every step of the functionalisation.

Initially, bare gold-coated cantilevers were used to perform force spectroscopy against the SAMs surfaces, to ensure that both the AFM tips and the SAMs surfaces were free of contaminants and to have it as a reference for the following functionalisation steps. Figure 4.1a shows the representative force curves of the gold-coated AFM tips against the SAMs surfaces. The shape of the force curves revealed single adhesion between the AFM tip and the CH_3 or the NH_2 surface, and no adhesion against the OH or the COOH surface. Furthermore, the absence of multiple peaks on the retracting part of the force curves, which would indicate the presence of contaminants, ensures that the AFM tip was free of contaminants and that there were no aggregates or residues from the SAMs molecules on the surface of the assembles.

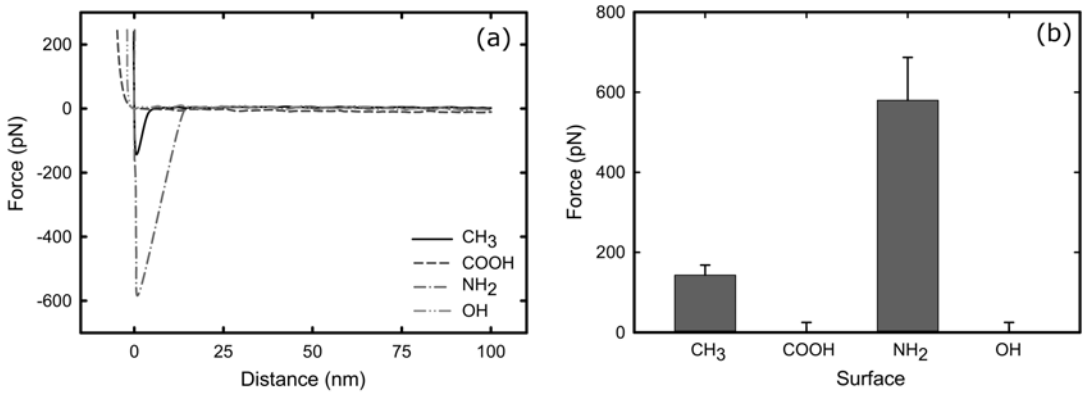

Figure 4.1: (a) Characteristic force-distance retraction curves of bare gold AFM tip against SAMs surfaces in 1 M HEPES solution, (b) adhesion of bare gold AFM tip against SAMs surfaces in 1 M HEPES solution. Data points represent mean values of n=64 force curves, with the error bars representing the standard error.

Figure 4.1b shows the desorption forces that are developed between the AFM tip and the SAMs surfaces. A small adhesion of approximately 143±25 pN was observed between AFM tip and CH_3 surfaces while the adhesion observed between AFM tip and NH_2 surfaces was approximately four times larger. The adhesion against the NH_2 surface indicates that the AFM tip possesses a negative charge. Although gold theoretically should be an uncharged surface, studies have showed that in aqueous conditions it becomes negatively charged due to adsorption of anions on its surface [211–214]. HEPES is a zwitterionic compound with an isoelectric point pI=5.0 [215]. Therefore, it is likely that hydroxide and HEPES anions are adsorbed onto the gold surface, which becomes negatively charged. Consequently, the adhesion between the AFM tip and the NH_2 surface is of electrostatic nature. The smallest adhesion observed between the AFM tip and the CH_3 surface could be due to the interfacial tension developed between a hydrophilic and a hydrophobic surface [188]. Lastly, no adhesion was observed between the gold-coated AFM tip and the OH or the COOH surface, because the surfaces were of the same charge as the AFM tip and hydrophilic.

4.3.2 Surface interaction with physisorbed fibronectin fragment

Before proceeding with the functionalisation of the AFM tip with the linker, the adhesion of a physisorbed fibronectin fragment on bare gold AFM tips against SAMs surfaces was studied. Because the fibronectin is not specifically attached onto the AFM tip, it can adopt different conformations on it. Consequently, the interaction with the SAMs surfaces will not be specific, as expected for the chemisorbed fibronectin. Furthermore, during retraction of the AFM tip from the SAMs surface the force of desorption will correspond to the weakest link. Consequently, the desorption force will not represent the fibronectin-SAMs interaction only, but also the fibronectin-gold interaction. It is hypothesized that the results from this section will highlight the importance of AFM tip functionalisation during single molecule force spectroscopy experiments.

The first observation made upon examining the produced force curves is that the retraction force curves exhibit multiple peaks and pulling events instead of single peaks that were being produced in the first control experiment. Since the surface of the SAMs surfaces was clear, as was discussed in the previous section, it suggests the presence of fibronectin adsorbed on the AFM tips. The shape of the retraction part of a force curve (in protein adsorption applications) is mainly depended on; (i) the speed that the AFM tip is retracted from the surface, (ii) the interaction between protein and surface, and (iii) the conformation of the protein upon adsorption [216]. As a result, the shape of the retraction force curves can reveal single or multiple peaks, a saw-tooth pattern (loop-like), extended plateau (train-like), or a combination of saw-tooth and plateau (mix) (Figure 4.2). Typically, in protein adsorption, saw-tooth patterns usually indicate unfolding of protein domains [217, 218], while plateau are associated with events such as desorption of proteins from charged or hydrophobic surfaces [219, 220] due to denaturation of protein upon adsorption [193].

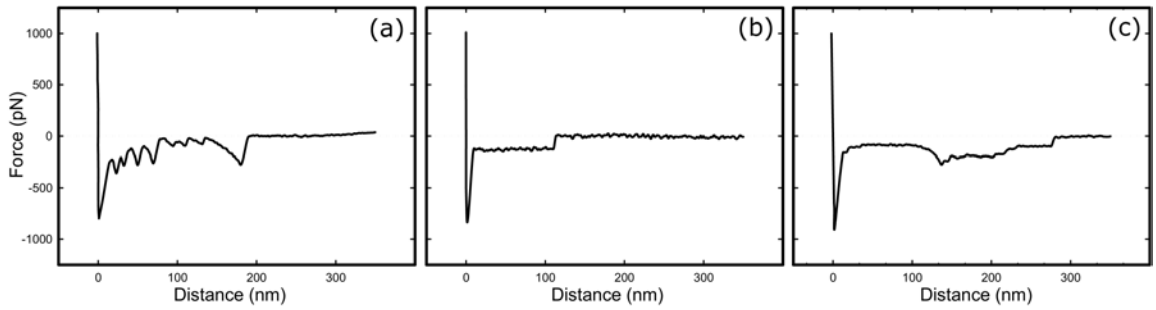

Figure 4.2: Characteristic force versus distance curves showing the retraction of (a) a loop-like event that indicates protein unfolding, (b) a train-like event that indicates protein desorption, (c) a mix-like event that indicates both desorption and unfolding. As desorption force is defined the last peak in the retraction curve where the protein detaches from the surface, while the distance where the protein detaches from the surface is defined as desorption distance.

Of the total 64 force curves collected on each SAMs surface, the percentage that displayed pulling events and was used for the analysis of the results was 50 %, 39 %, 36 %, and 27 % for the CH_3, COOH, NH_2, and OH respectively. The obtained retraction curves contain both train-like, loop-like and mix type curves as shown in Table 4.1. The large distribution of the interactions during desorption could be because the proteins were physisorbed on the AFM tip, resulting in non-specific interactions against the surface. Generally, the majority of the produced force curves had a mix-like nature. However, approximately 60 % of the force curves against the OH surface exhibits a loop-like shape, as opposed to only 6 % against the CH_3 surface. Since train-like events are associated with denaturation during adsorption [193], it is likely that CH_3 causes the greatest denaturation on the adsorbed fibronectin fragment, whilst the OH surface the least. The COOH and NH_2 are resulting in an intermediate denaturation.

The desorption forces developed between gold AFM tips with physisorbed fibronectin and SAMs surfaces are shown in Figure 4.3a. The adhesion of fibronectin against the COOH surface was the weakest, at approximately 90 pN. This could be attributed to the AFM tip, the SAMs surface, and the protein fragment all being negatively charged, and therefore the interaction between them was the least. In contrast, the adhesion was the largest onto the NH_2 surface, which is likely due to electrostatic interactions, followed by the adhesion on CH_3 and OH surfaces. Due to the non-specificity of the interactions

against an unknown number of protein, the analysis of the desorption distance against the SAMS surface is impossible (P=0.93) and a further investigation is needed.

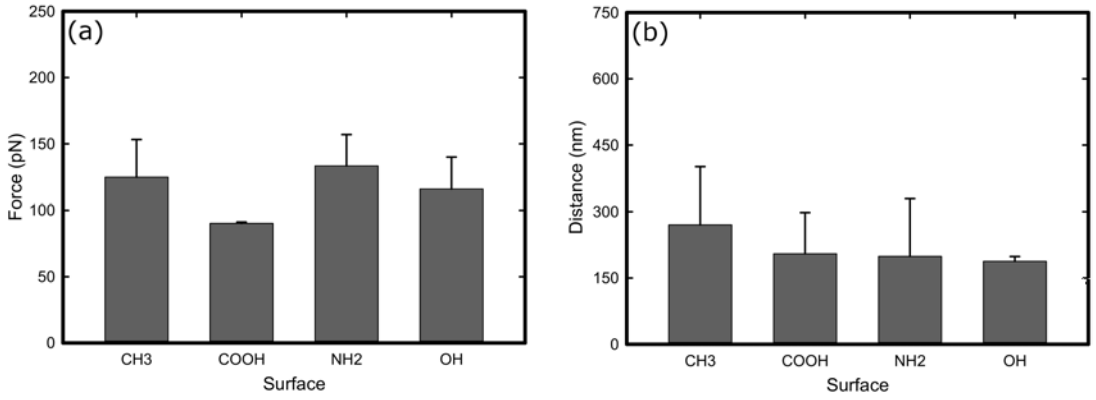

Figure 4.3: Gold tip coated with the FN fragment (physisorption) against SAMs in 1 M HEPES solution. (a) Desorption force of FN fragment against SAMs (P=0.008), (b) Desorption distance of FN fragment against SAMs (P=0.93). The bars represent the mean values of the force curves, while the error bars represent the standard error.

4.3.3 Surface interactions with linker

To ensure the functionalisation of the AFM tip with the linker, force spectroscopy was performed between the AFM tips functionalised with linker and the SAMs surfaces. Because the surface of the AFM tip was covered with a layer of OH SAMs and dispersed trisNTA-EG_3-C_{16}-SH molecules, it was expected to possess a negative charge due to the carboxylic acid groups present on the trisNTA. Of the total 64 force curves collected on each SAMs surface, the percentage that displayed pulling events and was used for the analysis of the results was 42 %, 23 %, 44 %, and 20 % for the CH_3, COOH, NH_2, and OH respectively. The analysis of the produced force curves revealed multiple pulling events, exhibiting both loop-like, train-like, and mix shapes as shown in Table 4.1. More specifically, most of the produced force curves between AFM tips and SAMs surfaces were of a mix type, with the OH and COOH surfaces revealing approximately 25 % loop-like interactions, whilst NH_2 surface was the only that revealed train-like shape (40%) in the produced force curves. The desorption force between the AFM tip and SAMs surfaces is shown in Figure 4.4a. The desorption forces against all types of surfaces were approximately 150 pN. However,

no further comparison can be done due to the non-specific events arising from aggregates that resulted in a very large P value (P=0.35). The NH_2 and CH_3 surfaces produced the largest desorption distances, approximately threefold larger than the OH and the COOH surface, as shown in Figure 4.4b.

From the above observations, it can be concluded that the pulling events present on the force curves are due to aggregates of OH SAMs and linker molecules present on the surface of the AFM tip after the functionalisation. The aggregates contain both negatively charged and hydrophobic regions, which could explain the higher adhesion towards the NH_2 and the CH_3 surfaces. The greater desorption distances could be due to larger aggregates present on these surfaces or due to a greater unfolding of the entangled aggregates.

A typical cleaning procedure requires sonication of the gold surfaces after functionalisation with SAMs. However, this cannot be applied on AFM cantilevers because they are damaged. Inevitably, OH SAMs and linker aggregates are expected to be present during attachment of fibronectin onto linker, and should be taken into consideration.

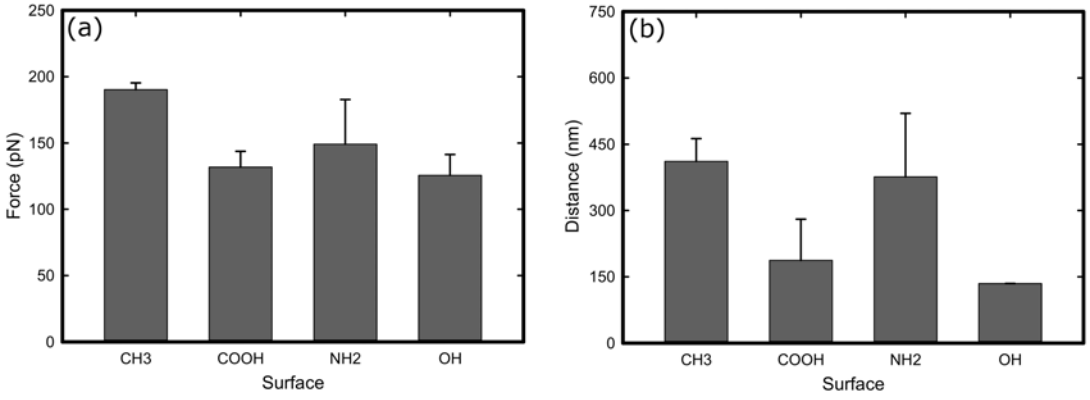

Figure 4.4: AFM tip functionalised with linker against SAMs in 1 M HEPES solution. (a) Desorption force of AFM tip containing linker against SAMs (P=0.35), (b) desorption distance of AFM tip containing linker against SAMs (P<0.001). The bars represent the mean values of the force curves, while the error bars represent the standard error.

4.3.4 Surface interactions with chemisorbed fibronectin fragment

Of the total 64 force curves collected on each SAMs surface, the percentage that displayed pulling events and was used for the analysis of the results was 59 %, 52 %, 68 %, and 56

% for the CH_3, COOH, NH_2, and OH respectively, which is significantly larger compared to the physisorbed fibronectin. The comparison between the force curves produced at every step of the functionalisation process provides enough evidence that it has been successful. Both the desorption forces and distances produced between the AFM tip and the SAMs surfaces were different for every step of the functionalisation. Furthermore, while chemisorbed fibronectin has higher affinity for the COOH and OH surface, physisorbed fibronectin prefers CH_3 and NH_2 surfaces. As shown in Table 4.1, the produced force curves from the physisorbed fibronectin do not exhibit any strong preference towards a force curve type. In contrast, over 80 % of the produced curves regarding the chemisorbed fibronectin showed a preference producing a loop-like or mix-like curve, highlighting a specific interaction arising from successful functionalisation.

Table 4.1: Distribution of the produced force curves between AFM tip and substrates.

		Conformation		
AFM tip	substrate	loop-like (%)	train-like (%)	mix (%)
Gold + FN	CH_3	6.3	40.6	53.1
	COOH	20.0	16.0	64.0
	NH_2	34.8	21.7	43.5
	OH	58.8	0.0	41.2
Linker	CH_3	0.0	0.0	100.0
	COOH	26.7	0.0	73.3
	NH_2	3.6	39.3	57.1
	OH	23.1	0.0	76.9
Linker + FN	CH_3	0.0	14.3	85.7
	COOH	75.8	0.0	24.2
	NH_2	0.0	18.6	81.4
	OH	94.3	0.0	5.7

In comparison with the results from the physisorbed fibronectin, fully functionalised AFM tips with chemically attached fibronectin revealed a target-specific conformation of the adsorbed fibronectin as can be seen in Table 4.1. The majority of the force curves between the chemisorbed fibronectin and the COOH and OH surfaces produced loop-like curves. More specifically, approximately 76 % for the COOH and 94 % for the OH produced force curves with a saw-tooth pattern, which could be a sign of protein unfolding.

In contrast, the CH_3 and NH_2 surfaces favoured a production of mix typed curves that indicates desorption and unfolding. Furthermore, the complete absence of loop-like curves for CH_3 and NH_2 surfaces could suggest a greater denaturation of fibronectin than on the OH and COOH surfaces.

Figure 4.5a shows that the fibronectin fragment has higher affinity towards the COOH and the OH surface, producing a desorption force of approximately 200 pN, which is twofold higher than that against the CH_3 and NH_2 surfaces. However, although the affinity is larger, the desorption distance on the COOH and OH surfaces is smaller and approximately 150 nm as opposed to 300 nm for the CH_3 and NH_2 (Figure 4.5b). Furthermore, the desorption forces showed a greater distribution for the OH and COOH surface, while CH_3 and NH_2 exhibited a greater distribution in desorption distance as seen in Figure 4.5c.

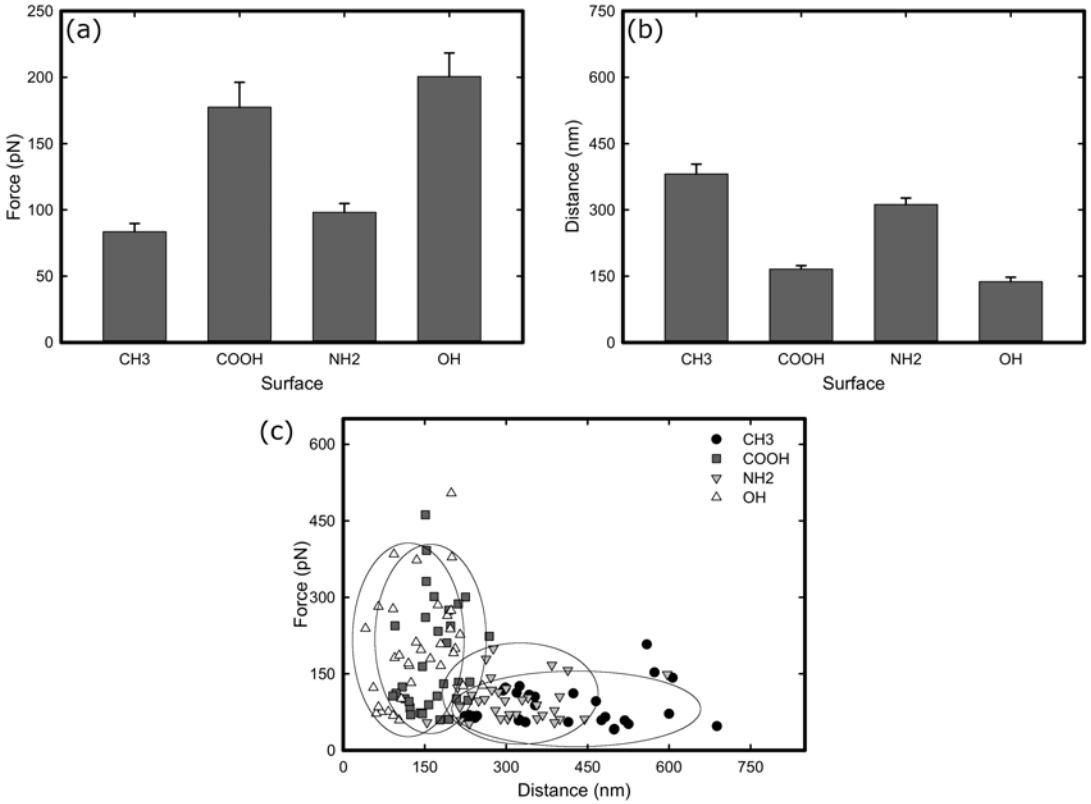

Figure 4.5: FN fragment chemisorbed on AFM tip against SAMs in 1 M HEPES solution. (a) Desorption force of FN fragment against SAMs (P<0.001), (b) Desorption distance of FN fragment against SAMs (P<0.001), (c) dependence of desorption force on the distance. The bars represent the mean values of the force curves, while the error bars represent the standard error.

Due to the different levels of interaction, it is likely that fibronectin adopts a different

conformation on the SAMs surfaces. It is possible that a large fraction of the fibronectin fragment is in contact with the surface during the adsorption on CH_3 and NH_2 surfaces, resulting in a "side-on" conformation. Generally, a stronger interaction between a surface and a protein results in a greater denaturation of the protein and, thus, a greater protein-surface interface [197, 221]. Since fibronectin has an overall negative charge, it is likely that a positively charged surface (NH_2) results in a greater denaturation of the adsorbed protein. Similarly, the adsorption of fibronectin on hydrophobic surface (CH_3) could result in a greater denaturation of the protein, because it exposes on the surface the hydrophobic core of the protein [13,27]. The term "side-on" is referred to an adsorption where the long axis of the protein is almost parallel to the adsorbing surface. In contrast, "head-on" adsorption is where the long axis of the protein is almost perpendicular to the surface. Although the results showed that the desorption forces were smaller for CH_3 and NH_2 surfaces, this force corresponds to the last peak in the retraction curve. Since the protein is being desorbed and unfolded over larger distances, only a small portion of it remained on the surface before the final desorption force was measured. This could explain the smaller desorption force as opposed to the COOH and OH surfaces. In contrast, the adsorption of fibronectin in OH and COOH surfaces resulted on a "head-on" adsorption, with a smaller area of the protein in contact with the surface. Although fibronectin has an overall negative charged, it contains positively charged regions that are attracted and eventually adsorbed on the surface. Similarly, the adsorption on the OH surface is mainly driven by Van der Waals interactions that are weak. Consequently, it is expected that OH and COOH surfaces to have less contact points with the protein than the CH_3 and NH_2 surfaces.

To provide further evidence of the above hypothesis, the adsorption of fibronectin onto SAMs was studied using a Quartz Crystal Microbalance. For practical reasons, for this part of the project full length human fibronectin was used instead of the previously used fibronectin fragment. It is expected that this will not have a significant impact on the results since it has been shown that the adsorption behaviour of the fibronectin domain

$FNIII^{7\text{-}10}$ is very similar to the whole fibronectin [196]. Figure 4.6a shows the adsorption kinetics of the fibronectin onto SAMs surfaces, while Figure 4.6b shows the total amount of fibronectin adsorbed onto those surfaces. Fibronectin has an isoelectric point of 5.5-6.0 and, therefore, it is expected to be negatively charged at pH=7.5 [222]. Consequently, it is no surprise that the largest amount of fibronectin was adsorbed onto the NH_2 surface (approximately 1500 ng/cm^2). The amount of adsorbed fibronectin on the COOH surface was slightly lower, while the adsorption kinetics was faster than the NH_2 surface. It is likely that fibronectin needs more time in order to be rearranged on the NH_2 surface. The least amount of fibronectin was adsorbed onto the CH_3 surface, approximately a third lower than the NH_2 surface.

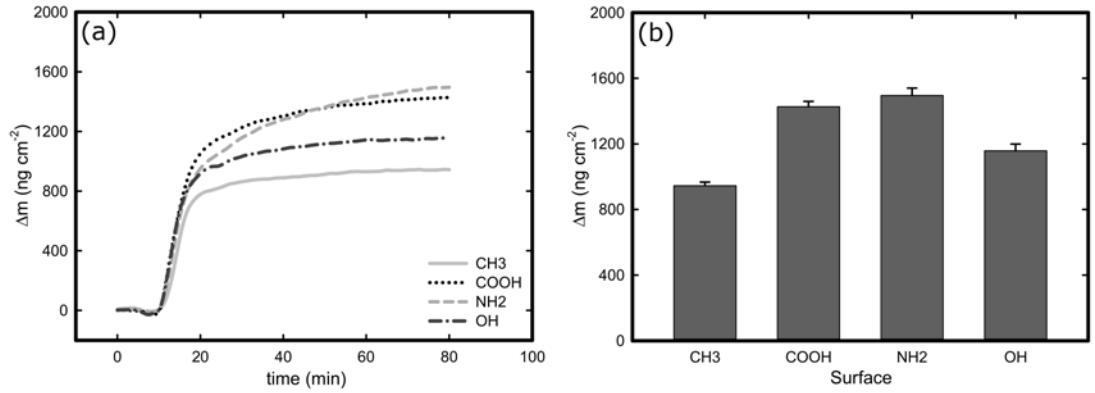

Figure 4.6: (a) Adsorption kinetics of fibronectin solution (25µg/mL in 1xPBS) onto SAMs, (b) amount of adsorbed fibronectin onto SAMs. Data points represent mean values of n=7 measurements, with the error bars representing the standard error.

Since the size of one molecule of adsorbed fibronectin is approximately 15 x 9 nm [223], then the amount of fibronectin needed to fill a densely-packed monolayer is approximately 540 ng/cm^2 if the protein adopts a "side-on" orientation, or approximately 900 ng/cm^2 for a head-on orientation. It is more likely that the protein will be a mix of both, so approximately 720 ng/cm^2 are needed for a monolayer with 50 % "side-on" and 50 % "head-on" oriented fibronectin. The QCM results show that a greater amount of fibronectin is needed to fill a monolayer on COOH than NH_2 surface, which indicates that fibronectin molecules prefer a "head-on" conformation on the former and a "side-on" conformation on the latter. Figure 4.6a shows that the rate of adsorption for the NH_2 and COOH

surface are the same up to approximately 800 ng/cm^2 for the former and 1100 ng/cm^2 for the latter. At this point it is likely that both surfaces have formed approximately a monolayer of fibronectin onto their surfaces. Because a greater amount is needed to nearly form a monolayer on COOH that NH_2, it is likely that a larger amount of fibronectin adopts a "head-on" conformation. Since the attraction is of long-range electrostatic nature, more proteins continued to adsorb on the already adsorbed proteins over time resulting in multilayers that need more time to adsorb and rearrange. The OH and CH_3 surfaces are possibly saturated with a monolayer of fibronectin since the interaction between surface and proteins are short ranged van der Waals forces and hydrophobic interactions. However, the largest amount needed for the OH surface indicates that more protein adopted a "head-on" adsorption. The above come in agreement with the results from the SMFS, which also indicated a "head-on" conformation for the COOH and OH and a "side-on" for the NH_2 and the CH_3.

4.4 Conclusions

In the present work, the effect of surface chemistry on the adsorption of fibronectin was studied and the following conclusions can be drawn. Initially, the functionalisation method combining gold-sulfur bond and His-tag system was tested and proven successful, which could provide a direct method to functionalise surfaces. Among the control tests the interaction between gold AFM tips and SAMs surfaces was studied and the results indicated that gold possesses a negative charge in 1 M HEPES solution. Furthermore, the comparison between SAMs and physisorbed or chemisorbed fibronectin highlighted the importance of AFM functionalisation in order to acquire target-specific results.

Single molecule force spectroscopy reveals a greater number of saw-tooth pattern curves for the hydrophilic and the negatively charged surfaces, indicating unfolding of proteins. In contrast, the shape of the retraction curves against the hydrophobic and positively charged surfaces was a combination of saw-tooth and plateau shape curves, suggesting unfolding and denaturation of proteins. It is suggested that on hydrophilic and negatively charged

surfaces the fibronectin molecules adopt a “head-on” conformation with less contact points with the surface, while on hydrophobic and positively charged surfaces they take a “side-on” conformation with more contact points between them that results in stronger adsorption and greater denaturation. This is further supported by the QCM results that showed a smaller amount of protein is needed to fill a monolayer in surfaces that favour “side-on” adsorption.

Chapter 5

Electrochemical behaviour of titanium in albumin solution

5.1 Introduction

Titanium is a widely used biomaterial in dental and orthopaedic applications due to its unique combination of physical properties and corrosion resistance [39, 224, 225]. Similar to that of most metallic materials used for bio-applications, corrosion resistance of titanium is highly dependent on the passive film developed on its surface [35]. When a passive metal, such as titanium, is exposed to ambient or liquid, an oxidation reaction takes place, resulting in the formation of a thin metal oxide with thickness of a few nanometres. Such oxide film not only protects the underlying material from corrosion, but also provides an excellent interface to interact with the surrounding tissue due to its biocompatibility and osseointegration [226–228]. Therefore, an in-depth understanding of the factors that determine the stability of the oxide film, particularly when being exposed to physiological environment, is vital for producing novel biomaterials with enhanced properties.

Under external mechanical impact, the passive film breaks down, releasing metal ions into the surrounding environment such as the tissue in contact. This happens either by passive diffusion or by forming metal-protein complexes with the adsorbed proteins and subsequent release of the formed complexes upon desorption of the proteins [229]. Consequences of releasing metal ions to the surrounding tissues range from discolouration to more severe biological reactions, such as cytotoxicity and tissue necrosis [9,37]. Furthermore,

the tissue in the areas of corrosion could recede, forming small pockets that facilitate the formation of a microenvironment suitable for bacterial and viral infections [229]. As a result, the film of adsorbed protein surrounding the implant could be infected, which in turn accelerates the corrosion process as a result of the metabolic product of the presence of bacteria, pH changes, and increases of local temperature [229].

Upon contact with biological fluids, the surface of an implant is covered with a dynamic film of proteins that dictates the initial cellular and, subsequently, the host response. Proteins play a key role in the integration of implants from the surrounding tissue as it is the first step in the cell adhesion process, since cells cannot adhere directly with the surface of an implant but instead through an intermediate interaction of adsorbed proteins [155,230]. Therefore, the interaction of proteins with passive films is an important factor that dictates the biocompatibility of a biomaterial. Albumin is the most abundant protein found in body fluids and has been studied extensively [122]. It has a molecular mass of approximately 65 kDa and is consisted of 585 residues that are organised in a highly helical structure with three sub-domains [229]. Due to its helical structure, albumin has high flexibility allowing a rapid expansion and contraction. Upon adsorption on solid substrates, the dimensions of albumin are ranging from 9.2 x 9.2 x 9.2 x 3.0 nm (triangular shape) on surfaces with low adhesion, to 25.0 x 2.1 x 2.1 nm (elongated shape) on surfaces with larger adhesion [231]. In comparison, the hydrodynamic radius, R_H, of BSA in solution is ranging from 3.3 to 4.3 nm [232]. Albumin can be found primarily in serum or synovial fluid with a concentration of 37.6 - 54.9 mg/mL and 6 - 10 mg/mL respectively [132]. The isoelectric point of albumin is 4.9 which means that it has an overall negative charge at pH=7 [233]. It has been found that albumin can be reduced to sulfhydryl groups via cleavage of its disulphide bonds at cathodic potential [234], whilst it can increase the dissolution rate of alloys in anodic potentials [235].

There have been several studies concerning the effect of proteins on the electrochemical behaviour of metal surfaces. It was found that on CoCrMo surfaces, in phosphate buffer saline (PBS) or sodium chloride (NaCl) solutions, bovine serum albumin (BSA) acts as a

cathodic inhibitor accelerating the anodic reaction and shifting the corrosion potential towards more cathodic values [236]. Consistent results were reported when titanium alloys were exposed to PBS solution in the presence of BSA or collagen [7]. It was suggested that protein molecules adsorb onto surface sites where oxygen reacts with electrons available on the surface, and consequently block the cathodic reaction. Furthermore, on Ti-6Al-4V surfaces, it was found that the presence of BSA in simulated inorganic plasma solutions is reducing the passive current density and thus indicating a lowering of the corrosion rate, while on platinum surfaces the adsorption of proteins such as insulin, myoglobin, casein, fibrinogen, and BSA could inhibit the growth of surface oxide layer at anodic conditions [235, 237].

On stainless steel surfaces, the reported results are less consistent. While BSA diluted in PBS acts as cathodic inhibitor, BSA diluted in NaCl has the opposite effect since it acts as an anodic inhibitor and accelerates the metal dissolution [236]. Furthermore, the adsorption of BSA on stainless steel decreases the corrosion activation energy at anodic conditions [238]. It was proposed that the decrease is due to the negatively charged carboxylate groups of the proteins that act as anchoring sites during the adsorption onto stainless steel - a process that is accompanied by transfer of charge. This is in agreement with another study concerning the adsorption of BSA and fibrinogen on titanium surfaces where the surface charge density was found directly proportional to the amount of adsorbed protein [229]. The same study suggests that the adsorption process is endothermic and entropically controlled, implying that the interaction between protein and titanium surface is chemisorption and denaturation occurs upon adsorption respectively. Denaturation of globular proteins was also observed onto the electrode surface of platinum [239]. Although a number of mechanisms are associated with the interaction between proteins and solid substrates, it has been shown that BSA generally acts as a cathodic inhibitor but can also increase the dissolution rate of materials.

To examine the adsorption process of protein under controlled electrochemical conditions, Electrochemical Quartz Crystal Microbalance (EQCM) has been used widely as it

not only quantifies the adsorption kinetics of proteins on selected substrates in-situ with sub-monolayer sensitivity, but also reveals the fine details related to the protein-surface interactions with modification to the passive film [120]. The device is comprised of a quartz crystal that is sandwiched between electrodes and driven at its resonance frequency. Any variation in the mass (Δm) sensed by the surface, due to protein adsorption/desorption, results in a shift in the resonance frequency (Δf_m). The change of mass can be calculated using the Sauerbrey equation. EQCM has been employed in the past to study the oxidation and the dissolution of metals. For instance, a study on CoCrMo surface has showed a build up of oxide film in low cathodic conditions, followed by a monotonic loss of mass during the passive domain and a large decrease of mass at the transpassive domain due to dissolution [123]. Another study of titanium in sulphuric acid showed that while moving from a cathodic region up to the passive region a loss in mass was observed as a result of dissolution of titanium, while an increase in mass was observed over the passive region for potentials up to 2 V [121].

The aim of the present study is to investigate the corrosion characteristics of pure titanium in phosphate buffer saline and BSA solutions. Pure titanium was a practical choice because it can be found both as bulk material and as coating for the QCM crystals, while its high purity enables correlation between different samples and eliminates inconsistencies arising from impurities. The use of an electrochemical quartz crystal microbalance allows the quantification of the formation of the passive film onto the surface of titanium, as well as the effect that BSA has on its formation. Following the characterization, the adsorption of bovine serum albumin onto pure titanium surfaces under different applied potentials is investigated.

5.2 Experimental

5.2.1 Materials

Pure titanium substrates (99.99+% purity) were purchased from Goodfellow (754-091-17, Huntingdon, UK). The sample was cut to 25 mm by 25 mm squares and was wet-ground with 500 to 4000 grit SiC paper. It was further polished with OP-Chem polishing cloths using 1μm diamond particles spray to achieve a mirror-like finishing and reduce inconsistencies arising from surface roughness. Following the polishing treatment, and prior to each test, the samples were rinsed and ultrasonically cleaned in subsequent baths of sodium dodecyl sulfate (SDS) solution and distilled water for 10 min respectively in order to remove any particles or protein from the surface. Subsequently, the samples were dried in a stream of compressed air. Polished AT-cut, 5 MHz, 1-inch diameter titanium coated quartz crystals (99.995 % purity) were purchased from Testbourne Ltd (750-1029-G1, Basingstoke, UK). The cleaning procedure for the QCM crystals was the same as with the bulk titanium. Fatty acid free (> 99%) bovine serum albumin (BSA) was purchased from Sigma-Aldrich (A0281, Dorset, UK). Phosphate buffer saline (PBS) tablets purchased from Fisher Scientific (P3203-100, Loughborough, UK) were dissolved in de-ionised water to prepare PBS buffer. BSA solutions were prepared using the PBS buffer.

5.2.2 Electrochemical measurements on titanium

All electrochemical measurements were controlled using a PSTAT 30 potentiostat (Metrohm Autolab B.V., Netherlands). The setup is a conventional three-electrode electrochemical cell with a platinum wire as a counter electrode and an Ag/AgCl (3M KCl) reference electrode. All potentials were referred to the reference electrode (0.205 V versus standard hydrogen electrode, SHE). The adsorbed mass was measured using an electrochemical quartz crystal microbalance by Inficon (RQCM, Switzerland). The topographic images were acquired in liquid tapping mode by an atomic force microscope (Nanowizard® II,

JPK, Germany), using SiNi cantilevers by BudgetSensors (SiNi-30, Bulgaria).

The same setup was used to compare between bulk titanium substrate and titanium-coated sensor. The bulk titanium specimen was mounted on a flat cell with its lower part insulated and connected to the potentiostat (working electrode) while its upper surface (0.785 cm^2) was exposed to 40 mL of the electrolyte solution. Similarly, a titanium-coated QCM crystal was loaded in the RQCM holder and immersed in 40 mL of the electrolyte solution, leaving its upper surface (1.332 cm^2) exposed. In both cases, the reference electrode was no further than 1 cm away from the surface. The experiments were carried out in two different electrolytes: (i) 1xPBS solution and (ii) 1 mg/mL BSA in 1xPBS. Two different electrochemical tests were conducted on the titanium surface: potentiodynamic curves and potentiostatic tests.

To generate the potentiodynamic curves, a cathodic cleaning was performed by applying -1200 $mV_{Ag/AgCl}$ for 300 seconds after the immersion of titanium in the electrolyte. This procedure removes any oxide species from the surface and ensures good reproducibility for the following experiments. The open circuit potential (OCP) was then measured for 30 min. Upon equilibrium, the potential was moved cathodically from OCP to -1200 $mV_{Ag/AgCl}$ with a scan rate of 2 mV s^{-1} and then anodically to +1000 $mV_{Ag/AgCl}$ with the same scan rate, while registering the response in current.

For the second part, the procedure started with a cathodic cleaning for 300 seconds at -1200 $mV_{Ag/AgCl}$ and measurement of the OCP for 30 min. Subsequently, the potential moved cathodically to -1200 $mV_{Ag/AgCl}$, or anodically to +1000 $mV_{Ag/AgCl}$, with a scan rate of 100 mV s^{-1}. Potentiostatic tests were carried out at the reported potentials for 30 min, registering the response in current and measuring the change in adsorbed mass on the crystal.

5.3 Results and discussion

5.3.1 Corrosion mechanisms

To ensure the electrochemical properties of the titanium-coated QCM sensor are comparable to that of bulk titanium, potentiodynamic tests in PBS solution were performed on both samples, with or without BSA. This would verify whether the titanium-coated sensor is a representative system for bulk titanium products that are commonly used in biomedical devices. Figure 5.1a shows the representative potentiodynamic curves acquired from one bulk titanium and a new titanium-coated QCM crystal in 1xPBS with or without BSA. The scan started from open circuit potential and moved cathodically to -1.2 $V_{Ag/AgCl}$. During the transition, the cathodic current density was found to remain unchanged until approximately -0.8 $V_{Ag/AgCl}$, and then increase (in absolute value) linearly until it reached a plateau at approximately -1.1 $V_{Ag/AgCl}$. It is widely accepted that the dominant mechanism responsible for surface corrosion on titanium, in the cathodic region studied here, is the reduction of dissolved oxygen with water as Reaction 5.1 shows [240, 241].

$$O_2 + 2\,H_2O + 4\,e^- \longrightarrow 4\,OH^- \tag{5.1}$$

$$H_2O + e^- \longrightarrow \frac{1}{2}\,H_2 + OH^- \tag{5.2}$$

Because the reduction reaction takes place on the titanium surface, the oxygen molecules have to be transported, mainly by diffusion process, from the bulk solution to the metal/liquid interface where they could interact with electrons. As the surface potential of the titanium becomes more negative, the rate of the reduction reaction increases linearly because electrons are transported faster from the bulk metal to the metal/liquid interface. Eventually, the rate of the reduction reaction reaches a maximum because it is limited by the rate of oxygen molecules being transported onto the solid/liquid interface. Such mechanism is confirmed by the results presented in Figure 5.1a, where after a linear correlation between the current density and the applied potential, the latter eventually

reaches a plateau at -1.1 $V_{Ag/AgCl}$. During this plateau phase, the mass transport of the oxidant (oxygen) to the titanium surface is expected to limit the current, which is also confirmed by another study [122].

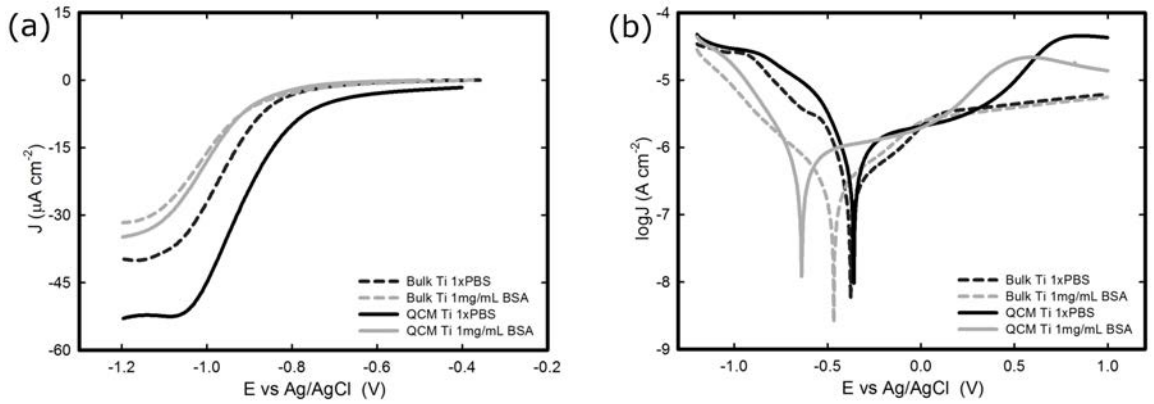

Figure 5.1: (a) i-E curves of bulk and fresh titanium coated QCM crystals in 1xPBS with and without BSA, and (b) potentiodynamic curves of bulk and fresh titanium coated QCM crystals in 1xPBS with or without BSA. The graphs represent the average values of n=3 measurements.

Figure 5.1a also shows that the titanium-coated QCM sensor possesses a slightly increased (in absolute value) current density in comparison to bulk titanium. A possible explanation is that the difference in the current density is caused from differences on the surface roughness between the two samples, attributed to a larger true surface area, as has been shown in a previous study [242, 243]. As it is shown in Figure 5.2, the QCM surface has a larger average surface roughness (R_a) than bulk titanium (R_a=8.78 nm for titanium-coated QCM sensor versus R_a=1.27 nm for bulk titanium). Consequently, because the true surface area is larger than the apparent area and increases with an increase in the average surface roughness, the cathodic reactions are taking place over a larger area which resulting in increased current density.

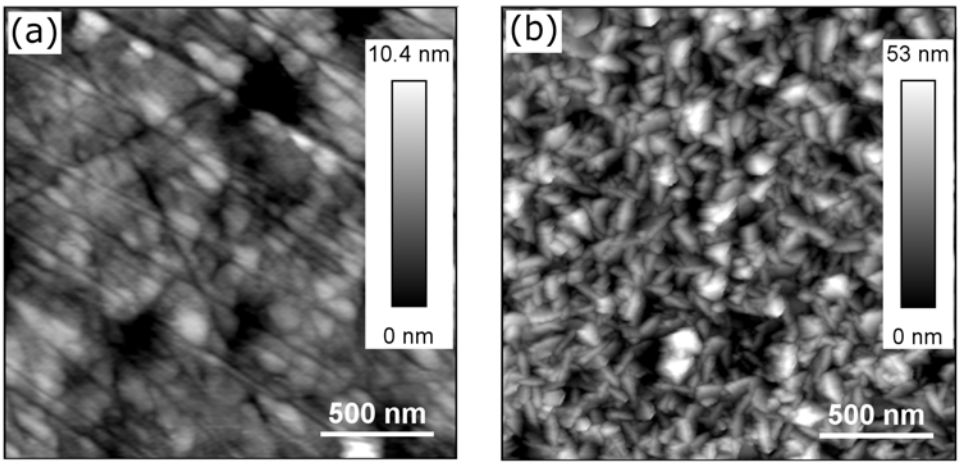

Figure 5.2: AFM images of (a) bulk titanium (R_a=1.27 nm), and (b) titanium-coated QCM sensor (R_a=8.78 nm).

The current density was found to reduce (in absolute value) with both specimens in the presence of BSA, while the plateau was shifted towards more cathodic values. The general trend of the curve acquired in BSA is very similar to that collected in PBS. As the potential moves towards more cathodic values, the current density initially shows a slight increase and then a steeper linear increase before it reaches a plateau. However, the magnitude of the current density is reduced. The reduction in current density due to the presence of BSA is consistent with previous work where the effect of BSA on titanium alloys and CoCrMo surfaces was studied. It was suggested that a surface adsorbed protein film, such as albumin or collagen, could hinder the transport of oxygen on the titanium surface and consequently inhibit the cathodic reaction of oxygen [7, 122, 236]. This is further supported by the shift of corrosion potential towards more cathodic values in the presence of BSA (Figure 5.1a). Because the corrosion potential is associated with corrosion resistance (a lower corrosion potential corresponds to a higher corrosion resistance [244]), it is highly likely that the presence of BSA increases the corrosion resistance of the titanium by inhibiting the cathodic reaction of oxygen.

The reverse scan is shown in Figure 5.1b. On the cathodic domain, from -1.2 $V_{Ag/AgCl}$ until the corrosion potential, the rate of cathodic reactions is larger than the rate of anodic reactions and the general trend is the same as in Figure 5.1a. As the potential

continues to increase, the rate of anodic reactions increases while the rate of cathodic reactions decreases. Eventually, at the corrosion potential, the rate of anodic and cathodic reactions becomes equal and the transition from cathodic to anodic potential takes place at approximately -0.4 $V_{Ag/AgCl}$ in PBS for both bulk titanium and QCM crystal. The presence of BSA causes the corrosion potential to shift towards more cathodic values for both types of samples, despite that the shift was greater for the QCM crystal than the bulk titanium. The shift in corrosion potential is because the adsorbed BSA inhibits the cathodic reaction, as described earlier. As the potential acquires values greater than the corrosion potential, the rate of anodic reaction becomes larger than the rate of the cathodic reactions. In this domain, the titanium anodically dissolves to ions and starts the formation of the passive oxide layer, as Reactions 5.5 and 5.8 show [245].

$$\mathrm{Ti} \longrightarrow \mathrm{Ti^{3+}} + 3\,\mathrm{e^-} \tag{5.3}$$

$$2\,\mathrm{Ti^{3+}} + 3\,\mathrm{H_2O} \longrightarrow \mathrm{Ti_2O_3} + 6\,\mathrm{H^+} \tag{5.4}$$

$$2\,\mathrm{Ti} + 3\,\mathrm{H_2O} \longrightarrow \mathrm{Ti_2O_3} + 6\,\mathrm{H^+} + 3\,\mathrm{e^-} \tag{5.5}$$

$$\mathrm{Ti} \longrightarrow \mathrm{Ti^{4+}} + 4\,\mathrm{e^-} \tag{5.6}$$

$$\mathrm{Ti^{4+}} + 2\,\mathrm{H_2O} \longrightarrow \mathrm{TiO_2} + 4\,\mathrm{H^+} \tag{5.7}$$

$$\mathrm{Ti} + 2\,\mathrm{H_2O} \longrightarrow \mathrm{TiO_2} + 4\,\mathrm{H^+} + 4\,\mathrm{e^-} \tag{5.8}$$

The current density continues to increase as the metal surface reacts with water to form a thin oxide film that covers the entire surface over time. The formation of such passive film slows down the rate of metal ions passing through, until they reach an equilibrium eventually [246]. After this point, the migration of metal ions, and thus the current,

becomes independent of the potential and remains reasonably constant. However, while the passive domain for the bulk titanium substrate is extended up to +1.0 $V_{Ag/AgCl}$, a different behaviour is observed for the titanium-coated QCM sensors where the passive region is extended to approximately 0.4 $V_{Ag/AgCl}$, after which an increase with the current density is observed. This increase in current could be caused by the oxygen reaction, which is highly dependent on the surface state of the electrode, in this case favoured on the QCM crystal.

As suggested by Figure 5.1b, the current density acquired from bulk titanium and titanium QCM crystal in the passive region is very close, with or without the presence of BSA. This confirms that the formed oxide layer during the passivation possesses the same thickness for titanium of different physical forms in both types of specimen.

5.3.2 Effect of titanium passivation

Unlike the consistent potentiodynamic results acquired from the bulk titanium samples over successive tests, there appeared some variation in the electrochemical behaviour of the titanium-coated QCM sensor over multiple potentiodynamic scans. To establish the cause of such variation, and identify the effect of the electrochemical process on the QCM sensor, an electrochemical quartz crystal microbalance (EQCM) was employed to monitor the mass change at the sensor surface whilst replicating the same potentiodynamic tests in the bulk solution. Figure 5.3a shows the cathodic potentiodynamic curves of a fresh titanium-coated QCM sensor and the same QCM sensor on the second repeating potentiodynamic scan from OCP to -1.2 $V_{Ag/AgCl}$. As for the fresh crystal, the current density in the region from OCP to -0.85 $V_{Ag/AgCl}$ is relatively low, and it decreases rapidly until -1.1 $V_{Ag/AgCl}$, before reaching a plateau. As explained earlier, the limiting factor in the cathodic reactions (reactions 5.1 and 5.2) is the rate by which the dissolved oxygen is transported onto the solid/liquid interface. Consequently, the rate of oxygen transport is reaching a maximum at -1.1 $V_{Ag/AgCl}$, which explains the plateau. Although the characteristics of potentiodynamic curves acquired from the used sensor are similar to that of fresh sensor, the current density

at the plateau is slightly lower than that in the used sensor, which could be attributed to a thicker passive film on the used sensor that was acquired by passivation during the first scan. The mass change on titanium surface (Δm) over the course was measured by the EQCM by converting the change in frequency to mass variation based on Sauerbrey's equation. For both specimens, the Δm was equal and approximately 40 ng/cm^2, as shown Figure 5.3b. The total mass gain during this transition is likely the result of oxide film building up on the surface, which interestingly happens at relatively low cathodic domains. A similar event of mass increase at the cathodic domain has been observed by EQCM in another study, during the electrochemical characterization of CoCrMo surfaces in PBS solutions [123]. However, the mass increase could also be related to other phenomena, such as adsorption events on the titanium surface.

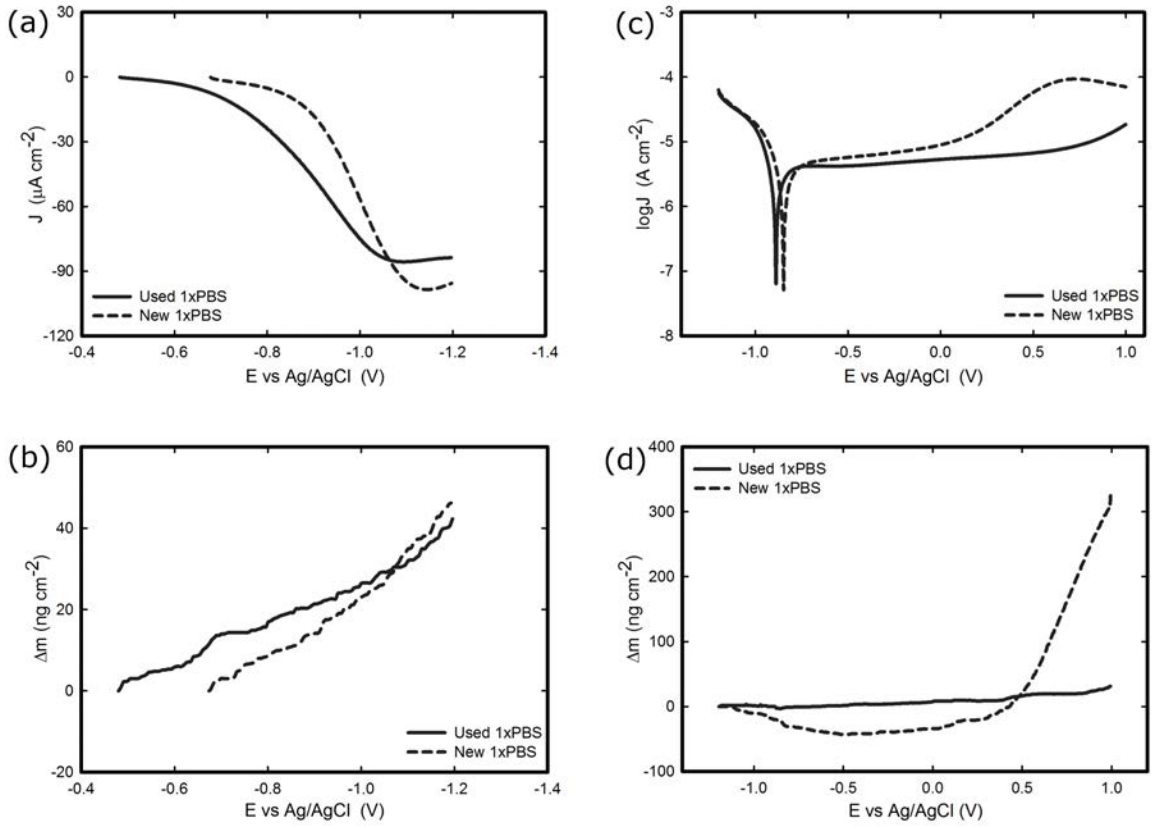

Figure 5.3: Comparison between a fresh titanium-coated QCM crystal and the same crystal after the initial run in 1xPBS. (a) i-E curves, (b) titanium change of mass during transition from OCP to -1.2V, (c) potentiodynamic curves, (d) titanium change of mass during transition from -1.2V to +1.0V.

The potentiodynamic curves for the reverse scan, moving anodically from -1.2 $V_{Ag/AgCl}$ to +1.0 $V_{Ag/AgCl}$, are shown in Figure 5.3c. As expected, all 3 distinguished domains, including the cathodic domain from -1.2 $V_{Ag/AgCl}$ until the corrosion potential, the transition from cathodic to anodic at the corrosion potential, and the passive domain are visible for both sensors. Although the corrosion potential was found to be around -0.4 $V_{Ag/AgCl}$ and -0.8 $V_{Ag/AgCl}$ for the same system, as shown in Figures 5.1b and 5.3c respectively, such variation was caused by the different scan rate of the potential employed (2 mV/s in the first case versus 10 mV/s in the latter), which has been reported in the past [247]. The current density of the fresh sensor at the passive domain is slightly greater than that of the used one, which could be attributed to a thicker passive film on the used sensor that was acquired by passivation during the first scan. The major difference between the two sensors was observed at around +0.3 $V_{Ag/AgCl}$, where an increase in the current density was observed with the fresh sensor. As explained earlier, this can be caused either by temporary passive film breakdown and repassivation due to insufficient protection from the passive film during immersion to electrolyte, or by transformation of TiO_2 to TiO(OH). To further investigate this behaviour, the mass change during this transition was examined.

Figure 5.3d shows that there is barely any change in surface mass for the used sensor during the potential scan, whilst the fresh sensor behaves differently - the surface mass of the fresh sensor decreases in the cathodic domain and remains constant in the passive domain, before starting to increase around the potential where the current density showed the increase in Figure 5.3c. The initial decrease, from -1.2 $V_{Ag/AgCl}$ until the corrosion potential, could be attributed to a loss of the passive film. However, the total mass gain is similar to the total mass loss during the transition from OCP to -1.2 $V_{Ag/AgCl}$ that was discussed earlier (Figure 5.3b). Consequently, it is unlikely that a potential scan on the same region to result once in mass loss and once in mass gain. It is more likely that the change in mass during this transition is due to adsorption/desorption of species, such as ions, on the surface of the titanium. This behaviour has been observed in the past where ions adsorbed onto a gold surface [248]. On the second region that shows the passive

domain, the change of mass remains approximately the same, similarly to the used sensor. This was expected since on this region the passive film grows very slowly due to slow transport of metal ions though the oxide film. On the third region that is absent from the used sensor, or moved to values above 1 V, both the current and the mass of the new QCM sensor were increased. If this increase is due to breakdown of the film then the mass should have shown a decrease. However, the mass is increased significantly, to approximately 320 ng/cm^2. A possible explanation, as described earlier, is that the passive semiconducting layer of TiO_2 was being transformed to TiO(OH). However, it is not clear whether this would result in such a large mass change. Furthermore, a previous study reports that the percentage of TiO in the oxide film of titanium is only 3 % at 1 $V_{Ag/AgCl}$, which increases the uncertainty of the previous suggestion [249]. A more likely explanation is that it is a combination of oxide transformation and oxide formation that causes this change. The results also indicate that the effect of this event was permanent, since it happened only during the first scan and affected the behaviour of the sensor in the following scans. Despite the behaviour of the fresh crystal, the potentiodynamic curves confirm that the titanium-coated QCM crystals could represent the bulk titanium substrate in terms of the electrochemical properties, as far as it is used after an initial passivation.

5.3.3 Influence of protein

Upon the comprehensive characterization of the titanium surface on QCM crystal, the effect of cathodic and anodic potential on the adsorption of BSA onto titanium was examined. The sensors were loaded onto the EQCM in PBS solution and the change of mass was recorded under cathodic and anodic conditions at two different protein concentrations, 10 μg/mL and 1 mg/mL. It should be noted that because of the nature of the experimental set-up, an undefined amount of protein molecules is expected to be adsorbed onto the surface of the sensor (in protein solutions) prior to the electrochemical experiment. Figure 5.4 shows the current density and mass evolution over time at applied potential equal to -1.2 $V_{Ag/AgCl}$, with or without the presence of BSA (in 2 different concentrations). For

all three solutions examined, the current density decreases (in absolute value) rapidly in the first few seconds upon the introduction of the cathodic potential, it then reaches a plateau. At the applied potential of -1.2 $V_{Ag/AgCl}$ water reduction is the main reaction and in all solutions a current density around -30 $\mu A/cm^2$ was registered. The initial current decrease can be explained by considering that prior to the application of the cathodic potential there was an excess of oxygen molecules at the solid/liquid interface. As soon as the potential was applied, the cathodic reactions consumed the oxygen molecules and the rate of the cathodic reactions was limited by the rate which the oxygen molecules are being transported on the titanium surface, resulting in a plateau.

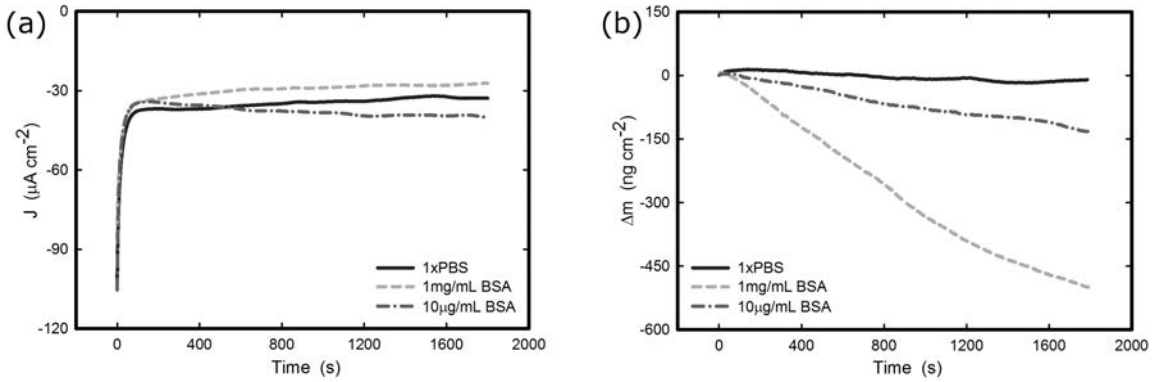

Figure 5.4: (a) Potentiostatic test of titanium with and without BSA at -1.2V, (b) evolution of mass change on the titanium surface with and without BSA at -1.2V. The graphs represent the average values of n=3 measurements.

The evolution of mass (Figure 5.4b) at the titanium-liquid interface, converted from frequency monitored by EQCM, shows that the mass remains the same during the measurements, indicating that the electrochemical condition has negligible impact on the titanium surface without the presence of BSA. As a contrast, the surface mass decreases when the titanium was exposed to BSA solutions, with a reduction of approximately 420 ng/cm^2 and 80 ng/cm^2 (5 times smaller) for 1 mg/mL and 10 μg/mL BSA solutions respectively (Figure 5.6). Since the effect of titanium in the mass loss is negligible, as confirmed by the experiments in PBS buffer, it is very likely that the mass reduction is due to the desorption of protein from the titanium surface. Considering the dimensions of an adsorbed BSA molecule, then the theoretically maximum amount of BSA molecules

that is needed to form a closed-packed monolayer is approximately 200 ng/cm^2 [122, 250]. Therefore, in 10 μg/mL BSA solution, the surface lost an amount of mass that is corresponded to approximately 75 % of a monolayer of BSA, while at 1 mg/mL the surface lost mass corresponding to approximately 2.5 layers of BSA from the titanium surface. Because the QCM sensor was immersed in protein solution prior to the application of potential, the initial total amount of the adsorbed BSA is unknown. However, previous studies concerning BSA adsorption on titanium show that the surface gets saturated by BSA with a density of 710±70 ng/cm^2 [251]. This suggests that nearly 70 % of the adsorbed BSA could be removed over a period of 30 min, as a result of electrostatic repulsion upon the application of cathodic potential, in 1 mg/mL BSA solution where the titanium surface is saturated with BSA. It has been shown that if the cathodic reactions are not fast enough to accommodate all of the provided electrons from the ionisation of metal atoms then the cathode surface is charged negatively [252]. In contrast, anodic polarisation results in electron depletion and thus the surface is charged positively. Therefore, since BSA has an overall negative charge in pH 7, it was desorbed from the cathodic titanium surface due to electrostatic repulsion.

The current and mass evolution over time for an applied potential of +1.0 $V_{Ag/AgCl}$ are shown in Figure 5.5. Upon application of an anodic potential, the current density diminishes quickly until it reaches a minimum value (Figure 5.5a). This is a classic passivation process where the current flow is reduced and reaches a plateau whilst the oxide film on the titanium surface grows thicker. The current density at the plateau was found to be approximately 44, 122, and 251 nA/cm^2 for PBS, 1 mg/mL, and 10 μg/mL solutions respectively. The slightly increased current densities in the presence of BSA suggest that the presence of protein could accelerate the anodic reaction. The EQCM data show that the mass remained unchanged in PBS and in 1 mg/mL BSA solutions, while for the solution with 10 μg/mL BSA there was a steady increase in the adsorbed mass until it reached approximately 305 ng/cm^2 (Figure 5.5b). This is due to the attractive electrostatic interaction between surface and protein upon application of anodic potential.

Also, since the variation in mass remains unchanged in PBS solution, it is suggested that the observed increase in mass was a result of BSA adsorption onto the surface of titanium upon application of an anodic current. The fact that protein adsorption was observed only for the 10 μg/mL BSA solution and not for the 1 mg/mL BSA solution suggests that the latter was already saturated with protein prior to application of the anodic potential.

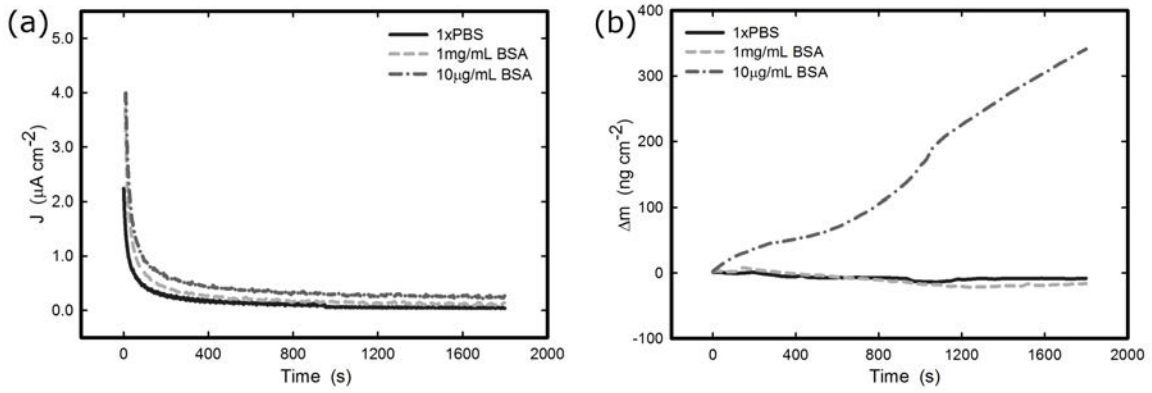

Figure 5.5: (a) Potentiostatic test of titanium with and without BSA at +1.0V, (b) evolution of mass change on the titanium surface with and without BSA at +1.0V. The graphs represent the average values of n=3 measurements.

The effect of anodic and cathodic conditions in the adsorption of BSA onto titanium surfaces can be summarised in Figure 5.6. It can be concluded that the application of a cathodic potential results in desorption of BSA from the titanium surface due to electrostatic repulsion, while the application of an anodic potential results in adsorption of BSA only if the titanium surface is not already saturated. In physiological conditions, the pH value of the biological fluids can have a similar effect on titanium surface - a basic environment will result on an excess of electrons on the surface, while an acidic environment will have the opposite result [253]. Consequently, since the pH value in wounds can vary from 3.5 to 9.0 [32], protein adsorption, and thus, biocompatibility of a biomaterial can be greatly affected.

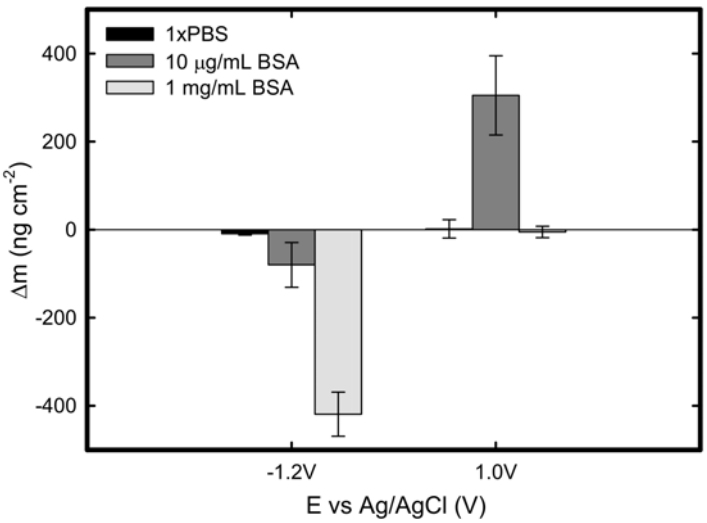

Figure 5.6: Total change of mass under cathodic and anodic conditions in PBS, 10 µg/mL BSA, and 1 mg/mL BSA solutions. Data points represent mean values of n=3 measurements, with the error bars representing the standard error.

5.4 Conclusions

In the present work, both the electrochemical characteristics of pure titanium in PBS buffer and protein solutions, and its influence on the adsorption of BSA onto titanium, were investigated systematically. The electrochemical properties of bulk titanium substrate and titanium-coated QCM sensors show small degree of discrepancy in PBS buffer, which are attributed to differences in their surface roughness. Furthermore, the comparison between new and used QCM sensors suggests that the oxide film formed on titanium surface during the potentiostatic tests at anodic potential is determining its electrochemical behaviour afterwards and cathodic cleaning is not sufficient to reproduce the same initial electrochemical response.

Applied cathodic potential in the water reduction domain causes the desorption of BSA due to electrostatic repulsions caused by an excessive amount of electrons on titanium surface, and thus an overall negative surface charge. In contrast, under anodic applied potential adsorption of BSA was facilitated only when the surface has not already been saturated with proteins.

Chapter 6

Tribocorrosion characteristics of titanium in albumin solution

6.1 Introduction

Due to a combination of outstanding mechanical properties and high biocompatibility, titanium and titanium alloys are widely used materials in bioengineering applications. Among others, they exhibit a high strength to weight ratio, a modulus of elasticity similar to bone that makes the bone-to-implant interface closely matched than many other metals, and an exceptional resistance to corrosion [6, 39, 224, 225]. Similar to most other metallic biomaterials, the corrosion resistance of titanium is highly depended on a thin and inert oxide film present on its surface, which is developed when the metal is exposed to ambient or liquid environments. This passive oxide layer contributes substantially towards the exceptional biocompatibility of titanium - it protects the underlying substrate from corrosion when being placed in a physiological environment, and provides an excellent interface to interact with the surrounding tissue that can prevent inflammatory responses [254]. Furthermore, the oxide layer acts as a barrier to restrict release of ions that could react with biomolecules and cause cytotoxicity, allergies, or other biological influences [37]. The titanium oxide has an isoelectric point of 5-6, which results in a slightly negatively charged surface in physiological pH [255].

The aforementioned characteristics enable titanium and its alloys to be used in a wide range of biomaterials, from dental implants to hip joints [255–258]. However, the

performance of titanium becomes poor when it is placed in a tribological environment because any damage to the passive film could affect its anti-corrosion properties [259]. Therefore, an in-depth understanding of the factors that affect the passive film in a tribological context will aid towards the design of novel biomaterials with enhanced performance.

A tribocorrosion system combines corrosion and mechanical wear as mechanisms of degradation. The two mechanisms cannot be considered separately but rather as a complex system where one is dependent on the other; corrosion is accelerated by wear, and similarly, wear can be affected by corrosion [46]. Upon friction, the oxide layer that covers the titanium surface is removed (depassivation), leaving the active titanium exposed to the aggressive physiological environment. As a result, the corrosion rate is increased (wear accelerated corrosion), which leads to a rapid degradation of the active titanium surface. The passive film is then progressively reformed on the surface (repassivation) and protects the substrate from further corrosion. However, the passive film can also have a negative influence on the mechanical response of titanium in tribocorrosion system, because it tends to accumulate on the mechanical contact upon damage and form third bodies that enhance the degradation of the surface [47].

The effect of the passive film on tribocorrosion process could be determined by the nature of the material, the prevailing conditions, and the surrounding environment. Various combinations of the aforementioned factors create a distinct tribocorrosion environment that affects differently the passive film of the metals and, thus, their corrosion process. For instance, studies on hafnium and pure titanium in NaCl solution showed that the passive film formed on their surface acts as a barrier to protect against corrosion, as expected, while mechanical damage disrupts the passive film that is quickly reformed when the damage is ceased [260]. However, hafnium shows a faster repassivation rate than pure titanium, highlighting the different anti-corrosion behaviour due to the nature of materials. Another study reported that thermally treated titanium exhibits improved corrosion resistance compared to untreated samples [261]. The nature of the materials

and the prevailing conditions also affect the mechanical damage of the passive film. For instance, when titanium is rubbed against polyethylene (PE), the wear of the titanium is insignificant since it has a greater hardness [129]. The absence of a passive film on DIN 34CrNiMo6 carbon steel in borate solution could reduce the rate of wear because the detached metallic particles are readily smeared back on the wear track under the applied pressure [262]. In contrast, the presence of a passive film in the same system results in detachment of wear particles from the surface of the steel, and the consequent wear-accelerated corrosion. Similar results with that of carbon steel were reported for CoCrMo implants, while it was further observed that the surface degradation is influenced by the prevailing electrochemical conditions [263]. It was shown that not only the corrosion is greater in the area where the metals rubbing with each other due to wear-accelerated corrosion, but also the area surrounding the contact site have increased corrosion due to galvanic coupling between the worn area and the surrounding passive metal.

Composition of liquid to which metal is exposed has been shown to have a crucial impact on the tribocorrosion process. Various ions and proteins present in the liquid, particularly in physiological environment, can affect the characteristics of the passive film [264]. However, the reported effects of proteins on the behaviour of passive film are inconsistent and highly depended on the nature of the metal and the type of protein used. Bovine serum albumin could act as both cathodic inhibitor and anodic catalyser when in contact with CoCrMo in PBS solution. Consequently, it reduces the rate of corrosion at cathodic potentials by inhibiting the cathodic reactions, but accelerates the rate of corrosion at anodic conditions by limiting the adsorption of phosphate [50]. Similar results were reported with a series of titanium alloys - the presence of protein can either reduce or increase the degradation of the material, depending on the alloy and the type of wear [51]. It was also suggested that the presence of BSA on pure titanium could accelerate the repassivation, which is caused by the adsorbed proteins that act as a barrier and prevent the water from reaching the titanium surface [52]. However, when abrasive particles are involved the presence of BSA leads to accelerated wear, which is attributed to an enhanced

particle entrainment and a greater rolling efficiency of the particles [53].

Although there have been several studies investigating various tribocorrosion systems, an in-depth understanding on the tribocorrosion characteristics of pure titanium in PBS and albumin solution, under cathodic and anodic applied potential, is missing. The aim of the present study is to examine the aforementioned characteristics on the micro- and nanoscale. A pin-on-disk tribometre, coupled with an electrochemical cell, was utilized in order to perform tribocorrosion experiments of pure titanium in PBS and albumin solutions. The experiments were performed both in cathodic and in anodic conditions to understand the effect of the prevailing conditions on the wear of the titanium surface. Furthermore, atomic force microscopy was employed to measure the interactions between the studied surfaces at the nanoscale and how they are affected by the presence of albumin.

6.2 Materials and methods

6.2.1 Materials

Pure titanium substrates (99.99+% purity) were purchased from Goodfellow (754-091-17, Huntingdon, UK). The sample was cut to 25 mm by 25 mm squares. Before each experiment, the sample was wet-ground with 500 to 4000 grit SiC paper and further polished with OP-Chem polishing cloths using 1 μm diamond particles spray to achieve a mirror-like finishing. Following the polishing treatment, the samples were ultrasonically cleaned in sodium dodecyl sulfate (SDS) solution followed by distilled water for 10 min respectively, which ensured the removal of any particles or protein from the surface. Lastly, the surfaces were dried in a stream of compressed air. Titanium coated QCM sensor crystals (99.995%) were purchased from Testbourne Ltd (750-1029-G1, Basingstoke, UK). Fatty acid free and globulin free (> 99%) bovine serum albumin (BSA) was purchased from Sigma Aldrich (A0281, Dorset, UK). Phosphate buffer saline (PBS) tablets purchased from Fisher Scientific (P3203-100, Loughborough, UK) were dissolved in de-ionised water to prepare PBS buffer. BSA solutions were prepared using the PBS buffer.

6.2.2 Tribocorrosion tests

All electrochemical measurements were carried out using a potentiostat (Solartron Analytical 1286). The set-up is a conventional three-electrode electrochemical cell, using a platinum wire as counter electrode and an Ag/AgCl (3M KCl) reference electrode. All potentials were referred to the reference electrode (0.205 V versus standard hydrogen electrode, SHE).

For the tribocorrosion tests, a pin-on-disk rotating tribometer coupled to a potentiostat was used. The titanium specimen was mounted on the tribometer with its lower part insulated and electrically connected to the working electrode of the potentiostat, while its upper surface (2.06 cm^2) was exposed to the electrolyte solution. The reference electrode was kept within 1 cm away from the titanium surface. An alumina sphere with a diameter of 6 mm was used as a counterpart, due to its excellent wear resistance and hardness [265]. A normal force of 5 N was applied on the counterpart, corresponding to a maximum contact pressure of approximately 950 MPa using the Hertzian contact stress model [266] (Poissons ratio equal to 0.23 and 0.34, and Youngs modulus equal to 380 and 103 GPa, for alumina and pure titanium respectively). The sliding velocity and duration were set to 60 rpm (equivalent to 1.13 m/min) and 30 min respectively, and the radius of the wear track was set at 3 mm. The aforementioned conditions were chosen based on previous work performed by collaborator [267, 268]. The tests were performed both in 1xPBS and protein solutions at 3 different surface potential conditions, including open circuit potential (OCP), -1.2 $V_{Ag/AgCl}$, and +1.0 $V_{Ag/AgCl}$. The applied potentials were selected to match the cathodic and the anodic areas of the titanium.

Confocal microscopy (Olympus LEXT OLS3000, Japan) was used to carry out the post examination of the wear track, including both surface morphology and the corresponding volume. Optical microscopy (Olympus LEXT OLS3000, Japan) and scanning electron microscopy (JEOL JSM-6300, Japan) were also used to image and analyse the wear tracks on the titanium surface and the alumina counterpart. A Nanoindenter (G200 Agilent

Technologies, USA) was used to determine the microhardness of the material both inside and outside the wear track by employing a diamond tip to apply a pressure of 0.2 kgf/mm^2 (1.96 MPa) for a duration of 15 s (Hv0.2/15). All measurements were repeated 3 times to ensure the reproducibility.

6.2.3 Force spectroscopy

Individual alumina particles purchased from Alfa Aesar (46025) were attached onto tipless AFM cantilevers (PNP-TR-TL, Nanoworld, Switzerland) using a two-part epoxy glue. The colloidal cantilevers were calibrated with the thermal method [24] before the attachment of the alumina particles on them (nominal spring constant is 0.08 N/m). Force measurements were conducted using an atomic force microscope (AFM) by JPK (Nanowizard II, Germany) that was coupled with a PGSTAT101 potentiostat (Autolab, Switzerland) which is conventional three-electrode electrochemical cell using a platinum wire as counter electrode and a Dri-Ref^{TM} (3M KCl) reference electrode (World Precision Instruments, USA). During the force spectroscopy measurements, titanium-coated QCM sensors instead of titanium sheet were used as substrate. The electrochemical characteristics of such titanium-coated QCM crystals were found to be similar to that of bulk titanium, as shown in chapter 5. The titanium coated QCM sensor crystal was mounted in the electrochemical cell (working electrode) with its upper surface (1.33 cm^2) exposed to the electrolyte. The experiments were conducted both in 1xPBS and in protein solution. A total of 240 force curves were collected over 16 different regions of the titanium surface to ensure that the result is statistically representative. Cantilever velocity was 2 μm/s with applied force being 5 nN. The alumina particle was kept in contact with the surface for 0.3 s before it was retracted.

6.2.4 Statistical analysis

All data were presented as mean values ± the standard error of the mean. A statistical comparison was made using a single factor analysis of variance (ANOVA) and post hoc

t-stat multiple comparison testing to evaluate the significance of the measured parameters.

6.3 Results

6.3.1 Tribocorrosion tests

To examine the electrochemical characteristics of titanium under tribological conditions, an alumina sphere slid against a titanium substrate under constant pressure of approximately 950 MPa with the presence of PBS buffer or 1 mg/mL BSA solution. The open circuit potential of the titanium was recorded as a function of time before, during, and after sliding (Figure 6.1). The averaged values of OCP are shown in Table 6.1. Upon the initiation of sliding, an abrupt reduction in OCP was observed, which is due to the mechanical removal of the passive film from the surface, leaving the active titanium underneath exposed to the aqueous solution. It also confirms the existence of a passive film on the titanium surface before rubbing. Whilst the alumina sphere was sliding over the titanium substrate, a fluctuation on the OCP of approximately 0.1 $V_{Ag/AgCl}$ was observed. It is highly likely due to the repetitive depassivation/repassivation process as the result of the passive film being removed and reformed continuously. The OCP during sliding was higher (in absolute value) in the protein solution than that in the PBS buffer, which could be due to the presence of adsorbed BSA molecules that inhibit the rate of cathodic reactions of oxygen and shift the corrosion potential towards more cathodic values [122]. Once the sliding stopped, an abrupt increase in the OCP of titanium was observed, which is slightly slower in the presence of BSA indicating a slower repassivation of titanium surface [260]. This, once again, confirms the formation of a passive film when the sliding stops. It is also worth noting that the potential when the sliding stopped was lower than prior to sliding that indicates a thinner passive film.

Table 6.1: Averaged values and standard errors of OCP before (OCP_0), during ($OCP_{sliding}$), and after (OCP_{final}) sliding of pure titanium against an alumina sphere in 1xPBS electrolyte, with or without BSA. Data represent mean values of n=3 measurements ± standard error.

Solution	OCP_0 (mV)	$OCP_{sliding}$ (mV)	OCP_{final} (mV)
1xPBS	-388±67	-882±82	-451±77
1 mg/mL BSA	-362±26	-1018±44	-505±34

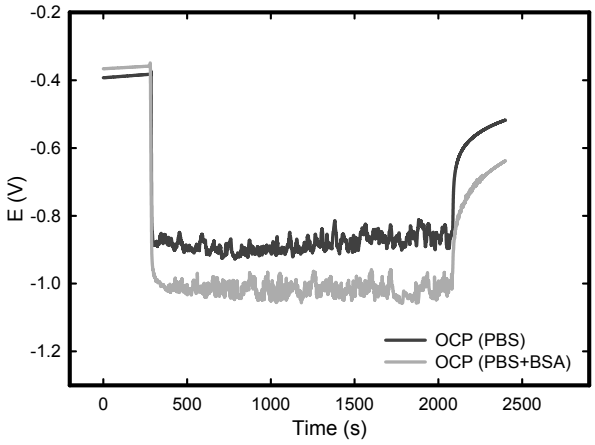

Figure 6.1: Evolution of the open circuit potential over time in PBS buffer with or without the presence of BSA. The graphs represent the mean values of n=3 measurements.

The tribocorrosion characteristics of titanium were studied at cathodic and anodic potential, in addition to open circuit potential. Figure 6.2a shows the evolution of current when a negative potential of -1.2 $V_{Ag/AgCl}$ was applied on the system. Similar to the observation in OCP conditions, a passive layer was found present on the titanium surface before the initiation of sliding. Such passive film was removed from the surface (depassivation process) as confirmed by an abrupt reduction in the current upon sliding, which results in the exposure of the active titanium and consequently increased current flow in the wear track. However, the change in the current is significantly reduced with the presence of BSA than that in PBS solution, indicating that the presence of BSA inhibits the rate of cathodic reactions. A fluctuation with the current of approximately 20 μA was observed during sliding, which could be due to the dynamic equilibrium between depassivation and repassivation of the surface. When the sliding was stopped, the current showed a steep increase due to repassivation of the surface.

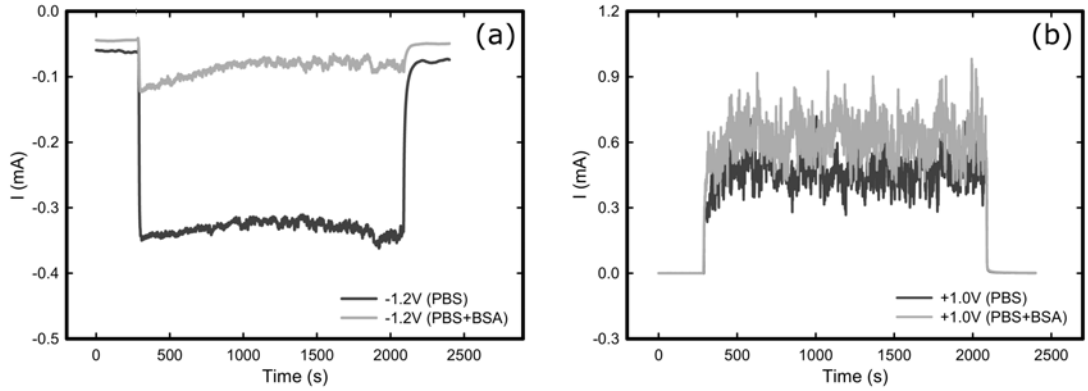

Figure 6.2: Evolution of the current of titanium in PBS buffer with or without the presence of BSA as a function of time at (a) -1.2 $V_{Ag/AgCl}$, and (b) +1.0 $V_{Ag/AgCl}$. The graphs represent the mean values of n=3 measurements.

The passive film formed on the titanium sample showed different characteristics when an anodic potential was applied. Figure 6.2b shows the current of the titanium surface upon application of a positive potential (+1.0 $V_{Ag/AgCl}$) as a function of time. Before the initiation of sliding, the current is approximately 0.5 μA, which indicates the presence of a thick passive layer blocking current flow. Upon sliding, a steep increase of the current was observed, suggesting the surface undergoes depassivation (mechanical removal of passive film). The fluctuation of the current is approximately 400 μA, a value that is significantly greater than that in cathodic conditions (20 μA). It is highly likely because the dynamic equilibrium on a titanium surface is much more unstable under anodic potential because the repassivation occurs much faster under such condition. Interestingly, the increase in current is slightly greater (∼30%) with the presence of BSA than that in PBS buffer, which suggests that the presence of BSA accelerates the rate of anodic reactions. When the sliding was stopped, an abrupt reduction of the current was observed as a result of fast repassivation of the surface.

The averaged values of current under each applied potential are summarized in Table 6.2, where I_0 is the current before the initiation of sliding, $I_{sliding}$ is the current during the sliding, and I_{final} is the current when the sliding was stopped. $I_{sliding}$ is the current that flows only through the wear track and was calculated by subtracting I_0 from the overall current during sliding. It was assumed that I_0 is approximately the current that flows

outside the wear track since the surface area was significantly larger than the area of the wear track [267]. The current values before and after sliding for anodic conditions are 2 orders of magnitude less than that in cathodic conditions, which could be due to the different rate of anodic and cathodic reactions but could also indicate a thicker passive film. Furthermore, the impact of the presence of BSA in cathodic conditions is greater than that in anodic conditions as shown by the current values when sliding starts. This suggests that the effect of BSA on the cathodic reactions is significantly greater than that in anodic reactions.

Table 6.2: Averaged values of current before (I_0), during ($I_{sliding}$), and after (I_{final}) sliding of pure titanium against an alumina sphere in 1xPBS electrolyte, with or without BSA, and in 2 different applied potentials. Data represent mean values of n=3 measurements ± standard error.

$E_{applied}$ ($V_{Ag/AgCl}$)	Solution	I_0 (μA)	$I_{sliding}$ (μA)	I_{final} (μA)
-1.2 V	1xPBS	-61±9	-268±38	-75±2
	1 mg/mL BSA	-45±3	-38±24	-44±7
+1.0 V	1xPBS	0.5±0.2	470±41	0.8±0.3
	1 mg/mL BSA	0.5±0.2	629±13	1.0±0.1

6.3.2 Wear quantification and morphology

After the tribocorrosion measurements, the volume of the wear track (V_{tot}) was calculated by multiplying the average cross-sectional of the wear track with the total length of the wear track, based on the acquired confocal microscopy images. Averaged wear track volumes acquired under various electrochemical conditions with or without BSA are shown in Figure 6.3. Under OCP condition, the material loss of titanium in PBS is approximately 0.18±0.02 mm^3, and is increased to approximately 0.22±0.02 mm^3 with the presence of protein. However, the difference is insignificant (P=0.28) and no further conclusions can be made. The effect of applied potential on the wear track volume is different at anodic and cathodic conditions. The application of cathodic potential resulted in the least material loss, approximately 30 % less than that in OCP. Also, the presence of BSA in these conditions does not change the amount of material loss, suggesting that the effect of

protein is negligible at cathodic conditions. In contrast, with the application of an anodic potential, the total material loss is significantly increased. In PBS it exhibits an increase of approximately 60 % in comparison to OCP, while the presence of protein could double the material loss. To further understand the mechanisms that result in material loss, the contribution of corrosion and mechanical removal was calculated.

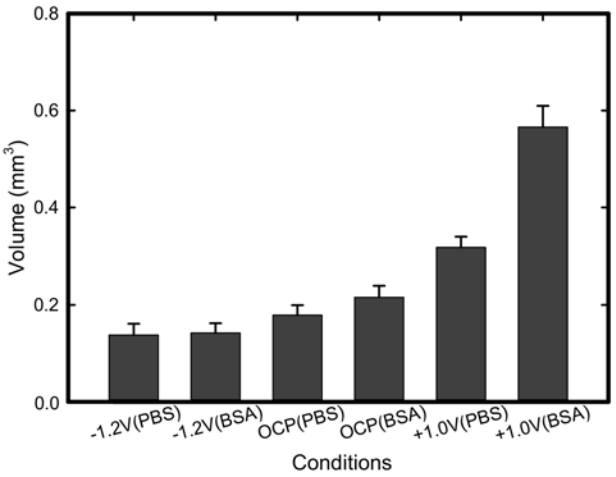

Figure 6.3: Wear track volume of the titanium disk under various conditions. Data points represent mean values of n=3 measurements ± standard error. The difference from the presence of protein is insignificant at -1.2 V and OCP, while it is significant at +1.0 V (P=0.002).

There are two major mechanisms that account for the overall material loss V_{tot} [269]: material removal by tribocorrosion on the sliding surface (both mechanical wear, V_{mech}, and wear-accelerated corrosion, V_{wac}) in addition to corrosion that occurs on a metallic surface when being exposed to electrolyte (V_{corr}). The latter could be considered as negligible on passive metals. Therefore, the total material loss can be expressed in Equation 6.1:

$$V_{\mathrm{tot}} = V_{\mathrm{mech}} + V_{\mathrm{wac}} \tag{6.1}$$

The wear-accelerated corrosion is a result of the depassivation and repassivation process that occurs in the wear track during the sliding process [43], and can be calculated using Faradays law (Equation 6.2):

$$V_{\text{wac}} = \frac{I_{\text{sliding}} \cdot t \cdot M}{n \cdot F \cdot \rho} \tag{6.2}$$

where $I_{sliding}$ is the current flowing from the wear track and can be calculated by subtracting the current before sliding from the current during sliding, t is the duration of sliding (1800 s), M is the atomic mass of titanium (47.88 g mol^{-1}), n is the oxidation valence (assumed 4 for titanium [43]), F is the Faraday constant (96500 C mol^{-1}), and ρ is the density of titanium (4.51 g cm^{-3}). The contribution of mechanical wear can then be calculated by subtracting the wear-accelerated corrosion from the total material loss. Table 6.3 summarizes the material loss at OCP and applied potential conditions. The material loss due to wear-accelerated corrosion in cathodic and OCP conditions is negligible and hence not shown. Consequently, the total material loss is attributed to mechanical wear. For anodic conditions, approximately 7 % of the total material loss is due to wear-accelerated corrosion in PBS. Although the presence of BSA increases almost by a third the wear-accelerated corrosion, the contribution in the total material loss is approximately 5 %. This indicates that the presence of BSA greatly enhances the mechanical wear in anodic conditions.

Table 6.3: Wear volumes (x 10^{-3} mm^3) of pure titanium in 1xPBS, with or without BSA. Data represent mean values of n=3 measurements ± standard error.

E ($V_{Ag/AgCl}$)	Solution	V_{wac}	V_{mech}	V_{tot}
-1.2 V	1xPBS	-	-	138±23
	1 mg/mL BSA	-	-	142±20
OCP	1xPBS	-	-	179±20
	1 mg/mL BSA	-	-	216±23
+1.0 V	1xPBS	23±2	296±21	319±21
	1 mg/mL BSA	31±1	535±43	566±43

Figure 6.4 shows the cross-sectional profiles of the wear track on titanium acquired at -1.2 $V_{Ag/AgCl}$, OCP, and +1.0 $V_{Ag/AgCl}$ in PBS solution with or without the presence of BSA. The width of the wear track is approximately the same in all of the cases,

showing accumulation of debris on the edges. Calculations indicate that the height of the circular segment corresponded to a 3 mm radius sphere with an arc of 1100 µm should be approximately 50 µm. While this is true for anodic conditions, as shown in Figure 6.4, the height of the circular segment for cathodic conditions is approximately 10 µm. This could indicate that at cathodic conditions a great percentage of the removed material is being smeared back onto the surface. Consequently, the maximum material loss was observed with anodic potential, while the least with cathodic potential. This is likely due to the thicker passive film formed under anodic conditions, which is delaminated from the surface and removed, as opposed to cathodic conditions were the material removed is being smeared back. It is expected that the plastic deformation at cathodic conditions hardens the metal (strain hardening), which is confirmed with a microindenter in subsection 6.3.3. For OCP and anodic potential, the presence of BSA could enhance the material loss and result in deeper wear tracks, which are attributed to the increased mechanical wear. Furthermore, the profiles revealed larger ridges when the BSA was present, which suggests accumulation of material at the sliding interface.

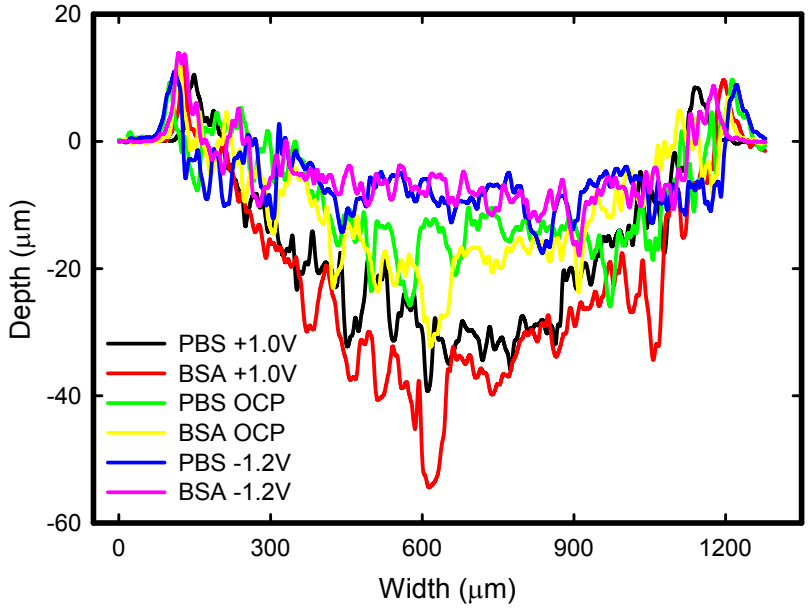

Figure 6.4: Wear track profile of the titanium disk under various conditions.

The profile of the wear track under cathodic conditions is less curved, while it reveals a

curvature under OCP and anodic conditions. This is reflected by the wear pattern on the alumina counterparts at the end of the tribocorrosion experiments, as shown in Figure 6.5. Since alumina is harder than titanium, its surface should remain intact during sliding on titanium. Therefore, the observed patterns on the alumina are due to transfer of titanium debris on the alumina surface [268, 270]. A further investigation of the alumina using energy-dispersive X-ray spectroscopy (EDX), X-ray photoelectron spectroscopy (XPS), or X-ray fluorescence (XRF) techniques, would confirm the transfer of debris and would be beneficial. Furthermore, a larger pattern on the alumina is observed under cathodic conditions as compared to OCP or anodic conditions, which indicates a greater amount of titanium transferred onto the alumina.

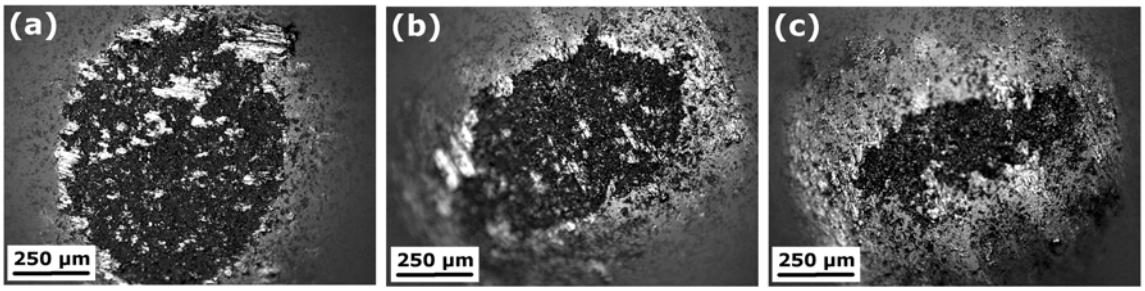

Figure 6.5: Optical microscopy images of alumina counterpart after the experiments in the presence of BSA at (a) -1.2 $V_{Ag/AgCl}$, (b) OCP, and (c) +1.0 $V_{Ag/AgCl}$.

The morphology of the area inside the wear tracks was acquired by SEM, as presented in Figure 6.6. Various levels of delamination and abrasion/plastic deformation are seen for all samples examined, which could be the major reason for the mechanical degradation of the surface. Numerous debris of different sizes is visible on the surface, which is attributed to the delamination of the passive film [271], while no major differences can be visually observed.

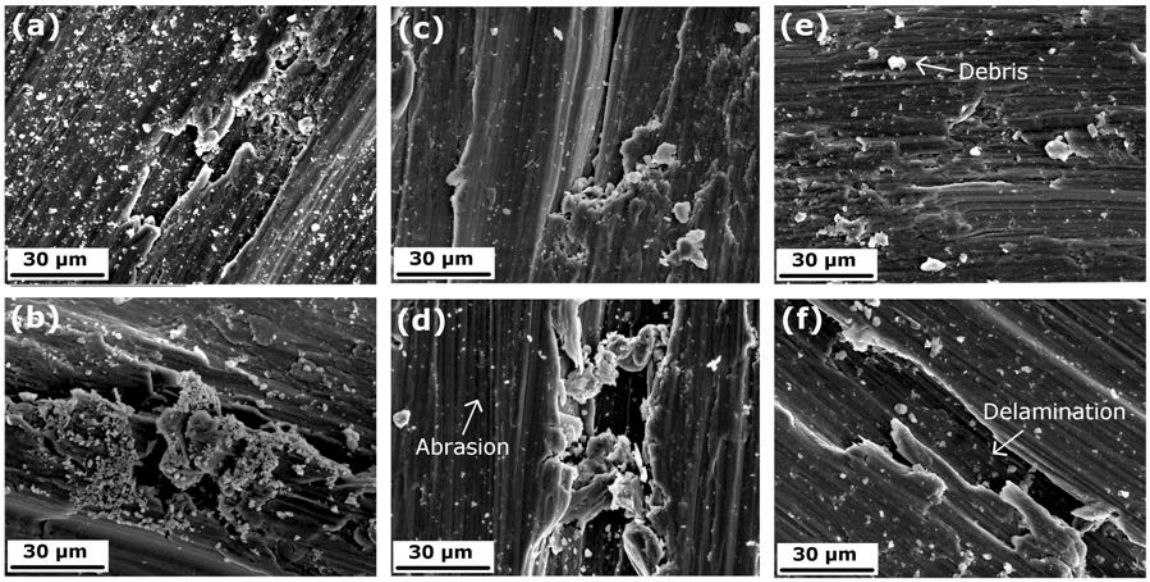

Figure 6.6: Scanning electron microscope images showing the topography of the wear track at (a) 1xPBS at -1.2 $V_{Ag/AgCl}$, (b) 1 mg/mL BSA in 1xPBS at -1.2 $V_{Ag/AgCl}$, (c) 1xPBS at OCP, (d) 1 mg/mL BSA in 1xPBS at OCP, (e) 1xPBS at +1.0 $V_{Ag/AgCl}$, and (f) 1 mg/mL BSA in 1xPBS at +1.0 $V_{Ag/AgCl}$.

In some occasions, the debris generated as the result of surface degradation was found to aggregate and form large third bodies, with a representative one shown in Figure 6.7. Such large particulates present at a sliding interface could act as third body abrasives and accelerate the rate of material loss, especially in the presence of BSA due to its capacity to mediate and increase the interaction between first and third body and, thus, enhancing particle entrainment [53]. Most importantly, the chance of forming large debris aggregates is greater in high anodic potential than it is in low anodic potential [272]. This could be due to that at anodic potential the repassivation rate is sufficient large in order for the ejected particles to repassivate and form third bodies. Therefore, the greater material loss at anodic conditions as compared to the cathodic at the present work is likely due to an increased amount of debris that enhances the mechanical wear.

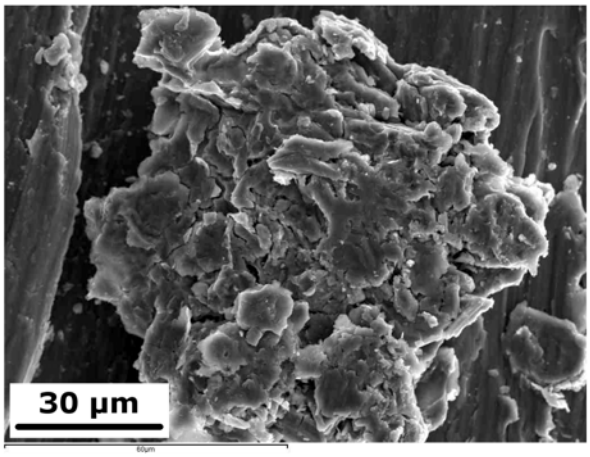

Figure 6.7: Scanning electron microscope image of aggregated debris inside the wear track.

6.3.3 Hardness

To further understand the cause of surface degradation, a microindenter was deployed to measure the hardness within and outside of the wear track, with Figure 6.8 showing the hardness of the titanium inside the wear track. The hardness outside the wear track is found to be equal to 120 HV. At cathodic and open circuit potential conditions, the hardness inside the wear track was found to be approximately 250 HV showing a twofold increase compared to the hardness outside the wear track, which is attributed to plastic deformation due to dislocation of atoms, in a process called strain hardening [273]. At anodic applied potential conditions the increase in the hardness was smaller with a value of approximately 220 HV. The effect of BSA under the cathodic and OCP conditions is not clear because the different is not significant. However, the presence of BSA slightly decreased the hardness at anodic conditions ($P < 0.05$).

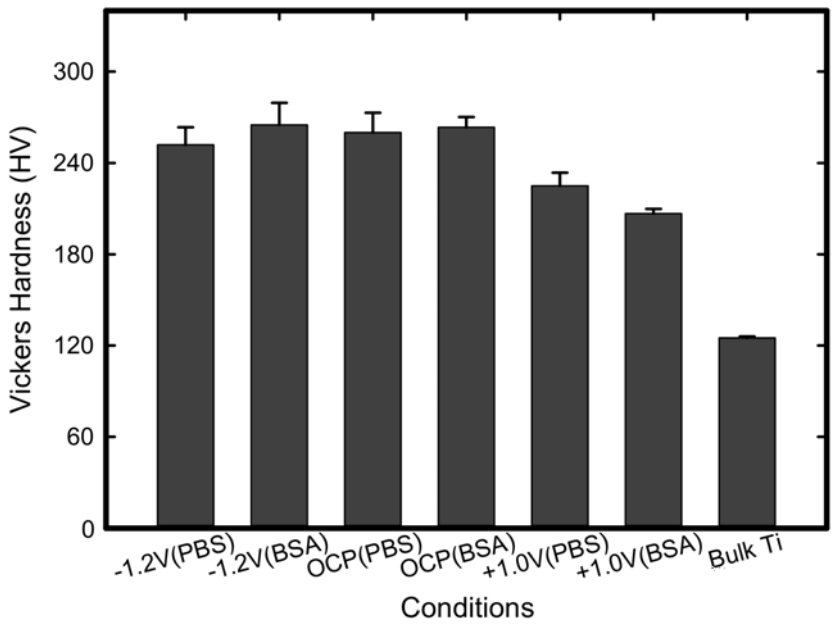

Figure 6.8: Hardness (Vickers) of the titanium inside and outside (bulk Ti) the wear track at various conditions. Data points represent mean values of n=4 measurements ± standard error. The difference from the presence of protein is insignificant at -1.2 V and OCP, while it is significant at +1.0 V ($P < 0.05$).

6.3.4 Nanoadhesion

Atomic force microscopy based force measurements were carried out to quantify the adhesive interaction between alumina particle and titanium surface, in the presence of BSA, under the same electrochemical conditions that were used in tribocorrosion experiments. Figure 6.9a shows representative force curves collected under three different surface potentials when an alumina particle was brought towards the titanium substrate, made the contact, and then separated. For clarity purpose, only the data recorded during the separation process is shown. In the retraction curve, there are multiple peaks, so called pulling events, corresponding to the desorption of proteins. The nanoadhesion measurements offer a unique approach to quantify the interaction between alumina particle, replicating the debris generated at a sliding interface, and the solid substrate. The adhesion between alumina and titanium in PBS solution is very small (< 20 pN) and not detectable, and hence are not shown here. With the presence of BSA, the adhesion force corresponds to the largest peak in the retraction curve. Throughout the nanoadhesion measurements, a

number of cantilevers with alumina particle fixed at the end were used. Because variation in the size of those particles determines the contact area, all adhesion forces acquired by each cantilever were normalised against that collected at -1.2 $V_{Ag/AgCl}$.

Averaged values of the normalised adhesion between alumina particles against titanium in the presence of BSA under each electrochemical condition are presented in Figure 6.9b. The maximum adhesion was observed at cathodic potential, followed by OCP, and anodic potential where it exhibited the smallest interaction. Because the interaction between alumina and titanium in PBS was measured to be negligible, the adhesion measured here corresponds to the force needed to separate BSA molecules from alumina and titanium surfaces. Furthermore, since the interaction between alumina and BSA is expected to be the same under all electrochemical conditions studied here, the observed variation in adhesion is due to the interaction between BSA and titanium. Therefore, the presence of BSA increases the adhesion of the debris at the interface between the sliding surfaces which in turn increases the friction and, thus, the mechanical wear. At anodic conditions, the adhesion is slightly decreased, which is likely to increase the rolling efficiency of the debris and in turn increase further the material loss.

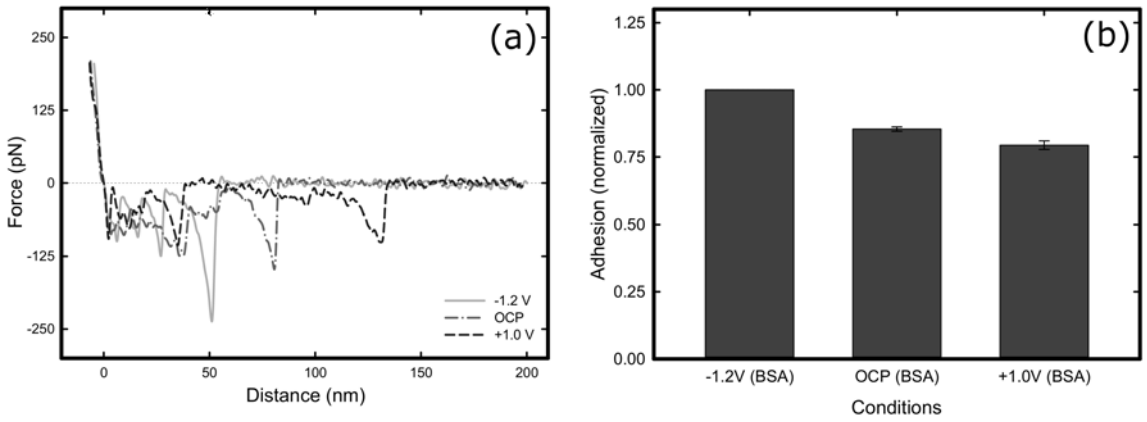

Figure 6.9: (a) Representatives force-distance curves of alumina against titanium, and (b) adhesion between alumina and titanium surface, in the presence of BSA at -1.2 $V_{Ag/AgCl}$, OCP, and +1.0 $V_{Ag/AgCl}$. Data points represent mean values of n=600 measurements ± standard error ($P < 0.001$).

6.4 Discussion

6.4.1 Effect of passive film on tribocorrosion characteristics of titanium

The passive film formed on the titanium surface is highly depended on the prevailing electrochemical conditions. Under cathodic applied potential reduction reactions (mainly water and oxygen) take place on the whole surface while under anodic applied potential the anodic reaction are favoured and thicker oxide films are formed. The presence of an oxide film on the surface of the titanium exposed to electrolyte was found under all electrochemical conditions in the present study. This was expected since it is widely accepted that the surface of passive metals is covered by a thin inert oxide film that protects the underlying titanium from corrosion [254]. Upon initiation of sliding, the passive film gradually degrades from the surface, leaving the active titanium underneath exposed and causing the OCP and the current to drop towards more active values. Without the passive film to protect the surface, the corrosion rate is greatly increased. When the sliding stops, the passive film is quickly regenerated on the titanium surface and protects from further corrosion.

During tribocorrosion, two wear mechanisms are present; wear accelerated corrosion that occurs with the elimination of the passive film by mechanical disruption and repassivation of the surface, and mechanical wear that include abrasion, delamination, and plastic deformation [262]. The total material loss is significantly increased at anodic conditions as oppose to the cathodic or the OCP. Although the corrosion is greatly increased upon removal of the passive film at anodic conditions, the contribution of the corrosion to the total mass loss is only 7 %, with the rest due to mechanical wear. Therefore, it is highly likely that the increased material loss is due to the presence of a thicker passive film, which is consistent with a previous study reporting that the presence of a passive film enhances the mechanical surface degradation over the oxide free metal [262]. It is

believed that the detached metallic particles are easily deformed and smeared back on the wear track area at cathodic potentials, which in turn reduced the rate of wear loss. As a result of the increased plastic deformation and smearing at cathodic conditions, the hardness of titanium is increased due to strain hardening, as suggested by the results in Figure 6.8. The increased mechanical wear at anodic conditions could also be attributed to an increased presence of debris at the sliding interface. This is in agreement with a previous study where it was found that the formed metallic debris particles were dissolved in the electrolyte at low anodic potential before they could form a large third body [272]. In contrast, at higher anodic current, the formed metallic debris have sufficient time to repassivate and form a large third body (Figure 6.7). The newly formed third bodies in turn act as abrasive particles during sliding that accelerates the mechanical material removal.

6.4.2 Effect of albumin on tribocorrosion characteristics of titanium

It has been found that albumin could act as a cathodic inhibitor in PBS solution - it reduces the rate of cathodic reactions, which in turn shifts the corrosion potential and the cathodic current towards more cathodic values [7]. This is consistent with the present work, as shown in Figure 6.2a, where the reduction in the rate of cathodic reactions at cathodic condition results in a decreased current flow in the presence of BSA. It was also suggested that the adsorbed BSA molecules on the titanium surface could hinder the transport of oxygen towards the solid/liquid interface, and consequently inhibit the rate of oxygen reduction [7, 50, 236]. At the same time, protein molecules could bound metal ions and carry them away from the solid/liquid interface, which in turn accelerates the rate of anodic reactions [233, 274]. This second mechanism is apparent in Figure 6.2b where the presence of BSA results in a current increase.

The presence of albumin in PBS solutions increases significantly the mechanical wear (Figure 6.3), which is attributed to two factors as was shown by the force curves. Firstly,

BSA increases the adhesion of debris onto the sliding surfaces, causing an increased amount of debris present at the sliding interface and, thus, greater mechanical wear. This is suggested by the nanoadhesion measurements between alumina and titanium - the adhesion is negligible in PBS but increases greatly in the presence of BSA. Secondly, the presence of protein in anodic conditions further increases the mechanical wear, which is likely due to a combination of an increased presence of debris and an increased capacity of BSA to act as lubricant at anodic potential (Figure 6.9b). This is consistent with previous study on CoCrMo surfaces where it was found that protein enhances the rolling efficiency of the abrasives (third bodies) and leads to larger material loss [53].

6.5 Conclusions

In the present study, the tribocorrosion characteristics of pure titanium and the effect of BSA have been studied systematically. The passive film formed on a titanium surface greatly decreases its corrosion process, and is present on the titanium surface both at cathodic and anodic conditions although thicker at the latter. Upon mechanical damage, the active titanium underneath is being exposed, and the corresponding corrosion rate is significantly increased. The total material loss during tribocorrosion of titanium is highly attributed to the mechanical wear, while the wear-accelerated corrosion is only a small fraction of the total loss. The mechanical wear is caused by plastic deformation and delamination, while it is further increased at anodic conditions due to greater presence of debris particles at the sliding interface.

The presence of BSA inhibits the repassivation rate of oxide film by hindering the rate of cathodic reaction, while it also accelerates the rate of anodic reactions. Furthermore, BSA was found to significantly increase the mechanical wear by increasing the adhesion of the debris on the sliding interface, while the rolling efficiency of the debris is enhanced at anodic conditions that could further increase the mechanical wear at the sliding interface.

Chapter 7

Conclusions

In the present thesis, a combination of molecular dynamics and advanced experimental techniques was used to study the effect of biomaterial surface chemistry on the adsorption of proteins, as well as the impact of protein adsorption on the wear of a metallic biomaterial. It was found that surface chemistry can have a significant impact on the protein adsorption mechanisms, because it affects the adsorption kinetics, the driving forces of adsorption, and the conformation and functionality of the adsorbed proteins. Furthermore, the adsorbed proteins could greatly affect the lifetime of a metallic biomaterial, especially in applications where the biomaterial surface is subjected to friction. The results are presented in detail in the following sections.

7.1 Effect of surface chemistry on protein adsorption

By combining Molecular Dynamics simulations with experimental techniques, it was possible to systematically study the effect of surface chemistry on the adsorption of proteins. It was found that the surface chemistry of a biomaterial has a significant impact on the protein adsorption mechanisms, and the following conclusions can be drawn.

In chapter 3 it was shown that the predominant driving forces of protein adsorption are electrostatic interactions, van der Waals forces, and hydrophobic interactions. Electrostatic interactions and van der Waals forces are important at the first stages of adsorption, while hydrophobic interactions are developed upon adsorption on hydrophobic surfaces and can increase the adhesion and denaturation of the adsorbed protein. Prior to adsorption, proteins are moving in a Brownian motion until they come in close proximity with the

biomaterial surface and interact with it. On charged surfaces, due the presence of long-range electrostatic interactions, the proteins are interacting with the surface from a greater distance, whilst on non-charged surfaces, the proteins are required to come closer to the surface and interact via van der Waals forces. Once the protein is in close proximity with the surface, the anchoring takes place either with a polar uncharged or with a charged residue, which highlights the importance of hydrophilic residues (charged or uncharged) at the first stages of adsorption. In contrast, anchoring with a hydrophobic residue was not observed in any case, which could be attributed to the majority of hydrophobic residues being buried in the core of the protein, and could explain why the rate of adsorption on hydrophobic surfaces is slightly lower than it is on the rest of the surfaces, as was shown in chapter 4.

Proteins adopt different conformations on different surfaces depending on the forces that are acting on them, as was shown in chapters 3 and 4. On positively charged and hydrophobic surfaces proteins favour a “side-on” conformation, while on negatively charged and polar uncharged surfaces proteins prefer a “head-on” conformation. It was also found that the conformation of proteins upon adsorption is in direct relation to their denaturation - a “side-on” conformation results in greater denaturation while a “head-on” conformation has smaller impact on the structural integrity of the adsorbed protein. For instance, because the protein used in this thesis has an overall negative charge, a larger force is acting on it during adsorption on a positively charged surface that favour a ‘side-on” adsorption and denaturates the protein. The denaturation of the protein on a hydrophobic surface is attributed to hydrophobic interactions between the surface and hydrophobic residues present on the core of the protein. The exposure of core hydrophobic residues on the surface not only denaturate the protein but also lead to a stronger protein-surface interaction. In contrast, adsorption on polar uncharged and negatively charged surfaces has a smaller impact on the structural integrity of the protein. Adsorption on a negatively charged surface takes place with electrostatic interaction against positively charged patches on the protein which could result in an unfavourable ”head-on” adsorption that has a lesser

impact on the structural integrity of the protein. Similarly, adsorption on hydrophilic surface does not affect the structural integrity of the protein, due to the weak nature and the short-range of van der Waals forces.

In chapter 3 it was also found that on charged surfaces the adsorption is specific, which is attributed to the polarity of the protein molecule and the electric field above the charged surfaces. Consequently, depending on the polarity of the protein, a specific charged surface will have a specific impact on the active site of a protein. For instance, adsorption of fibronectin on positively charged surface will always result will the cell-binding site active, while on negatively charged surface it will likely be inactive. In contrast, adsorption on uncharged surfaces is non-specific, and the protein could adopt a range of different conformations depending on the trajectory of the protein during adsorption. Consequently, it is likely that the cell-binding site will be active for some adsorbed molecules and inactive for some others.

Protein adsorption could also be affected by the rate of cathodic and anodic reactions on the surface of a passive metal, as was shown in chapter 5. More specifically, the application of a cathodic potential could result in an excessive amount of electrons on the surface, which in turn result in protein desorption due to electrostatic repulsion. In contrast, an anodic potential could cause electron depletion on the surface, which could facilitate protein adsorption. This could highlight the effect of pH on biomaterials. For instance, at basic environments the titanium surface becomes more negative that could result in protein desorption, while an acidic environment could increase protein adsorption on the surface of a biomaterial.

7.2 Other factors affecting protein adsorption

The presence of ions could effectively screen the electrostatic interactions between protein and surface above the Debye length, as was shown in chapter 3. Consequently, an increased number of ions could facilitate the adsorption of protein on surfaces with same charge, or hinder the adsorption on surfaces with opposite charge than the protein. At the same

time, because ions are strongly bound on charged surfaces, protein adsorption could be further inhibited.

Chapter 3 also highlighted the important role of water in protein adsorption, which is apparent only in MD simulations with explicit solvent. It was shown that a layer of water molecules adjacent to the surface could inhibit protein adsorption. This was particularly apparent in cases of charged surfaces where the water molecules were strongly bound on the surface.

Another factor that could affect protein adsorption is the flexibility of a surface. It was found in chapter 3 that the mobility of adsorbed proteins is reduced upon adsorption on SAMs surfaces with increased flexibility, which was attributed to the increased interface between protein and surface. It is likely that systems similar to SAMs, such as some polymeric surfaces, could increase the adhesion of proteins, as opposed to solid surfaces such as metals or ceramics.

7.3 Impact of protein on metallic biomaterials

Chapters 5 and 6 focus on the impact of protein adsorption on metallic biomaterials. It was found that protein adsorption could greatly affect the lifetime of a biomaterial, and the following conclusions can be drawn.

In chapter 5 was found that the presence of albumin could affect the corrosion rate of a titanium surface, by hindering the rate of cathodic reactions and accelerating the rate of anodic reactions. The impact of protein adsorption in the degradation of biomaterials is even larger in applications where the surface of a metallic biomaterial is subjected to friction, as was shown in chapter 6. Although BSA could increase the rate of repassivation of the titanium surface at anodic conditions and, thus, decrease the corrosion, when this is combined with friction it results in accelerated corrosion that is attributed to a different mechanism of mechanical wear. When the repassivation is low the main mechanism of mechanical wear is plastic deformation, which shifts to delamination as the passive film grown thicker.

Furthermore, in chapter 6 was found that protein increases the presence of debris at the sliding interface, which in turn accelerates significantly the mechanical wear. This is attributed to a greater adhesion between the debris particles and the surface at the interface. It is likely that the concentration of debris will be increased on positively charged and hydrophobic surfaces, as opposed to negatively charged or polar uncharged surfaces. In addition, protein could enhance the rolling efficiency of the debris at anodic conditions, which could further accelerate the mechanical wear.

7.4 Other findings

In chapter 4 was shown that the method followed for the functionalization of the AFM cantilever, consisted of two steps that utilize the sulphur-gold and the His-Tag interactions, was successful. However, a better cleaning procedure of the functionalized AFM tip is suggested for improved results. Furthermore, it was found that gold surface possesses a negative charge when it is immersed in HEPES solution at pH=7, which was attributed to the adsorption of ions on the gold surface.

Lastly, at chapter 5 was shown that surface roughness is a factor that could affect the corrosion of titanium. Generally, a greater roughness results to an increased corrosion due to a larger effective area where cathodic reactions can take place. Furthermore, it was found that passivation of titanium could result in a permanent phase transition of the passive film present on its surface.

7.5 Implications of the findings to the field

The findings of this thesis can find use in a plethora of applications. By controlling the surface chemistry of a biomaterial, the adsorption of proteins and, consequently, tissue could be enhanced or hindered. For instance, in applications where a strong bond between biomaterial and surrounding tissue is desired, such as in bone plates and screws, a surface chemistry that enhances protein adsorption is preferable. In contrast, in applications where

adhesion of tissue on biomaterials in not desired, such as in repairs in the cardiovascular area, a surface chemistry that inhibits protein adsorption is a better choice. Furthermore, this work highlights the impact of protein adsorption at sliding interfaces, as well as the effect of the prevailing conditions, such as pH, on the biocompatibility of the implant. Because mechanical wear at sliding interfaces deteriorate the protective oxide layer of metallic biomaterials, which could cause various implications, novel coatings can be developed that eliminate this effect. Also, because the pH in the oral cavity or in wounds can vary greatly, the rate of corrosion and wear of implants can be affected and, thus, it is another factor that should be taken under consideration when designing biomaterials. Overall, this thesis can provide a guide not only in designing surfaces that produce a specific response towards the surrounding tissue, but also in increasing their lifetime at sliding interfaces or corrosive environments.

Chapter 8

Future work

8.1 Future work

The understanding of the interactions between proteins and biomaterials underpins the development of novel biomaterials with tailored properties. The combination of Molecular Dynamics simulations and advanced experimental techniques that were used in this thesis, contributed to the understanding of the aforementioned interactions. However, future work could take this project a step further. Below are some suggestions regarding the continuation and the development of this project that will lead towards a better understanding of the protein-surface interactions.

First of all, possibly the immediate next step of this thesis would be to perform Steered Molecular Dynamics (SMD) simulations on the adsorbed fibronectin fragment. In SMD a pulling force can be applied on the adsorbed protein, which could provide an insight on the desorption mechanism of a protein. It is likely that when the fibronectin fragment is strongly adsorbed onto a surface, a pulling force would unfold the protein. In contrast, a pulling force on a weakly adsorbed protein is possible to result in desorption without affecting the structural integrity of the protein. Consequently, performing SMD on the adsorbed fibronectin molecules could lead to a correlation with the results acquired by single molecule force spectroscopy (SMFS) in chapter 4.

Although fibronectin is one of the major adhesive cell-binding proteins, it is very large to be studied in its native form with explicit solvent MD simulations. Therefore, it would be beneficial if MD and experimental work were combined to systematically study the

adsorption of a smaller protein. A proposed system is albumin that is a small protein that has been studied extensively. It is likely that an SMD study, combined with SMFS, could provide a direct correlation on the desorption mechanism that would lead to better understanding of the protein-surface interactions.

Self-assembled monolayers were proven to be a sufficient system to investigate the effect of surface chemistry on protein adsorption. It was observed in chapter 3 that the flexibility of SAMs molecules could affect the mobility of protein upon adsorption. It would be beneficial if this could be confirmed experimentally because it could be a link between the effect of surface chemistry and topography on protein adsorption. Therefore, it is suggested for protein adsorption to be studied on SAMs surfaces with varying length, using a quartz crystal microbalance to quantify the adsorption and single molecule force spectroscopy to measure the adhesion.

Another interesting perspective would be to study the effect of ion concentration on protein adsorption. It was shown in chapter 3 that ion concentration could greatly affect the adsorption mechanisms. This comes as no surprise because it is a behaviour that has been observed and studied in the past [275–278]. However, the effect of ionic strength on the system fibronectin-SAMs has not been investigated in the past. Therefore, the quantification of this effect on various surfaces with SMFS and QCM, and a possible correlation with the MD results would provide a further insight on this phenomenon.

Lastly, it would be beneficial if a procedure for an improved cleaning of the functionalized cantilever could be developed. The functionalization method followed in this thesis could be a fast and convenient method to functionalize cantilevers with a wide range of molecules and proteins in order to study the adsorption phenomena. It is common for the SAMs surfaces to be cleaned with sonication after the functionalization. However, this cannot be applied in AFM cantilevers because they are damaged. Therefore, an alternative cleaning method could be developed to improve the results acquired by single molecule force spectroscopy.

Appendix A

Molecular Dynamics information

This chapter provides supplementary information relevant to anyone attempting to verify, replicate, or continue this work.

A.1 Protein structure

Initially a folder is created that will contain all the files and scripts that will be used during the simulation. In order to simulate protein adsorption, the protein structure needs to be downloaded from the protein data bank (PDB) website [279]. The data bank contains a large number of protein structures solved by NMR or X-ray. The desired protein is then downloaded in the computer in the pdb format and is given a filename. The protein structure used in this thesis is the 1FNF and was named `1FNF.pdb`. Subsequently, the pdb file is loaded in the VMD software that is used to visualize the protein. The file can be loaded by typing the following command line on the linux terminal:

```
$ vmd 1FNF.pdb
```

The downloaded file contains the 7^{th} to 10^{th} type III fibronectin modules ($FNIII^{7\text{-}10}$). In order to truncate the protein at the desire length, the pdb file is opened by a text editor (vi or emacs editors recommended) in latex and the coordinates corresponding to the $FNIII^{7}$ module are deleted. The resulted modified fragment, containing the coordinates for the 8^{th} to 10^{th} type III modules ($FNIII^{8\text{-}10}$), is given a filename, such as `FN_truncated.pdb`. The pdb file could be loaded again on the VMD software to visualize the new fragment.

A.2 Simulations in water

The `FN_truncated.pdb` contains only the initial coordinates of the protein atoms. An additional file is needed to be created that will contain the rest of the information needed to apply a particular force field on the protein, such as bond length, bond angles, charges, van der Waals, etc. The psf file is created based on the `FN_truncated.pdb` and the topology file (see section for parameters). To produce the psf file, `script1.pdb` is used (see in section Script 1). The script is then executed by typing the following command line:

```
$ ./script1.inp > log
```

The command creates three new files: `FN8_10.pdb`, `FN8_10.psf`, and the `log` file that contains additional information. The new files can then be loaded in VMD to visualize it by typing:

```
$ vmd FN8_10.psf FN8_10.pdb                                    (A.1)
```

The above files contain only the protein structure and information. The next step is to add water and ions. On VMD with the loaded structure (command A.1) the Tk console is open from the main menu (`Main menu` → `Tk Console`) and the molecule is solvated by typing:

```
% solvate FN8_10.psf FN8_10.pdb -t 20 -o FN8_10_S              (A.2)
```

The above command (A.2) places the protein in a water box extending 20 Å from the protein in the x,y, and z direction. The dimensions can be changed, depending on the protein size and the available processing power. A typical number for such systems is 100,000 atoms in total. However, it is recommended that the water is extended at least 15 Å from the sides of the protein to avoid interactions from "image" proteins due to

the periodic conditions (see Methodology chapter). Command A.2 produces 2 new files, `FN8_10_S.pdb` and `FN8_10_S.psf`, which contain the solvated structure of the protein.

Following solvation, ions are added in the system as follows. The solvated protein structure is opened in VMD by typing:

```
$ vmd FN8_10_S.psf FN8_10_S.pdb
```

This opens a VMD environment that visualizes the solvated protein. Subsequently, ions are added from the VMD environment (`Main menu` → `Extensions` → `Modelling` → `Add Ions`). The open window requires the following input: the psf and pdb files of the solvated protein (`FN8_10_S.pdb` and `FN8_10_S.psf`), the output prefix (a filename for the pdb and psf files containing the ions such as `FN_005M_S`), and the desired ion concentration (0.05 mol/L NaCl). Following clicking the `Autoionize` button, the ions are added in the system and 2 new files are produced that contain the protein, the water, and the ions: `FN_005M_S.psf` and `FN_005M_S.pdb`.

The next step is to centre the water box and decide which atoms will be fixed during various steps of the simulation. To centre the water box the `ctrbox.tcl` script is used (see section Script 2). Initially, the structure containing the protein, the water, and the ions is open in VMD:

```
$ vmd FN_005M_S.psf FN_005M_S.pdb
```

Subsequently, in the open VMD environment, the following commands are given in the Tk console:

```
% play ctrbox.tcl
% ctrbox FN_005M_S.psf FN_005M_S.pdb FN_005M_SC
```

The above commands centre the water box and produce 2 new files: `FN_005M_SC.psf` and `FN_005M_SC.pdb`. These files will be used to run the simulation of protein in water. The

FN_005M_SC.pdb file contains the coordinates for all the atoms present in the protein,water, and ions. However, all the atoms are fixed in space. In order to run the simulation, the water atoms and the ions must be allowed to move in the system. The steps necessary are the following: First the file FN_005M_SC.pdb is opened with the vi editor. At the bottom of the file are the coordinates of the cell centre, which need to be copied because they will be used at a later step. After the coordinates have been copied, the file is exited. Subsequently, the following command is given:

```
$ cp FN_005M_SC.pdb FN_005M_SCF.pdb
```

This creates a copy of the file FN_005M_SC.pdb named as FN_005M_SCF.pdb. Subsequently, file FN_005M_SCF.pdb is opened with vi editor as follows:

```
$ vi FN_005M_SCF.pdb
```

On the opened by the vi editor file, the column that follow the coordinates of each atom, 1.00, needs to be replaced by 0.00. For instance, the line regarding the protein, the water, or the ion will end with PRO, WT, or ION respectively as shown below:

```
ATOM   1   N    VAL B 1      −7.191   −8.018   49.678   1.00   0.00        PRO   N
ATOM   2   SOD SOD I 2      −47.218  25.113   −8.359   1.00   0.00        ION  NA
ATOM   3   OH2 TIP3W 3      −40.815   3.949   72.457   1.00   0.00        WT    O
```

To replace 1.00 by 0.00, the following commands are typed in the vi editor:

```
:%s/␣ ␣ 1.00 ␣ ␣ 0.00 ␣ ␣ ␣ ␣ ␣ ␣ ION/␣ ␣ 0.00 ␣ ␣ 0.00 ␣ ␣ ␣ ␣ ␣ ␣ ION/
:%s/␣ ␣ 1.00 ␣ ␣ 0.00 ␣ ␣ ␣ ␣ ␣ ␣ WT/␣ ␣ 0.00 ␣ ␣ 0.00 ␣ ␣ ␣ ␣ ␣ ␣ WT/
```

The end result will look like the example below:

```
ATOM   1   N    VAL B 1      −7.191   −8.018   49.678   1.00   0.00        PRO   N
ATOM   2   SOD SOD I 2      −47.218  25.113   −8.359   0.00   0.00        ION  NA
ATOM   3   OH2 TIP3W 3      −40.815   3.949   72.457   0.00   0.00        WT    O
```

The last step is to run the simulation, which contains three steps: i) water equilibration (D0 dynamics), ii) heating of the system (D1 dynamics), and iii) the simulation (D2 and further). The scripts for each step (D0.inp, D1.inp, and D2.inp) are given in sections

Script 3, Script 4, and Script 5 respectively. The script `D2.inp` produces only 10 ns of simulation. To add 10 more ns, the file is copied as `D3.inp` and the names in the file are replaced accordingly (`D1` → `D2` and `D2` → `D3`). The job is ready for submission.

A.3 Adsorption simulations

The SAMs surfaces were build upon existing amino acids found in the parameters and topology files, which were modified as shown in section for the parameters below. Subsequently, the pdb files containing the coordinates for the SAMs molecules were transferred to excel any they were replicated in order to build a surface with the desired length (Chapter 3).

The steps in the adsorption simulation are similar to the simulation in water, with the inclusion of the desired surface. Initially a folder is created that contains the pdb file for the protein (`FN.pdb`) and the surface (`Surface.pdb`), the topology and parameter files, as well as all the scripts that will be used. Subsequently, the surface and protein files are opened in vmd:

```
$ vmd FN.pdb Surface.pdb
```
(A.3)

It is likely that the surface and the protein are not in the proper position in respect to each other. Therefore, the coordinates need to be modified. This can be done by opening the `Surface.pdb` in an editor, copying the coordinates to an excel file, and adding or subtracting the necessary number to bring the surface at the proper distance from the surface with a proper alignment. A typical distance between protein and surface is ranging between 10 and 20 Å depending on the system. In this example the protein is set at a distance equal to 20 Å from the surface. When the surface and protein are in the desired distance and orientation in respect with each other, then the protein is solvated. The procedure is similar with the one in the above section (simulations in water). The difference is that the water box that will be added around the protein should not exceed

the limits set by the surface. For instance, if the distance of the protein from the surface is 20 Å in the +z direction, then the protein has to be solvated with the water extending 20 Å in the -z direction. Similarly, since the protein is centred above the surface, the water added in the x and y direction should not exceed the edges of the surface. For instance, if the distance in the x and y direction is 10 and 15 Å respectively, then the command in the Tk console will be:

```
% solvate FN.psf FN.pdb +x 10 -x 10 +y 15 -y 15 +z 20 -z 20 -o FN_S
```

Following solvation, ions are added in the system similarly to the simulation is water. After ions are added in the system, two files will be produced, such as `FN_005M_S.psf` and `FN_005M_S.pdb`. Subsequently, file `FN_005M_S.pdb` is copied as `FN_005M_S_ions.pdb` and is open in vi editor where only the lines corresponding to the ions are kept and everything else is deleted (the lines referring to ions are ending in `ION` as shown in the water simulation section). The resulted file will contain only the coordinates of the ions. Subsequently, the surface and the ions files are opened in VMD:

```
$ vmd Surface.pdb FN_005M_S_ions.pdb
```

If any ions are overlapping with the surface then `FN_005M_S_ions.pdb` is opened in vi editor and the coordinates of the overlapping ion are slightly modified to move the ion in an appropriate position. Once it is verified that no atoms and ions are overlapping with each, then VMD is exited. Subsequently, the surface, protein, and ions are integrated in one system with `script6.inp` (see section Script 6). The script returns files `FN_Sur_Ions.pdb` and `FN_Sur_Ions.psf`, which contain the protein, the surface, and the ions, which are then opened with VMD:

```
$ vmd FN_Sur_Ions.psf FN_Sur_Ions.pdb
```

Afterwards, the opened structure is solvated. For the solvation, all the directions are kept 0 apart from the one moving away from the protein. In this example, since the protein is at +z direction in respect to the surface, then only the +z direction is solvated. For instance:

```
% solvate *.psf *.pdb +x 0 -x 0 +y 0 -y 0 +z 10 -z 0 -o FN_S
```

The +z can be increased or reduced until a total number of approximately 100,000 atoms is achieved. Subsequently, the system is centred by executing the script `ctrbox.tcl` as described is the previous section. The script produces files `FN_Sur_Ions_SC.pdb` and `FN_Sur_Ions_SC.psf`.

Similarly to the example in water, for the production of the adsorption simulations some atoms need to be fixed. Therefore, `FN_Sur_Ions_SC.pdb` is copied as `FN_Sur_Ions_SCF.pdb` and opened with vi editor. This file will be used for the water minimization dynamics (step `D0`) where the protein and surface structure need to remain fix, while the water and ions have to be able to move. Accordingly, for all the lines corresponding to ions (`ION`) and water (`WT`), `1.00` has to be changed to `0.00` as in the above section. Afterwards, `FN_Sur_Ions_SCF.pdb` is copied as `FN_Sur_Ions_FIX.pdb`, and `1.00` is changed to `0.00` for the protein atoms (`PRO`). The `FN_Sur_Ions_FIX.pdb` file will be used for heating of the system dynamics (`D1.inp`), and the simulations (`D2.inp`, `D3.inp`, ...).

Files `D0.inp`, `D1.inp`, `D2.inp`, etc. are produced as shown in the water simulation example (Scripts 3, 4, 5). Once the scripts are produced the job is ready for submission.

A.4 Parameters

The protein structure file (PSF) contains all the information needed to apply a particular force field to a specific molecule. The CHARMM force field used for the molecular dynamics simulations of this thesis is divided in the topology and the parameter files. The topology file is used to generate the PSF file and defines the atom types used in the force field: the

atom names, types, bonds, and partial charges of each residue [280]. The parameter file provides specific numerical values for the calculation of the CHARMM potential function. The topology and parameters can be downloaded from the CHARMM website [281], while in this thesis were based on existing files that were modified by collaborator Karina Kubiak-Ossowska. Below are given the modifications done in the topology and parameter files in order to build the SAMs molecules used in chapter 3. For further explanation of the parameters refer to the appropriate pages on the NAMD website [280, 282, 283].

A.4.1 Topology file

```
!SAMs atoms added
MASS    115 kCT2    12.01100 C ! aliphatic sp3 C for CH2
MASS    116 kCT3    12.01100 C ! aliphatic sp3 C for CH3
!MASS   117 kHA      1.00800 H ! nonpolar H
MASS    118 kOH1    15.99900 O ! hydroxyl oxygen
MASS    119 kH       1.00800 H ! polar H
MASS    120 kNH3    14.00700 N ! ammonium nitrogen
MASS    121 kHC      1.00800 H ! N-ter H
MASS    122 kCC     12.01100 C ! carbonyl C, asn,asp,gln,glu,cter,ct2
MASS    123 kOC     15.99900 O ! carboxylate oxygen
MASS    124 kS      32.06000 S ! sulphur
!MASS   125 kHS      1.00800 H ! thiol hydrogen

!IONS and metal ions by Heindrich Heinz
MASS    100 SOD  22.989770 NA ! Sodium Ion
MASS    101 MG   24.305000 MG ! Magnesium Ion
MASS    102 POT  39.102000 K  ! Potassium Ion! check masses
MASS    103 CES 132.900000 CS ! Cesium Ion
MASS    104 CAL  40.080000 CA ! Calcium Ion
MASS    105 CLA  35.450000 CL ! Chloride Ion
MASS    106 ZN   65.370000 ZN ! zinc (II) cation
MASS    107 AG  107.868200 AG ! Silver metal (HH et al. 2008)
MASS    108 AL   26.981539 AL ! Aluminium metal (HH et al. 2008)
MASS    109 AU  196.966500 AU ! Gold metal (HH et al. 2008)
MASS    110 CU   63.546000 CU ! Copper metal (HH et al. 2008)
MASS    111 NI   58.693400 NI ! Nickel metal (HH et al. 2008)
MASS    112 PB  207.200000 PB ! Lead metal (HH et al. 2008)
MASS    113 PD  106.420000 PD ! Palladium metal (HH et al. 2008)
MASS    114 PT  195.084000 PT ! Platinum metal (HH et al. 2008)

!SAMs parameters
!SILE - SAM with CH3 end (as in isoleucine)
!SSER - SAM with OH end (as in serine)
!SLYS - SAM with NH3 end (as in lysine)
!SASP - SAM with COO end (as in aspartic acid)
!SCYS - SAM with SH end (as in cysteine)
!always the first C is supposed to be frozen, then 3 CH2 groups, then the
!end group parameters for all CH2 as in ARG, LYS, ASP for CB, CG, CD aroms
```

```
RESI SILE          0.00
ATOM CSF   kCT2    -0.18 !
ATOM HF1   HA       0.09 !
ATOM HF2   HA       0.09 !
ATOM CS1   kCT2    -0.18 !     HF1    H1C1   H1C2   H1C3   H1C4
ATOM H1C1  HA       0.09 !      |      |      |      |      |
ATOM H2C1  HA       0.09 !     CSF----CS1----CS2----CS3----CS4--H3C4
ATOM CS2   kCT2    -0.18 !      |      |      |      |      |
ATOM H1C2  HA       0.09 !     HF2    H2C1   H2C2   H2C3   H2C4
ATOM H2C2  HA       0.09 !
ATOM CS3   kCT2    -0.18 !
ATOM H1C3  HA       0.09 !
ATOM H2C3  HA       0.09 !
ATOM CS4   kCT3    -0.27               !end group as in ILE
ATOM H1C4  HA       0.09
ATOM H2C4  HA       0.09
ATOM H3C4  HA       0.09
BOND CSF HF1 CSF HF2 CSF CS1 CS1 H1C1 CS1 H2C1 CS1 CS2 CS2 H1C2 CS2 H2C2
BOND CS2 CS3 CS3 H1C3 CS3 H2C3 CS3 CS4 CS4 H1C4 CS4 H2C4 CS4 H3C4
PATCHING FIRS NONE LAST NONE

RESI SSER          0.00
ATOM CSF   kCT2    -0.18 !
ATOM HF1   HA       0.09 !
ATOM HF2   HA       0.09 !
ATOM CS1   kCT2    -0.18 !     HF1    H1C1   H1C2   H1C3
ATOM H1C1  HA       0.09 !      |      |      |      |
ATOM H2C1  HA       0.09 !     CSF----CS1----CS2----CS3----OSH--HSH
ATOM CS2   kCT2    -0.18 !      |      |      |      |
ATOM H1C2  HA       0.09 !     HF2    H2C1   H2C2   H2C3
ATOM H2C2  HA       0.09 !
ATOM CS3   kCT2     0.05 !
ATOM H1C3  HA       0.09 !
ATOM H2C3  HA       0.09 !
ATOM OSH   kOH1    -0.66          !end group as in SER
ATOM HSH   H        0.43
BOND CSF HF1 CSF HF2 CSF CS1 CS1 H1C1 CS1 H2C1 CS1 CS2 CS2 H1C2 CS2 H2C2
BOND CS2 CS3 CS3 H1C3 CS3 H2C3 CS3 OSH OSH HSH
PATCHING FIRS NONE LAST NONE

RESI SLYS          1.00
ATOM CSF   kCT2    -0.18 !
ATOM HF1   HA       0.09 !
ATOM HF2   HA       0.09 !
ATOM CS1   kCT2    -0.18 !     HF1    H1C1   H1C2   H1C3    HSZ1
ATOM H1C1  HA       0.09 !      |      |      |      |      /
ATOM H2C1  HA       0.09 !     CSF----CS1----CS2----CS3----NSZ--HSZ2
ATOM CS2   kCT2    -0.18 !      |      |      |      |      \
ATOM H1C2  HA       0.09 !     HF2    H2C1   H2C2   H2C3    HSZ3
ATOM H2C2  HA       0.09 !
ATOM CS3   kCT2     0.21 !
ATOM H1C3  HA       0.05 !
ATOM H2C3  HA       0.05 !
ATOM NSZ   kNH3    -0.30 !             !end group as in LYS
ATOM HSZ1  kHC      0.34 !
ATOM HSZ2  kHC      0.34 !
```

```
ATOM HSZ3 kHC       0.34 !
BOND CSF HF1 CSF HF2 CSF CS1 CS1 H1C1 CS1 H2C1 CS1 CS2 CS2 H1C2 CS2 H2C2
BOND CS2 CS3 CS3 H1C3 CS3 H2C3 CS3 NSZ NSZ HSZ1 NSZ HSZ2 NSZ HSZ3
DONOR HSZ1 NSZ
DONOR HSZ2 NSZ
DONOR HSZ3 NSZ
PATCHING FIRS NONE LAST NONE


RESI SASP           -1.00
ATOM CSF   kCT2     -0.18 !
ATOM HF1   HA        0.09 !
ATOM HF2   HA        0.09 !
ATOM CS1   kCT2     -0.18 !     HF1    H1C1   H1C2   H1C3    ODS1
ATOM H1C1  HA        0.09 !      |      |      |      |      //
ATOM H2C1  HA        0.09 !     CSF----CS1----CS2----CS3----CSG
ATOM CS2   kCT2     -0.18 !      |      |      |      |      \
ATOM H1C2  HA        0.09 !     HF2    H2C1   H2C2   H2C3    ODS2(-)
ATOM H2C2  HA        0.09 !
ATOM CS3   kCT2     -0.28 !
ATOM H1C3  HA        0.09 !
ATOM H2C3  HA        0.09 !
ATOM CSG   kCC       0.62 !              !end group as in ASP
ATOM ODS1  kOC      -0.76 !
ATOM ODS2  kOC      -0.76 !
BOND CSF HF1 CSF HF2 CSF CS1 CS1 H1C1 CS1 H2C1 CS1 CS2 CS2 H1C2 CS2 H2C2
!BOND CS2 CS3 CS3 H1C3 CS3 H2C3 CS3 CSG CSG ODS2
!DOUBLE CSG ODS1
BOND CS2 CS3 CS3 H1C3 CS3 H2C3 CS3 CSG CSG ODS1 CSG ODS2
ACCEPTOR ODS1 CSG
ACCEPTOR ODS2 CSG
PATCHING FIRS NONE LAST NONE

RESI ASP            -1.00
GROUP
ATOM N     NH1      -0.47  !      |
ATOM HN    H         0.31  !   HN-N
ATOM CA    CT1       0.07  !      |    HB1    OD1
ATOM HA    HB        0.09  !      |    |      //
GROUP                      !   HA-CA--CB--CG
ATOM CB    CT2      -0.28  !      |    |      \
ATOM HB1   HA        0.09  !      |    HB2    OD2(-)
ATOM HB2   HA        0.09  !    O=C
ATOM CG    CC        0.62  !      |
ATOM OD1   OC       -0.76
ATOM OD2   OC       -0.76
GROUP
ATOM C     C         0.51
ATOM O     O        -0.51
BOND CB CA   CG CB   OD2 CG
BOND N   HN   N  CA    C    CA   C +N
BOND CA HA   CB HB1   CB HB2
DOUBLE   O    C    CG   OD1
IMPR N    -C CA   HN   C CA  +N O
!IMPR OD1 CB OD2 CG
IMPR CG   CB OD2 OD1
```

```
DONOR HN N
ACCEPTOR OD1 CG
ACCEPTOR OD2 CG
ACCEPTOR O C
IC -C   CA   *N   HN    1.3465 125.3100  180.0000 112.9400  0.9966
IC -C   N    CA   C     1.3465 125.3100  180.0000 105.6300  1.5315
IC N    CA   C    +N    1.4490 105.6300  180.0000 117.0600  1.3478
IC +N   CA   *C   O     1.3478 117.0600  180.0000 120.7100  1.2330
IC CA   C    +N   +CA   1.5315 117.0600  180.0000 125.3900  1.4484
IC N    C    *CA  CB    1.4490 105.6300  122.3300 114.1000  1.5619
IC N    C    *CA  HA    1.4490 105.6300 -116.4000 106.7700  1.0841
IC N    CA   CB   CG    1.4490 111.1000  180.0000 112.6000  1.5218
IC CG   CA   *CB  HB1   1.5218 112.6000  119.2200 109.2300  1.1086
IC CG   CA   *CB  HB2   1.5218 112.6000 -121.6100 110.6400  1.1080
IC CA   CB   CG   OD1   1.5619 112.6000  180.0000 117.9900  1.2565
IC OD1  CB   *CG  OD2   1.2565 117.9900 -170.2300 117.7000  1.2541

RESI SCYS           0.00
ATOM CSF  kCT2     -0.18 !
ATOM HF1  HA        0.09 !
ATOM HF2  HA        0.09 !
ATOM CS1  kCT2     -0.18 !     HF1   H1C1  H1C2  H1C3
ATOM H1C1 HA        0.09 !      |     |     |     |
ATOM H2C1 HA        0.09 !     CSF---CS1---CS2---CS3---SSG
ATOM CS2  kCT2     -0.18 !      |     |     |     |     \
ATOM H1C2 HA        0.09 !     HF2   H2C1  H2C2  H2C3   HSG1
ATOM H2C2 HA        0.09 !
ATOM CS3  kCT2     -0.11 !
ATOM H1C3 HA        0.09 !
ATOM H2C3 HA        0.09 !
ATOM SSG  kS       -0.23 !          !end group as in CYS
ATOM HSG1 HS        0.16 !
BOND CSF HF1 CSF HF2 CSF CS1 CS1 H1C1 CS1 H2C1 CS1 CS2 CS2 H1C2 CS2 H2C2
BOND CS2 CS3 CS3 H1C3 CS3 H2C3 CS3 SSG SSG HSG1
DONOR HSG1 SSG
PATCHING FIRS NONE LAST NONE
```

A.4.2 Parameter file

```
BONDS

!V(bond) = Kb(b - b0)**2
!
!Kb: kcal/mole/A**2
!b0: A
!
!atom type Kb          b0
!
HAS  OAS   495.000     0.945
SA   OAS   300.000     1.6800
!From Siddarth JACS paper
!
!beginning of SAMs (according to existing amino acids)
!
kCT2 kCT2     222.500     1.5300
HA   kCT2     309.000     1.1110
```

```
kCT3 kCT2      222.500      1.5280
HA   kCT3      322.000      1.1110
kOH1 kOH1      428.000      1.4200
kCT2 kOH1      428.000      1.4200
kOH1 H         545.000      0.9600
kNH3 kCT2      200.000      1.4800
kNH3 kHC       403.000      1.0400
kCT2 kCC       200.000      1.5220
kOC  kCC       525.000      1.2600
kS   kCT2      198.000      1.8180
kS   HS        275.000      1.3250
!
!end SAMS
```

ANGLES

```
!V(angle) = Ktheta(Theta - Theta0)**2
!
!V(Urey-Bradley) = Kub(S - S0)**2
!
!Ktheta: kcal/mole/rad**2
!Theta0: degrees
!Kub: kcal/mole/A**2 (Urey-Bradley)
!S0: A
!
!atom types      Ktheta    Theta0   Kub      S0
!
SA   OAS  HAS   50.00      115.00
!
!beginning of SAMs (according to existing amino acids)
!
! angles with original spring constants
!kCT2 kCT2 kCT2  58.350    113.60   11.16    2.56100
!kCT3 kCT2 kCT2  58.000    115.00    8.00    2.56100
!kHA  kCT3 kCT2  34.600    110.10   22.53    2.17900
!kHA  kCT2 kCT3  34.600    110.10   22.53    2.17900
!kHA  kCT2 kHA   35.500    109.00    5.40    1.80200
!kHA  kCT2 kCT2  26.500    110.10   22.53    2.17900
!kHA  kCT3 kHA   35.500    108.40    5.40    1.80200
!kOH1 kCT2 kCT2  75.700    110.1000
!kH   kOH1 kCT2  57.500    106.0000
!kOH1 kCT2 kHA   45.900    108.8900
!kNH3 kCT2 kCT2  67.700    110.0000
!kHC  kNH3 kCT2  30.000    109.50   20.00    2.07400
!kNH3 kCT2 kHA   45.000    107.50   35.00    2.10100
!kHC  kNH3 kHC   44.000    109.5000
!kCT2 kCT2 kCC   52.000    108.0000
!kOC  kCC  kCT2  40.000    118.00   50.00    2.38800
!kHA  kCT2 kCC   33.000    109.50   30.00    2.16300
!kOC  kCC  kOC  100.000    124.00   70.00    2.22500
!kS   kCT2 kCT2  58.000    114.5000
!kHS  kS   kCT2  38.800     95.0000
!kS kCT2   kHA   46.100    111.3000
!
!below angles with bigger spring constants on C atoms
```

```
!everywhere "5" added at the beginning, one was 100.00 now is 500.000
kCT2 kCT2 kCT2   558.350    113.60    11.16    2.56100
kCT3 kCT2 kCT2   558.000    115.00     8.00    2.56100
HA   kCT3 kCT2   534.600    110.10    22.53    2.17900
HA   kCT2 kCT3   534.600    110.10    22.53    2.17900
HA   kCT2 HA     535.500    109.00     5.40    1.80200
HA   kCT2 kCT2   526.500    110.10    22.53    2.17900
HA   kCT3 HA     535.500    108.40     5.40    1.80200
kOH1 kCT2 kCT2   575.700    110.1000
H    kOH1 kCT2   557.500    106.0000
kOH1 kCT2 HA     545.900    108.8900
kNH3 kCT2 kCT2   567.700    110.0000
kHC  kNH3 kCT2   530.000    109.50    20.00    2.07400
kNH3 kCT2 HA     545.000    107.50    35.00    2.10100
kHC  kNH3 kHC    544.000    109.5000
kCT2 kCT2 kCC    552.000    108.0000
kOC  kCC  kCT2   540.000    118.00    50.00    2.38800
HA   kCT2 kCC    533.000    109.50    30.00    2.16300
kOC  kCC  kOC    500.000    124.00    70.00    2.22500
kS   kCT2 kCT2   558.000    114.5000
HS   kS   kCT2   538.800     95.0000
kS   kCT2 HA    546.100    111.3000
!
!HA is used instead of kHA to allow Shake-H
!end SAMS

DIHEDRALS

!V(dihedral) = Kchi(1 + cos(n(chi) - delta))
!
!Kchi: kcal/mole
!n: multiplicity
!delta: degrees
!
!atom types             Kchi    n   delta
!
!beginning of SAMs (according to existing amino acids)
!
kCT2  kCT2  kCT2  kCT2  0.1500  1      0.00
kCT3  kCT2  kCT2  kCT2  0.1500  1      0.00
kCT2  kCT2  kCT3  HA    0.1600  3      0.00 ! X    CT2  CT3  X
HA    kCT2  kCT2  HA    0.1950  3      0.00 ! X    CT2  CT2  X
kCT2  kCT2  kCT2  kOH1  0.1950  3      0.00 ! X    CT2  CT2  X
H     kOH1  kCT2  kCT2  0.4200  3      0.00
HA    kCT2  kOH1  H     0.1400  3      0.00 ! X    CT2  OH1  X
kCT2  kCT2  kCT2  kNH3  0.1950  3      0.00 ! X    CT2  CT2  X
kCT2  kCT2  kNH3  kHC   0.1000  3      0.00
HA    kCT2  kNH3  kHC   0.1000  3      0.00
kCT2  kCT2  kCT2  kCC   0.1950  3      0.00 ! X    CT2  CT2  X
kCT2  kCT2  kCC   kOC   0.0500  6    180.00 ! X    CT2  CC   X
HA    kCT2  kCC   kOC   0.0500  6    180.00 ! X    CT2  CC   X
kCT2  kCT2  kCT2  kS    0.1950  3      0.00 ! X    CT2  CT2  X
HS    kS    kCT2  kCT2  0.2700  3      0.00
HS    kS    kCT2  HA    0.2000  3      0.00
kS    kCT2  kCT2  HA    0.0100  3      0.00
kCT2  kCT2  kCT2  HA    0.0400  3      0.00
```

```
HA     kCT2   kCT2   kCT3   0.0400   3      0.00
HA     kCT2   kCT3   HA     0.0400   3      0.00
HA     kCT2   kCT2   kOH1   0.1950   3      0.00 ! X     CT2  CT2  X
HA     kCT2   kCT2   kNH3   0.1950   3      0.00 ! X     CT2  CT2  X
HA     kCT2   kCT2   kCC    0.0000   1      0.00 ! as for H    NH1  CT2  CC
!
!
!end SAMS

IMPROPER

!V(improper) = Kpsi(psi - psi0)**2
!
!Kpsi: kcal/mole/rad**2
!psi0: degrees
!note that the second column of numbers (0) is ignored
!
!atom types            Kpsi                   psi0
!

!
!beginning of SAMs (according to existing amino acids)
kCC   X     X      kCT2     96.0000          0       0.0000
HA    kCT2  kCT2   HA       20.0000          0       0.0000
HA    HA    kCT2   kCT2     20.0000          0     180.0000
!
!end SAMS

Lennard-Jones

!V(Lennard-Jones) = Eps,i,j[(Rmin,i,j/ri,j)**12 - 2(Rmin,i,j/ri,j)**6]
!
!epsilon: kcal/mole, Eps,i,j = sqrt(eps,i * eps,j)
!Rmin/2: A, Rmin,i,j = Rmin/2,i + Rmin/2,j
!
!atom   ignored    epsilon      Rmin/2   ignored    eps,1-4       Rmin/2,1-4
!

SI         0.0        -0.585      2.15
OK         0.0        -0.1521     1.77
SA         0.0        -0.05       4.00
OA         0.0        -0.25       3.50
HAS        0.0        -0.046000     0.224500 ! the same as in TIP3P
OAS        0.0        -0.152100     1.768200 ! the same as in TIP3P
!
!beginning of SAMs (according to existing amino acids)
!
kCT2   0.000000   -0.055000     2.175000   0.000000   -0.010000     1.900000
kCT3   0.000000   -0.080000     2.060000   0.000000   -0.010000     1.90000
!kHA    0.000000   -0.022000     1.320000
kOH1   0.000000   -0.152100     1.770000
kH     0.000000   -0.046000     0.224500
kNH3   0.000000   -0.200000     1.850000
kHC    0.000000   -0.046000     0.224500
kCC    0.000000   -0.070000     2.000000
kOC    0.000000   -0.120000     1.700000
```

```
kS     0.000000   -0.450000      2.000000
!kHS    0.000000   -0.100000      0.450000'
!
!end SAMS

!The most recent parameters file
ZN      0.000000   -0.250000      1.090000 ! ALLOW  ION
                 ! RHS March 18, 1990
FE      0.010000    0.000000      0.650000 ! ALLOW HEM
                 ! Heme (6-liganded): Iron atom (KK 05/13/91)
HE      0.000000   -0.021270      1.4800   !
                 ! helium, experimental pot. energy surface, adm jr., 12/95
NE      0.000000   -0.086000      1.5300
                 ! neon, semiempirical pot. energy surface, adm jr., 12/95
CLAL    0.000000   -0.030000      1.908200 ! chlorine from Jorgensen/BOSS
                 ! for choroacetaldehyde
DUM     0.000000   -0.000000      0.000000 !
                 ! dummy atom
AG        0.0       -4.56          1.4775 ! HH et al. (2008)
AL        0.0       -4.02          1.4625 ! HH et al. (2008)
AU        0.0       -5.29          1.4755 ! HH et al. (2008)
CU        0.0       -4.72          1.3080 ! HH et al. (2008)
NI        0.0       -5.65          1.2760 ! HH et al. (2008)
PB        0.0       -2.93          1.7825 ! HH et al. (2008)
PD        0.0       -6.15          1.4095 ! HH et al. (2008)
PT        0.0       -7.80          1.4225 ! HH et al. (2008)

HBOND CUTHB 0.5  ! If you want to do hbond analysis (only), then use
                 ! READ PARAM APPEND CARD
                 ! to append hbond parameters from the file: par_hbond.inp

END
```

A.5 Scripts

Below are given various scripts needed to produce the simulations. All files need to be executable.

A.5.1 Script 1

The following script (`script1.inp`) produces the necessary psf file for the pdb file containing only protein atoms.

Initially the script requires the name of the name of the topology file that will be used, in this case `top_filename.inp`. Then, the script changes the names of some residues and ions in order to be compatible with NAMD. Subsequently, the filename of the pdb that

will be used to calculate the psf file and the corresponding pdb file is inserted, in this case `FN_truncated.pdb`. Lastly, a desired filename for the resulted psf and pdb files is inserted, in this case `FN8_10.pdb`.

```
psfgen << ENDMOL

topology top_filename.inp

alias residue HIS HSD
alias atom ILE CD1 CD
alias residue HOH TIP3
alias atom HOH O OH2
alias residue NA SOD
alias residue CL CLA

segment PRO {
pdb FN_truncated.pdb
}

coordpdb FN_truncated.pdb PRO

writepsf FN8_10.psf

guesscoord

writepdb FN8_10.pdb

ENDMOL
```

A.5.2 Script 2

The following script (`ctrbox.tcl`) centres the water box.

```
# centre waterbox

proc ctrbox { in_psf in_pdb out_pfx } {

        resetpsf
        readpsf $in_psf
        coordpdb $in_pdb

        mol load psf $in_psf pdb $in_pdb

        set all [ atomselect top all ]
        set minmax [ measure minmax $all ]

        foreach {min max} $minmax { break }
        foreach {xmin ymin zmin} $min { break }
```

```
        foreach {xmax ymax zmax} $max { break }

        set mx [ expr $xmin + abs(($xmin - $xmax) / 2) ]
        set my [ expr $ymin + abs(($ymin - $ymax) / 2) ]
        set mz [ expr $zmin + abs(($zmin - $zmax) / 2) ]

        $all moveby [ vecsub {0 0 0} [list $mx $my $mz] ]

        foreach atom [$all get {segid resid name x y z}] {
                foreach {segid resid name x y z} $atom { break }
                coord $segid $resid $name [list $x $y $z]
        }

        writepsf $out_pfx.psf
        writepdb $out_pfx.pdb

        set minmax [ measure minmax $all ]
        foreach {min max} $minmax { break }
        foreach {xmin ymin zmin} $min { break }

          set vec1 [ expr 2 * abs($xmin) + 0.5 ]
          set vec2 [ expr 2 * abs($ymin) + 0.5 ]
          set vec3 [ expr 2 * abs($zmin) + 0.5 ]

        set fp [ open "$out_pfx.pdb" a+ ]
          puts $fp "REMARK cellBasisVector1     $vec1    0.0      0.0"
          puts $fp "REMARK cellBasisVector2     0.0      $vec2    0.0"
          puts $fp "REMARK cellBasisVector3     0.0      0.0      $vec3"
          puts $fp "REMARK cellOrigin           0.0      0.0      0.0"

        close $fp

        mol delete top
}
```

A.5.3 Script 3

The following script (`D0.inp`) is used for the water equilibration dynamics. For further information about the individual details refer to the NAMD website [284].

```
structure         FN_005M_SC.psf   #pdb file for protein, water, ions
coordinates       FN_005M_SC.pdb   #pdb file for protein, water, ions

paratypecharmm    on
parameters        par_filename.inp   #parameters file
exclude           scaled1-4
1-4scaling        1.0

switching         on
switchdist        10
```

```
cutoff          12
pairlistdist    14
margin          2
stepspercycle   20

wrapWater       on
wrapAll         on
rigidBonds      all

timestep 1.0   #in fs

outputenergies  100
outputtiming    100
binaryoutput    yes
outputname      FN_005M_PME_300K_D0   #output files name
dcdfreq         100

restartfreq     100000
restartname     rest_FN_005M_PME_300K_D0

temperature     300

PME             yes
PMEGridSpacing  1.0

langevin            on
langevinDamping     5
langevinTemp        300
langevinHydrogen    no

useFlexibleCell         no
useGroupPressure        yes

LangevinPiston          on
LangevinPistonTarget    1.01325
LangevinPistonPeriod    200
LangevinPistonDecay     100
LangevinPistonTemp      300

cellBasisVector1         110.75999450683594     0.0       0.0   #coordinates
cellBasisVector2         0.0      74.59300231933594       0.0   #taken from
cellBasisVector3         0.0      0.0      149.5709991455078     #SC file
cellOrigin               0.0      0.0      0.0

fixedAtoms      on
fixedAtomsFile  FN_005M_SCF.pdb   #fixed atoms
fixedAtomsCol   O

minimize 1000   #water minimization 1000 steps
run 100000      #heating water for 100 ps
```

A.5.4 Script 4

The following script (`D1.inp`) is used for the heating of the system dynamics, from 0 K up to the desired temperature (300 K). For further information about the individual details refer to the NAMD website [284].

```
structure          FN_005M_SC.psf
coordinates        FN_005M_SC.pdb
bincoordinates     FN_005M_PME_300K_D0.coor    #the last structure from
                                               #the water equilibration
paratypecharmm     on                          #stage
parameters         par_filename.inp
exclude            scaled1-4
1-4scaling         1.0

switching          on
switchdist         10
cutoff             12
pairlistdist       14
margin             0
stepspercycle      20

wrapWater          on
wrapAll            on
rigidBonds         all

timestep 1.0

outputenergies     100
outputtiming       100
binaryoutput       yes
outputname         FN_005M_PME_300K_D1
dcdfreq            100

temperature        0   #initial temperature

reassignFreq       1000
reassignIncr       10
reassignHold       300

#langevin              on
#langevinDamping       5
#langevinTemp          300
#langevinHydrogen      no

PME                yes
PMEGridSpacing     1.0

extendedSystem     FN_005M_PME_300K_D0.xsc

fixedAtoms         on
```

```
fixedAtomsFile   FN_005M_SCF.pdb
fixedAtomsCol    O


minimize 10000    #number of minimization steps
run 600000        #total simulation time (heating+equilibration)
```

A.5.5 Script 5

The following script (`D2.inp`) is used for the simulation steps. For further information about the individual details refer to the NAMD website [284].

```
structure          FN_005M_SC.psf
coordinates        FN_005M_SC.pdb
bincoordinates     FN_005M_PME_300K_D1.coor

paratypecharmm     on
parameters         par_filename.inp
exclude            scaled1-4
1-4scaling         1.0

switching          on
switchdist         10
cutoff             12
pairlistdist       14
margin             0
stepspercycle      20

wrapWater          on
wrapAll            on
rigidBonds         all

timestep  2.0

outputenergies     100
outputtiming       100
binaryoutput       yes
outputname         FN_005M_PME_300K_D2
dcdfreq            200
restartfreq        100000
restartname        rest_FN_005M_PME_300K_D2

binvelocities      FN_005M_PME_300K_D1.vel

PME                yes
fullElectFrequency 2
PMEGridSpacing     1.0

useGroupPressure      yes   ;
```

```
langevin              on
langevinDamping       5
langevinTemp          300
langevinHydrogen      no

fixedAtoms        on
fixedAtomsFile    FN_005M_SCF.pdb
fixedAtomsCol     O

extendedSystem    FN_005M_PME_300K_D1.xsc

run 5000000   #total simulation time 10ns
```

A.5.6 Script 6

The following script (`script6.inp`) merges the protein and the surface in one file and produces the necessary psf and pdb files. The input is similar to `script1.inp`.

```
psfgen << ENDMOL

topology top_filename.inp

alias residue HIS HSD
alias atom ILE CD1 CD
alias residue HOH TIP3
alias atom HOH O OH2
alias residue NA SOD
alias residue CL CLA

segment PRO {
pdb FN.pdb
}

segment SUR {
pdb Surface.pdb
}

segment ION {
pdb FN_005M_S_ions.pdb
}

coordpdb FN.pdb PRO
coordpdb Surface.pdb SUR
coordpdb FN_005M_S_ions.pdb

writepsf FN_Sur_Ions.psf

guesscoord

writepdb FN_Sur_Ions.pdb

ENDMOL
```

List of References

[1] N. Huebsch and D. J. Mooney, "Inspiration and application in the evolution of biomaterials," *Nature*, vol. 462, pp. 426–432, Nov 2009.

[2] *Biomaterials market by type of material - Global forecast to 2021*, 2016. Available at `http://www.marketsandmarkets.com/Market-Reports/biomaterials-393.html`.

[3] B. D. Ratner, A. S. Hoffman, F. J. Schoen, and J. E. Lemons, *Biomaterials science: an introduction to materials in medicine*. Academic Press, 2013.

[4] J. M. Anderson, "Biological Responses to Materials," *Annu. Rev. Mater. Res.*, vol. 31, pp. 81–110, Aug 2001.

[5] J. M. Anderson, A. Rodriguez, and D. T. Chang, "Foreign body reaction to biomaterials," *Semin. Immunol.*, vol. 20, pp. 86–100, Apr 2008.

[6] M. Nosonovsky and B. Bhushan, "Green tribology: principles, research areas and challenges," *Philos. Trans. R. Soc. A Math. Phys. Eng. Sci.*, vol. 368, pp. 4677–4694, Oct 2010.

[7] S. Hiromoto and S. Mischler, "The influence of proteins on the fretting-corrosion behaviour of a Ti6Al4V alloy," *Wear*, vol. 261, pp. 1002–1011, Nov 2006.

[8] Y. Yan, *Bio-tribocorrosion in biomaterial and medical implants*. Elsevier, 2013.

[9] Y. Yan, A. Neville, and D. Dowson, "Biotribocorrosion of CoCrMo orthopaedic implant materials - Assessing the formation and effect of the biofilm," *Tribol. Int.*, vol. 40, pp. 1492–1499, Oct 2007.

[10] J. Berg, J. Tymoczko, and L. Stryer, *Biochemistry*. W.H. Freeman and company, 2002.

[11] K. C. Dee, D. A. Puleo, and R. Bizios, *An introduction to tissue-biomaterial interactions*. John Wiley & Sons, Inc., 2002.

[12] A. Varki, R. D. Cummings, J. Esko, H. Freeze, P. Stanley, C. Bertozzi, G. Hart, and M. Etzler, *Essentials of glycobiology*. Cold Spring Harbor Laboratory Press, Dec 2017.

[13] E. Pearlstein, L. Gold, and A. Garcia-Pardo, "Fibronectin: a review of its structure and biological activity," *Mol. Cell. Biochem.*, vol. 29, pp. 103–128, Feb 1980.

[14] R. J. Bingham and J. R. Potts, "Fibronectin structure: a new piece of the puzzle emerges," *Structure*, vol. 18, pp. 660–661, Jun 2010.

[15] R. P. Mecham, *The extracellular matrix: an overview*. Springer, 2011.

[16] J. Pelta, H. Berry, G. C. Fadda, E. Pauthe, and D. Lairez, "Statistical conformation of human plasma fibronectin," *Biochemistry*, vol. 39, pp. 5146–5154, May 2000.

[17] J. R. Potts and I. D. Campbell, "Structure and function of fibronectin modules," *Matrix Biol.*, vol. 15, pp. 313–320, Nov 1996.

[18] D. J. Romberger, *Fibronectin*. Elsevier, 1997.

[19] K. A. Majorek, P. J. Porebski, A. Dayal, M. D. Zimmerman, K. Jablonska, A. J. Stewart, M. Chruszcz, and W. Minor, "Structural and immunologic characterization of bovine, horse, and rabbit serum albumins," *Mol. Immunol.*, vol. 52, pp. 174–182, Oct 2012.

[20] K. Kubiak-Ossowska, K. Tokarczyk, B. Jachimska, and P. A. Mulheran, "Bovine serum albumin adsorption at a silica surface explored by simulation and experiment," *J. Phys. Chem. B*, vol. 121, pp. 3975–3986, Apr 2017.

[21] S. Sugio, A. Kashima, S. Mochizuki, M. Noda, and K. Kobayashi, "Crystal structure of human serum albumin at 2.5 Å resolution," *Protein Eng. Des. Sel.*, vol. 12, pp. 439–446, Jun 1999.

[22] X. M. He and D. C. Carter, "Atomic structure and chemistry of human serum albumin," *Nature*, vol. 358, pp. 209–215, Jul 1992.

[23] M. Rothschild, M. Oratz, and S. Schreiber, "Serum albumin," *Hepatology*, vol. 8, pp. 385–401, Mar 1988.

[24] R. Requejo, T. R. Hurd, N. J. Costa, and M. P. Murphy, "Cysteine residues exposed on protein surfaces are the dominant intramitochondrial thiol and may protect against oxidative damage," *FEBS J.*, vol. 277, pp. 1465–1480, Mar 2010.

[25] Y. Yuan, X. Wang, B. Mei, D. Zhang, A. Tang, L. An, X. He, J. Jiang, and G. Liang, "Labeling thiols on proteins, living cells and tissues with enhanced emission induced by FRET," *Sci. Rep.*, vol. 3, p. 3523, Dec 2013.

[26] K. Siriwardana, A. Wang, M. Gadogbe, W. E. Collier, N. C. Fitzkee, and D. Zhang, "Studying the effects of cysteine residues on protein interactions with silver nanoparticles," *J. Phys. Chem. C*, vol. 119, pp. 2910–2916, Feb 2015.

[27] K. Velonia, "Protein-polymer amphiphilic chimeras: recent advances and future challenges," *Polym. Chem.*, vol. 1, no. 7, p. 944, 2010.

[28] S. Ariyasu, H. Hayashi, B. Xing, and S. Chiba, "Site-specific dual functionalization of cysteine residue in peptides and proteins with 2-azidoacrylates," *Bioconjug. Chem.*, vol. 28, pp. 897–902, Apr 2017.

[29] M. P. Gispert, A. P. Serro, R. Colaço, and B. Saramago, "Bovine serum albumin adsorption onto 316L stainless steel and alumina: a comparative study using depletion, protein radiolabeling, quartz crystal microbalance and atomic force microscopy," *Surf. Interface Anal.*, vol. 40, pp. 1529–1537, Dec 2008.

[30] S. D. Bruck, *Properties of biomaterials in the physiological environment.* Taylor & Francis Inc, 1980.

[31] D. F. Williams, *Definitions in biomaterials: proceedings of a consensus conference of the European society for biomaterials.* Elsevier, 1987.

[32] J. Y. Wong and J. D. Bronzino, *Biomaterials.* CRC Press, 2007.

[33] P. Vadgama, *Surfaces and interfaces for biomaterials.* Elsevier, 2005.

[34] F. Mahyudin, L. Widhiyanto, and H. Hermawan, "Biomaterials in orthopaedics," *Adv. Struct. Mater.*, vol. 58, pp. 161–181, July 2016.

[35] Y. Okazaki, T. Tateishi, and Y. Ito, "Corrosion resistance of implant alloys in pseudo physiological solution and role of alloying elements in passive films," *Mater. Trans. JIM*, vol. 38, no. 1, pp. 78–84, 1997.

[36] M. Niinomi, T. Narushima, and M. Nakai, eds., *Advances in metallic biomaterials*, vol. 3 of *Springer Series in Biomaterials Science and Engineering.* Berlin, Heidelberg: Springer Berlin Heidelberg, 2015.

[37] T. Hanawa, "Metal ion release from metal implants," *Mater. Sci. Eng. C*, vol. 24, pp. 745–752, Dec 2004.

[38] K. Firm, R. Boyer, and G. Welsch, *Materials properties handbook: titanium alloys.* ASM International, 1994.

[39] M. Niinomi, "Mechanical properties of biomedical titanium alloys," *Mater. Sci. Eng. A*, vol. 243, pp. 231–236, Mar 1998.

[40] S. Minagar, J. Wang, C. C. Berndt, E. P. Ivanova, and C. Wen, "Cell response of anodized nanotubes on titanium and titanium alloys," *J. Biomed. Mater. Res. Part A*, vol. 101A, pp. 2726–2739, Sep 2013.

[41] K. E. Heusler, D. Landolt, and S. Trasatti, "Electrochemical corrosion nomenclature," *J. Electroanal. Chem.*, vol. 274, no. 1-2, pp. 345–348, 1989.

[42] D. Landolt, *Corrosion and surface chemistry of metals*. EPFL press, 2007.

[43] S. Mischler, "Triboelectrochemical techniques and interpretation methods in tribocorrosion: a comparative evaluation," *Tribol. Int.*, vol. 41, pp. 573–583, Jul 2008.

[44] R. H. Brown and R. B. Mears, "The electrochemistry of corrosion," *Trans. Electrochem. Soc.*, vol. 74, no. 1, p. 495, 1938.

[45] D. Landolt and S. S. Mischler, *Tribocorrosion of passive metals and coatings*. Woodhead Pub, 2011.

[46] S. Barril, N. Debaud, S. Mischler, and D. Landolt, "A tribo-electrochemical apparatus for in vitro investigation of fretting-corrosion of metallic implant materials," *Wear*, vol. 252, pp. 744–754, May 2002.

[47] A. Vieira, A. Ribeiro, L. Rocha, and J. Celis, "Influence of pH and corrosion inhibitors on the tribocorrosion of titanium in artificial saliva," *Wear*, vol. 261, pp. 994–1001, Nov 2006.

[48] Z. Panossian, L. Mariaca, M. Morcillo, S. Flores, J. Rocha, J. Peña, F. Herrera, F. Corvo, M. Sanchez, O. Rincon, G. Pridybailo, and J. Simancas, "Steel cathodic protection afforded by zinc, aluminium and zinc/aluminium alloy coatings in the atmosphere," *Surf. Coatings Technol.*, vol. 190, pp. 244–248, Jan 2005.

[49] P. Pedeferri, "Cathodic protection and cathodic prevention," *Constr. Build. Mater.*, vol. 10, pp. 391–402, Jul 1996.

[50] A. I. Munoz and S. Mischler, "Interactive effects of albumin and phosphate ions on the corrosion of CoCrMo implant alloy," *J. Electrochem. Soc.*, vol. 154, no. 10, pp. C562–C570, 2007.

[51] M. Khan, R. Williams, and D. WIliams, "Conjoint corrosion and wear in titanium alloys," *Biomaterials*, vol. 20, pp. 765–772, Apr 1999.

[52] T. Hanawa, Y. Kohayama, S. Hiromoto, and A. Yamamoto, "Effects of biological factors on the repassivation current of titanium," *Mater. Trans.*, vol. 45, no. 5, pp. 1635–1639, 2004.

[53] D. Sun, J. A. Wharton, and R. J. K. Wood, "Effects of proteins and pH on tribocorrosion performance of cast CoCrMo - a combined electrochemical and tribological study," *Tribol. - Mater. Surfaces Interfaces*, vol. 2, pp. 150–160, Sep 2008.

[54] W. Senaratne, L. Andruzzi, and C. K. Ober, "Self-assembled monolayers and polymer brushes in biotechnology: current applications and future perspectives," *Biomacromolecules*, vol. 6, pp. 2427–2448, Sep 2005.

[55] A. Ulman, "Formation and structure of self-assembled monolayers," *Chem. Rev.*, vol. 96, pp. 1533–1554, Jan 1996.

[56] J. C. Love, L. A. Estroff, J. K. Kriebel, R. G. Nuzzo, and G. M. Whitesides, "Self-assembled monolayers of thiolates on metals as a form of nanotechnology," *Chem. Rev.*, vol. 105, pp. 1103–1170, Apr 2005.

[57] E. Pensa, E. Cortés, G. Corthey, P. Carro, C. Vericat, M. H. Fonticelli, G. Benítez, A. A. Rubert, and R. C. Salvarezza, "The chemistry of the sulfur-gold interface: in search of a unified model," *Acc. Chem. Res.*, vol. 45, pp. 1183–1192, Aug 2012.

[58] F. Khan, M. Tanaka, and S. R. Ahmad, "Fabrication of polymeric biomaterials: a strategy for tissue engineering and medical devices," *J. Mater. Chem. B*, vol. 3, no. 42, pp. 8224–8249, 2015.

[59] M. Ozboyaci, D. B. Kokh, S. Corni, and R. C. Wade, "Modeling and simulation of protein-surface interactions: achievements and challenges," *Q. Rev. Biophys.*, vol. 49, p. 45, Jan 2016.

[60] W. Norde, "Driving forces for protein adsorption at solid surfaces," *Macromol. Symp.*, vol. 103, pp. 5–18, Jan 1996.

[61] S. L. Hirsh, D. R. McKenzie, N. J. Nosworthy, J. A. Denman, O. U. Sezerman, and M. M. Bilek, "The Vroman effect: competitive protein exchange with dynamic multilayer protein aggregates," *Colloids Surfaces B Biointerfaces*, vol. 103, pp. 395–404, Mar 2013.

[62] S. F. Sun, *Physical chemistry of macromolecules*. John Wiley & Sons, Inc., 2004.

[63] Y. Wang, C. Li, and G. J. Pielak, "Effects of proteins on protein diffusion," *J. Am. Chem. Soc.*, vol. 132, pp. 9392–9397, Jul 2010.

[64] Patiha, E. Heraldy, Y. Hidayat, and M. Firdaus, "The Langmuir isotherm adsorption equation: the monolayer approach," *IOP Conf. Ser. Mater. Sci. Eng.*, vol. 107, p. 012067, Feb 2016.

[65] R. A. Latour, "The langmuir isotherm: A commonly applied but misleading approach for the analysis of protein adsorption behavior," *J. Biomed. Mater. Res. Part A*, vol. 103, pp. 949–958, Mar 2015.

[66] P. Koutsoukos, W. Norde, and J. Lyklema, "Protein adsorption on hematite (α-Fe2O3) surfaces," *J. Colloid Interface Sci.*, vol. 95, pp. 385–397, Oct 1983.

[67] M. Rabe, D. Verdes, and S. Seeger, "Understanding protein adsorption phenomena at solid surfaces," *Adv. Colloid Interface Sci.*, vol. 162, pp. 87–106, Feb 2011.

[68] Y. Zhang and P. Cremer, "Interactions between macromolecules and ions: the Hofmeister series," *Curr. Opin. Chem. Biol.*, vol. 10, pp. 658–663, Dec 2006.

[69] C. A. K. Harvey Lodish, Arnold Berk, *Molecular cell biology*. W. H. Freeman, 2016.

[70] D. Voet and J. G. Voet, *Biochemistry*. Cambridge University Press, 2015.

[71] A. Karshikoff, *Non-covalent interactions in proteins*. Imperial College Press, 2006.

[72] G. Binnig, C. F. Quate, and C. Gerber, "Atomic force microscope," *Phys. Rev. Lett.*, vol. 56, pp. 930–933, Mar 1986.

[73] P. C. Braga and D. Ricci, *Atomic force microscopy.* Humana press, 2003.

[74] P. Frederix, B. Hoogenboom, D. Fotiadis, D. Müller, and A. Engel, "Atomic force microscopy of biological samples," *MRS Bull.*, vol. 29, pp. 449–455, Jul 2004.

[75] Y. L. Lyubchenko, "Preparation of DNA and nucleoprotein samples for AFM imaging," *Micron*, vol. 42, pp. 196–206, Feb 2011.

[76] H. G. Hansma, J. Vesenka, C. Siegerist, G. Kelderman, H. Morrett, R. L. Sinsheimer, V. Elings, C. Bustamante, and P. K. Hansma, "Reproducible imaging and dissection of plasmid DNA under liquid with the atomic force microscope," *Science*, vol. 256, pp. 1180–1184, May 1992.

[77] Y. L. Lyubchenko and L. S. Shlyakhtenko, "Visualization of supercoiled DNA with atomic force microscopy in situ," *Proc. Natl. Acad. Sci.*, vol. 94, pp. 496–501, Jan 1997.

[78] K. Vallières, P. Chevallier, C. Sarra-Bournet, S. Turgeon, and G. Laroche, "AFM imaging of immobilized fibronectin: does the surface conjugation scheme affect the protein orientation/conformation?," *Langmuir*, vol. 23, pp. 9745–9751, Sep 2007.

[79] C. González-García, S. R. Sousa, D. Moratal, P. Rico, and M. Salmerón-Sánchez, "Effect of nanoscale topography on fibronectin adsorption, focal adhesion size and matrix organisation," *Colloids Surfaces B Biointerfaces*, vol. 77, pp. 181–190, Jun 2010.

[80] M. Bergkvist, J. Carlsson, and S. Oscarsson, "Surface-dependent conformations of human plasma fibronectin adsorbed to silica, mica, and hydrophobic surfaces, studied with use of Atomic Force Microscopy," *J. Biomed. Mater. Res.*, vol. 64A, pp. 349–356, Feb 2003.

[81] A. Orasanu-Gourlay and R. Bradley, "Protein adsorption by basal plane graphite surfaces: molecular images and nano-structured films," *Adsorpt. Sci. Technol.*, vol. 24, pp. 117–130, Mar 2006.

[82] J. R. Hull, G. S. Tamura, and D. G. Castner, "Structure and reactivity of adsorbed fibronectin films on mica," *Biophys. J.*, vol. 93, pp. 2852–2860, Oct 2007.

[83] S. G. Kaminskyj and T. E. Dahms, "High spatial resolution surface imaging and analysis of fungal cells using SEM and AFM," *Micron*, vol. 39, pp. 349–361, Jun 2008.

[84] L. Chopinet, C. Formosa, M. Rols, R. Duval, and E. Dague, "Imaging living cells surface and quantifying its properties at high resolution using AFM in QI mode," *Micron*, vol. 48, pp. 26–33, May 2013.

[85] D. J. Müller and Y. F. Dufrêne, "Atomic force microscopy as a multifunctional molecular toolbox in nanobiotechnology," *Nat. Nanotechnol.*, vol. 3, pp. 261–269, May 2008.

[86] H. Yamashita, A. Taoka, T. Uchihashi, T. Asano, T. Ando, and Y. Fukumori, "Single-molecule imaging on living bacterial cell surface by high-speed AFM," *J. Mol. Biol.*, vol. 422, pp. 300–309, Sep 2012.

[87] D. Fotiadis, S. Scheuring, S. A. Müller, A. Engel, and D. J. Müller, "Imaging and manipulation of biological structures with the AFM," *Micron*, vol. 33, pp. 385–397, Feb 2002.

[88] H. Wang, X. Hao, Y. Shan, J. Jiang, M. Cai, and X. Shang, "Preparation of cell membranes for high resolution imaging by AFM," *Ultramicroscopy*, vol. 110, pp. 305–312, Mar 2010.

[89] E. Florin, V. Moy, and H. Gaub, "Adhesion forces between individual ligand-receptor pairs," *Science*, vol. 264, pp. 415–417, Apr 1994.

[90] M. Pfreundschuh, D. Alsteens, R. Wieneke, C. Zhang, S. R. Coughlin, R. Tampé, B. K. Kobilka, and D. J. Müller, "Identifying and quantifying two ligand-binding sites while imaging native human membrane receptors by AFM," *Nat. Commun.*, vol. 6, p. 8857, Nov 2015.

[91] P. Hinterdorfer, W. Baumgartner, H. J. Gruber, K. Schilcher, and H. Schindler, "Detection and localization of individual antibody-antigen recognition events by atomic force microscopy," *Proc. Natl. Acad. Sci.*, vol. 93, pp. 3477–3481, Apr 1996.

[92] T. Boland and B. D. Ratner, "Direct measurement of hydrogen bonding in DNA nucleotide bases by atomic force microscopy.," *Proc. Natl. Acad. Sci.*, vol. 92, pp. 5297–5301, Jun 1995.

[93] M. Sotomayor and K. Schulten, "Single-molecule experiments in vitro and in silico," *Science*, vol. 316, pp. 1144–1148, May 2007.

[94] C. L. Frewin, *Atomic force microscopy investigations into biology - from cell to protein*. InTech, 2012.

[95] A. Baró and R. Reifenberger, *Atomic force microscopy in liquid: biological applications*. Wiley-VCH, 2012.

[96] C. T. Gibson, G. S. Watson, and S. Myhra, "Lateral force microscopy - a quantitative approach," *Wear*, vol. 213, pp. 72–79, Dec 1997.

[97] W. R. Bowen and N. Hilal, *Atomic force microscopy in process engineering : introduction to AFM for improved processes and products*. Butterworth-Heinemann, 2009.

[98] W. Han, S. M. Lindsay, and T. Jing, "A magnetically driven oscillating probe microscope for operation in liquids," *Appl. Phys. Lett.*, vol. 69, pp. 4111–4113, Dec 1996.

[99] T. Fukuma, Y. Ueda, S. Yoshioka, and H. Asakawa, "Atomic-scale distribution of water molecules at the mica-water interface visualized by three-dimensional scanning force microscopy," *Phys. Rev. Lett.*, vol. 104, p. 016101, Jan 2010.

[100] J. Tamayo, A. Humphris, R. Owen, and M. Miles, "High-Q dynamic force microscopy in liquid and its application to living cells," *Biophys. J.*, vol. 81, pp. 526–537, Jul 2001.

[101] S. W. Stahl, E. M. Puchner, and H. E. Gaub, "Photothermal cantilever actuation for fast single-molecule force spectroscopy," *Rev. Sci. Instrum.*, vol. 80, p. 073702, Jul 2009.

[102] V. Bellitto and C. C. By, *Atomic force microscopy - imaging, measuring and manipulating surfaces at the atomic scale*. InTech, 2012.

[103] H. J. Butt, B. Cappella, and M. Kappl, "Force measurements with the atomic force microscope: technique, interpretation and applications," *Surf. Sci. Rep.*, vol. 59, pp. 1–152, Oct 2005.

[104] J. L. Hutter and J. Bechhoefer, "Calibration of atomic force microscope tips," *Rev. Sci. Instrum.*, vol. 64, pp. 1868–1873, Jul 1993.

[105] F. Rusmini, Z. Zhong, and J. Feijen, "Protein immobilization strategies for protein biochips," *Biomacromolecules*, vol. 8, pp. 1775–1789, Jun 2007.

[106] G. Sauerbrey, "Verwendung von schwingquarzen zur wagung dunner schichten und zur mikrowagung," *Zeitschrift fur Phys.*, vol. 155, pp. 206–222, Apr 1959.

[107] K. A. Marx, "Quartz crystal microbalance: a useful tool for studying thin polymer films and complex biomolecular systems at the solution-surface interface," *Biomacromolecules*, vol. 4, pp. 1099–1120, Sep 2003.

[108] A. L. Schofield, T. R. Rudd, D. Martin, D. G. Fernig, and C. Edwards, "Real-time monitoring of the development and stability of biofilms of Streptococcus mutans using

the quartz crystal microbalance with dissipation monitoring," *Biosens. Bioelectron.*, vol. 23, pp. 407–413, Oct 2007.

[109] V. Reipa, J. Almeida, and K. D. Cole, "Long-term monitoring of biofilm growth and disinfection using a quartz crystal microbalance and reflectance measurements," *J. Microbiol. Methods*, vol. 66, pp. 449–459, Sep 2006.

[110] T. Hianik, V. Ostatná, M. Sonlajtnerova, and I. Grman, "Influence of ionic strength, pH and aptamer configuration for binding affinity to thrombin," *Bioelectrochemistry*, vol. 70, pp. 127–133, Jan 2007.

[111] R. Yamasaki, M. Ito, B. Lee, H. Jung, H. Lee, and T. Kawai, "Single probe nucleic acid immobilization on chemically modified single protein by controlling ionic strength and pH," *Anal. Chim. Acta*, vol. 603, pp. 76–81, Nov 2007.

[112] V. Heitmann and J. Wegener, "Monitoring cell adhesion by piezoresonators: impact of increasing oscillation amplitudes," *Anal. Chem.*, vol. 79, pp. 3392–3400, May 2007.

[113] S. Hong, E. Ergezen, R. Lec, and K. A. Barbee, "Real-time analysis of cell-surface adhesive interactions using thickness shear mode resonator," *Biomaterials*, vol. 27, pp. 5813–5820, Dec 2006.

[114] N. F. Steinmetz, K. C. Findlay, T. R. Noel, R. Parker, G. P. Lomonossoff, and D. J. Evans, "Layer-by-layer assembly of viral nanoparticles and polyelectrolytes: the film architecture is different for spheres versus rods," *ChemBioChem*, vol. 9, pp. 1662–1670, Jul 2008.

[115] B. Yuan, M. Pham, and T. H. Nguyen, "Deposition kinetics of bacteriophage MS2 on a silica surface coated with natural organic matter in a radial stagnation point flow cell," *Environ. Sci. Technol.*, vol. 42, pp. 7628–7633, Oct 2008.

[116] R. E. Hamlin, T. L. Dayton, L. E. Johnson, and M. S. Johal, "A QCM study of the immobilization of β-Galactosidase on polyelectrolyte surfaces: effect of the terminal polyion on enzymatic surface activity," *Langmuir*, vol. 23, pp. 4432–4437, Apr 2007.

[117] E. Briand, M. Salmain, C. Compère, and C.-M. Pradier, "Anti-rabbit immunoglobulin G detection in complex medium by PM-RAIRS and QCM," *Biosens. Bioelectron.*, vol. 22, pp. 2884–2890, Jun 2007.

[118] V. Payet, T. Dini, S. Brunner, A. Galtayries, I. Frateur, and P. Marcus, "Pre-treatment of titanium surfaces by fibronectin: in situ adsorption and effect of concentration," *Surf. Interface Anal.*, vol. 42, pp. 457–461, Apr 2010.

[119] Y. Kusakawa, E. Yoshida, and T. Hayakawa, "Protein adsorption to titanium and zirconia using a quartz crystal microbalance method," *Biomed Res. Int.*, vol. 2017, pp. 1–8, 2017.

[120] D. A. Buttry and M. D. Ward, "Measurement of interfacial processes at electrode surfaces with the electrochemical quartz crystal microbalance," *Chem. Rev.*, vol. 92, pp. 1355–1379, Sep 1992.

[121] M. Herranen and J. O. Carlsson, "An electrochemical quartz crystal microbalance and in situ SFM study of Ti in sulphuric acid," *Corros. Sci.*, vol. 43, pp. 365–379, Feb 2001.

[122] A. I. Muñoz and S. Mischler, "Electrochemical quartz crystal microbalance and X-Ray photoelectron spectroscopy study of cathodic reactions in bovine serum albumin containing solutions on a physical vapour deposition-CoCrMo biomedical alloy," *Electrochim. Acta*, vol. 180, pp. 96–103, Oct 2015.

[123] C. V. Vidal, A. I. Munoz, C. O. A. Olsson, and S. Mischler, "Passivation of a CoCrMo PVD alloy with biomedical composition under simulated physiological conditions studied by EQCM and XPS," *J. Electrochem. Soc.*, vol. 159, pp. C233–C243, Mar 2012.

[124] A. Janshoff, H. J. Galla, and C. Steinem, "Piezoelectric mass-sensing devices as biosensors - an alternative to optical biosensors?," *Angew. Chemie*, vol. 39, pp. 4004–4032, Nov 2000.

[125] D. Johannsmann, *The quartz crystal microbalance in soft matter research*. Springer International Publishing, 2015.

[126] E. Fields and S. E. Fields, *Encyclopedia of applied electrochemistry*. Springer New York, 2014.

[127] Z. Ali, "Acoustic wave mass sensors," *J. Therm. Anal. Calorim.*, vol. 55, pp. 397–412, Mar 1999.

[128] L. Wilches, J. Uribe, and A. Toro, "Wear of materials used for artificial joints in total hip replacements," *Wear*, vol. 265, pp. 143–149, Jun 2008.

[129] N. More, N. Diomidis, S. Paul, M. Roy, and S. Mischler, "Tribocorrosion behavior of β titanium alloys in physiological solutions containing synovial components," *Mater. Sci. Eng. C*, vol. 31, pp. 400–408, Mar 2011.

[130] A. C. Alves, F. Oliveira, F. Wenger, P. Ponthiaux, J.-P. Celis, and L. A. Rocha, "Tribocorrosion behaviour of anodic treated titanium surfaces intended for dental implants," *J. Phys. D Appl. Phys.*, vol. 46, pp. 404001–9, Sep 2013.

[131] N. Diomidis, S. Mischler, N. More, and M. Roy, "Tribo-electrochemical characterization of metallic biomaterials for total joint replacement," *Acta Biomater.*, vol. 8, pp. 852–859, Feb 2012.

[132] W. Murphy, J. Black, and G. Hastings, *Handbook of biomaterial properties*. Springer, 2016.

[133] H. F. Chen, "Computational study of the binding mode of epidermal growth factor receptor kinase inhibitors," *Chem. Biol. Drug Des.*, vol. 71, pp. 434–446, May 2008.

[134] B. Fischer, K. Fukuzawa, and W. Wenzel, "Receptor-specific scoring functions derived from quantum chemical models improve affinity estimates for in-silico drug discovery," *Proteins Struct. Funct. Bioinforma.*, vol. 70, pp. 1264–1273, Sep 2007.

[135] L. P. Ehrlich, M. Nilges, and R. C. Wade, "The impact of protein flexibility on protein-protein docking," *Proteins Struct. Funct. Bioinforma.*, vol. 58, pp. 126–133, Oct 2004.

[136] S. Costantini, G. Colonna, and A. Facchiano, "Simulation of conformational changes occurring when a protein interacts with its receptor," *Comput. Biol. Chem.*, vol. 31, pp. 196–206, Jun 2007.

[137] P. J. Bond and M. S. P. Sansom, "Insertion and assembly of membrane proteins via simulation," *J. Am. Chem. Soc.*, vol. 128, pp. 2697–2704, Mar 2006.

[138] M. T. Hyvönen, K. Öörni, P. T. Kovanen, and M. Ala-Korpela, "Changes in a phospholipid bilayer induced by the hydrolysis of a phospholipase A2 enzyme: a molecular dynamics simulation study," *Biophys. J.*, vol. 80, pp. 565–578, Feb 2001.

[139] S. Höfinger, B. Almeida, and U. H. E. Hansmann, "Parallel tempering molecular dynamics folding simulation of a signal peptide in explicit water," *Proteins Struct. Funct. Bioinforma.*, vol. 68, pp. 662–669, May 2007.

[140] S. Jang, E. Kim, and Y. Pak, "All-atom level direct folding simulation of a $\beta\beta\alpha$ miniprotein," *J. Chem. Phys.*, vol. 128, p. 105102, Mar 2008.

[141] R. D. Schaeffer, A. Fersht, and V. Daggett, "Combining experiment and simulation in protein folding: closing the gap for small model systems," *Curr. Opin. Struct. Biol.*, vol. 18, pp. 4–9, Feb 2008.

[142] M. Karplus and J. A. McCammon, "Molecular dynamics simulations of biomolecules," *Nat. Struct. Biol.*, vol. 9, pp. 646–652, Sep 2002.

[143] R. A. Latour Jr., "Molecular modeling of biomaterial surfaces," *Curr. Opin. Solid State Mater. Sci.*, vol. 4, pp. 413–417, Aug 1999.

[144] Q. Wang, M. h. Wang, K. f. Wang, Y. Liu, H. p. Zhang, X. Lu, and X. d. Zhang, "Computer simulation of biomolecule-biomaterial interactions at surfaces and interfaces," *Biomed. Mater.*, vol. 10, p. 032001, Jun 2015.

[145] D. R. Lewis, V. Kholodovych, M. D. Tomasini, D. Abdelhamid, L. K. Petersen, W. J. Welsh, K. E. Uhrich, and P. V. Moghe, "In silico design of anti-atherogenic biomaterials," *Biomaterials*, vol. 34, pp. 7950–7959, Oct 2013.

[146] C. Peng, J. Liu, D. Zhao, and J. Zhou, "Adsorption of hydrophobin on different self-assembled monolayers: the role of the hydrophobic dipole and the electric dipole," *Langmuir*, vol. 30, pp. 11401–11411, Sep 2014.

[147] K. Kubiak-Ossowska, B. Jachimska, and P. A. Mulheran, "How negatively charged proteins adsorb to negatively charged surfaces: a molecular dynamics study of BSA adsorption on silica," *J. Phys. Chem. B*, vol. 120, pp. 10463–10468, Oct 2016.

[148] A. Wei and C. Deng, "Adsorption of protein on a Au surface studied by all-atom atomistic simulations," *J. Phys. Chem. C*, vol. 120, pp. 13103–13112, Jun 2016.

[149] C. Liao, Y. Xie, and J. Zhou, "Computer simulations of fibronectin adsorption on hydroxyapatite surfaces," *RSC Adv.*, vol. 4, p. 15759, Mar 2014.

[150] H. Wang, Y. He, B. D. Ratner, and S. Jiang, "Modulating cell adhesion and spreading by control of FnIII7-10 orientation on charged self-assembled monolayers (SAMs) of alkanethiolates," *J. Biomed. Mater. Res. Part A*, vol. 77A, pp. 672–678, Jun 2006.

[151] V. P. Raut, M. A. Agashe, S. J. Stuart, and R. A. Latour, "Molecular dynamics simulations of peptide-surface interactions," *Langmuir*, vol. 21, pp. 1629–1639, Feb 2005.

[152] K. Kubiak-Ossowska and P. A. Mulheran, "What governs protein adsorption and immobilization at a charged solid surface?," *Langmuir*, vol. 26, pp. 7690–7694, Jun 2010.

[153] M. Panos, T. Z. Sen, and M. G. Ahunbay, "Molecular simulation of fibronectin adsorption onto polyurethane surfaces," *Langmuir*, vol. 28, pp. 12619–12628, Aug 2012.

[154] A. J. Bordner, C. N. Cavasotto, and R. A. Abagyan, "Direct derivation of van der Waals force field parameters from quantum mechanical interaction energies," *J. Phys. Chem. B*, vol. 107, pp. 9601–9609, Sep 2003.

[155] D. A. Puleo and R. Bizios, *Biological interactions on materials surfaces*. Springer, 2009.

[156] J. C. Phillips, R. Braun, W. Wang, J. Gumbart, E. Tajkhorshid, E. Villa, C. Chipot, R. D. Skeel, L. Kalé, and K. Schulten, "Scalable molecular dynamics with NAMD," *J. Comput. Chem.*, vol. 26, pp. 1781–1802, Dec 2005.

[157] R. A. Latour, "Molecular simulation of protein-surface interactions: benefits, problems, solutions, and future directions (Review)," *Biointerphases*, vol. 3, pp. FC2–FC12, Sep 2008.

[158] U. Essmann, L. Perera, M. L. Berkowitz, T. Darden, H. Lee, and L. G. Pedersen, "A smooth particle mesh Ewald method," *J. Chem. Phys.*, vol. 103, pp. 8577–8593, Nov 1995.

[159] S. W. de Leeuw, J. W. Perram, and E. R. Smith, "Simulation of electrostatic systems in periodic boundary conditions. I. lattice sums and dielectric constants," *Proc. R. Soc. A Math. Phys. Eng. Sci.*, vol. 373, pp. 27–56, Oct 1980.

[160] C. Bertonati, B. Honig, and E. Alexov, "Poisson-Boltzmann calculations of non-specific salt effects on protein-protein binding free energies," *Biophys. J.*, vol. 92, pp. 1891–1899, Mar 2007.

[161] A. D. MacKerell, D. Bashford, M. Bellott, R. L. Dunbrack, J. D. Evanseck, M. J. Field, S. Fischer, J. Gao, H. Guo, S. Ha, D. Joseph-McCarthy, L. Kuchnir, K. Kuczera, F. T. K. Lau, C. Mattos, S. Michnick, T. Ngo, D. T. Nguyen, B. Prodhom, W. E. Reiher, B. Roux, M. Schlenkrich, J. C. Smith, R. Stote, J. Straub, M. Watanabe, J. Wiórkiewicz-Kuczera, D. Yin, and M. Karplus, "All-atom empirical potential for molecular modeling and dynamics studies of proteins," *J. Phys. Chem. B*, vol. 102, pp. 3586–3616, Apr 1998.

[162] S. Bauer, P. Schmuki, K. von der Mark, and J. Park, "Engineering biocompatible implant surfaces. Part I: Materials and surfaces," *Prog. Mater. Sci.*, vol. 58, pp. 261–326, Oct 2012.

[163] H. P. Erickson, "Reversible unfolding of fibronectin type III and immunoglobulin domains provides the structural basis for stretch and elasticity of titin and fibronectin.," *Proc. Natl. Acad. Sci. U. S. A.*, vol. 91, pp. 10114–8, Oct 1994.

[164] L. Liu, C. Qin, W. T. Butler, B. D. Ratner, and S. Jiang, "Controlling the orientation of bone osteopontin via its specific binding with collagen I to modulate osteoblast adhesion," *J. Biomed. Mater. Res. Part A*, vol. 80A, pp. 102–110, Jan 2007.

[165] Y. Arima and H. Iwata, "Effect of wettability and surface functional groups on protein adsorption and cell adhesion using well-defined mixed self-assembled monolayers," *Biomaterials*, vol. 28, pp. 3074–3082, Jul 2007.

[166] S. S. Cheng, K. K. Chittur, C. N. Sukenik, L. A. Culp, and K. Lewandowska, "The conformation of fibronectin on self-assembled monolayers with different surface composition: an FTIR/ATR study," *J. Colloid Interface Sci.*, vol. 162, pp. 135–143, Jan 1994.

[167] K. Prime and G. Whitesides, "Self-assembled organic monolayers: model systems for studying adsorption of proteins at surfaces," *Science*, vol. 252, pp. 1164–1167, May 1991.

[168] J. L. Eisenberg, J. L. Piper, and M. Mrksich, "Using self-assembled monolayers to model cell adhesion to the 9th and 10th type III domains of fibronectin," *Langmuir*, vol. 25, pp. 13942–13951, Dec 2009.

[169] E. Ostuni, L. Yan, and G. M. Whitesides, "The interaction of proteins and cells with self-assembled monolayers of alkanethiolates on gold and silver," *Colloids Surfaces B Biointerfaces*, vol. 15, pp. 3–30, Aug 1999.

[170] P. Y. Meadows and G. C. Walker, "Force microscopy studies of fibronectin adsorption and subsequent cellular adhesion to substrates with well-defined surface chemistries," *Langmuir*, vol. 21, pp. 4096–4107, Apr 2005.

[171] T. E. Benavidez, D. Torrente, M. Marucho, and C. D. Garcia, "Adsorption of soft and hard proteins onto OTCEs under the influence of an external electric field," *Langmuir*, vol. 31, pp. 2455–2462, Mar 2015.

[172] K. Kubiak-Ossowska, P. A. Mulheran, and W. Nowak, "Fibronectin module FN III 9 adsorption at contrasting solid model surfaces studied by atomistic molecular dynamics," *J. Phys. Chem. B*, vol. 118, pp. 9900–9908, Aug 2014.

[173] K. Kubiak-Ossowska, M. Cwieka, A. Kaczynska, B. Jachimska, and P. A. Mulheran, "Lysozyme adsorption at a silica surface using simulation and experiment: effects of pH on protein layer structure," *Phys. Chem. Chem. Phys.*, vol. 17, pp. 24070–24077, Aug 2015.

[174] P. A. Mulheran, D. J. Connell, and K. Kubiak-Ossowska, "Steering protein adsorption at charged surfaces: electric fields and ionic screening," *RSC Adv.*, vol. 6, pp. 73709–73716, Jul 2016.

[175] K. Wilson, S. J. Stuart, A. Garcia, and R. A. Latour, "A molecular modeling study of the effect of surface chemistry on the adsorption of a fibronectin fragment spanning the 7-10th type III repeats," *J. Biomed. Mater. Res.*, vol. 69A, pp. 686–698, Jun 2004.

[176] J. W. Shen, T. Wu, Q. Wang, and H. H. Pan, "Molecular simulation of protein adsorption and desorption on hydroxyapatite surfaces," *Biomaterials*, vol. 29, pp. 513–532, Feb 2008.

[177] W. Humphrey, A. Dalke, and K. Schulten, "VMD: Visual molecular dynamics," *J. Mol. Graph.*, vol. 14, pp. 33–38, Feb 1996.

[178] N. A. Vellore, J. A. Yancey, G. Collier, R. A. Latour, and S. J. Stuart, "Assessment of the transferability of a protein force field for the simulation of peptide-surface interactions," *Langmuir*, vol. 26, pp. 7396–7404, May 2010.

[179] D. J. Leahy, I. Aukhil, and H. P. Erickson, "2.0 Å crystal structure of a four-domain segment of human fibronectin encompassing the RGD loop and synergy region," *Cell*, vol. 84, pp. 155–164, Jan 1996.

[180] K. Kubiak-Ossowska, G. Burley, S. V. Patwardhan, and P. A. Mulheran, "Spontaneous membrane-translocating peptide adsorption at silica surfaces: a molecular dynamics study," *J. Phys. Chem. B*, vol. 117, pp. 14666–14675, Nov 2013.

[181] S. V. Patwardhan, F. S. Emami, R. J. Berry, S. E. Jones, R. R. Naik, O. Deschaume, H. Heinz, and C. C. Perry, "Chemistry of aqueous silica nanoparticle surfaces and the mechanism of selective peptide adsorption," *J. Am. Chem. Soc.*, vol. 134, pp. 6244–6256, Apr 2012.

[182] K. P. Fears, S. E. Creager, and R. A. Latour, "Determination of the surface pK of carboxylic- and amine-terminated alkanethiols using surface plasmon resonance spectroscopy," *Langmuir*, vol. 24, pp. 837–843, Feb 2008.

[183] A. Ulman, J. E. Eilers, and N. Tillman, "Packing and molecular orientation of alkanethiol monolayers on gold surfaces," *Langmuir*, vol. 5, pp. 1147–1152, Sep 1989.

[184] B. Gottenbos, H. C. van der Mei, F. Klatter, D. W. Grijpma, J. Feijen, P. Nieuwenhuis, and H. J. Busscher, "Positively charged biomaterials exert antimicrobial effects on gram-negative bacilli in rats," *Biomaterials*, vol. 24, pp. 2707–2710, Jul 2003.

[185] J. Kyte and R. F. Doolittle, "A simple method for displaying the hydropathic character of a protein," *J. Mol. Biol.*, vol. 157, pp. 105–132, May 1982.

[186] J. H. Lin, H. Y. Chang, W. L. Kao, K. Y. Lin, H. Y. Liao, Y. W. You, Y. T. Kuo, D. Y. Kuo, K. J. Chu, Y. H. Chu, and J. J. Shyue, "Effect of surface potential on extracellular matrix protein adsorption," *Langmuir*, vol. 30, pp. 10328–10335, Sep 2014.

[187] S. J. Knak Jensen, T.-H. Tang, and I. G. Csizmadia, "Hydrogen-bonding ability of a methyl group," *J. Phys. Chem. A*, vol. 107, pp. 8975–8979, Oct 2003.

[188] G. Papastavrou, S. Akari, and H. Möhwald, "Interactions between hydrophilic and hydrophobic surfaces on microscopic scale and the influence of air bubbles as observed by scanning force microscopy in aqueous and alcoholic mediums," *Europhys. Lett.*, vol. 52, pp. 551–556, Dec 2000.

[189] G. B. Sigal, M. Mrksich, and G. M. Whitesides, "Effect of surface wettability on the adsorption of proteins and detergents," *J. Am. Chem. Soc.*, vol. 120, pp. 3464–3473, Apr 1998.

[190] C. A. Scotchford, C. P. Gilmore, E. Cooper, G. J. Leggett, and S. Downes, "Protein adsorption and human osteoblast-like cell attachment and growth on alkylthiol on gold self-assembled monolayers," *J. Biomed. Mater. Res.*, vol. 59, pp. 84–99, Jan 2002.

[191] F. A. Denis, P. Hanarp, D. S. Sutherland, J. Gold, C. Mustin, P. G. Rouxhet, and Y. F. Dufrêne, "Protein adsorption on model surfaces with controlled nanotopography and chemistry," *Langmuir*, vol. 18, pp. 819–828, Feb 2002.

[192] P. Mandracci, F. Mussano, P. Rivolo, and S. Carossa, "Surface treatments and functional coatings for biocompatibility improvement and bacterial adhesion reduction in dental implantology," *Coatings*, vol. 6, p. 7, Jan 2016.

[193] P. Y. Meadows, J. E. Bemis, and G. C. Walker, "Single-molecule force spectroscopy of isolated and aggregated fibronectin proteins on negatively charged surfaces in aqueous liquids," *Langmuir*, vol. 19, pp. 9566–9572, Nov 2003.

[194] B. G. Keselowsky, D. M. Collard, and A. J. García, "Surface chemistry modulates fibronectin conformation and directs integrin binding and specificity to control cell adhesion," *J. Biomed. Mater. Res. Part A*, vol. 66A, pp. 247–259, Aug 2003.

[195] K. Michael, B. Keselowsky, V. Vernekar, R. Latour, and A. Garcia, "Conformational changes in fibronectin due to adsorption to well-defined surface chemistries," vol. 1, pp. 601–602, Oct 2002.

[196] K. E. Michael, V. N. Vernekar, B. G. Keselowsky, J. C. Meredith, R. A. Latour, and A. J. García, "Adsorption-induced conformational changes in fibronectin due to interactions with well-defined surface chemistries," *Langmuir*, vol. 19, pp. 8033–8040, Sep 2003.

[197] N. Pernodet, M. Rafailovich, J. Sokolov, D. Xu, N. L. Yang, and K. McLeod, "Fibronectin fibrillogenesis on sulfonated polystyrene surfaces," *J. Biomed. Mater. Res.*, vol. 64A, pp. 684–692, Mar 2003.

[198] R. B. Best, D. J. Brockwell, J. L. Toca-Herrera, A. W. Blake, D. Smith, S. E. Radford, and J. Clarke, "Force mode atomic force microscopy as a tool for protein folding studies," *Anal. Chim. Acta*, vol. 479, pp. 87–105, Mar 2003.

[199] N. I. Abu-Lail, T. Ohashi, R. L. Clark, H. P. Erickson, and S. Zauscher, "Understanding the elasticity of fibronectin fibrils: unfolding strengths of FN-III and GFP domains measured by single molecule force spectroscopy," *Matrix Biol.*, vol. 25, pp. 175–184, Apr 2006.

[200] F. Li, S. D. Redick, H. P. Erickson, and V. T. Moy, "Force measurements of the $\alpha 5\beta 1$ integrin-fibronectin interaction," *Biophys. J.*, vol. 84, pp. 1252–1262, Feb 2003.

[201] A. F. Oberhauser, C. Badilla-Fernandez, M. Carrion-Vazquez, and J. M. Fernandez, "The mechanical hierarchies of fibronectin observed with single-molecule AFM," *J. Mol. Biol.*, vol. 319, pp. 433–447, May 2002.

[202] M. Rief, M. Gautel, A. Schemmel, and H. E. Gaub, "The mechanical stability of immunoglobulin and fibronectin III domains in the muscle protein titin measured by atomic force microscopy," *Biophys. J.*, vol. 75, pp. 3008–3014, Dec 1998.

[203] L. Li, H. H. L. Huang, C. L. Badilla, and J. M. Fernandez, "Mechanical unfolding intermediates observed by single-molecule force spectroscopy in a fibronectin type III module," *J. Mol. Biol.*, vol. 345, pp. 817–826, Jan 2005.

[204] M. T. Dickerson, M. B. Abney, C. E. Cameron, M. Knecht, L. G. Bachas, and K. W. Anderson, "Fibronectin binding to the treponema pallidum adhesin protein fragment rTp0483 on functionalized self-assembled monolayers," *Bioconjug. Chem.*, vol. 23, pp. 184–195, Feb 2012.

[205] Sigma-Aldrich, "Preparing self-assembled monolayers (SAMs) a step-by-step guide for solution-based self-assembly," *Technical Bulletin AL-266*, 2017.

[206] Sigma-Aldrich, "Molecular self-assembly," *Mater. Matters*, vol. 1, no. 2, pp. 1–19, 2006.

[207] D. Y. Petrovykh, H. Kimura-Suda, A. Opdahl, L. J. Richter, M. J. Tarlov, and L. J. Whitman, "Alkanethiols on platinum: multicomponent self-assembled monolayers," *Langmuir*, vol. 22, pp. 2578–2587, Mar 2006.

[208] J. Hoypierres, V. Dulong, C. Rihouey, S. Alexandre, L. Picton, and P. Thébault, "Two methods for one-point anchoring of a linear polysaccharide on a gold surface," *Langmuir*, vol. 31, pp. 254–261, Jan 2015.

[209] Z. Wang, S. L. Nania, and S. K. Shaw, "Structure of aqueous water films on textured OH-terminated self-assembled monolayers," *Langmuir*, vol. 31, pp. 2382–2389, Mar 2015.

[210] H. J. Gruber, "Functionalization of AFM tips with tris-NTA for binding of His6-tagged proteins," pp. 1–11, 2008. Available at `http://citeseerx.ist.psu.edu/viewdoc/summary?doi=10.1.1.702.3616`.

[211] S. Biggs, P. Mulvaney, C. F. Zukoski, and F. Grieser, "Study of anion adsorption at the gold-aqueous solution interface by atomic force microscopy," *J. Am. Chem. Soc.*, vol. 116, pp. 9150–9157, Oct 1994.

[212] R. R. Kumal, T. E. Karam, and L. H. Haber, "Determination of the surface charge density of colloidal gold nanoparticles using second harmonic generation," *J. Phys. Chem. C*, vol. 119, pp. 16200–16207, Jul 2015.

[213] M. Kasuya, T. Sogawa, T. Masuda, T. Kamijo, K. Uosaki, and K. Kurihara, "Anion adsorption on gold electrodes studied by electrochemical surface forces measurement," *J. Phys. Chem. C*, vol. 120, pp. 15986–15992, Jul 2016.

[214] D. W. Thompson and I. R. Collins, "Electrical properties of the gold-aqueous solution interface," *J. Colloid Interface Sci.*, vol. 152, pp. 197–204, Aug 1992.

[215] M. A. Al-Ghobashy, "Electrophoretic behavior of charge regulated zwitter ionic buffers in covalently and dynamically coated fused silica capillaries," *Bull. Fac. Pharmacy, Cairo Univ.*, vol. 52, pp. 71–78, Jun 2014.

[216] Z. Zhang, M. R. Tomlinson, R. Golestanian, and M. Geoghegan, "The interfacial behaviour of single poly(N,N-dimethylacrylamide) chains as a function of pH," *Nanotechnology*, vol. 19, p. 035505, Jan 2008.

[217] T. E. Fisher, A. F. Oberhauser, M. Carrion-Vazquez, P. E. Marszalek, and J. M. Fernandez, "The study of protein mechanics with the atomic force microscope," *Trends Biochem. Sci.*, vol. 24, pp. 379–384, Oct 1999.

[218] M. Carrion-Vazquez, A. F. Oberhauser, S. B. Fowler, P. E. Marszalek, S. E. Broedel, J. Clarke, and J. M. Fernandez, "Mechanical and chemical unfolding of a single protein: A comparison," *Proc. Natl. Acad. Sci.*, vol. 96, pp. 3694–3699, Mar 1999.

[219] S. Kienle, T. Pirzer, S. Krysiak, M. Geisler, and T. Hugel, "Measuring the interaction between ions, biopolymers and interfaces - one polymer at a time," *Faraday Discuss.*, vol. 160, pp. 329–340, Jun 2013.

[220] D. Horinek, A. Serr, M. Geisler, T. Pirzer, U. Slotta, S. Q. Lud, J. A. Garrido, T. Scheibel, T. Hugel, and R. R. Netz, "Peptide adsorption on a hydrophobic surface results from an interplay of solvation, surface, and intrapeptide forces," *Proc. Natl. Acad. Sci.*, vol. 105, pp. 2842–2847, Feb 2008.

[221] J. B. Lhoest, E. Detrait, P. van den Bosch de Aguilar, and P. Bertrand, "Fibronectin adsorption, conformation, and orientation on polystyrene substrates studied by radiolabeling, XPS, and ToF SIMS," *J. Biomed. Mater. Res.*, vol. 41, pp. 95–103, Jul 1998.

[222] B. Boughton and A. Simpson, "The biochemical and functional heterogeneity of circulating human plasma fibronectin," *Biochem. Biophys. Res. Commun.*, vol. 119, pp. 1174–1180, Mar 1984.

[223] D. E. MacDonald, B. Markovic, M. Allen, P. Somasundaran, and A. L. Boskey, "Surface analysis of human plasma fibronectin adsorbed to commercially pure titanium materials.," *J. Biomed. Mater. Res.*, vol. 41, pp. 120–30, Jul 1998.

[224] M. Roach, "Base metal alloys used for dental restorations and implants," *Dent. Clin. North Am.*, vol. 51, pp. 603–627, Jul 2007.

[225] M. Koike and H. Fujii, "The corrosion resistance of pure titanium in organic acids," *Biomaterials*, vol. 22, pp. 2931–2936, Nov 2001.

[226] G. Wang, J. Li, K. Lv, W. Zhang, X. Ding, G. Yang, X. Liu, and X. Jiang, "Surface thermal oxidation on titanium implants to enhance osteogenic activity and in vivo osseointegration," *Sci. Rep.*, vol. 6, p. 31769, Oct 2016.

[227] L. Carlsson, T. Röstlund, B. Albrektsson, T. Albrektsson, and P. I. Brånemark, "Osseointegration of titanium implants," *Acta Orthop. Scand.*, vol. 57, pp. 285–289, Jan 1986.

[228] S. Kothari, P. V. Hatton, and C. W. I. Douglas, "Protein adsorption to titania surfaces," *J. Mater. Sci. Mater. Med.*, vol. 6, pp. 695–698, Dec 1995.

[229] D. R. Jackson, S. Omanovic, and S. G. Roscoe, "Electrochemical studies of the adsorption behavior of serum proteins on titanium," *Langmuir*, vol. 16, pp. 5449–5457, Jun 2000.

[230] E. A. Dubiel, Y. Martin, and P. Vermette, "Bridging the gap between physicochemistry and interpretation prevalent in cell-surface interactions," *Chem. Rev.*, vol. 111, pp. 2900–2936, Apr 2011.

[231] B. Jachimska, K. Tokarczyk, M. Łapczyńska, A. Puciul-Malinowska, and S. Zapotoczny, "Structure of bovine serum albumin adsorbed on silica investigated by quartz crystal microbalance," *Colloids Surfaces A Physicochem. Eng. Asp.*, vol. 489, pp. 163–172, Jan 2016.

[232] B. Jachimska, M. Wasilewska, and Z. Adamczyk, "Characterization of globular protein solutions by dynamic light scattering, electrophoretic mobility, and viscosity measurements," *Langmuir*, vol. 24, pp. 6866–6872, Jul 2008.

[233] M. Khan, R. Williams, and D. Williams, "The corrosion behaviour of Ti-6Al-4V, Ti-6Al-7Nb and Ti-13Nb-13Zr in protein solutions," *Biomaterials*, vol. 20, pp. 631–637, Apr 1999.

[234] M. T. Stankovich and A. J. Bard, "The electrochemistry of proteins and related substances part III. Bovine serum albumin," *J. Electroanal. Chem. Interfacial Electrochem.*, vol. 86, pp. 189–199, Jan 1978.

[235] N. Padilla and A. Bronson, "Electrochemical characterization of albumin protein on Ti-6AL-4V alloy immersed in a simulated plasma solution," *J. Biomed. Mater. Res. Part A*, vol. 81A, pp. 531–543, Jun 2007.

[236] C. Valero Vidal and A. Igual Muñoz, "Electrochemical characterisation of biomedical alloys for surgical implants in simulated body fluids," *Corros. Sci.*, vol. 50, pp. 1954–1961, Jul 2008.

[237] N. P. Cosman and S. G. Roscoe, "Electrochemical quartz crystal nanobalance (EQCN) studies of protein interfacial behavior at Pt," *Langmuir*, vol. 20, pp. 1711–1720, Mar 2004.

[238] S. Omanovic and S. G. Roscoe, "Electrochemical studies of the adsorption behavior of bovine serum albumin on stainless steel," *Langmuir*, vol. 15, pp. 8315–8321, Nov 1999.

[239] S. G. Roscoe and K. L. Fuller, "Interfacial behavior of globular proteins at a platinum electrode," *J. Colloid Interface Sci.*, vol. 152, pp. 429–441, Sep 1992.

[240] F. Contu, "The cathodic behavior of titanium: serum effect," *J. Biomed. Mater. Res. Part B Appl. Biomater.*, vol. 100B, pp. 544–552, Feb 2012.

[241] C. Song and J. Zhang, *PEM fuel cell electrocatalysts and catalyst Layers*. Springer, 2008.

[242] B. Sivakumar, L. C. Pathak, and R. Singh, "Role of surface roughness on corrosion and fretting corrosion behaviour of commercially pure titanium in Ringer's solution for bio-implant application," *Appl. Surf. Sci.*, vol. 401, pp. 385–398, Apr 2017.

[243] A. S. Toloei, V. Stoilov, and D. O. Northwood, "Simultaneous effect of surface roughness and passivity on corrosion resistance of metals," vol. 90, pp. 355–367, Apr 2015.

[244] B. Burnat, M. Walkowiak-Przybyło, T. Błaszczyk, and L. Klimek, "Corrosion behaviour of polished and sandblasted titanium alloys in PBS solution," *Acta Bioeng. Biomech.*, vol. 15, no. 1, pp. 87–95, 2013.

[245] T. Fu, Z. Zhan, L. Zhang, Y. Yang, Z. Liu, J. Liu, L. Li, and X. Yu, "Effect of surface mechanical attrition treatment on corrosion resistance of commercial pure titanium," *Surf. Coatings Technol.*, vol. 280, pp. 129–135, Oct 2015.

[246] P. Heljo, K. Wolff, K. Lahtonen, M. Valden, P. Berger, H. Majumdar, and D. Lupo, "Anodic oxidation of ultra-thin Ti layers on ITO substrates and their application in organic electronic memory elements," *Electrochim. Acta*, vol. 137, pp. 91–98, Aug 2014.

[247] X. Zhang, Z. Jiang, Z. Yao, Y. Song, and Z. Wu, "Effects of scan rate on the potentiodynamic polarization curve obtained to determine the Tafel slopes and corrosion current density," *Corros. Sci.*, vol. 51, pp. 581–587, Mar 2009.

[248] A. P. Abbott, D. C. Loveday, and A. R. Hillman, "Quartz crystal microbalance study of the adsorption of ions onto gold from non-aqueous solvents," *J. Chem. Soc. Faraday Trans.*, vol. 90, no. 11, p. 1533, 1994.

[249] I. Van De Keere, S. Svedhem, H. Hogberg, J. Vereecken, B. Kasemo, and A. Hubin, "In situ control of the oxide layer on thermally evaporated titanium and lysozyme adsorption by means of electrochemical quartz crystal microbalance with dissipation," *ACS Appl. Mater. Interfaces*, vol. 1, pp. 301–310, Feb 2009.

[250] C. Valero-Vidal, A. Igual-Munoz, C. O. A. Olsson, and S. Mischler, "Adsorption of BSA on passivated CoCrMo PVD alloy: an EQCM and XPS investigation," *J. Electrochem. Soc.*, vol. 161, pp. C294–C301, Apr 2014.

[251] V. Payet, S. Brunner, A. Galtayries, I. Frateur, and P. Marcus, "Cleaning of albumin-contaminated Ti and Cr surfaces: An XPS and QCM study," *Surf. Interface Anal.*, vol. 40, no. 3-4, pp. 215–219, 2008.

[252] M. Ohring, *Reliability and Failure of Electronic Materials and Devices*. Academic Press, 1998.

[253] Y. Tanaka, H. Saito, Y. Tsutsumi, H. Doi, N. Nomura, H. Imai, and T. Hanawa, "Effect of pH on the interaction between zwitterions and titanium oxide," *J. Colloid Interface Sci.*, vol. 330, pp. 138–143, Feb 2009.

[254] M. Niinomi, "Biologically and mechanically biocompatible titanium alloys," *Mater. Trans.*, vol. 49, pp. 2170–2178, Sep 2008.

[255] C. N. Elias, J. H. C. Lima, R. Valiev, and M. A. Meyers, "Biomedical applications of titanium and its alloys," *JOM*, vol. 60, pp. 46–49, Mar 2008.

[256] S. Prasad, M. Ehrensberger, M. P. Gibson, H. Kim, and E. A. Monaco, "Biomaterial properties of titanium in dentistry," *J. Oral Biosci.*, vol. 57, pp. 192–199, Nov 2015.

[257] A. Tathe, M. Ghodke, and A. Nikalje, "A brief review: biomaterials and their application," *Int. J. Pharm. Pharm. Sci.*, vol. 2, pp. 19–23, Jul 2010.

[258] H. Rack and J. Qazi, "Titanium alloys for biomedical applications," *Mater. Sci. Eng. C*, vol. 26, pp. 1269–1277, Sep 2006.

[259] N. Manam, W. Harun, D. Shri, S. Ghani, T. Kurniawan, M. Ismail, and M. Ibrahim, "Study of corrosion in biocompatible metals for implants: a review," *J. Alloys Compd.*, vol. 701, pp. 698–715, Apr 2017.

[260] J. Rituerto Sin, A. Neville, and N. Emami, "Corrosion and tribocorrosion of hafnium in simulated body fluids," *J. Biomed. Mater. Res. Part B Appl. Biomater.*, vol. 102, pp. 1157–1164, Aug 2014.

[261] R. Bailey and Y. Sun, "Corrosion and tribocorrosion performance of thermally oxidized commercially pure titanium in a 0.9% NaCl solution," *J. Mater. Eng. Perform.*, vol. 24, pp. 1669–1678, Apr 2015.

[262] S. Mischler, A. Spiegel, and D. Landolt, "The role of passive oxide films on the degradation of steel in tribocorrosion systems," *Wear*, vol. 225-229, pp. 1078–1087, Apr 1999.

[263] S. Mischler and A. I. Muñoz, "Wear of CoCrMo alloys used in metal-on-metal hip joints: a tribocorrosion appraisal," *Wear*, vol. 297, pp. 1081–1094, Jan 2013.

[264] M. Altura and T. Altura, "Composition of interstitial fluid," vol. 41, no. 10, pp. 1522–1525, 1995.

[265] R. Munro, "Evaluated material properties for a sintered alpha-alumina," *J. Am. Ceram. Soc.*, vol. 80, pp. 1919–1928, Jan 2005.

[266] G. Adams and M. Nosonovsky, "Contact modeling forces," *Tribol. Int.*, vol. 33, pp. 431–442, May 2000.

[267] M. P. Licausi, A. Igual Muñoz, and V. A. Borrás, "Tribocorrosion mechanisms of Ti 6 Al 4 V biomedical alloys in artificial saliva with different pHs," *J. Phys. D. Appl. Phys.*, vol. 46, p. 404003, Oct 2013.

[268] V. G. Pina, A. Dalmau, F. Devesa, V. Amigó, and A. I. Muñoz, "Tribocorrosion behavior of beta titanium biomedical alloys in phosphate buffer saline solution," *J. Mech. Behav. Biomed. Mater.*, vol. 46, pp. 59–68, Jun 2015.

[269] A. Bazzoni, S. Mischler, and N. Espallargas, "Tribocorrosion of pulsed plasma-nitrided CoCrMo implant alloy," *Tribol. Lett.*, vol. 49, pp. 157–167, Jan 2013.

[270] A. Igual Muñoz and S. Mischler, "Effect of the environment on wear ranking and corrosion of biomedical CoCrMo alloys," *J. Mater. Sci. Mater. Med.*, vol. 22, pp. 437–450, Mar 2011.

[271] A. Molinari, G. Straffelini, B. Tesi, and T. Bacci, "Dry sliding wear mechanisms of the Ti6Al4V alloy," *Wear*, vol. 208, pp. 105–112, Jul 1997.

[272] D. Landolt, S. Mischler, M. Stemp, and S. Barril, "Third body effects and material fluxes in tribocorrosion systems involving a sliding contact," *Wear*, vol. 256, pp. 517–524, Mar 2004.

[273] D. R. Askeland, *The science and engineering of materials*. Springer, 1995.

[274] A. C. Lewis, M. R. Kilburn, P. J. Heard, T. B. Scott, K. R. Hallam, G. C. Allen, and I. D. Learmonth, "The entrapment of corrosion products from CoCr implant alloys in the deposits of calcium phosphate: a comparison of serum, synovial fluid, albumin, EDTA, and water," *J. Orthop. Res.*, vol. 24, pp. 1587–1596, Aug 2006.

[275] S. Pasche, J. Vörös, H. J. Griesser, N. D. Spencer, and M. Textor, "Effects of ionic strength and surface charge on protein adsorption at PEGylated surfaces.," *J. Phys. Chem. B*, vol. 109, pp. 17545–52, Sep 2005.

[276] M. F. Delcroix, S. Demoustier-Champagne, and C. C. Dupont-Gillain, "Quartz crystal microbalance study of ionic strength and pH-dependent polymer conformation and protein adsorption/desorption on PAA, PEO, and mixed PEO/PAA brushes," *Langmuir*, vol. 30, pp. 268–277, Jan 2014.

[277] T. S. Tsapikouni and Y. F. Missirlis, "Measuring the force of single protein molecule detachment from surfaces with AFM," *Colloids Surfaces B Biointerfaces*, vol. 75, pp. 252–259, Jan 2010.

[278] T. S. Tsapikouni and Y. F. Missirlis, "pH and ionic strength effect on single fibrinogen molecule adsorption on mica studied with AFM," *Colloids Surfaces B Biointerfaces*, vol. 57, pp. 89–96, May 2007.

[279] *Protein Database*, 2017. Available at `http://www.rcsb.org/pdb/home/home.do`.

[280] *PSF files, NAMD*, 2017. Available at `http://www.ks.uiuc.edu/Training/Tutorials/namd/namd-tutorial-unix-html/node23.html`.

[281] *CHARMM Force Field*, 2017. Available at `http://mackerell.umaryland.edu/charmm_ff.shtml`.

[282] *Topology files, NAMD*, 2017. Available at `http://www.ks.uiuc.edu/Training/Tutorials/namd/namd-tutorial-win-html/node25.html`.

[283] *Parameter files, NAMD*, 2017. Available at `http://www.ks.uiuc.edu/Training/Tutorials/namd/namd-tutorial-win-html/node26.html`.

[284] *NAMD manual*, 2017. Available at `http://www.ks.uiuc.edu/Training/Tutorials/namd/namd-tutorial-unix-html`.